THE UNIVERSITY OF QUEENSLAND

AUSTRALIA

Structural Modelling of Silicon Carbide-Derived Microporous Carbon and its Application in CO_2 Capture and Separation of Volatile Gases from Moist Streams

Amir Hajiahmadi Farmahini

B.Eng. - M.Sc.

A thesis submitted for the degree of Doctor of Philosophy at

The University of Queensland in 2015

School of Chemical Engineering

Abstract

The adsorption of volatile gases in microporous materials has wide applications in gas separation, including CO_2 capture and natural gas dehydration. It has also attracted a large amount of attention for energy storage applications such as electrochemical energy storage in supercapacitors and adsorptive methane/hydrogen storage. Nevertheless, the development of efficient gas storage/separation technologies requires fundamental knowledge of fluid transport in narrow pore spaces, since the behavior of fluids under tight confinement differs markedly from that in the bulk. Along with the rapid development of a broad range of new microporous materials such as carbide derived carbons (CDCs), carbon nanotubes and metal–organic frameworks, there has been wide growth in their potential applications, especially in emerging nanotechnologies, thus the development of this understanding has become even more crucial.

This study contributes to such understanding by investigating adsorption and transport of industrially important gases in the microporous structure of silicon carbide-derived carbon (SiC-DC). Initially, a realistic model of silicon carbide-derived carbon is developed using the hybrid reverse Monte Carlo (HRMC) method, which reliably represents the atomistic structure of the actual carbon sample and successfully predicts its gas adsorption and fluid transport properties. Following this part, structural characteristics of the constructed model are investigated using different computational methods to reveal the underlying correlations between such characteristics and the behavior of fluid transport in the highly disordered structure of SiC-DC. This study also explores adsorption and self-diffusion of fluid molecules in the amorphous SiC-CD model, providing more insight into the internal resistances and energy barriers to gas diffusion. The strong influence of structural heterogeneity arising from the disordered nature of the microporous carbon on molecular diffusion is also examined here using a range of computational techniques. The computational methods employed include molecular dynamics (MD) simulation, nudged elastic band (NEB) method and analysis of the free energy map of the system. It is shown that disordered structure of SiC-DC has larger energy barriers to diffusion of carbon dioxide, rather than methane despite smaller molecular size of CO_2. It is also demonstrated that activation energy barriers for methane obtained from MD simulation are in remarkable agreement with that of macroscopic kinetic uptake at low loading, which is an indication of accuracy of the HRMC constructed model in capturing internal resistances and constrictions of the actual sample. However, quasi elastic neutron scattering (QENS) measurements suggests a smaller activation energy barrier for methane compared to the results obtained from MD simulations and macroscopic kinetic uptake experiments, which is due to the much smaller length scale in QENS compared to the macroscopic length scale.

Due to the significance of water adsorption in industrial applications, one chapter of this study is exclusively dedicated to investigate adsorption and transport of water vapor in the hydrophobic microporous structure of SiC-DC. It is shown that the cooperative effect of pore confinement and electrostatically mediated hydrogen bonding has a critical influence, by facilitating the formation of water clusters. These clusters are shown to ultimately lead to pore blockage and disrupting fluid transport within pore network.

Further, this research focuses on the development of a fluorine-doped water-rejective structure, constructed based on the HRMC model of SiC-DC. In a unique study, the fluorine-doped structure of silicon carbide-derived carbon is modelled to investigate adsorption and transport of water vapor and carbon dioxide in an apparently hydrophobic microporous carbon structure. A new first-principles force field is developed to serve this purpose. It is demonstrated that while fluorination generates more hydrophilic carbon surfaces, they actually act as super-hydrophobic structures due to enhanced energy barriers in the disordered network of microporous carbon. This novel finding, in addition to the investigations of this study on internal energy barriers for non-polar gases, provides better understanding of the energy barriers to molecular transport in SiC-DC and the apparently dual effect of fluorination. It is demonstrated that such activation energy barriers stem from binding of fluid molecules inside the pore network, rather than repulsion or steric hindrance to the diffusion of molecules through narrow pore entries. It is shown that fluorination not only decreases adsorption of carbon dioxide in contrast to water, but also lowers the activation energy barrier for CO_2 diffusion in the microporous structure, thus it appears that fluorination can improve selectivity of CO_2 over water vapor in CO_2/H_2O gas mixtures.

The results obtained from this study not only help to provide better understanding of gas adsorption and fluid transport mechanisms in the pristine and fluorine-doped structure of disordered microporous carbon, but also to realise limitations of the current computational and experimental techniques for characterization of the structure, and investigations of the transport. This in turn will assist in providing directions for development of new modelling and characterization techniques.

Finally, it is noted that current thesis is organised based on publications, so that each chapter is self-subsistent, with its own independent nomenclature. Nevertheless, efforts have been made to organise the publications into chapters in logical and consistent sequence.

Declaration by author

This thesis is composed of my original work, and contains no material previously published or written by another person except where due reference has been made in the text. I have clearly stated the contribution by others to jointly-authored works that I have included in my thesis.

I have clearly stated the contribution of others to my thesis as a whole, including statistical assistance, survey design, data analysis, significant technical procedures, professional editorial advice, and any other original research work used or reported in my thesis. The content of my thesis is the result of work I have carried out since the commencement of my research higher degree candidature and does not include a substantial part of work that has been submitted to qualify for the award of any other degree or diploma in any university or other tertiary institution. I have clearly stated which parts of my thesis, if any, have been submitted to qualify for another award.

I acknowledge that an electronic copy of my thesis must be lodged with the University Library and, subject to the policy and procedures of The University of Queensland, the thesis be made available for research and study in accordance with the Copyright Act 1968 unless a period of embargo has been approved by the Dean of the Graduate School.

I acknowledge that copyright of all material contained in my thesis resides with the copyright holder(s) of that material. Where appropriate I have obtained copyright permission from the copyright holder to reproduce material in this thesis.

Publications during candidature

Peer-reviewed journal papers

1. Amir H. Farmahini, David S. Sholl, Suresh. K. Bhatia, Fluorinated carbide-derived carbon: more hydrophilic, yet apparently more hydrophobic. J. Am. Chem. Soc. (JACS), 2015. 137 (18): p. 5969-5979.
2. Amir H. Farmahini, Suresh K. Bhatia, Hybrid reverse Monte Carlo simulation of amorphous carbon: Distinguishing between competing structures obtained using different modeling protocols. Carbon, 2015. 83(0): p. 53-70.
3. Amir H. Farmahini, Suresh K. Bhatia, Differences in the adsorption and diffusion behaviour of water and non-polar gases in nanoporous carbon: Role of cooperative effects of pore confinement and hydrogen bonding. J. Mol. Sim., 2014. 41(5-6): p. 432-445.
4. Amir H. Farmahini, Ali Shahtalebi, Herve Jobic, Suresh K. Bhatia, Influence of structural heterogeneity on diffusion of CH_4 and CO_2 in silicon carbide-derived nanoporous carbon, , J. Phys. Chem. C, 2014. 118(22): p. 11784–11798.
5. Amir H. Farmahini, George Opletal, Suresh K. Bhatia, Structural modelling of silicon carbide-derived nanoporous carbon by hybrid reverse Monte Carlo simulation, J. Phys. Chem. C 2013. 117(27): p. 14081-14094.
6. Ali Shahtalebi, Pradeep Shukla, Amir H. Farmahini, Suresh K. Bhatia, Barriers to diffusion of CO_2 in microporous carbon derived from silicon carbide. Carbon, 2015. 88(0): p. 1-15.
7. Ali Shahtalebi, Amir H. Farmahini, Pradeep Shukla, Suresh K. Bhatia, Slow diffusion of methane in ultra-micropores of silicon carbide-derived carbon, Carbon, 2014. 77(0): p. 560-576.

Conference abstracts (speaker underlined)

1. Amir H. Farmahini, David S. Sholl, Suresh K. Bhatia, Simulation of the effect of fluorine-doping on the adsorption and transport of water and carbon-dioxide in silicon carbide-derived carbon, Carbon 2015, Dresden - Germany, July 12-17, 2015.
2. Suresh K. Bhatia, Amir H. Farmahini, Ali Shahtalebi, Effect of ultra-microporosity on equilibrium and transport of gases in carbons as revealed by simulation and experiment, Characterization of Porous Materials (CPM-7), Florida - USA, May 3-6, 2015.
3. Amir. H. Farmahini, Ali Shahtalebi, Herve Jobic, Suresh. K. Bhatia, Influence of structural heterogeneity on the transport of gases in microporous silicon carbide-derived carbon, OZ Carbon 2014 as part of RACI National Congress, Adelaide - Australia, Dec. 7-12, 2014.

4. Amir H. Farmahini, Ali Shahtalebi, Suresh K. Bhatia, Computational and experimental characterization of microporous silicon-carbide derived carbon, 10th International Symposium on the Characterization of Porous Solids (COPS-10), Granada - Spain, May 11-14, 2014.
5. Amir H. Farmahini, Suresh K. Bhatia, Structural modelling of microporous silicon carbide-derived carbon, 11th International Conference on the Fundamentals of Adsorption (FOA11), Baltimore - USA, May 19-24, 2013.
6. Amir H. Farmahini, Suresh K. Bhatia, Atomistic modelling of the structure of silicon carbide-derived nanoporous carbon, 1st International Conference on Emerging Advanced Nanomaterials (ICEAN 2012), Brisbane - Australia, Oct. 22-25, 2012.
7. Amir H. Farmahini, George Opletal, Suresh K. Bhatia, Atomistic modelling of microporous carbide derived carbons using hybrid reverse Monte Carlo (HRMC) approach, Carbon 2012, Krakow - Poland, June 17-22, 2012.

Publications included in this thesis

1. Farmahini, A. H., Sholl, D. S., Bhatia, S. K., Fluorinated carbide-derived carbon: more hydrophilic, yet apparently more hydrophobic. J. Am. Chem. Soc. (JACS), 2015. 137 (18): p. 5969-5979.

Contributor	Statement of contribution
Farmahini, Amir. H. (Candidate)	Performed simulations and modeling (100%) Analyzed and interpreted the results (100%) Wrote and edited the paper (80%)
Sholl, David. S.	Commented on the paper (10%)
Bhatia, Suresh K.	Commented on and edited the paper (10%)

2. Farmahini, A. H., Bhatia, S. K., Hybrid reverse Monte Carlo simulation of amorphous carbon: Distinguishing between competing structures obtained using different modeling protocols. Carbon, 2015. 83(0): p. 53-70.

Contributor	Statement of contribution

Farmahini, Amir. H. (Candidate)	Performed simulations and modeling (100%) Analyzed and interpreted the results (100%) Wrote and edited the paper (80%)
Bhatia, Suresh K.	Commented on and edited the paper (20%)

3. Farmahini, A. H., Bhatia, S. K., Differences in the adsorption and diffusion behaviour of water and non-polar gases in nanoporous carbon: Role of cooperative effects of pore confinement and hydrogen bonding. J. Mol. Sim., 2014. 41(5-6): p. 432-445.

Contributor	Statement of contribution
Farmahini, Amir. H. (Candidate)	Performed simulations and modeling (100%) Analyzed and interpreted the results (100%) Wrote and edited the paper (80%)
Bhatia, Suresh K.	Commented on and edited the paper (20%)

4. Farmahini, A. H., Shahtalebi, A., Jobic, H., Bhatia, S. K., Influence of structural heterogeneity on diffusion of CH_4 and CO_2 in silicon carbide-derived nanoporous carbon, J. Phys. Chem. C, 2014. 118(22): p. 11784–11798.

Contributor	Statement of contribution
Farmahini, Amir. H. (Candidate)	Performed simulations and modeling (100%) Analyzed and interpreted the results (100%) Wrote and edited the paper (80%)
Shahtalebi, A.	Performed kinetic uptake experiments (100%)
Jobic, H.	Performed QENS experiments (100%)
Bhatia, Suresh K.	Commented on and edited the paper (20%)

5. Farmahini, A. H., Opletal, G., Bhatia, S. K., Structural modelling of silicon carbide-derived nanoporous carbon by hybrid reverse Monte Carlo simulation, J. Phys. Chem. C 2013. 117(27): p. 14081-14094.

Contributor	Statement of contribution
Farmahini, Amir. H. (Candidate)	Performed simulations and modeling (100%) Analyzed and interpreted the results (100%) Wrote and edited the paper (80%)
Opletal, G.	Wrote HRMC code (100%)
Bhatia, Suresh K.	Commented and edited the paper (20%)

Contributions by others to the thesis

Nil.

Statement of parts of the thesis submitted to qualify for the award of another degree

Nil.

Acknowledgements

Achieving a Ph.D. degree has been always an important professional aspiration for me, and today that this dream is finally coming true, I am more than ever grateful to all those people, who made this achievement possible.

First and the foremost, I owe my deepest gratitude to my principal advisor, Prof. Suresh Kumar Bhatia, who offered me the opportunity to join his distinguished research group as a Ph.D. candidate. My Ph.D. studies under his supervision have been a fruitful endeavor, during which I could significantly improve my knowledge. He is not only a great advisor, but a supportive teacher and a leading scientist and intellectual. It has been my biggest honor to work with him.

I wish to thank my co-advisor Dr. Timothy Nicholson, as well as members of my candidature examination committee Prof. Victor Rudolph and Prof. Duong Do for their instructive recommendations during my candidature.

It has been an honor and privilege to work with Prof. David S. Sholl, head of the School of Chemical and Biomolecular Engineering in the Georgia Institute of Technology, USA. I am thankful to him for his invitation to work with his research group for a period of six months as a visiting research scholar during my Ph.D. candidature.

I am absolutely delighted to have worked with the following individuals, who generously shared their knowledge and time with me and contributed to my learning process:

Prof. David Nicholson, Prof. Debra Bernhardt and Dr. Mauricio Rincon Bonilla from University of Queensland (UQ), Dr. George Opletal of RMIT University, Dr. Lev Sarkisov from University of Edinburgh and Dr. Hanjun Fang from Georgia Institute of Technology.

There were also many other individuals, who made this Ph.D. study an unforgettable experience. I am particularly grateful to my friends and fellow Ph.D. students in the School of Chemical Engineering at UQ. From my visit to the Georgia Institute of Technology, I cannot forget Ross Verploegh, a fellow Ph.D. student, whose honest friendship has been so valuable to me. At the end of the friends list that I would like to thank is a true friend of mine, Hamed Sanjabi, who is and will ever be my closest friend. His selfless friendship, even when he has not been by my side, has been always felt in my heart.

I would also like to take this opportunity to extend my appreciation to all my teachers, from my first grade elementary school in Iran to my post-graduate education in Norway, USA and Australia. I owe them all, what I am today!

Finally, I wish to acknowledge the UQI scholarship provided by the School of Chemical Engineering and the Graduate School of the University of Queensland to support my Ph.D. studies at UQ.

Keywords

nanoporous materials, adsorption, diffusion, separation process, gas dehydration, fluorine-doped microporous carbon, hybrid reverse Monte Carlo, molecular dynamics, Density functional theory, ab-initio calculations.

Australian and New Zealand Standard Research Classifications (ANZSRC)

ANZSRC code: 090401 Carbon Capture Engineering (excl. Sequestration) 50%

ANZSRC code: 090404 Membrane and Separation Technologies 50%

Fields of Research (FoR) Classification

FoR code: 0904, Chemical Engineering, 100%

گر راه نمایی، همه عالم راهست

ور دست نگیری، همه عالم چاهست

«سعدی»

Dedication

I would like to dedicate this present work to my family, to whom I am forever indebted; my dear father, Faramarz; my beloved mother, Azam; and my lovely sisters, Baharak and Taraneh. Whatever I have achieved in my life, I owe it to my family. I like to thank them for their endless and unconditional love and support during my entire life.

Table of content

List of Figures

List of Tables

List of Abbreviations

AC	Activated Carbon
ACF	Auto Correlation Function
ACF	Activated Carbon Fiber
ADM	Advective-Diffusive Model
ANU	Australian National University
ARC	Australian Research Council
BET	Brunauer–Emmett–Teller
CDC	Carbide-Derived Carbon
COF	Covalent Organic Framework
CRMC	Constrained Reverse Monte Carlo
DDEC	Density-Derived Electrostatic and Chemical
DFT	Density Functional Theory
DGM	Dusty Gas Model
EDIP	Environment Dependent Interaction Potential
EMD	Equilibrium Molecular Dynamics
FWT-DFT	Finite-Wall Thickness Density Functional Theory
GaTech	Georgia Institute of Technology
GCMC	Grand Canonical Monte Carlo
GGA	Generalized Gradient Approximation
GULP	General Utility Lattice Program
HB	hydrogen bond
HRMC	Hybrid Reverse Monte Carlo
HRTEM	High-Resolution Transmission Electron Microscopy
hTST	Harmonic Approximation of the Transition State Theory
ILL	Institut Laue-Langevin
IUPAC	International Union of Pure and Applied Chemistry
LAMMPS	Large-scale Atomic/Molecular Massively Parallel Simulator
LJ	Lennard-Jones
LoC	Lab-on-a Chip
MD	Molecular Dynamics
MEP	Minimum Energy Path
MMC	Metropolis Monte Carlo
MOF	Metal Organic Frameworks
MS	Maxwell-Stefan
MSD	Mean-Squared Displacement
NCI	National Computational Infrastructure
NEB	Nudged-Elastic Band
OPLS	Optimized Potentials for Liquid Simulations
PACE	Partnership for an Advanced Computing Environment
PAW	Projector Augmented Wave
PBC	Periodic Boundary Conditions
PBE	Perdew-Burke-Ernzerhof
PDF	Probability Distribution Function
PES	Potential Energy Surface
PFG-NMR	Pulsed Field Gradient-Nuclear Magnetic Resonance

PNM	Pore Network Modelling
PSD	Pore Size Distribution
QENS	Quasi Elastic Neutron Scattering
QMD	Quench Molecular Dynamics
QSDFT	Quenched Solid Density Functional Theory
REBO	Reactive Empirical Bond Order
RDF	Radial Distribution Function
RMC	Reverse Monte Carlo
RSS	Reaction State Summation
SA	Surface Area
SANS	Small Angle Neutron Scattering
SF	Structure Factor
SPC	Simple Point Charge
SPC/E	Extended Simple Point Charge
SPE	Single Point Energy
STW	Stone-Thrower-Wales
TraPPE	Transferable Potentials for Phase Equilibria Force Field
UFF	Universal Force Field
UQ	University of Queensland
VASP	Vienna Ab-initio Simulation Package
vdW	van der Waals
XRD	X-Ray Crystallography
ZIF	Zeolitic Imidazolate Framework
ZLC	Zero Length Column

1. Introduction

1.1. Background

Modeling gas adsorption and transport of volatile gases in heterogeneous structure of microporous materials is currently an important topic in the field of gas processing and separation technologies [1, 2]. This topic has received considerable attention over the last century, however its new popularity is due to dramatic increase in fabrication and synthesis of novel classes of microporous materials such as carbon nanotubes [3, 4], metal–organic frameworks (MOFs) [5-7], zeolites [8, 9] and carbonaceous compounds [10, 11]. Enhanced understanding of fluidic phenomena and transport properties of fluid molecules in nanoscale confinement of heterogeneous pore spaces is critical for advancing emerging technologies in nanofluidics, gas storage and separation, petroleum refining, heterogeneous catalysis, electrochemical energy storage, nanotechnology and materials screening [2, 12].

An important class of microporous materials is synthesized from carbonaceous precursors [10, 11], among which the so-called carbide-derived carbons (CDCs) hold promise for a wide range of applications [11, 13, 14]. They have demonstrated a broad range of functionality coming from their unique structural properties, which combine high capacity and high surface area with tunability of the pore size distribution [13]. Although much attention has been paid to synthesis and experimental characterization of carbide-derived carbons [13, 15-24], fundamental studies on understanding fluid transport in pore network structure of these materials still require comprehensive investigations, considering transport properties of fluid molecules in microporous materials are not very well understood. In this regard, established theoretical approaches such as those of dusty gas model (DGM) [25] or Knudsen model have limited applications in nanoscale confinements [26, 27]. Moreover, Maxwell-Stefan type models [2, 28, 29] neglect the effect of fluid inhomogeneities in mixture adsorption [2] and more robust models based on the Boltzman equation rely on approximations [30], which are not necessarily accurate in narrow nanopores [26]. Nonetheless, molecular simulation techniques including grand canonical Monte Carlo (GCMC) and molecular dynamics (MD) simulation can provide rigorous predictions of gas adsorption and fluid transport in confined spaces, if realistic models of the pore network structure, as well as reliable force fields for interatomic interactions are provided.

Hitherto, many studies concerning modeling gas adsorption and fluid transport in CDCs and other carbonaceous materials have relied on the use of idealistic models of pore structure (e.g. slit-pore or

cylindrical models), neglecting or diminishing important effects of structural heterogeneity on adsorption process [16, 31-40], nevertheless realistic modeling of pore structure is now within reach using methods such as hybrid reverse Monte Carlo (HRMC) [41-43]. Therefore, new studies of fluid transport in disordered materials are expected to appropriately address this issue to provide more insight into the effect of structural heterogeneity, topology and morphology of the pore network on fluid transport using such realistic models. A handful of recent studies, which have been conducted based on these modeling techniques have proven reliability and advantages of this approach over the use of traditional slit-pore models [44-49]. Added to this, having access to accurately constructed atomistic models of porous media has provided us with a unique opportunity to further explore functionalized forms of these pore networks, which is crucial for design and development of adsorbent structures with enhanced adsorption capacity or improved hydrophobicity. We can now study effect of heteroatom doping of the pore network on fluid transport to provide more insight into the underlying mechanisms, which lead to enhancement of gas uptake, increase of fluid mobility and promotion of hydrophobicity / hydrophilicity in the system. This type of knowledge is important for improvement of the design and fabrication of new generation of adsorbents required in emerging gas separation technologies.

1.2. Scope of the work

Modeling and characterization of microporous carbons in addition to investigation of fluid transport in nanoporous materials have been of continuous interest for this laboratory in recent years [24, 31, 50-54]. In pursuit of these efforts, this thesis seeks to address some of the most challenging issues in modeling gas adsorption and transport of volatile gases in highly amorphous structure of silicon carbide-derived carbon (SiC-DC), which is shown to be a promising candidate for carbon dioxide capture due to its high-capacity and high-surface area structure [16, 31, 55]. SiC-DC is also seen as a novel material for gas separation and manufacturing high rate electrochemical capacitors because of its narrow distribution of micropores [13, 56].

It was noted that except a handful of recent studies, most of the previous investigations on modeling gas adsorption and fluid transport in microporous carbon materials suffer from the use of simplified adsorbent models. In contrast, this study aims at providing a realistic atomistic model of the highly disordered microporous structure of SiC-DC. The hybrid reverse Monte Carlo (HRMC) modeling technique is employed to construct a realistic model of this material, which is subsequently used for modeling gas adsorption and investigation of fluid transport in this structure. After the modeling stage is completed, the final HRMC constructed model is characterized using different

computational techniques. It is also validated against a wide range of experimental structural characterization data, equilibrium adsorption isotherms and macroscopic uptake transport data.

As stated before, the effect of structural heterogeneity has been largely disregarded or simplified in studies related to investigation of fluidic phenomena in amorphous carbon, nevertheless in this work, effect of structural heterogeneity on transport properties of industrially important gases such as methane, carbon dioxide and water is exclusively studied to elucidate the effect of internal energy barriers arising from structural heterogeneity of the pore network on fluid transport in nanoscale confinement of microporous materials. Subsequently, this study discusses advantages of the realistic approaches in modeling of pore morphology and topology of the system.

This thesis is also framed to investigate intriguing features of water adsorption and diffusion in the hydrophobic structure of SiC-DC, arising from cooperative effect of pore confinement and hydrogen bonding. This section delivers better understanding of important mechanisms, which lead to pore blocking phenomenon as a result of water adsorption in micropores. This understanding is specifically crucial for development of tailored adsorbents for gas dehydration applications, considering co-adsorption of water and carbon dioxide can have negative effect on capacity of the carbon capture facilities due to adsorption of large amount of water.

To provide a solution to undesired co-adsorption of water and CO_2 in the microporous carbon materials, this study conducts comprehensive investigations on fluorination of the amorphous structure of silicon carbide-derived carbon. For the first time, in this study, fluorination of microporous carbon is thoroughly investigated based on a realistic model, which can accurately reproduce experimental characteristics of the actual carbon sample. In the last chapter of this thesis, the design and modeling of three different fluorine-doped SiC-DC models are reported. Due to the lack of reliable force fields for simulation of adsorption and diffusion of water and carbon dioxide in fluorinated porous carbon, a novel first-principles force field is developed using ab-inito calculations. Subsequently, adsorption and diffusion of CO_2 and water vapor in the fluorinated structure of SiC-DC is investigated, highlighting effect of internal energy barriers arising from fluorination of the SiC-DC on hydrophobicity of the fluorinated carbon. This study reveals dual effect of fluorination on water adsorption, showing that fluorine-doped SiC-DC consists of more hydrophilic carbon surfaces compared to the virgin carbon, while apparently having extremely retarded water adsorption kinetics due to its internal energy barriers, which make the structure super-hydrophobic in real applications.

1.3. Structure of the thesis

This thesis is structured based on peer-reviewed publications, which have been made throughout Ph.D. studies of the candidate. Nevertheless, the journal papers are organised into chapters in a logical and consistent sequence.

Chapter 1 – Introduction

Chapter 1 briefly introduces this study by defining the goals and scope of the work. It provides a short background of this study, while drawing attention to the gaps and existing questions in the field. It also introduces structure of the thesis and clarifies direction of the study.

Chapter 2 – Literature review

Chapter 2 explains background of the study in greater details. Available literature related to the topic of the thesis is reviewed from a critical stand point and computational methods employed in this research is presented.

Chapter 3 - Structural modelling of silicon carbide-derived nanoporous carbon by hybrid reverse Monte Carlo simulation

This chapter describes realistic modeling of silicon carbide-derived carbon using hybrid reverse Monte Carlo (HRMC) modeling technique. It explains the procedure followed for construction of a reliable atomistic model of the amorphous SiC-DC, which is the fundamental part of this study, considering the following chapters rely upon accuracy and reliability of this model. The chapter also discusses structural characteristics of the constructed model including pore volume, specific surface area, pore size distribution (PSD) and associated structural defects. Chapter 3 provides evidence for validation of the constructed model against experimental equilibrium adsorption isotherms of argon, carbon dioxide and methane.

Chapter 4 - Hybrid reverse Monte Carlo simulation of amorphous carbon: Distinguishing between competing structures obtained using different modelling protocols

Due to importance of the structural modeling topic, as well as complexities of realistic modeling of highly disordered carbon structures such as SiC-DC, Chapter 4 is designed to provide an in-depth understanding of how different modeling protocols and simulation parameters affect structural features of the HRMC constructed models. This chapter specifically aims at distinguishing between different competing models, each of which constructed based on a different modeling protocol. The

information provided here will be useful for other researchers who are interested in modeling of similar complex structures using the HRMC method. Additionally, Chapter 4 emphasizes the standpoint of this investigation on necessity of comprehensive validations of the constructed models against a wide range of experimental data. It also provides further evidence for reliability of the chosen HRMC constructed model introduced in Chapter 3.

Chapter 5 - Influence of structural heterogeneity on diffusion of CH_4 and CO_2 in silicon carbide-derived nanoporous carbon

Chapter 5 investigates fluid transport and transport properties of carbon dioxide and methane in microporous structure of SiC-DC due to their importance in industrial separation processes. The chapter provides tangible evidence on the effect of structural heterogeneity and internal energy barriers on transport of fluid molecules in disordered structure of SiC-DC using a combination of experimental and computational studies including quasi elastic neutron scattering (QENS), kinetic uptake measurements, molecular dynamics (MD) simulation and nudged elastic band (NEB) technique.

Chapter 6 - Differences in the adsorption and diffusion behaviour of water and non-polar gases in nanoporous carbon: Role of cooperative effects of pore confinement and hydrogen bonding

Chapter 6 studies adsorption and diffusion of a range of different non-polar gases including neopentane, sulfur hexafluoride, propene, carbon dioxide, methane and argon in microporous structure of SiC-DC and compares the results with those of water, highlighting intriguing features of water transport in nanoporous structure of SiC-DC, especially cooperative effect of hydrogen bonding and pore space confinement. This chapter reveals interesting information regarding different forms of internal energy barriers against transport of water and non-polar gases arising from different sources. The information provided in this chapter helps to explain how water adsorbs in hydrophobic microporous structure of pristine SiC-DC. It also provides the crucial understanding required for the design and development of super-hydrophobic models of fluorine-doped SiC-DC, which are discussed in Chapter 7.

Chapter 7 – Fluorinated carbide-derived carbon: More hydrophilic, yet apparently more hydrophobic

This chapter forms an important part of the current thesis. It presents a unique study on the effect of fluorination on adsorption and diffusion of water vapor and carbon dioxide in fluorinated structure

of SiC-DC. The chapter also reports on development of a novel first-principles force field for adsorption and transport of these gases in fluorinated microporous carbon. This study reveals dual effect of fluorination on water adsorption, showing that fluorine-doped SiC-DC increases surface hydrophilicity, but at the same time enhances internal energy barriers of the system, which make the structure more hydrophobic.

Chapter 8 – Conclusion and recommendations

Chapter 8 explains contributions of the current Ph.D. thesis to the field by summarizing the most important findings of this study. Further investigations, as well as directions for the future studies are also recommended in this chapter.

Following diagram provides a visual illustration of different topics, discussed in each chapter of this thesis:

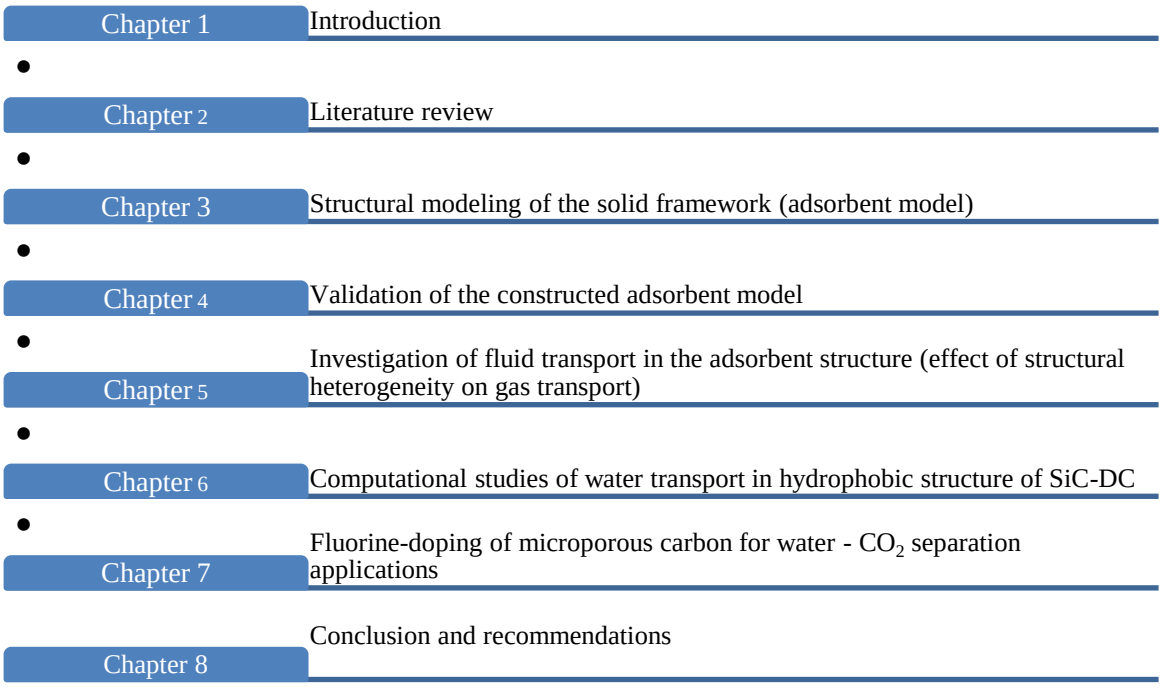

1.4. References

1. Gubbins, K.E., et al., *The role of molecular modeling in confined systems: impact and prospects.* Physical Chemistry Chemical Physics, 2011. **13**(1): p. 58-85.
2. Bhatia, S.K., M.R. Bonilla, and D. Nicholson, *Molecular transport in nanopores: a theoretical perspective.* Physical Chemistry Chemical Physics, 2011. **13**(34): p. 15350-15383.
3. Zhou, W., et al., *Synthesis, Structure, and Properties of Single-Walled Carbon Nanotubes.* Advanced Materials, 2009. **21**(45): p. 4565-4583.
4. Thostenson, E.T., Z. Ren, and T.-W. Chou, *Advances in the science and technology of carbon nanotubes and their composites: a review.* Composites Science and Technology, 2001. **61**(13): p. 1899-1912.
5. Mueller, U., et al., *Metal-organic frameworks-prospective industrial applications.* Journal of Materials Chemistry, 2006. **16**(7): p. 626-636.
6. James, S.L., *Metal-organic frameworks.* Chemical Society Reviews, 2003. **32**(5): p. 276-288.
7. Czaja, A.U., N. Trukhan, and U. Muller, *Industrial applications of metal-organic frameworks.* Chemical Society Reviews, 2009. **38**(5): p. 1284-1293.
8. Čejka, J., et al., *Introduction to Zeolite Science and Practice*. 2007, Amsterdam Elsevier.
9. McLeary, E.E., J.C. Jansen, and F. Kapteijn, *Zeolite based films, membranes and membrane reactors: Progress and prospects.* Microporous and Mesoporous Materials, 2006. **90**(1–3): p. 198-220.
10. Marsh, H., *Activated Carbon Compendium*. First ed. 2001: Elsevier Science Ltd. 320.
11. Gogotsi, Y., *Carbon Nanomaterials*. 2006, Boca Raton, FL Taylor & Francis. 326
12. Schoch, R.B., J. Han, and P. Renaud, *Transport phenomena in nanofluidics.* Reviews of Modern Physics, 2008. **80**(3): p. 839-883.
13. Gogotsi, Y., et al., *Nanoporous carbide-derived carbon with tunable pore size.* Nature Materials, 2003. **2**(9): p. 591-594.
14. Presser, V., M. Heon, and Y. Gogotsi, *Carbide-Derived Carbons – From Porous Networks to Nanotubes and Graphene.* Advanced Functional Materials, 2011. **21**(5): p. 810-833.
15. Gogotsi, Y., et al., *Tailoring of Nanoscale Porosity in Carbide-Derived Carbons for Hydrogen Storage.* Journal of the American Chemical Society, 2005. **127**(46): p. 16006-16007.
16. Nguyen, T.X., J.S. Bae, and S.K. Bhatia, *Characterization and Adsorption Modeling of Silicon Carbide-Derived Carbons.* Langmuir, 2009. **25**(4): p. 2121-2132.
17. Dash, R.K., A. Nikitin, and Y. Gogotsi, *Microporous carbon derived from boron carbide.* Microporous and Mesoporous Materials, 2004. **72**(1-3): p. 203-208.
18. Gogotsi, Y., et al., *Conversion of silicon carbide to crystalline diamond-structured carbon at ambient pressure.* Nature, 2001. **411**(6835): p. 283-287.
19. Gogotsi, Y.G. and M. Yoshimura, *Formation of carbon films on carbides under hydrothermal conditions.* Nature, 1994. **367**(6464): p. 628-630.
20. Nguyen, T.X. and S.K. Bhatia, *Characterization of accessible and inaccessible pores in microporous carbons by a combination of adsorption and small angle neutron scattering.* Carbon, 2012. **50**(8): p. 3045-3054.
21. Sevilla, M. and R. Mokaya, *Activation of carbide-derived carbons: a route to materials with enhanced gas and energy storage properties.* Journal of Materials Chemistry, 2011. **21**(13): p. 4727-4732.
22. Welz, S., M.J. McNallan, and Y. Gogotsi, *Carbon structures in silicon carbide derived carbon.* Journal of Materials Processing Technology, 2006. **179**(1-3): p. 11-22.

23. Bae, J.-S., T.X. Nguyen, and S.K. Bhatia, *Influence of Synthesis Conditions and Heat Treatment on the Structure of Ti3SiC2-Derived Carbons.* The Journal of Physical Chemistry C, 2009. **114**(2): p. 1046-1056.
24. Bae, J.-S., T.X. Nguyen, and S.K. Bhatia, *Pore accessibility of Ti3SiC2-derived carbons.* Carbon, 2014. **68**(0): p. 531-541.
25. Mason, E.A. and A.P. Malinauskas, *Gas Transport in Porous Media: The Dusty-Gas Model*. 1983, Amsterdam: Elsevier.
26. Bhatia, S.K. and D. Nicholson, *Modeling Self-Diffusion of Simple Fluids in Nanopores.* Journal of Physical Chemistry B, 2011: p. 11700–11711.
27. Bhatia, S.K. and D. Nicholson, *Some pitfalls in the use of the Knudsen equation in modelling diffusion in nanoporous materials.* Chemical Engineering Science, 2011. **66**(3): p. 284-293.
28. Krishna, R., *Multicomponent surface diffusion of adsorbed species: a description based on the generalized Maxwell—Stefan equations.* Chemical Engineering Science, 1990. **45**(7): p. 1779-1791.
29. Krishna, R., *Problems and pitfalls in the use of the fick formulation for intraparticle diffusion.* Chemical Engineering Science, 1993. **48**(5): p. 845-861.
30. Bhatnagar, P.L., E.P. Gross, and M. Krook, *A Model for Collision Processes in Gases. I. Small Amplitude Processes in Charged and Neutral One-Component Systems.* Physical Review, 1954. **94**(3): p. 511-525.
31. Bonilla, M.R.n., et al., *Heat Treatment-Induced Structural Changes in SiC-Derived Carbons and their Impact on Gas Storage Potential.* The Journal of Physical Chemistry C, 2010. **114**(39): p. 16562-16575.
32. Bhatia, S.K., et al., *High-Pressure Adsorption Capacity and Structure of CO2 in Carbon Slit Pores: Theory and Simulation.* Langmuir, 2004. **20**(22): p. 9612-9620.
33. McCallum, C.L., et al., *A Molecular Model for Adsorption of Water on Activated Carbon: Comparison of Simulation and Experiment.* Langmuir, 1998. **15**(2): p. 533-544.
34. Nguyen, T.X. and S.K. Bhatia, *Characterization of Pore Wall Heterogeneity in Nanoporous Carbons Using Adsorption: the Slit Pore Model Revisited.* The Journal of Physical Chemistry B, 2004. **108**(37): p. 14032-14042.
35. Nguyen, T.X., S.K. Bhatia, and D. Nicholson, *Prediction of High-Pressure Adsorption Equilibrium of Supercritical Gases Using Density Functional Theory.* Langmuir, 2005. **21**(7): p. 3187-3197.
36. Liu, J.C. and P.A. Monson, *Does Water Condense in Carbon Pores?†.* Langmuir, 2005. **21**(22): p. 10219-10225.
37. Tan, Z. and K.E. Gubbins, *Selective adsorption of simple mixtures in slit pores: a model of methane-ethane mixtures in carbon.* The Journal of Physical Chemistry, 1992. **96**(2): p. 845-854.
38. Shigeta, T., J. Yoneya, and T. Nitta, *Monte Carlo Simulation Study of Adsorption Characteristics in Slit-Like Micropores Under Supercritical Conditions.* Molecular Simulation, 1996. **16**(4-6): p. 291-305.
39. Jiang, S., J.A. Zollweg, and K.E. Gubbins, *High-Pressure Adsorption of Methane and Ethane in Activated Carbon and Carbon Fibers.* The Journal of Physical Chemistry, 1994. **98**(22): p. 5709-5713.
40. Lastoskie, C., K.E. Gubbins, and N. Quirke, *Pore size distribution analysis of microporous carbons: a density functional theory approach.* The Journal of Physical Chemistry, 1993. **97**(18): p. 4786-4796.
41. Opletal, G., et al., *Hybrid approach for generating realistic amorphous carbon structure using metropolis and reverse Monte Carlo.* Molecular Simulation, 2002. **28**(10-11): p. 927-938.

42. Opletal, G., et al., *HRMC_2.0: Hybrid Reverse Monte Carlo method with silicon, carbon and germanium potentials.* Computer Physics Communications, 2013. **184**(8): p. 1946-1957.
43. Jain, S.K., et al., *Molecular Modeling of Porous Carbons Using the Hybrid Reverse Monte Carlo Method.* Langmuir, 2006. **22**(24): p. 9942-9948.
44. Palmer, J.C., et al., *Detailed structural models for activated carbons from molecular simulation.* Carbon, 2009. **47**(12): p. 2904-2913.
45. Coasne, B., S.K. Jain, and K.E. Gubbins, *Adsorption, structure and dynamics of fluids in ordered and disordered models of porous carbons.* Molecular Physics, 2006. **104**(22-24): p. 3491-3499.
46. Coasne, B., S.K. Jain, and K.E. Gubbins, *Adsorption and dynamics of argon in porous carbons.* The European Physical Journal Special Topics, 2007. **141**(1): p. 121-125.
47. Pikunic, J. and K. Gubbins, *Molecular dynamics simulations of simple fluids confined in realistic models of nanoporous carbons.* European Physical Journal E: Soft Matter and Biological Physics, 2003. **12**(1): p. 35-40.
48. Nguyen, T.X., et al., *Structure of saccharose-based carbon and transport of confined fluids: hybrid reverse Monte Carlo reconstruction and simulation studies.* Molecular Simulation, 2006. **32**(7): p. 567-577.
49. Nguyen, T.X., et al., *New Method for Atomistic Modeling of the Microstructure of Activated Carbons Using Hybrid Reverse Monte Carlo Simulation.* Langmuir, 2008. **24**(15): p. 7912-7922.
50. Nguyen, T.X., *Characterization of nanoporous carbons*, in *School of Chemical Engineering*. 2006, The University of Queensland (UQ): Brisbane. p. 301.
51. Rincon Bonilla, M., *Multiscale modelling of transport in porous media*, in *School of Chemical Engineering*. 2013, The University of Queensland: Brisbane. p. 282.
52. Nicholson, D. and S.K. Bhatia, *Fluid transport in nanospaces.* Molecular Simulation, 2009. **35**(1-2): p. 109-121.
53. Bhatia, S.K. and D. Nicholson, *Friction between Solids and Adsorbed Fluids is Spatially Distributed at the Nanoscale.* Langmuir, 2013. **29**(47): p. 14519-14526.
54. Nguyen, T.X., H. Jobic, and S.K. Bhatia, *Microscopic Observation of Kinetic Molecular Sieving of Hydrogen Isotopes in a Nanoporous Material.* Physical Review Letters, 2010. **105**(8): p. 085901.
55. Bhatia, S.K. and T.X. Nguyen, *Potential of Silicon Carbide-Derived Carbon for Carbon Capture.* Industrial & Engineering Chemistry Research, 2011. **50**(17): p. 10380-10383.
56. Korenblit, Y., et al., *High-Rate Electrochemical Capacitors Based on Ordered Mesoporous Silicon Carbide-Derived Carbon.* ACS Nano, 2010. **4**(3): p. 1337-1344.

2. Literature Review

2.1. Introduction

Porous media form an important class of materials [1, 2] with significant industrial and scientific applications. From vehicular natural gas storage [3] to hydrogen storage [4], from carbon dioxide capture [5] to gas separation [6-8] and from miniaturized screening devices [9] to lab-on-a chip technology [10] porous materials have seen a broad range of applications. A large variety of ordered and disordered porous materials including Zeolites [11, 12], Metal Organic Frameworks (MOFs) [13-15] and porous carbons [16-19] has been synthesized and tailored for these applications. According to the classification of the International Union of Pure and Applied Chemistry (IUPAC), porous materials with pore width not exceeding 20 Å are considered as microporous media. On the other hand, porous structures with pore width larger than 0.05 μm are classified as macroporous materials. The intermediate range covers mesoporous materials[1]. In this classification, microporous or the so-called nanoporous materials have attracted enormous attention due to the intriguing features of the gas adsorption and fluid transport in tight confinements of their pore spaces. Fluid dynamics will be even more complex, if transport occurs in microporous structures with disordered topology and morphology. In such special circumstances, classical theories including the Knudsen model [20], dusty gas model (DGM) [21], Maxwell-Stefan type models [22, 23] and even more accurate models based on the Boltzman equation [24] provide inadequate description of fluid transport. Inadequacy of classical models is discussed in the following sections of this chapter. In contrast, molecular simulation study of gas adsorption and fluid dynamic based on accurately constructed atomistic models of porous adsorbents emerge as a promising approach for investigation of fluid transport in confined pore spaces of heterogeneous materials. This approach is discussed in this review and extensively applied in this thesis.

2.2. Carbide derived-carbon: structure and adsorption properties

Carbide-derived carbons (CDCs) form an important group of carbonaceous materials derived from crystalline structure of metal carbides. This class of porous materials attracts considerable attention due to their wide applications in adsorptive separation of gases, water/air purification, gas storage, battery electrodes, supercapacitors and petrochemical applications [16, 17]. CDCs can be synthesized using a variety of controlled chemical and physical metal extraction techniques such as acid etching, reactions with inorganic salts, halogenation, hydrothermal treatment and vacuum decomposition, during which metals or metalloids are eliminated from the main carbide template

[1] IUPAC Gold Book website: goldbook.iupac.org

[16, 17]. Historically, halogenation is the first method used for synthesis of a CDC [25]. In this method, dry halogen gas (most commonly Chlorine) is exposed to the hot carbide precursor (usually above 200℃) at ambient pressure undergoing the following reaction:

$$SiC(s) + 2Cl_2(g) \rightarrow SiCl_4(g) + C(s) \quad (2\text{-}1)$$

The resulting CDC product is post-treated by hydrogenation process, during which any residual halogen containing component trapped in the CDC porous structure is removed [17]. Figure 2-1 illustrates a schematic diagram of the horizontal tube furnace and gas flow control system used for CDC growth.

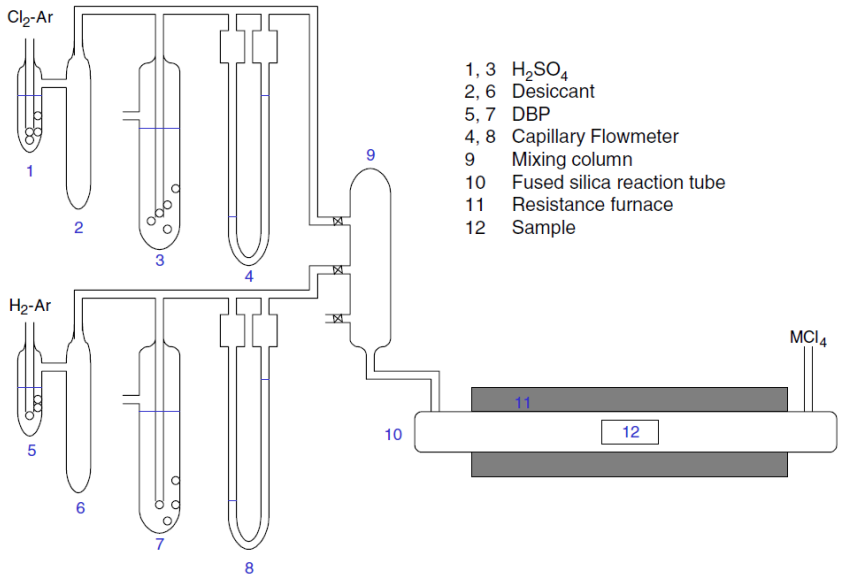

Figure 2-1. Schematic diagram of experimental set-up for CDC synthesis. Figure from Lee et. al. [26]

Conversion of carbide precursor to CDC through halogenation is considered a conformational transformation because this process usually does not alter shape and volume of the precursor [17, 27]. Nevertheless, pore size distribution, porosity and level of structural disorder largely depends on precursor structure, as well as time and temperature of the halogenation process. In principle, faster synthesis and lower halogenation temperature lead to formation of more amorphous structures. In contrary, given adequate time, higher temperatures of up to 1000 ℃ enhance structural order of the product [17]. Other factors such as halogen/carbide ratio, composition of reacting gas mixture, existence of impurities in the precursor carbide, as well as the post synthesis treatment can also affect kinetics of CDC growth, which in turn influences final structure of the CDC [16, 17, 28].

To date, a wide range of metal carbides including SiC, TiC, ZrC, TaC, NbC, SrC_2, Ta_2C, Ti_3SiC_2, Ti_3AlC_2, have been synthesized to produce high-capacity and high-surface area CDCs [17, 28-34].

Depending on the synthesis condition, different carbon structures with different level of structural disorder are obtained including amorphous carbon, planar graphite, nanodiamonds, polyhedral nanotubes and carbon onions [30, 35, 36]. Structural disorder and heterogeneity of pore structure in nano-scale (e.g. pore wall roughness, existence of bottle necks, dead-ends and pore mouth restrictions) are important in dictating different transport scenarios to diffusion of fluid molecules within the pore network. Such microscopic transport mechanisms eventually affect overall macroscopic performance of the material for gas storage or separation.

CDCs became popular for gas storage and CO_2 capture applications based on their unique structural properties such as high capacity and high surface area. Moreover, their synthesis process can be tuned to tailor products with desired pore size distribution (PSD) [16]. This property is especially useful in design and production of CDC-based membranes with narrow PSD suitable for gas separation. In the same way, SiC-DC and its heat treated samples have been demonstrated to be promising materials for gas separation and CO_2 capture purposes due to their narrow pore size distribution, high surface area and high capacity structure [28, 30, 37]. These materials are also shown to be good candidates for hydrogen storage [30].

2.3. Structural modelling of microporous carbon

It has been a continuous challenge for scientists to relate transport properties of fluid particles in microscopic scale with the observable fluid flux of the system at macroscopic level. This requires a clear image of physochemical interactions at solid-fluid interface inside the pore. It is also important to have access to a realistic representation of pore network structure. Transport properties of the system are not only dictated by the reaction rates and diffusion coefficients of the fluid mixture, but they are also strongly influenced by topology and morphology of the porous medium [38]. Pore Network Modelling (PNM) is a primary step in modeling gas adsorption mechanisms and transport properties of fluid particles in confined spaces. PNM has been subject of many research and development (R&D) efforts over the last few decades due to significance and complexity of structural modeling of porous materials. In this chapter, three classes of PNM techniques including (1) macroscale continuum models, (2) discrete models and (3) atomistic models are discussed.

2.3.1. Macroscale continuum models

In macroscale continuum modeling, no assumption is made regarding geometry of pore space but effective transport properties of the system are described based on averages of its microscopic values [38, 39], in which mass, energy and momentum differential equations are derived taking into account initial and boundary conditions of the system [38]. Nevertheless, the system boundaries at

solid-fluid interface are often hardly known due to high level of irregularity of the pore walls [39]. Under such circumstances, differential equations of flow motion are very complex and rarely solvable [39]. To address this difficulty, differential equations of flow transport are averaged over a small volume element, within which the porous medium is continuous. This volume element should be small enough compared to the size of the system and large enough to disregard complexity of the solid-fluid interface at the pore level and hold its continuity [39]. As long as continuity of the system holds, transport properties of this volume element can be integrated over the continuous system to calculate macroscopic flux (effective transport properties) of porous medium [38]. There are various models associated with this approach. Advective-diffusive model (ADM) is one subclass of the continuum models, where advection and diffusion transports are defined separately based on Darcy's and Fick's laws [40]. The Darcy's law for a single phase flow in anisotropic continuum porous media derived from the volume averaging method follows [39]

$$\langle v_\beta \rangle = \frac{\boldsymbol{K}}{\eta_\beta}(\boldsymbol{\nabla}\langle P_\beta \rangle^\beta - \rho_\beta g) \tag{2-2}$$

where subscript β denotes fluid phase. $\langle v \rangle$, η and ρ stand for average velocity, viscosity and density of the fluid respectively. K is the permeability tensor, P pressure and g the gravity vector. Diffusion contribution of mass transport is described by a Fickian model following [39]

$$\boldsymbol{j}(C) = -D_e(C)\boldsymbol{\nabla}\mathrm{C} \tag{2-3}$$

where j, D_e and ∇C are the flux, effective diffusivity and gradient of concentration respectively. The effective diffusivity itself is an average of the corresponding microscopic quantities over the volume element [39]

$$D_e = \frac{\int D(r).\varepsilon_t(r).dr}{\tau} \tag{2-4}$$

here, D_e and $D(r)$ refer to effective diffusivity and diffusion coefficient respectively, $\varepsilon_t(r)$ stands for porosity and τ denotes tortuosity of the system.

The continuum models greatly simplify the task by disregarding the pore morphology. They do not take into account fundamental properties such as pore size distribution and pore connectivity of the system. Application of continuum models is also limited to the systems, where continuity criterion remains valid. Nevertheless, this approach ceases to provide reliable predictions, where drastic

changes in connectivity of the pore network occur such as occurrence of pore blockage or accessibility problems, which frequently happens in amorphous porous materials such as CDCs [38].

2.3.2. Discrete models

The concept of discrete models is closely associated with "network representation of pore medium" [38]. The idea of network representation originally developed by Fatt [41] and later extended by others [12, 42] employing a random network of interconnected pores to equivalently map disordered structure of porous materials so that transport properties of the actual sample can be modeled through such an equivalent porous structure. Compared to the continuum models, discrete models transform the problem from a set of partial differential equations, which have to be solved analytically over the continuum, into numerical solutions of the conservation laws at the level of pore network, which is analogous to the solution of electrical networks using the Kirchhoff's circuit law [38]. This class of models does not suffer from the aforementioned discontinuity limitations caused by pore plugging and pore fragmentation phenomena [38]. Nonetheless, the solution of the network equations can be computationally very expensive for large networks so that realistic representation of porous materials might be highly complex.

Prior to development of the idea of pore network representation by Fatt [41], different attempts had been made for discrete modeling of pore network structures. The initially proposed sphere pack model at the late 19th - early 20th century was not a very successful effort due to complexity of the pore geometry generated by spheres packs, which made the flow analysis impossible [41]. The later efforts undertook application of a simple bundle of capillary tubes, by which accurate analytical derivation of flow properties became practical. However, results obtained from such highly simplified models were not accurately consistent with experimental data, mainly because these types of models do not include effect of cross-connections between pores [41]. In addition, this approach does not account for isotropicity of the actual porous media with respect to fluid flow, as explained by Fatt [41]. Consequently, Fatt [41] proposed his model for a "network of tubes" instead of simply a bundle of tubes. This model combines both advantages of sphere pack and bundle of tubes models, in such a way that pore spaces of sphere pack model were replaced by cylindrical tubes. The model also takes into account effect of the cross-connections between pores. **Figure 2-2** illustrates two dimensional representation of the networks proposed by Fatt [41].

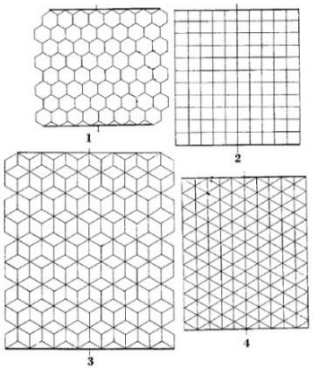

Figure 2-2. Four different types of networks of capillary tubes proposed by Fatt. Figure from Fatt [41]

As computational resources became more available for scientific applications, investigation of more complex systems became feasible. One of the major steps in developments of disordered pore network models was development of randomly distributed pore models such as Voronoi tessellation, in which the model is subdivided into randomly created convex polygons or polyhedra in two or three dimensions respectively [43]. The random creation of polytopes is based on random distribution of scattering points (Poisson points). The network itself is built by positioning a site at each Poisson point and then replacing every face of the polyhedron by a bond connecting the corresponding Poisson point to its neighboring site [44]. Target porosity of the actual sample is later achieved by applying the corresponding void fraction into the created network and removing the random polyhedra after labeling them as void space, so that the desired total pore volume of the system is generated. More realistic models based on Voronoi tessellation technique have been also constructed by adjusting pore size distribution and average coordination number of model using experimental characterization data [45, 46]. **Figure 2-3**, illustrates a 2D representation of Voronoi pore network.

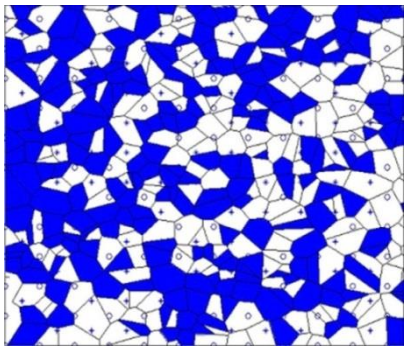

Figure 2-3. 2D representation of Voronoi pore network with the blue polygons representing the voids. Figure from Rajabbeigi et al. [46].

Although application of Voronoi tessellation in modeling of the porous networks has led to great improvements of discrete modeling techniques, this method is still unable to reproduce a fully realistic structural representation of the system specially in terms of generating the real positions of atoms within the pore network.

2.3.3. Atomistic models

As highlighted in the previous section, discrete models are meant to construct an "equivalent random network" [38] for porous media, however they cannot provide a realistic representation of the porous structure which should include correct topology and morphology of the system. Consequently, the atomistic modeling approach was proposed to alleviate this major pitfall. This class of modeling techniques strives to reproduce spatial positions of atoms within the pore network in order to realistically construct topology and morphology of the system. It is important that such models can reproduce structural heterogeneity, as well as pore wall roughness of the material. Atomistic modelling of disordered porous media has recently become more popular due to availability of high speed computational resources and development of novel computer algorithms. In general, this class of modeling is divided into two major categories of reconstruction techniques and mimetic methods, which are discussed in the following sections.

2.3.3.1. Stochastic reconstructive modelling of porous materials

Reconstructive modelling of disordered porous media makes use of a set of target experimental structural data, based on which atomistic model of the system is constructed using the stochastic sampling techniques. Nevertheless, reverse reconstruction of 3D models based on the experimental data set, which is mainly one or two dimensional, is a daunting task. The solution to this type of modeling problem suffers from the so-called uniqueness problem, which is the difficulty of solving an inverse problem based on inadequate experimental structural data [47]. Another difficulty in this type of modelling is that diffraction experiments such as X-ray or neutron scattering cannot fully capture structural features of the actual sample, which should be reconstructed via the computer modeling techniques.

2.3.3.1.1. Density Field Modelling

The density field modelling technique constructs 2D or 3D models of pore network matrix based on a density field function, which is zero at points belonging to the pore network and one for the void spaces [48, 49]. The method was initially proposed by Joshi at the early 1970s achieving a geometrically realistic two dimensional model for porous media [50]. It was extended later to three dimensions by Quiblier [49] so that 3D structure of the sample was constructed to match structural characteristics of a thin layer of the sample. In this technique construction of a 3D model was

undertaken based on a "digital map" obtained from a "black and white" 2D image of a thin slice of the sample. The image was initially obtained from measurement of the intensity of reflected or transmitted light beams by each point of the sample. The light intensity information (spectrum) was then digitized and stored into a digital map, which contains a continuous set of numbers (*Z*) between 0 - 1. This spectrum of numbers is a reflection of continuous nature of the light intensity in the image. The simulation was then performed in a large cubic simulation box (of the order of millimeters), in which every point was labelled by a random number [49]. The labeled numbers were utilized to specify whether these points belong to the pore network or the voids. The experimental input data, against which the above mentioned random numbers had to be examined were probability distribution function (PDF) and autocorrelation function (ACF) of the digital map [49]. The PDF divides the continuous range of numbers from set *Z* into limited classes of intensities to demonstrate relative frequency of each class. Alternatively, the ACF provides information regarding the pore network following the relation

$$f(H) = \frac{E\{[z(P+H) - m].[z(P) - m]\}}{E\{[z(P) - m]^2\}} \tag{2-5}$$

where *m* represents the mean value of the numbers constituting set *Z*. *z*(*P*) refers to intensity of light measured at point *P*, and *z*(*P*+*H*) is the intensity at point *P*+*H*. The numerator is the mean value of the expressions between brackets for all points *P*, and *H* is the remaining constant. The denominator is the variance of set *Z* [49]. This equation explains probability of point *P*+*H* to be part of the matrix network, when *P* belongs to this matrix.

In this method, the goal is to reproduce experimental PDF and ACF of the actual sample using simulation of random points. The algorithm extracts the void spaces (corresponding to the light transmission values in the digital map) from the pore network so that porosity and pore distribution of the experimental sample is achieved. Details of this procedure are tedious and outside the scope of this review, however interested readers are referred to the works of Joshi [50] and Quiblier [49]. **Figure 2-4** illustrates 2D image of the constructed model of the sample which is compared to the experimental image obtained from emission of the light beam.

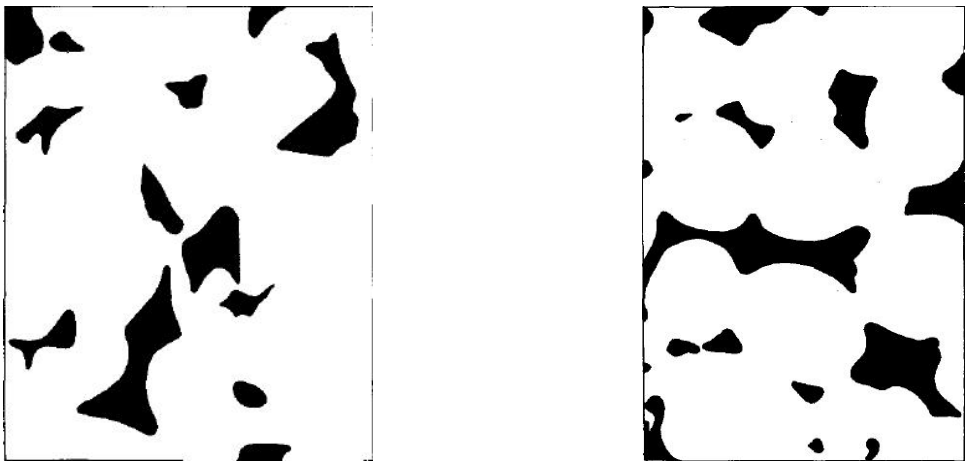

(a) **(b)**

Figure 2-4. 2D representation of the constructed model (a) compared to the experimental image obtained from light transmission of the thin sample (b). White and black areas represent existence of void and matrix respectively. Figure from Quiblier [49]

As illustrated here, the constructed model does not precisely represent the experimental image. To better construct structure of the porous material, scientists have utilized different correlation functions to capture structural characteristics of the pore network. However, in most cases the correlation functions do not provide adequate morphological information of the experimental sample, which means they cannot sufficiently capture structural features of the material. Despite attracting some attention in the past [48, 51-54], another important drawback of the density field modelling technique is that it is unable to provide any information regarding heterogeneity and chemistry of the pore network, which is crucial for modeling of gas adsorption and fluid transport in porous materials.

2.3.3.1.2. Reverse Monte Carlo Simulation (RMC)

Development of reconstruction techniques based on matching experimental correlation functions with those of molecular simulations obtained from stochastic sampling of the amorphous materials was pioneered by Kaplow et al. [55], who matched radial distribution functions of amorphous and hexagonal selenium obtained from X-ray diffraction with that of the perturbed atomic configuration of the model. Nevertheless, the well-known reverse Monte Carlo (RMC) algorithm was first introduced two decades later by McGreevy and Pusztai [56], as a major improvement in modelling of the liquid and amorphous structures. The reverse Monte Carlo scheme makes use of this simple assumption that atomic structure of amorphous materials can be modelled in 3D space, if simulated structure factor (SF) of the model matches that of diffraction experiment within certain minimum discrepancy [56]. The matching procedure is performed based on minimization of an error term

written for the discrepancy of either the experimental SF or the radial distribution function (RDF) with simulation in every MC trial move, following [56]

$$\chi^2 = \sum_{i=1}^{n_{exp.}} \left(g_{sim.}(r_i) - g_{exp.}(r_i)\right)^2 / \sigma^2_{exp.}(r_i) \tag{2-6}$$

where n_{exp} is the number of experimental data points, σ_{exp} is the experimental error and $g(r)$ is the radial distribution function. The experimental structure factor $s(q)$ can be obtained using various experimental methods such as neutron, electron or X-ray scattering. The radial distribution function of the sample is then determined by the Fourier inverse transform of the experimental structure factor data [57]

$$s(q) = 1 + \frac{4\pi\rho}{q} \int r(g(r) - 1) \sin(qr)\, dr \tag{2-7}$$

here, ρ is the number of atoms per unit volume and q is the magnitude of the scattering vector as a function of the scattering angle θ, and the scattering radiation wavelength λ, given by [57]

$$q = \frac{4\pi . \sin\left(\frac{\theta}{2}\right)}{\lambda} \tag{2-8}$$

The RMC algorithm performs based on conventional Monte Carlo (MC) trial moves. The trial moves will be accepted as long as the χ^2_{new} is smaller than its preceding step. Otherwise the algorithm accepts the trial move only if the following probability relation is satisfied [58]

$$P = min\left\{1, exp\left[-\frac{x^2_{new} - x^2_{old}}{2}\right]\right\} \tag{2-9}$$

The RMC algorithm terminates when error norm χ^2 is converged within a small discrepancy and no further improvement is achieved [56]. In theory, the RMC simulation can be started from any arbitrary initial configuration, while atomic configuration of the system is evolved though consecutive MC moves and makes no assumption regarding interatomic potential of the system [59]. Although the RMC was a major step forward in atomistic modeling of amorphous materials, it still suffers from the so-called uniqueness problem, which is the intrinsic characteristic of solving inverse problems, as also explained in previous section for the density field modeling. McGreevy

and Pusztai [56] were among the first people who stressed existence of this drawback. Nevertheless, they correctly highlighted the fact that although there are multiple constructed configurations consistent with a unique experimental diffraction data, the difference between these structures "may or may not be significant, depending on the application" [56]. Another important pitfall associated with RMC technique was that this method does not consider interatomic potential of the evolving system. Therefore, the final configurations obtained from RMC may contain unphysical structural features such as highly strained 3-membered or 4-membered rings in carbonaceous materials [58, 60]. To address these pitfalls, constrained reverse Monte Carlo (CRMC) algorithms were developed to limit the number of structures that can be generated using a similar structure factor data set.

Rigden and Newport [60] developed a variation of the CRMC for the modeling of diamond-like amorphous hydrogenated carbon with unusual properties. Their new RMC algorithm constrains the formation of 3-membered carbon rings in addition to carbon atoms that are bonded to more than four atoms in their neighborhood. Later, O'Malley and colleagues [59] introduced a CRMC algorithm for modeling of the structure of glassy carbon utilizing a new constraint on the atomic coordination number of the system, as given by

$$X^2_{coord.} = (f_{RMC} - f_{req.})^2 / w^2_{coord.} \tag{2-10}$$

where f_{RMC} is the fraction of properly coordinated atoms in the RMC configuration, f_{req} is the target fraction of properly coordinated atoms and w_{coord} is the weighting factor. Other authors extended applications of the CRMC algorithms with some success. For instance, Walters et al. [61] utilized several constrains based on the concept of "near-neighbor distance" for modeling different covalently bonded carbon atoms (tetrahedral sp^3, sp^2, planar mixed sp^3-sp^2 and linear sp^2) in tetrahedral amorphous carbon structure. They found that putting constraints merely on the local bond order of the system may yield formation of inaccurate "intermediate-range order". Therefore, to better control the system bond order, they proposed constraining carbon bond types for the second nearest neighbors in addition to the first nearest neighbors. Based on relative success achieved in modeling porous materials using their RMC algorithm, they finally suggested that application of an energy-based constraint seems inevitable for accurate modeling of network structure using RMC algorithms [61].

Thomson and Gubbins [62] also developed a modified version of the RMC algorithm for reconstructive modeling of activated mesocarbon microbead (a-MCMB), in which three different trial moves including conventional MC configurational moves, plate creation/annihilation trial

moves and ring creation/annihilation trial moves were employed. In their work, an initial graphitic carbon structure was created based on "inter-plate" and "intra-plate" radial distribution function ($g(r)$) of the target sample, where the first two types of MC moves applied on the carbon plates, while the ring creation/annihilation moves only affects the carbon rings within each plate. The experimental RDF was the only constraint controlling evolution of the carbon structure. It was found that the final constructed model only partially reproduces structural properties of the experimental sample so that the simulated nitrogen adsorption isotherm obtained based on this model could not match the experimental adsorption isotherm at pressures close to the atmospheric pressure [62]. The work from Thomson and Gubbins also showed that despite an acceptable match between simulated and experimental RDF, the final constructed model may still be an inaccurate representation of the real structure. This work was followed by Pikunic and co-workers [63, 64] using a new CRMC algorithm to construct a saccharose-based carbon model. The new CRMC algorithm benefits from the use of an angle bending and coordination number constraints in addition to the conventional RDF constraint, taking into account effect of angular bond order and carbon atom hybridization in the structure. Assuming a perfect graphitic structure with sp^2 hybridization (equilibrium bond angle equal to $2\pi/3$), the new constraints are given following equations [63]

$$\psi^2 = \sum_{i=1}^{n_\theta} [\theta_i - \frac{2\pi}{3}]^2 \tag{2-11}$$

$$\delta^2 = 1 - \frac{N_3}{N} \tag{2-12}$$

where, θ_i and n_q refer to different bond angles and the total number of bond angles respectively. N_3 stands for the number of atoms with three neighbors and N is the total number of atoms in the simulation box. To ensure that the system is not trapped in a local minimum, χ^2, ψ^2 and δ were simultaneously minimized using the simulated annealing (SA) procedure, considering it is a powerful mathematical tool to solve combinatorial optimization problems [65].

2.3.3.1.3. Hybrid Reverse Monte Carlo (HRMC)

Despite some success obtained from the use of RMC technique for modeling of disordered materials, the major improvement was achieved after development of the hybrid reverse Monte Carlo (HRMC) technique [58, 66-68]. It had been shown that the RMC algorithm intrinsically leads to the formation of unphysical configurations in the final model due neglecting the important role of interatomic potential during simulation [57, 58]. The new HRMC algorithm performs conventional CRMC simulation, while simultaneously implementing an energy minimization scheme using

reactive force fields. As such, the final constructed models obtained from HRMC-based algorithms are energetically stable and physically more meaningful, while at the same time mimicking experimental structural factor data. Here, the simulation benefits from conventional trial MC moves to minimize a new total error χ^2, which includes the energy term [58]

$$\chi^2_{total} = \frac{\chi^2_{g(r)} + \chi^2_{s(q)}}{2} + \frac{E}{k_B T} \tag{2-13}$$

where, the structural error norm $\chi^2_{g(r)}$ and $\chi^2_{s(q)}$ are scaled by their corresponding σ^2_{exp}, which are the RMC weighting factor for the *ith* data point. Likewise, the energy constraint *E* is scaled by the Boltzmann weighting factor $k_B.T$. Similar to the CRMC algorithms, any extra constraint can also be imposed on the system to better reproduce structural features of the experimental sample, so that for every extra constraint a new error term will be added to the total error norm along with its corresponding weighting factor. Therefore, the total error can be rewritten as the "sum of individual cost functions" following [69]

$$\chi^{old}_{total} = \sum_i \sum_j \frac{({A_{ij}}^{exp} - {A_{ij}}^{old})^2}{W_i} + \frac{E^{old}}{kT} \tag{2-14}$$

where, the sum *i* is calculated over the number of constraints and *j* over the number of fitted data points within the *ith* constraint. Every cost function is a squared difference between the experimental or target value of ${A_{ij}}^{exp}$. and the simulation value of ${A_{ij}}^{old}$, scaled by weighting factor W_i, as described by Opletal et al. [69]. The acceptance probability can also be rewritten as

$$P = e^{(\chi^{old}_{total} - \chi^{new}_{total})} \tag{2-15}$$

In this new approach, convergence of the HRMC algorithm, as well as the nature of the final constructed model is heavily influenced by the quality of the employed potential [66]. For instance, it has been demonstrated that the use of Environment Dependent Interaction Potential (EDIP) developed by Marks [70] provides a reliable physical description of disordered carbon structure [66]. EDIP captures fairly long-range interatomic interactions covering distances of up to the graphite interlayer spacing gap (cut-off = 3.2 Å), which makes it suitable for modelling of disordered carbon structures compared to other potentials with shorter cut-off such as Reactive Empirical Bond Order (REBO) potential [71]. Nevertheless, modelling of low density amorphous carbon structures (density below 1.5 g/cc) might be still subject to some degrees of difficulty,

considering the long range carbon-carbon interactions induced by the porous structure of such low density materials may not be completely captured by these potentials, as highlighted by Nguyen et al. [72].

Although there is a variety of interatomic potentials available for modelling of amorphous carbon, they either demonstrate a poor description of carbon-carbon interaction potentials such as Reaction State Summation (RSS) force field developed by Shi [73], which "lacks long-range van der Waals (vdW) forces" [74] or they are computationally very demanding such as ReaxFF [75, 76], thus making them unsuitable for mainly unparallelized algorithms such as the HRMC [74]. In contrast, the EDIP is considered a "fast and robust" potential, which is also successfully used for a broad range of situations in modelling of amorphous carbon materials [77]. The EDIP potential is a transferable empirical potential, which describes the potential energy of the carbon as a sum of a two-body pair energy term (U_2) and a three-body angular penalty (U_3) following [70]

$$U_i = \sum_j U_2(r_{ij}, Z_i) + \sum_{j<k} U_3(r_{ij}, r_{ik}, \theta_{jik}, Z_i) \tag{2-16}$$

The two-body pair energy U_2 and the three-body angular potential U_3 are functions of interatomic distance (r_{ij}), bond angle (θ_{jik}) and generalized atomic coordination (Z_i) given by [70]

$$Z_i = z_i + \pi_3(z_i)X_i^{dih} + \pi_3(z_i)X_i^{rep3} + \pi_2(z_i)X_i^{rep2} \tag{2-17}$$

here, z_i is the spherical coordination component, π_2 and π_3 are switching functions identifying two and three coordinated atoms, X_i describes dihedral rotation, π-repulsion at a threefold site, and π-repulsion at a twofold site [70].

2.3.3.2. Mimetic methods

Mimetic approach is a more recent technique in atomistic modeling of amorphous materials, which is designed to simulate the actual synthesis process of the porous structure. In this method no empirical structural parameter is used. However, this technique is still at its early stages of development, considering our current knowledge of the mechanisms active during the synthesis process at the atomistic level is very limited, and the actual experimental synthesis time is still well-beyond the capability of available computational resources [74]. Nevertheless, pseudo-mimetic modelling techniques such as quench molecular dynamics (QMD) have recently opened a new avenue in mimetic modeling of porous materials, which seem more feasible. This new variation of mimetic techniques has been proposed to alleviate general pitfalls of this class of modeling methods [73, 74, 78], so that the topology and morphology of the pore network can be reproduced using

conventional molecular dynamics simulation with reactive force fields. The simulation usually initiates from elevated temperatures at vapor or liquid phase and performs a thermal quenching procedure to eventually cool down the system at ambient temperature [74, 78]. Hitherto, qualitative agreement of pore structure, including pore size, pore volume and surface area of the simulated models with that of experiment have been reported using such quenching schemes [73, 74, 78-81]. One example of successful application of QMD technique is the model developed by Gelb and Gubbins [82] which mimics production process of Vycor glass and controlled-pore glasses. Nevertheless, it should be noted that in general QMD has only shown moderate success in atomistic modeling of disordered materials, so that topological and morphological characteristics of the experimental sample have not been reproduced satisfactorily using this technique. The expanding lattice method [83] is also another technique in pseudo-mimetic modelling of porous materials, where the pore network is generated by lowering density of the super cell (by increasing the volume) followed by ab-initio or "Tersoff-based" MD simulations at different temperatures below the bulk melting point of the material. At the end, atomic configuration of the system is finalized by performing geometry optimization. Similar to QMD, this method shows little success, so that the models constructed using the expanding lattice technique provides only qualitative agreement with the experimental data and the evidence provided for reliability of this method is not convincing yet [83].

To summarize, it appears that in contrast to all the modeling techniques discussed here, the hybrid reverse Monte Carlo (HRMC) is still the most promising method in realistic modeling of disordered porous materials, considering many characteristic properties of the experimental sample can be reproduced using this method, as reported by several authors [68, 72, 84]. In this thesis, it is shown that with more efforts, not only structural features of the sample and equilibrium gas adsorption data of the system can be successfully predicted using the HRMC method, but also internal energy barriers and transport properties of fluid in confined spaces of the pore network can be accurately reproduced.

2.4. Modelling gas adsorption

Gas adsorption is significant for storage and separation of volatile gases in many scientific and industrial applications. It is also very important in characterization of porous media. Two popular approaches for modelling of gas adsorption include classical density functional theory (DFT) and grand canonical Monte Carlo (GCMC) simulation techniques, each of which bears certain advantage or disadvantages. The fluid density functional theory (DFT) is a widely used technique for characterization and modelling of gas adsorption in porous materials, while GCMC is a

stochastic sampling approach in molecular simulations, which has been employed extensively in determination of adsorption isotherms at small scale systems and require a rigorous atomistic model of the adsorbent structure.

2.4.1. Density functional theory (DFT)

The fluid density functional theory (DFT) is a well-established formalism that its basic concept is very similar to that of electronic density functional theory applied in quantum mechanics (QM). Whilst the former calculates free energy of the adsorbed phase in porous network as a functional of density profile, the latter calculates energy of an electronic system as a functional of the electron probability density [85]. This is based on the fact that the grand potential function is at its global minimum, when a system is at equilibrium. In other words, equilibrium density of the adsorbed phase can be determined by minimizing free energy with respect to density in an iterative manner [47] following

$$\Omega[\rho(r)] = F[\rho(r)] - \int dr\rho(r)[\mu - U_{ext}(r)] \tag{2-18}$$

where, $\Omega[\rho(r)]$ is the grand thermodynamic potential of fluid confined in a pore at a given chemical potential μ. Here, T is temperature, $F[\rho(r)]$ is the intrinsic Helmholtz free energy functional and $U_{ext}(r)$ is the external solid-fluid potential imposed by the pore walls [86].

DFT usually employs idealized pore network descriptions such as graphitic slit-pore or cylindrical pore models. There are also DFT studies using slightly more complex pore models such as model of spherical cavities or space-filling polyhedra model [87]. Despite being a high precision and computationally inexpensive method [47], DFT is unable to provide explicit information concerning effect of pore topology and pore morphology of the network on gas adsorption. For instance it does not take into account important role of pore network connectivity or surface heterogeneity during adsorption process. However, this method still remains very popular for prediction of gas adsorption, as well as determination of pore size distribution of porous materials based on an experimentally measured adsorption isotherm [28, 30, 87-96]. The following equation explains how DFT provides a theoretical basis for prediction of the pore size distribution (PSD) [62]

$$\theta_{exp}(P,T) = \int \theta_{sim}(P,T,H)f(H)dH \tag{2-19}$$

here, θ_{exp} and θ_{sim} are the experimental and simulated isotherms respectively and $f(H)$ is the PSD, which can be calculated from experimental isotherm by inverting the above integral.

More recently, quenched solid density functional theory (QSDFT) was developed by Ravikovitch and Neimark which accounts for the surface heterogeneity and is more suitable for characterization of disordered porous materials [97, 98]; nevertheless this method still uses slit or cylindrical pore models, considering application of realistic pore models in DFT will be computationally very expensive.

2.4.2. Grand canonical Monte Carlo simulation (GCMC)

The grand canonical Monte Carlo (GCMC) simulation technique is routinely used for stochastic sampling of adsorbed phase. In contrary to the conventional ensembles used in molecular dynamics (MD) simulation such as canonical (NVT) or microcanonical (NVE) ensembles, application of grand canonical ensemble (VTμ) allows the number of particles in the system to fluctuate at a constant temperature and pressure. This is usually achieved by connecting the target system to a particle reservoir. The GCMC algorithm ensures that chemical potential (μ) of the system remains constant by exchanging particles between the system and the reservoir. This is particularly favorable for simulation of adsorbed phase, considering only chemical potential μ and temperature T have to be known between the bulk and adsorbed phase in order to define equilibrium. This is also an inexpensive technique for modeling gas adsorption compared to MD [99]. The GCMC algorithm employs conventional conformational Monte Carlo moves (displacement/rotation) in addition to the exchange trial moves (insertion/deletion) in such a way that it accepts any move, which decreases energy level of the system, otherwise the trial moves will be only accepted within the following acceptance probability criteria for displacement $P(U)$, insertion $F(U)$ and deletion $T(U)$ given by [99]

$$P(U)_{s\to s'} = \min\{1, \exp[-\beta(\Delta U)]\} \tag{2-20}$$

$$F(U)_{N\to N+1} = min\left\{1, [\frac{N+1}{zV} exp(\beta\Delta U)]^{-1}\right\} \tag{2-21}$$

$$T(U)_{N\to N-1} = min\left\{1, [\frac{zV}{N} exp(\beta\Delta U)]^{-1}\right\} \tag{2-22}$$

where, U stands for potential energy and ß denotes reciprocal temperature $\frac{1}{k_B.T}$ with k_B to be the Boltzmann's constant. z, Λ, N and V are activity, thermal de Borglie wavelength ($\Lambda = (\frac{h^2}{2\pi m k_B T})^{1/2}$),

number of particles and volume respectively [99] with activity being defined as $z = \exp(\beta\mu)/\Lambda^3$ where μ is the chemical potential [100].

Although GCMC can be employed to describe adsorbed phase in disordered and complex pore network structures, it requires lengthy simulation runs in reasonably large unit cells to provide reliable results. Paradoxically, the use of lengthy simulations in such large systems can be expensive and introduce statistical uncertainties into the simulation results [47].

2.5. Modelling of transport in microporous materials

Understanding transport properties of fluid molecules in confined spaces of the pore network is crucial due to intriguing features of fluidic phenomena at the nano-scale [101-103]. A large variety of industrial applications including gas storage and separation, petroleum refining, electrochemical energy storage, nanofluidics and materials screening require fundamental understanding of fluid properties in porous materials. Although, there has been considerable efforts to develop reliable models to explain transport properties of fluid molecules in tight confinements, our knowledge of these phenomena is still limited. In first part of this section, classical theories of fluid transport in porous materials are briefly reviewed and then molecular dynamics (MD) simulation is explained in the subsequent part, which is the main approach chosen for investigation of transport phenomena in this thesis.

2.5.1. Classical theories of transport phenomena

Historically, there have been popular established approaches in classical modeling of transport phenomena in confined spaces. The Knudsen model [20] was originally developed by Martin Knudsen for low density non-interacting hard sphere gases diffusing in a tube surface. At such low densities, the mean free path of the diffusing particle λ is assumed to be large in comparison with the tube diameter d (Knudsen limit $K_n = \frac{\lambda}{d} \gg 1$), thus the frequency of molecular collision would be negligible compared to the wall-molecule contacts [104]. Consequently, wall-molecule collisions, as well as the pressure gradient are the only driving forces of molecular diffusion in this model [104]. The corrected version of Knudsen's theory follows [105]

$$D_k = \frac{d}{3}\sqrt{\frac{8k_BT}{\pi m}} \tag{2-23}$$

where, D_k is the diffusion coefficient in tube, d is the effective diameter of tube, m is the molecular mass and T is temperature.

Nevertheless, adsorption of gases in mesoporous materials deviates from the Knudsen model due to the highly complex disordered structure of solid network [106], which do not meet requirement of the Knudsen model [104].

Another class of theory concerns bulk and wall-mediated diffusion in macro and mesoporous materials, where fluid density falls outside the Knudsen limit ($K_n \ll 1$ or $K_n \approx 1$). Here, the Maxwell–Stefan (MS) description of mass transfer appears to provide the most promising approach [104, 107]. Chapman and Enskog [108], as well as Hirschfelder, Curtiss and Bird [109] have derived the generalized Maxwell–Stefan diffusion equations [104]. Although, the original version of these derivations did not include shear forces, the later version refined by Zhdanov et al. [110] did include the shear term [104]. The complete form of the generalized Maxwell–Stefan equations for an n-components mixture is given by [104]

$$\sum_{\substack{j=1 \\ i\neq j}}^{n} \frac{x_i x_j (v_i - v_i)}{Đ_{ij}} + \sum_{\substack{j=1 \\ i\neq j}}^{n} x_j x_i \left(\frac{D_i^T}{\rho_i^m} - \frac{D_i^T}{\rho_j^m}\right) \nabla T = d_i \quad i = 1, \ldots, n \tag{2-24}$$

In this equation, x_i is the mole fraction of component i, v_i is mean local velocity of this component, $D^T{}_i$ is its thermal diffusion coefficient, $\rho^m{}_i$ stands for the mass density of component i, and $Đ_{ij}$ refers to the Maxwell–Stefan binary diffusion coefficient of species i and j. As explained by Bhatia et al. [104] "mutual diffusion", which describes the "drag" applied by the molecules of species j on the molecules of species i is given by the first term in the left hand side. The second term however, explains the "thermal diffusion" term representing the "thermal segregation phenomena", which is associated with temperature gradients in the fluid [104].

The most commonly used Maxwell–Stefan type model is the dusty gas model (DGM) [21]. The model was originally introduced by Evans and colleagues between 1961-1963 [4, 6, 7] and later modified by Mason et al. [111]. The main point of this new development was to include combined wall-mediated and bulk diffusion in a unified framework [104]. Despite the model popularity, Bhatia and co-workers [104] have recently criticized this model and demonstrated that the DGM formulation has serious flaws in its derivation and the theory fails to rigorously predict behavior of experimental diffusion. This includes inconsistencies in the assumptions used to derive the equations in addition to the "conflicting choices of the frame of reference used for different terms in the analysis" [104]. The other classical models, which have been developed based on the Maxwell–Stefan diffusion equations are the interfacial friction-based models. According to Bhatia et al. [104], "the fluid–wall momentum exchange" is generally handled using the concept of interfacial friction,

which acts at the pore surface, so that the corresponding friction coefficient accounts for "viscous and wall–molecule collisions effects" [104]. Overall, it appears that the models which strive to unify bulk and wall-mediated diffusion in a same framework are not fulfilling the expectations of accepted theories and suffer from both derivation errors and wrong theoretical presumptions [104]. Moreover, in most cases these models neglect effect of adsorption on fluid diffusion, which is particularly significant in nanoporous materials [104, 112]. Several authors attempted to develop predictive models for transport of fluid in presence of adsorption fields including the "molecular path tracing" method of Nicholson and colleagues [113-116], the kinetic theory approach by Pozhar and Gubbins [117] and its various treatments by others [118-120], nevertheless none of these efforts yields a fully satisfactory model [104]. More recently, Krishna and co-workers [22, 23, 121], as well as Bhatia and his colleagues [122-124] opened new avenues by development of new treatments based on Maxwell–Stefan (MS) theory to provide more successful models for diffusion in presence of adsorption [104]. The former group extended the Maxwell–Stefan formulation by introducing a model for surface diffusion, while the latter group developed the "statistical mechanical Oscillator Model" to describe "the low-density transport coefficient of a LJ fluid in a confined space, whose particles are oscillating between diffuse wall collisions under the action of a conservative one-dimensional fluid–solid interaction potential", as originally explained by Bhatia et al [104].

In summary, it is shown that the Knudsen model neglects important effect of fluid–solid interactions in presence of adsorption. This drawback is also inherited to the DGM model, which makes it unsuitable for modeling fluid transport in nanoscale confinements [104]. Other theories developed based on Maxwell–Stefan formalism such as generalized MS approach or the Oscillator model provide more flexibility and take into account effect of adsorbed phase field on diffusion more successfully, however Maxwell-Stefan type models generally disregard effect of fluid inhomogeneities in mixture adsorptions [104]. In contrast to these theoretical approaches, Molecular Dynamics (MD) simulation can provide exact results for prediction of fluid properties in confined spaces based on the potential models used to corroborate theoretical models. Nowadays, MD simulation is very powerful due to development of more efficient algorithms, as well as availability of supercomputer facilities, which provide tremendous computational resources for these types of simulations. As explained by Bhatia et al. [104] prediction of fluid transport "beyond the single pore level" and "to that of a realistic material with a disordered structure" require further development in the classical theories which are not currently available, however MD simulation has barely any limitation in this sense, if the required computational resources are provided.

2.5.2. Molecular dynamics (MD) simulation

Investigation of transport properties of fluid molecules in nano-scale confined spaces of pore network is crucially important for nanotechnology and nano-engineering applications and for development of nano-devices such as catalysts and membranes. In general, fluid flux at confined space is driven by chemical potential gradients. Nonetheless, nanofluidic phenomena are also correlated with intermolecular forces, as well as molecular geometry of adsorbate molecules, structure of the solid framework and temperature [103]. At very narrow pores, frictional resistances arise from both intermolecular and wall-molecule collisions with the wall-fluid events dominating transport of adsorbate molecules [103, 104]. Due to highly tortuous nature of the pore wall, existence of dead-ends and random distribution of inaccessible pores, determination of fluid transport in amorphous materials is not an easy task. Notwithstanding the complexity, molecular dynamics (MD) still provides a powerful simulation tool for investigation of fluid transport in this class of materials.

MD is a popular computational technique for calculation of equilibrium and transport properties of many-body systems [99]. It can provide sufficiently accurate results for prediction of fluid properties in confined spaces based on the potential models used. The assumptions and simplifications, which are usually the main disadvantages of the theoretical transport models, do not play a role in MD. The accuracy of solution of the many-body systems can be only limited by the choice of potential models, if appropriate algorithm and time step are chosen [99].

In MD, diffusion of a single molecule through fluid in equilibrium (self-diffusivity) can be calculated using velocity autocorrelation function (VAF) or mean-squared displacement (MSD) of the diffusing molecule following [125]

$$D^s = \frac{1}{Nd}\int_0^\infty \langle \sum_{i=1}^{N} v_i(t).v_i(0)\rangle \, dt \tag{2-25}$$

$$D^s = \frac{1}{2Nd}\lim_{t\to\infty}\frac{1}{t}\langle \sum_{i=1}^{N} |r_i(t) - r_i(0)|^2\rangle \tag{2-26}$$

where, r_i (t) is the center of mass position vector of molecule i at time t, v_i (t) is the center of mass velocity vector of molecule i, N is the number of molecules and d is the dimensionality of the system. The brackets indicate an ensemble average taken over the simulation run. On the other

hand, chemical potential is the source of transport and collective diffusivities in fluidic systems. These two parameters are related to the diffusive motion of the entire fluid. Transport diffusivity of the fluid originated from the Fick's first law follows [125]

$$D^T(c) = \frac{k_B T}{c} L(c) \Gamma = D^C(c) \Gamma \tag{2-27}$$

where, thermodynamic factor Γ is defined as [125]

$$\Gamma \equiv \frac{1}{k_B T} \left(\frac{\partial \mu}{\partial \ln c}\right)_T \tag{2-28}$$

here, $D^T{}_C$ is collective diffusivity, c and μ are concentration and chemical potential respectively, L is the Onsager transport coefficient, k_B the Boltzmann's constant and T is temperature of the system [125]. The thermodynamic factor Γ is obtained from the equilibrium adsorption isotherms using GCMC simulation following [125]

$$\Gamma \equiv \left(\frac{\partial \ln f}{\partial \ln c}\right)_T \tag{2-29}$$

where, f is the fugacity of the bulk phase at equilibrium and c is the concentration of the adsorbed phase. Collective diffusivity of a single component fluid can also be evaluated from simulation trajectories of the system using equilibrium molecular dynamics (EMD) simulation following [125]

$$D^C = \frac{1}{2Nd} \lim_{t \to \infty} \frac{1}{t} \left\langle \left| \sum_{i=1}^{N} [r_i(t) - r_i(0)] \right|^2 \right\rangle \tag{2-30}$$

$$D^C = \frac{1}{Nd} \int_0^\infty \left\langle \left(\sum_{i=1}^{N} v_i(t) \right) . \left(\sum_{i=1}^{N} v_i(0) \right) \right\rangle dt \tag{2-31}$$

Collective diffusion, as described by equations (2-30) and (2-31), is diffusive motion of the center of mass of the entire fluid due to concentration gradient, which is affected by cooperative motions of many particles inside the fluid, however self-diffusion (equations (2-25) and (2-26)) is defined based on movements of a single tagged particle through the fluid medium.

2.6. Development of first-principles force fields for molecular simulations

As discussed so far, molecular simulations such GCMC and MD provide powerful tools for prediction of different properties of matter, so that they can be used as a complement to the experimental investigations. Nevertheless, reliability of the results obtained from a wide range of

molecular simulation techniques is subject to the use of accurate and transferable sets of interaction parameters (the so-called force fields parameters), which define potential energy of the interacting particles as a function of their coordinates [126]. In molecular mechanics, simulations such as GCMC and MD are performed based on the use of classical force fields with reasonable computing costs, considering they are developed to disregard electronic structure of the matter. If our calculations are required to take into account electronic structure of the system, the first-principles quantum mechanical (QM) calculations have to be performed; however these types of calculations are rather complicated and computationally highly demanding. Consequently, transferable classical force fields are designed to avoid these types of complex calculations for every molecule.

In literature, three major types of force fields namely generic, empirical (experimentally-derived) and first-principles force fields are classified based on their development techniques [126]. While reliable force fields are widely available for adsorbate-adsorbate interactions of simple molecules including those of Darkrim-Levesque force field for hydrogen [127], EPM2 for carbon dioxide [128] TIP5P [129] and SPC/E [130] for water and TraPPE[2] for alkanes, alkene and alcohols [131-134]; development of intermolecular interactions for flexible adsorbent structures is more daunting [126]. Zeolites [135, 136], MOFs [137-139], COFs[3] [140, 141] and ZIFs[4] [142, 143] are some famous examples of such flexible frameworks. Generic force fields are developed to cover intermolecular interactions between large groups of molecules. Universal force field (UFF) [144], Dreiding [145] and the OPLS-all atom [146] are some examples of generic force fields, which are developed using a combination of "general rules and atomic parameters" [126], GCMC data fitted to experimental observations and quantum chemistry calculations [126]. On the other hand, empirical force fields are developed by fitting simulated adsorption isotherms to those of experiments using appropriate forms of potential functions [126].

Generic and empirical force fields suffer from several drawbacks such as lack of transferability [147-150] and inaccuracy [151] for some materials. In case of empirical force fields, lack of "explicit physical basis" [126, 152] in addition to the errors inherited from erroneous experimental data [126, 153] can also be the problem. Lack of physical basis may refer to purely experimental basis of the empirical force fields (e.g. force fields obtained based on reproducing experimental isotherms), which sometimes fail to accurately predict other thermodynamic properties such as molecular diffusion [126, 151]. To avoid these pitfalls, quantum mechanics (QM) has provided us

[2] TraPPE: Transferable Potentials for Phase Equilibria Force Field
[3] COF: Covalent Organic Framework
[4] ZIF: Zeolitic Imidazolate Framework

with an alternative approach in developing first-principles force fields. If careful considerations are taken in using reliable QM methods, first-principles force fields yield accurate and transferable predictions of intermolecular interactions [126]. Several reviews have discussed development of first-principles force fields for molecular simulations [126, 154-157], nevertheless Fang et al. [126] has provided the most comprehensive review on the technical details, as well as the procedure required for development of first-principles force fields. In this procedure, a reliable QM method (which can correctly capture guest-host interactions), a realistic adsorbent (host) model, adequate number of molecular configurations covering all significant states of the guest molecules in the framework, an appropriate and "physically meaningful" potential model for fitting and finally a "reliable parameterization algorithm" are required [126]. Initially, realistic model of adsorbent framework should be constructed using an appropriate structural modelling technique (as described in section 2.3). Then, a large number of configurations for adsorbate molecules are generated using GCMC or MD to sufficiently fill pore spaces of the framework. Afterwards, QM calculations are performed using a suitable technique to determine adsorbate-adsorbent potential energy of the system. Using a reliable parameterization algorithm, an appropriate form of the potential function is fitted to the fluid-solid potential energy calculated from QM to determine interaction parameters of the force field under development. This force field can be later validated against QM calculations using higher level of theory or against available experimental data.

Among different QM methods, the coupled-cluster theory is currently seen as the most reliable QM technique for calculation of non-covalent interactions [158, 159], however its highly expensive computational requirements make it unsuitable for large atomic systems [126]. Møller–Plesset second-order perturbation (MP2) theory is another QM technique, which can accurately calculate adsorbate-adsorbent interactions of guest-host systems [160, 161] based on the cluster models. MP2 is very popular due to its accuracy and good performance/cost ratio [126]. Added to these techniques, the symmetry-adapted perturbation theory (SAPT) [162] has also received much attention. The method is capable of calculating fundamental components of the total interaction energy separately including exchange-repulsion, electrostatic, induction, dispersion and so on. This is very advantageous for separate fitting of individual energy components [126]. Nevertheless, the down side of methods such as MP2 and SAPT is that they cannot be extended to periodic systems and are only suitable for small clusters of atoms [126]. To overcome limitations of these methods for large and periodic systems, Kohn-Sham density functional theory (DFT) is used [163, 164]. Until recently, DFT method was unsuccessful to describe long range electron correlations or the so-called electron dispersion forces [165], which play a critical role in adsorption process. This was

because the exchange-correlation functionals - responsible for treating inter-electron interactions - were unable to describe dispersion interactions [165, 166]. Nevertheless, recent developments have totally changed this picture. Empirical dispersion-corrected density functional theory (DFT-D) method of Grimme [167-169], as well as the ab-initio van der Waals density functional techniques (vdW-DFT) developed by several authors [170-174] are now available and proven to be promising computational techniques [153, 165, 175]. In DFT-D method, the total energy between every pair of atoms is augmented by a dispersion-like contribution following [166]

$$E_{DFT-D} = E_{DFT} - S\sum_{i\neq j}\frac{C_{ij}}{r_{ij}^{6}} f_{damp}(r_{ij}) \tag{2-32}$$

where, r_{ij} is the interatomic distance, C_{ij} is dispersion coefficient, f_{damp} is a damping function to avoid unphysical behavior of the dispersion correction for small distances and S is an empirical scaling factor. In vdW-DFT, exchange correlation functional is given by [165]

$$E_{xc} = E_x^{GGA} + E_c^{LDA} + E_c^{nl} \tag{2-33}$$

here, E_{xc} is the exchange correlation energy, E_x^{GGA} is exchange energy in the revised Perdew-Burke-Ernzerhof approximation [176], E_c^{LDA} refers to the correlation energy in the local density approximation (LDA) and E_c^{nl} stands for the non-local correlation energy term.

2.7. Carbon dioxide adsorption in porous materials

Greenhouse gas mitigation is nowadays a global concern due to catastrophic effects of global warming arising from emission of large amounts of greenhouse gases such as CO_2 and CH_4. CH_4 lifetime in the atmosphere is shorter than CO_2; while its warming potential is much larger. Nevertheless more attention has been paid to emission of carbon dioxide, due to its larger global emission[5].

In addition to several national and inter-regional agreements, the United Nations Framework Convention on Climate Change (UNFCCC), Kyoto protocol and Copenhagen Accord urge reduction of CO_2 emission to control the global warming consequences. As carbon dioxide is believed to have the major contribution in global warming among other greenhouse gases, development of industrially efficient and economically feasible carbon capture and sequestration technologies is critical. The need for more mature carbon capture and sequestration (CCS)

[5] IPCC Fourth Assessment Report on Climate Change 2007 - accessed on-line: 15 May 2015. https://www.ipcc.ch/publications_and_data/ar4/wg1/en/ch2s2-10-2.html

technologies is also driven by the growing demand for natural gas, which may contain up to 40-60% CO_2 depending on the source of the gas [177, 178].

Hitherto, several CO_2 capture technologies have been developed to reduce the level of carbon emission such as absorption of carbon dioxide using aqueous alkanolamine solutions (amine scrubbing), membrane separation of carbon dioxide and physical adsorption of CO_2 using physical adsorbents [177]. Although, amine scrubbing technology seems to be the most applicable technology before 2030 [177, 179], it suffers from several drawbacks including costly regeneration process, high equipment corrosion rate, large absorber volume required and rate-limiting CO_2 diffusion through gas-liquid interface [180]. Membrane separation of carbon dioxide has been popular due to its simplicity, high selectivity and low energy requirement [177], nevertheless it is not suitable for separation applications with low CO_2 partial pressure [177, 181]. As for the physical separation of carbon dioxide, diffusion of CO_2 from bulk phase to the internal pore spaces of mesoporous adsorbents appears to be several orders of magnitude larger than that of CO_2 diffusion across gas-liquid interface in absorption-based technologies [182], yet physical adsorption of carbon dioxide does not appear to be an industrially applicable method. The adsorption process is usually implemented in a pressure-swing adsorption (PSA) or temperature-swing adsorption (TSA) set-up for operation [177]. Two main drawbacks here include low adsorption capacity of available adsorbent materials at reduced temperatures and competing co-adsorption of water vapor and other gases, which can potentially hinder adsorption of carbon dioxide [180]. As highlighted in several review papers, a suitable adsorbent for industrial scale applications should prove to have low-cost synthesis process, low-cost raw materials, low heat capacity, high rate kinetics, high adsorption capacity, high CO_2 selectivity, tolerance to the presence of moisture and other impurities in the feed and thermal, chemical and mechanical stabilities under extensive adsorption-desorption cycling [180, 181, 183]. To date, an extensive number of adsorbent materials have been synthesized to meet these requirements, among them zeolites, metal-organic frameworks (MOFs) and carbonaceous adsorbents have received much attention [177, 181, 184]. Zeolites, as a class of porous crystalline aluminosilicates with a periodic array of SiO_4 or AlO_4 tetrahedra, have extensive applications in separation technology due their ability of molecular sieving [181]. Metal organic frameworks (MOFs) or the so-called “porous coordination polymers“ are also a new class of crystalline solids consisting of organic–inorganic hybrid networks formed by multiple metal–ligand bonds [177, 181]. These materials have proven to have useful structural properties such as high surface area, high porosity and high thermal and chemical stability [177, 185, 186]. The other class of popular adsorbents is the carbonaceous materials. Activated carbons form a big part of this category, which

have been studied widely for CO_2 separation applications [181]. These materials have an advantage over other adsorbents because of their lower cost of raw materials [181]. They are also popular because they can be synthesized from many different sources of carbon [25] including coals, industrial byproducts, wood or biomass sources [181, 187]. This also gives a large flexibility to synthesize materials with a wide range of pore size distribution and pore structure for different industrial applications [181, 188] Other classes of carbonaceous materials including carbon molecular sieves [189-191], carbon nanotubes [18, 19], and carbide-derived carbons (CDC) [16, 17, 192] have also attracted enormous attention for gas separation applications including CO_2 capture. Recent studies show that CDC materials, which can be easily synthesized from almost any carbide precursor, have large adsorption capacity, high specific surface area and high atomic level of tunability [16, 28, 193]. Pore size distributions narrower than those of single-wall carbon nanotubes and activated carbons which are even comparable with PSD of zeolites can be easily achieved through chlorination of carbide precursors [16]. Their manufacturing flexibility has made it possible to tailor CDCs for very particular applications such as CO_2 separation, gas storage and transport, water/air purification, petrochemical applications, catalysts, molecular sieving and as electrode in batteries and super capacitors [16, 193-195]. They are particularly shown to be a promising class of carbonaceous adsorbents for CO_2 capture [37]. Another advantage of CDC materials is their hydrophobicity, which can be achieved by full conversion of carbide precursor via chlorination process, so that the final CDC product is free of any oxidized sites (which can unfavorably encourage adsorption pf water). As such, properly synthesized CDCs are more suitable for water separation applications than other carbonaceous materials, which have many hydrophilic active sites.

2.8. Water adsorption and transport in microporous carbon

Understanding water adsorption in porous materials is crucial due to its relevance to adsorptive drying technology and adsorptive separations, where the co-adsorption of water vapor has significant effects on capacity, selectivity and diffusion for other molecules including carbon dioxide and methane [196-201]. Nevertheless, the mechanisms causing co-adsorption of water are not very well understood, especially in hydrophobic carbon materials. Adsorption and diffusion of water in confined spaces of microporous carbon differ radically from those of non-polar gases, due to the hydrophobic nature of porous carbon, existence of strong dipole moments on water molecules (which are the source of hydrogen bonding between water molecules) and the water clustering effect [202, 203]. As a result of these phenomena, dispersion interactions lose their superiority in adsorption of water in carbonaceous materials, in contrast to most organic and inorganic substances,

where dispersion interactions play the main role [203]. Microporous carbon materials are known to have hydrophobic pore network structures [204-206] due to the non-polar nature of the graphitic carbon sheets inherent to their structure and the weaker carbon-water interactions compared to water-water interactions, which are dominated by electrostatic effects. This gives rise to an adverse adsorption isotherm at low loading, in which the level of electrostatically mediated hydrogen bonding is reduced. Lack of hydrogen bonding usually destabilizes formation of the adsorbed phase inside the pore [200, 205, 207-209]. Therefore, occurrence of water adsorption in such hydrophobic pore networks depends on the formation of stable hydrogen bonds-facilitated water clusters. Due to this behavior, most theoretical isotherms which are proposed to describe unusual shape of water isotherms over the entire range of P/P_o have failed to succeed [203, 210-215].

Ohba et al. have shown that larger water clusters have deeper potential depths inside the pore space [204], an indication of the adsorbed phase stabilization. Also, according to Kimura et al. [205], the affinity change between water molecules and the pore wall may occur due to reduction of dipole moment of the water cluster, which gives rise to higher affinity of the water cluster towards the hydrophobic carbon wall at the level of pore filling. As such, pore filling occurs on the account of water-cluster growth due to hydrogen bonding [216]. In this mechanism, the formation of adsorbed phase monolayers are not seen, as opposed to dispersion driven adsorption of simple fluids [207, 216]. Different studies suggest that pore filling can occur below or above saturation pressure depending on different factors such as the existence of functional groups and activated sites in the sample, topological and morphological characteristics of the carbon framework, as well as the pore size [200, 205, 217]. GCMC simulation studies of water adsorption in slit-pore models reveal that condensation does not take place below the saturation pressure of water in pores larger than 10 Å [217]. There is also evidence that condensation can occur below P_o for pores comparable to the size of molecules, however for highly narrow pores (~6 Å) condensation will not occur until pressure is raised beyond P_o [217]. Different studies indicate that predicted water adsorption isotherms for disordered carbon do not show a consistent behavior all the time. The complex topology and morphology of carbon materials, in addition to their different pore size distribution and pore connectivity, lead to a variety of anomalies associated with adsorption and diffusion of water in this class of adsorbents [218-221]. It is shown that due to highly inter-connected and complex pore network structure of disordered carbon, adsorption of water may block pore entries, hindering the co-adsorbing molecules (e.g. CO_2, CH_4) to easily diffuse through empty pore spaces [219]. Investigation of the pore-accessibility and pore blockage phenomena, as well as other issues such as structure of adsorbed phase inside micropore are not within the reach of experimental methods;

nevertheless molecular simulations can provide valuable information about them. Despite the great need for better understanding of water adsorption in non-ideal models, simulation studies of water adsorption in non-slit pore structures, which can take into account effects of structural disorder on adsorption and transport of water are scarce [218-221]. This thesis tries to fill this gap and improve our knowledge on this topic.

2.9. Heteroatom doping of porous materials for gas adsorption and separation

To promote or demote affinity of solid adsorbents towards particular molecules, promoter functional groups are usually incorporated into the original pore network of the pristine structure. The so-called molecular basket sorbents (MBSs), where a polymer - acting as a promoter - is grafted within the pore network of solid, are the most commonly synthesized functionalized adsorbent materials [222-224]. One of the main applications of MBSs is to effectively enhance adsorption capacity and adsorption rate of carbon dioxide in solid adsorbents and to simultaneously reduce energy demand of the overall process [182, 225-228]. The philosophy of using amine-decorated adsorbent materials for CO_2 capture is very much similar to that of activated aqueous alkanolamine solutions in absorption technology, where affinity of amine-functional groups towards CO_2 is the key driving force of the promoting mechanism [229-232]. This technology is also applicable in high capacity adsorption of other gaseous such as H_2S, NO_2 and SO_2 by incorporating different promoters into the solid structure [224, 233, 234]. A similar approach is recently chosen for amine-decorated metal organic frameworks (AD-MOFs), which are shown to be highly effective and economic for post-combustion capture of carbon dioxide [8, 235-237]. Similar to MBSs, pore walls in AD-MOFs are decorated with CO_2-philic nitrogen containing organic groups, in which nitrogen is mainly responsible for enhancement of CO_2 adsorption. In fact, interaction of localized dipoles generated by incorporation of nitrogen-containing functional groups with the quadrupole moment of CO_2 gives rise to stronger dispersion and electrostatic forces, which in turn yield increase of carbon dioxide adsorption [237]. There are a variety of nitrogen-functionalized MOFs including “heterocycle derivatives, aromatic amine derivatives, and alkylamine bearing frameworks” [237].

Another technology to tailor adsorption properties of porous solid for various applications is heteroatom doping of adsorbent structure. The concept here is very similar to those of MBSs and AD-MOFs. In general, different types of dopants are used to encourage specific mechanisms alongside the adsorption process. Heteroatom doped carbon materials have already found many potential applications in energy storage and gas separation. Different types of nitrogen, boron, sulfur, phosphorus and fluorine doped or co-doped carbon materials have been shown to form a new

and promising class of adsorbents with applications in fuel cells, oxygen reduction reaction (ORR), supercapacitors, lithium ion batteries, hydrogen storage, electrocatalysts and water separation [238-242]. An important chapter of this thesis will focus on fluorination of carbon for water separation applications using fluorine-doped SiC-DC; therefore a higher emphasis will be put on this topic in the following sections of this review.

2.9.1. Fluorine doping of microporous carbon for water vapor separation

Fluorine-doped carbon materials form covalently-bonded substances consisting of a wide range of different structures, nevertheless in addition to covalent bonding, C-F bonds include semi-ionic, ionic and van der Waals interactions [243]. The variety of C-F covalent bonds is also significant due to complex and diversity of carbon hybridization in different carbon structures [243]. This property gives rise to a wide range of functionalities, making fluorine-doped carbon materials an important class of compounds for many different applications. Fluorination of porous carbon [244-248] is an established approach in engineering novel classes of carbonaceous materials with increased hydrophobicity. Fluorinated carbons have also other potential applications in emerging technologies. Fluorine-doped graphite (poly carbon monofluoride) possesses good thermal conductivity, low shear strength, good electrical insulation and super-hydrophobicity [249]. It has potential applications in primary lithium cells, batteries, low surface energy coatings, lubricants [249] and wide-gap semiconductors [243, 249, 250]. Other forms of carbons have been also investigated for fluorine doping. Fluorination of multi-wall carbon nanotubes was initially reported by Nakajima et al. [251] and Hamwi et al. [247], while fluorinated single-wall carbon nanotubes (SW-CNT) were later synthesized by Mickelson et al. [248]. The latter group showed that fluorination alters conductivity of the SW-CNT from a good conductor to an insulator [248]. There has been ongoing studies on fluorination of carbon nanotubes [248, 252-258], while investigations of other types of carbon has been limited to a few studies on fullerene [259], activated carbon [241, 260-263] and graphene [249, 264]. Most of these studies only focus on new synthesis methods of fluorinated carbons and just a very few of them have explored adsorption properties of these materials for gas adsorption and separation applications [241, 260-263]. In this review, adsorption properties of fluorinated activated carbons are discussed due to their analogous structure and adsorption properties with those of CDCs.

Setoyama et al. [260] have studied adsorption of nitrogen on fluorinated activated carbon fiber (F-ACF) at 77 K. They have demonstrated that nitrogen adsorption is decreased on the fluorinated samples compared to their pristine structure due to the decrease of pore volume, surface area and pore width, as well as low energy microporous surface of F-ACF, as illustrated in Figure 2-5.

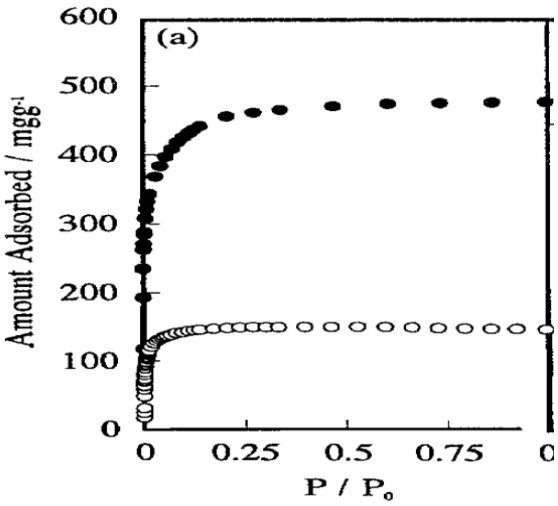

Figure 2-5. Adsorption isotherms of nitrogen on F-ACF (open symbols) compared to its pristine structure (solid symbols). Figure from Setoyama et al. [260].

Lee et al. [262] have also carried out a similar study for nitrogen adsorption on activated carbon fiber demonstrating essentially the same phenomena, as depicted in Figure 2-6.

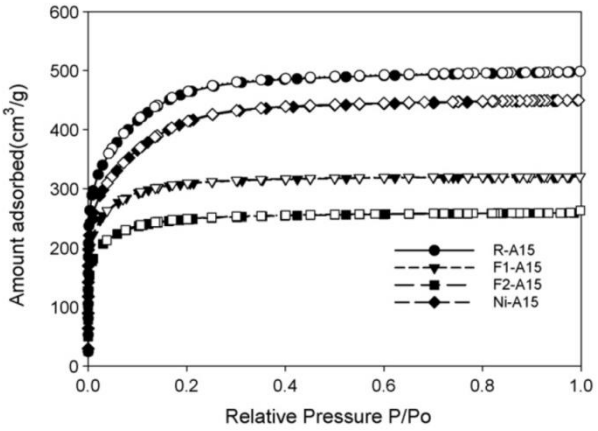

Figure 2-6. Adsorption isotherms of nitrogen on F-ACF for R-A15 (virgin ACF), F1-A15 (lightly fluorinated ACF), F2-A15 (heavily fluorinated ACF) and Ni-A15 (Nickel-doped ACF). Figure from Lee et al. [262].

As seen here, adsorption of nitrogen decreases with an increase in the fluorination level. They have also shown that level of fluorination has an inverse relation with pore volume, surface area and average pore width of the sample [262]. Pore size distribution of their samples is shown in Figure 2-7.

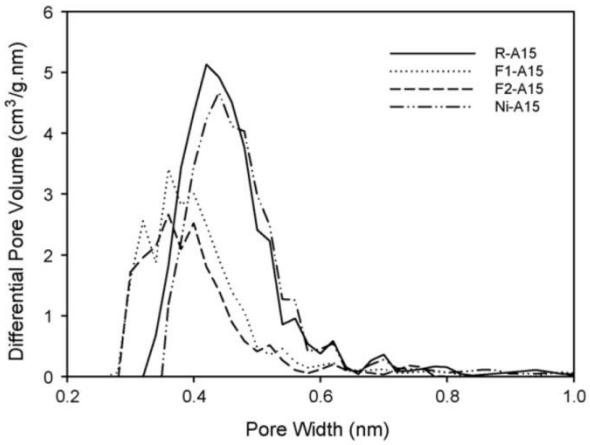

Figure 2-7. Pore size distributions (PSD) of R-A15 (virgin ACF), F1-A15 (lightly fluorinated ACF), F2-A15 (heavily fluorinated ACF) and Ni-A15 (Nickel-doped ACF) samples. Figure from Lee et al. [262]

In similar studies, Li and co-workers [241, 261] have investigated effect of fluorination on water adsorption in activated carbon samples. They have shown that water adsorption is significantly decreased by fluorination. According to Li et al. [241] water was not completely adsorbed until relative pressure was increased to 0.8, while for the virgin ACF sample, water adsorption starts at relative pressure equal to 0.4. They also show that water adsorption decreases more than 50 times at P/P_o = 0.9 on the fluorinated sample compared to its virgin counterpart [241]. Based on comparison of the nitrogen adsorption isotherms of F-ACF and ACF, they have demonstrated that basic microporous structure of the ACF is not altered considerably by fluorination; thus the decrease in the amount of water adsorption is due to hydrophobic nature of fluorine atoms [241]. Figure 2-8 illustrates comparison of water adsorption isotherms in F-ACF and ACF samples, as measured by Li et al. [241].

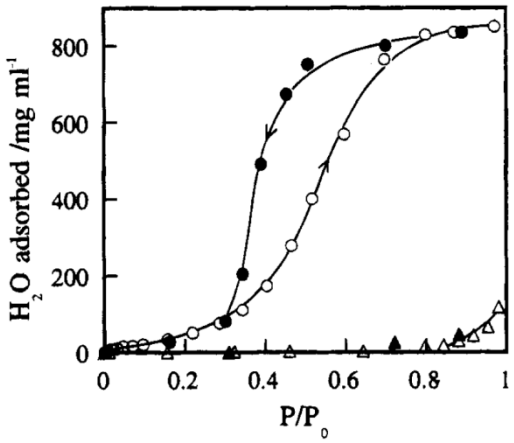

Figure 2-8. Adsorption isotherms water for ACF (circle) and F-ACF (triangle) at 303 K. Open symbols stand for adsorption and solid symbols for desorption branch. Figure from Li et al. [241]

To provide further insight into hydrophobicity of F-ACF, Li and co-workers [261] have compared effect of fluorination on adsorption of water, methanol and ethanol. They report that micropore volume; specific surface area and pore width of ACF is decreased by fluorination. Nevertheless, they emphasize that higher hydrophobicity of F-ACF is the main reason for decrease of water adsorption rather than the pore volume reduction. According to their study, water clusters cannot be formed on fluorinated surface of F-ACF due to polar nature of water molecules, however methanol and ethanol do adsorb in the form of molecular clusters due to having non-polar functional groups, which contribute to strong attractive vdW interactions with hydrophobic surface of F-ACF.

In a more recent study, Parmentier et al. [263] carried out nitrogen and water adsorption on mildly fluorinated activated carbon samples (initial F/C ratio ~0.4) and compared the results with that of pristine structure. Similar to other investigations, their results show a decrease in the amount of nitrogen adsorption on the fluorinated activated carbon samples, as depicted in Figure 2-9.

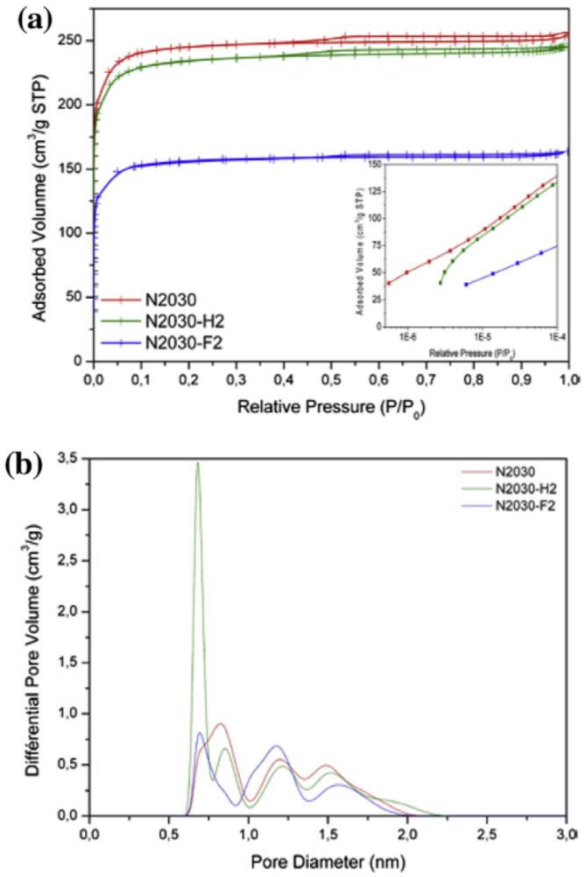

Figure 2-9. Comparison of nitrogen adsorption isotherms at 77 K on virgin (N2030), hydrogenated (N2030 –H2) and fluorinated (N2030-F2) activated carbon samples (a); as well as the corresponding NLDFT pore size distributions for N2030, N2030-H2 and N2030-F2 (b). Figure from Parmentier et al. [263]

Using several experimental measurements, they have also reported that even such mild fluorinations result in decrease of water adsorption due to the increase of hydrophobicity, as illustrated in Figure 2-10.

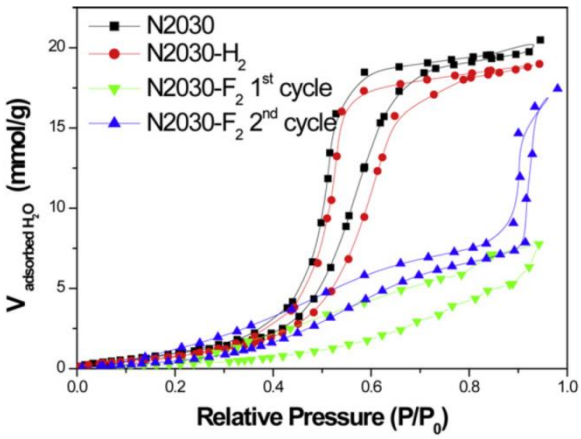

Figure 2-10. Water adsorption isotherms for virgin (N2030), hydrogenated (N2030 –H2) and fluorinated (N2030-F2) activated carbon samples. Figure from Parmentier et al. [263].

As evident from a handful of experimental studies discussed so far, fluorination decreases uptake of water vapor in carbonaceous materials. Nevertheless, our knowledge about underlying mechanisms of water adsorption in fluorine doped porous carbons is extremely limited due to the lack of fundamental studies in this area. Recently, Schrier [265] studied physisorption of several gases including carbon dioxide, nitrogen and water on two dimensional fluorographene and fluoro-polyphenylene using GCMC simulation and compared the results with non-fluorinated graphene and polyphenylene sheets. In his work, dispersion interaction parameters of carbon and fluorine atom for the fluorinated materials were taken from an older study by Gomes and Pádua [266], who in turn had obtained the parameters from OPLS-all atom force field [146, 267]. Here, electrostatic charge distributions of fluorinated compounds were calculated using ab-initio DFT calculation [265]. Schrier's results predict that fluorination "reduces the attractive dispersion interactions" for both fluorographene and fluoro-polyphenylene [265]. These interactions are more important for adsorption of nonpolar molecules [265]. In contrast, molecular properties of water including its large dipole moment and small attractive dispersion favor stronger adsorption of water below 300 K on the fluorinated models in comparison with the graphene model [265]. In the same vein, a recent first principles study on adsorption of water in C_4F (a stable fluorocarbon derivative of graphene) reveals anomalous super-hydrophilicity of the fluorinated graphene [268]. Surprisingly, another first principles study conducted by Murugan et al. [269] predicts higher hydrophobicity of fluorinated graphene compared to its pristine structure. According to this study, fluorinated graphene sheets can

be engineered specifically for increase of water repelling during co-adsorption of water and carbon dioxide [269].

Following above discussion, it is clear that although experimental investigations consistently report on reduction of water adsorption in fluorinated porous carbon, computational studies predict both hydrophobic and hydrophilic effects of fluorine-doped carbon based on strength of attractive interatomic interactions. As explained by Ho et al. [270], a surface is classified as hydrophilic or hydrophobic in macroscopic scale depending on the contact angle of water droplet on the surface, nevertheless the border line between a hydrophobic and hydrophilic surface is not very clear since even a hydrophilic surface can demonstrate properties associated with a hydrophobic surface. On the other hand, Godawat et al. defines hydrophobicity of a surface in molecular scale based on probability of cavity formation and the free energy of binding of hydrophobic solutes to interfaces [271]. According to them, these properties correlate with macroscopic wetting properties of the surface. Therefore, it appears that interpretation of the experimental results in macroscopic scale for explanation of the concept of "hydrophobicity" or "water repelling" in microscale fluorine-doped porous carbon is not straightforward. Chapter 7 of this thesis is dedicated to shed more light on this issue and elucidate the mechanisms underlying reduction of water adsorption in fluorinated porous carbon. It reports on comprehensive computational studies on adsorption and diffusion of water in fluorine-doped structure of SiC-DC using a new first principles force field to describe hydrophobicity/hydrophilicity of fluorinated SiC-DC based on reduction/increase of water adsorption in this material and strength of attractive interatomic interactions between water and the solid phase.

2.10. References

1. Davis, M.E., *Ordered porous materials for emerging applications.* Nature, 2002. **417**(6891): p. 813-821.
2. Cheetham, A.K., G. Férey, and T. Loiseau, *Open-Framework Inorganic Materials.* Angewandte Chemie International Edition, 1999. **38**(22): p. 3268-3292.
3. Menon, V.C. and S. Komarneni, *Porous Adsorbents for Vehicular Natural Gas Storage: A Review.* Journal of Porous Materials, 1998. **5**(1): p. 43-58.
4. Evans, R.B., G.M. Watson, and E.A. Mason, *Gaseous Diffusion in Porous Media. II. Effect of Pressure Gradients.* The Journal of Chemical Physics, 1962. **36**(7): p. 1894-1902.
5. Yang, H., et al., *Progress in carbon dioxide separation and capture: A review.* Journal of Environmental Sciences, 2008. **20**(1): p. 14-27.
6. Evans, R.B., G.M. Watson, and E.A. Mason, *Gaseous Diffusion in Porous Media at Uniform Pressure.* The Journal of Chemical Physics, 1961. **35**(6): p. 2076-2083.
7. Mason, E.A., R.B. Evans, and G.M. Watson, *Gaseous Diffusion in Porous Media. III. Thermal Transpiration.* The Journal of Chemical Physics, 1963. **38**(8): p. 1808-1826.
8. Li, J.-R., J. Sculley, and H.-C. Zhou, *Metal–Organic Frameworks for Separations.* Chemical Reviews, 2011. **112**(2): p. 869-932.
9. Sheehan, A.D., et al., *The Development of Novel Miniaturized Immuno-sensing Devices: A Review of a Small Technology with a Large Future.* Analytical Letters, 2003. **36**(3): p. 511-537.
10. Herold, K.E.R., Avraham, *Lab on a Chip Technology (Vol. 1): Fabrication and microfluidics*. Vol. 1. 2009, Norfolk: Caister Academic Press.
11. Čejka, J., et al., *Introduction to Zeolite Science and Practice*. 2007, Amsterdam Elsevier.
12. Xu, R., et al., *Chemistry of Zeolites and Related Porous Materials: Synthesis and Structure*. 2007, New York: Wiley.
13. Furukawa, H., et al., *Ultrahigh Porosity in Metal-Organic Frameworks.* Science, 2010. **329**(5990): p. 424-428.
14. Liu, J., et al., *A novel series of isoreticular metal organic frameworks: realizing metastable structures by liquid phase epitaxy.* Scientific Reports, 2012. **2**: p. 921.
15. Li, H., et al., *Design and synthesis of an exceptionally stable and highly porous metal-organic framework.* Nature, 1999. **402**(6759): p. 276-279.
16. Gogotsi, Y., et al., *Nanoporous carbide-derived carbon with tunable pore size.* Nature Materials, 2003. **2**(9): p. 591-594.
17. Presser, V., M. Heon, and Y. Gogotsi, *Carbide-Derived Carbons – From Porous Networks to Nanotubes and Graphene.* Advanced Functional Materials, 2011. **21**(5): p. 810-833.
18. Zhou, W., et al., *Synthesis, Structure, and Properties of Single-Walled Carbon Nanotubes.* Advanced Materials, 2009. **21**(45): p. 4565-4583.
19. Thostenson, E.T., Z. Ren, and T.-W. Chou, *Advances in the science and technology of carbon nanotubes and their composites: a review.* Composites Science and Technology, 2001. **61**(13): p. 1899-1912.
20. Knudsen, M., *Die Gesetze der Molekularströmung und der inneren Reibungsströmung der Gase durch Röhren.* Annalen der Physik, 1909. **333**(1): p. 75-130.
21. Mason, E.A. and A.P. Malinauskas, *Gas Transport in Porous Media: The Dusty-Gas Model*. 1983, Amsterdam: Elsevier.
22. Krishna, R., *Multicomponent surface diffusion of adsorbed species: a description based on the generalized Maxwell—Stefan equations.* Chemical Engineering Science, 1990. **45**(7): p. 1779-1791.
23. Krishna, R., *Problems and pitfalls in the use of the fick formulation for intraparticle diffusion.* Chemical Engineering Science, 1993. **48**(5): p. 845-861.

24. Bhatnagar, P.L., E.P. Gross, and M. Krook, *A Model for Collision Processes in Gases. I. Small Amplitude Processes in Charged and Neutral One-Component Systems.* Physical Review, 1954. **94**(3): p. 511-525.
25. Sircar, S., T.C. Golden, and M.B. Rao, *Activated carbon for gas separation and storage.* Carbon, 1996. **34**(1): p. 1-12.
26. Allen, L., Z. Ranyi, and M. McNallan, *Kinetics of conversion of silicon carbide to carbide derived carbon.* Journal of Physics: Condensed Matter, 2006. **18**(32): p. S1763.
27. Thomas, K.M., *Hydrogen adsorption and storage on porous materials.* Catalysis Today, 2007. **120**(3–4): p. 389-398.
28. Nguyen, T.X., J.S. Bae, and S.K. Bhatia, *Characterization and Adsorption Modeling of Silicon Carbide-Derived Carbons.* Langmuir, 2009. **25**(4): p. 2121-2132.
29. Bae, J.-S., T.X. Nguyen, and S.K. Bhatia, *Influence of Synthesis Conditions and Heat Treatment on the Structure of Ti3SiC2-Derived Carbons.* The Journal of Physical Chemistry C, 2009. **114**(2): p. 1046-1056.
30. Bonilla, M.R.n., et al., *Heat Treatment-Induced Structural Changes in SiC-Derived Carbons and their Impact on Gas Storage Potential.* The Journal of Physical Chemistry C, 2010. **114**(39): p. 16562-16575.
31. Dash, R., et al., *Titanium carbide derived nanoporous carbon for energy-related applications.* Carbon, 2006. **44**(12): p. 2489-2497.
32. Dash, R.K., A. Nikitin, and Y. Gogotsi, *Microporous carbon derived from boron carbide.* Microporous and Mesoporous Materials, 2004. **72**(1-3): p. 203-208.
33. Yushin, G., et al., *Carbide-Derived Carbons: Effect of Pore Size on Hydrogen Uptake and Heat of Adsorption.* Advanced Functional Materials, 2006. **16**(17): p. 2288-2293.
34. Urbonaite, S., et al., *EELS studies of carbide derived carbons.* Carbon, 2007. **45**(10): p. 2047-2053.
35. Welz, S., M.J. McNallan, and Y. Gogotsi, *Carbon structures in silicon carbide derived carbon.* Journal of Materials Processing Technology, 2006. **179**(1-3): p. 11-22.
36. Farmahini, A.H., G. Opletal, and S.K. Bhatia, *Structural Modelling of Silicon Carbide-Derived Nanoporous Carbon by Hybrid Reverse Monte Carlo Simulation.* Journal of Physical Chemistry C, 2013. **117**(27): p. 14081-14094.
37. Bhatia, S.K. and T.X. Nguyen, *Potential of Silicon Carbide-Derived Carbon for Carbon Capture.* Industrial & Engineering Chemistry Research, 2011. **50**(17): p. 10380-10383.
38. Sahimi, M., G.R. Gavalas, and T.T. Tsotsis, *Statistical and continuum models of fluid-solid reactions in porous media.* Chemical Engineering Science, 1990. **45**(6): p. 1443-1502.
39. Sahimi, M., *Flow and transport in porous media and fractured rock : from classical methods to modern approaches*. 1995, Weinheim, Germany: Wiley-VCH. 482.
40. Pruess, K., *Numerical Codes for Continuum Modeling of Gas Transport in Porous Media*, C.K. Ho and S.W. Webb, Editors. 2006, Springer Netherlands. p. 213-220.
41. Fatt, I., *The Network Model of Porous Media.* Petroleum Transactions, AIME, 1956. **207**: p. 38.
42. Lin, C. and M.H. Cohen, *Quantitative methods for microgeometric modeling.* Journal of Applied Physics, 1982. **53**(6): p. 4152-4165.
43. Winterfeld, P.H., L.E. Scriven, and H.T. Davis, *Percolation and conductivity of random two-dimensional composites.* Journal of Physics C: Solid State Physics, 1981. **14**(17): p. 2361.
44. Jerauld, G.R., L.E. Scriven, and H.T. Davis, *Percolation and conduction on the 3D Voronoi and regular networks: a second case study in topological disorder.* Journal of Physics C: Solid State Physics, 1984. **17**(19): p. 3429.

45. Ghassemzadeh, J., et al., *Statistical Mechanics and Molecular Simulation of Adsorption in Microporous Materials: Pillared Clays and Carbon Molecular Sieve Membranes†.* The Journal of Physical Chemistry B, 2000. **104**(16): p. 3892-3905.
46. Rajabbeigi, N., et al., *Molecular pore-network model for nanoporous materials. I: Application to adsorption in silicon-carbide membranes.* Journal of Membrane Science, 2009. **335**(1–2): p. 5-12.
47. Gelb, L.D., *Modeling Amorphous Porous Materials and Confined Fluids.* MRS Bulletin, 2009. **34**: p. 9.
48. Levitz, P., *Off-lattice reconstruction of porous media: critical evaluation, geometrical confinement and molecular transport.* Advances in Colloid and Interface Science, 1998. **76–77**(0): p. 71-106.
49. Quiblier, J.A., *A new three-dimensional modeling technique for studying porous media.* Journal of Colloid and Interface Science, 1984. **98**(1): p. 84-102.
50. Joshi, M.Y., *A class of stochastic models for porous media*. 1974, University of Kansas: United States -- Kansas. p. 163 p.
51. Roberts, A.P., *Statistical reconstruction of three-dimensional porous media from two-dimensional images.* Physical Review E, 1997. **56**(3): p. 3203-3212.
52. Yeong, C.L.Y. and S. Torquato, *Reconstructing random media.* Physical Review E, 1998. **57**(1): p. 495-506.
53. Yeong, C.L.Y. and S. Torquato, *Reconstructing random media. II. Three-dimensional media from two-dimensional cuts.* Physical Review E, 1998. **58**(1): p. 224-233.
54. Rozman, M.G. and M. Utz, *Efficient reconstruction of multiphase morphologies from correlation functions.* Physical Review E, 2001. **63**(6): p. 066701.
55. Kaplow, R., T.A. Rowe, and B.L. Averbach, *Atomic Arrangement in Vitreous Selenium.* Physical Review, 1968. **168**(3): p. 1068-1079.
56. McGreevy, R.L. and L. Pusztai, *Reverse Monte Carlo Simulation: A New Technique for the Determination of Disordered Structures.* Molecular Simulation, 1988. **1**(6): p. 359-367.
57. Opletal, G., et al., *HRMC: Hybrid Reverse Monte Carlo method with silicon and carbon potentials.* Computer Physics Communications, 2008. **178**(10): p. 777-787.
58. Opletal, G., et al., *Hybrid approach for generating realistic amorphous carbon structure using metropolis and reverse Monte Carlo.* Molecular Simulation, 2002. **28**(10-11): p. 927-938.
59. O'Malley, B., I. Snook, and D. McCulloch, *Reverse Monte Carlo analysis of the structure of glassy carbon using electron-microscopy data.* Physical Review B, 1998. **57**(22): p. 14148-14157.
60. Rigden, J.S. and R.J. Newport, *A Reverse Monte Carlo Modeling Study of Diamond-like Carbon.* Journal of The Electrochemical Society, 1996. **143**(1): p. 292-296.
61. Walters, J.K., et al., *Progress in modeling the chemical bonding in tetrahedral amorphous carbon.* Physical Review B, 1998. **58**(13): p. 8267-8276.
62. Thomson, K.T. and K.E. Gubbins, *Modeling Structural Morphology of Microporous Carbons by Reverse Monte Carlo.* Langmuir, 2000. **16**(13): p. 5761-5773.
63. Pikunic, J., et al., *Realistic molecular models for saccharose-based carbons.* Applied Surface Science, 2002. **196**(1–4): p. 98-104.
64. Pikunic, J., et al., *Structural Modeling of Porous Carbons: Constrained Reverse Monte Carlo Method.* Langmuir, 2003. **19**(20): p. 8565-8582.
65. Kirkpatrick, S., C.D. Gelatt, and M.P. Vecchi, *Optimization by Simulated Annealing.* Science, 1983. **220**(4598): p. 671-680.
66. Opletal, G., et al., *The structure of disordered carbon solids studied using a hybrid reverse Monte Carlo algorithm.* Journal of Physics: Condensed Matter, 2005. **17**(17): p. 2605.

67. Jain, S.K., et al., *Molecular Modeling of Porous Carbons Using the Hybrid Reverse Monte Carlo Method.* Langmuir, 2006. **22**(24): p. 9942-9948.
68. Nguyen, T.X., et al., *Structure of saccharose-based carbon and transport of confined fluids: hybrid reverse Monte Carlo reconstruction and simulation studies.* Molecular Simulation, 2006. **32**(7): p. 567-577.
69. Opletal, G., et al., *HRMC_2.0: Hybrid Reverse Monte Carlo method with silicon, carbon and germanium potentials.* Computer Physics Communications, 2013. **184**(8): p. 1946-1957.
70. Marks, N.A., *Generalizing the environment-dependent interaction potential for carbon.* Physical Review B, 2000. **63**(3): p. 035401.
71. Brenner, D.W., *Empirical potential for hydrocarbons for use in simulating the chemical vapor deposition of diamond films.* Physical Review B, 1990. **42**(15): p. 9458.
72. Nguyen, T.X., et al., *New Method for Atomistic Modeling of the Microstructure of Activated Carbons Using Hybrid Reverse Monte Carlo Simulation.* Langmuir, 2008. **24**(15): p. 7912-7922.
73. Shi, Y., *A mimetic porous carbon model by quench molecular dynamics simulation.* Journal of Chemical Physics, 2008. **128**(23).
74. Palmer, J.C. and K.E. Gubbins, *Atomistic models for disordered nanoporous carbons using reactive force fields.* Microporous and Mesoporous Materials, 2012. **154**(0): p. 24-37.
75. van Duin, A.C.T., et al., *ReaxFF: A Reactive Force Field for Hydrocarbons.* The Journal of Physical Chemistry A, 2001. **105**(41): p. 9396-9409.
76. Chenoweth, K., A.C.T. van Duin, and W.A. Goddard, *ReaxFF Reactive Force Field for Molecular Dynamics Simulations of Hydrocarbon Oxidation.* The Journal of Physical Chemistry A, 2008. **112**(5): p. 1040-1053.
77. Marks, N.A., *Amorphous Carbon and Related Materials*, in *COMPUTER-BASED MODELING OF NOVEL CARBON SYSTEMS AND THEIR PROPERTIES*, L. Colombo and A. Fasolino, Editors. 2010, Springer. p. 129-169.
78. Palmer, J.C., et al., *Modeling the structural evolution of carbide-derived carbons using quenched molecular dynamics.* Carbon, 2010. **48**(4): p. 1116-1123.
79. Tersoff, J., *Empirical Interatomic Potential for Carbon, with Applications to Amorphous Carbon.* Physical Review Letters, 1988. **61**(25): p. 2879-2882.
80. Stephan, U. and M. Haase, *A molecular dynamics study and the electronic properties of amorphous carbon using the Tersoff potential.* Journal of Physics: Condensed Matter, 1993. **5**(49): p. 9157.
81. Lopez, M.J., I. Cabria, and J.A. Alonso, *Simulated porosity and electronic structure of nanoporous carbons.* The Journal of Chemical Physics, 2011. **135**(10): p. 104706-9.
82. Gelb, L.D. and K.E. Gubbins, *Characterization of Porous Glasses: Simulation Models, Adsorption Isotherms, and the Brunauer−Emmett−Teller Analysis Method.* Langmuir, 1998. **14**(8): p. 2097-2111.
83. Romero, C., et al., *A New Approach to the Computer Modeling of Amorphous Nanoporous Structures of Semiconducting and Metallic Materials: A Review.* Materials, 2010. **3**(1): p. 467-502.
84. Palmer, J.C., et al., *Detailed structural models for activated carbons from molecular simulation.* Carbon, 2009. **47**(12): p. 2904-2913.
85. Atkins, P.W. and R.S. Friedman, *Molecular Quantum Mechanics*. 4th. ed. 2005, New York: Oxford University Press. 573.
86. Ravikovitch, P.I., G.L. Haller, and A.V. Neimark, *Density functional theory model for calculating pore size distributions: pore structure of nanoporous catalysts.* Advances in Colloid and Interface Science, 1998. **76–77**(0): p. 203-226.

87. Ravikovitch, P.I. and A.V. Neimark, *Density Functional Theory of Adsorption in Spherical Cavities and Pore Size Characterization of Templated Nanoporous Silicas with Cubic and Three-Dimensional Hexagonal Structures.* Langmuir, 2002. **18**(5): p. 1550-1560.
88. Nguyen, T.X. and S.K. Bhatia, *Probing the Pore Wall Structure of Nanoporous Carbons Using Adsorption.* Langmuir, 2004. **20**(9): p. 3532-3535.
89. Nguyen, T.X. and S.K. Bhatia, *Characterization of Pore Wall Heterogeneity in Nanoporous Carbons Using Adsorption: the Slit Pore Model Revisited.* The Journal of Physical Chemistry B, 2004. **108**(37): p. 14032-14042.
90. Nguyen, T.X. and S.K. Bhatia, *Characterization of activated carbon fibers using argon adsorption.* Carbon, 2005. **43**(4): p. 775-785.
91. Nguyen, T.X., S.K. Bhatia, and D. Nicholson, *Prediction of High-Pressure Adsorption Equilibrium of Supercritical Gases Using Density Functional Theory.* Langmuir, 2005. **21**(7): p. 3187-3197.
92. Bhatia, S.K., *Adsorption of Binary Hydrocarbon Mixtures in Carbon Slit Pores: A Density Functional Theory Study.* Langmuir, 1998. **14**(21): p. 6231-6240.
93. Bhatia, S.K., *Density Functional Theory Analysis of the Influence of Pore Wall Heterogeneity on Adsorption in Carbons.* Langmuir, 2002. **18**(18): p. 6845-6856.
94. Ravikovitch, P.I., et al., *Capillary Hysteresis in Nanopores: Theoretical and Experimental Studies of Nitrogen Adsorption on MCM-41*. Langmuir, 1995. **11**(12): p. 4765-4772.
95. Lueking, A., et al., *Tests of Pore-Size Distributions Deduced from Inversion of Simulated and Real Adsorption Data.* Journal of Low Temperature Physics, 2009. **157**(3): p. 410-428.
96. Kierlik, E. and M.L. Rosinberg, *Density-functional theory for inhomogeneous fluids: Adsorption of binary mixtures.* Physical Review A, 1991. **44**(8): p. 5025-5037.
97. Ravikovitch, P.I. and A.V. Neimark, *Density Functional Theory Model of Adsorption on Amorphous and Microporous Silica Materials.* Langmuir, 2006. **22**(26): p. 11171-11179.
98. Neimark, A.V., et al., *Quenched solid density functional theory and pore size analysis of micro-mesoporous carbons.* Carbon, 2009. **47**(7): p. 1617-1628.
99. Frenkel, D. and B. Smit, *Understanding Molecular Simulation: From Algorithms to Applications*. 2nd. ed. 2001, San Diego: Academic Press. 664.
100. Allen, M.P. and D.J. Tildesley, *Computer Simulation of Liquids*. 1989: CLARENDON PRESS. 408.
101. Dubbeldam, D. and R.Q. Snurr, *Recent developments in the molecular modeling of diffusion in nanoporous materials.* Molecular Simulation, 2007. **33**(4-5): p. 305-325.
102. Whitby, M. and N. Quirke, *Fluid flow in carbon nanotubes and nanopipes.* Nature Nanotechnology, 2007. **2**(2): p. 87-94.
103. Nicholson, D. and S.K. Bhatia, *Fluid transport in nanospaces.* Molecular Simulation, 2009. **35**(1-2): p. 109-121.
104. Bhatia, S.K., M.R. Bonilla, and D. Nicholson, *Molecular transport in nanopores: a theoretical perspective.* Physical Chemistry Chemical Physics, 2011. **13**(34): p. 15350-15383.
105. v. Smoluchowski, M., *Zur kinetischen Theorie der Transpiration und Diffusion verdünnter Gase.* Annalen der Physik, 1910. **338**(16): p. 1559-1570.
106. Sonwane, C.G. and S.K. Bhatia, *Structural Characterization of MCM-41 over a Wide Range of Length Scales.* Langmuir, 1999. **15**(8): p. 2809-2816.
107. Krishna, R. and J.A. Wesselingh, *The Maxwell-Stefan approach to mass transfer*. Chemical Engineering Science, 1997. **52**(6): p. 861-911.
108. Chapman, S. and T.G. Cowling, *Mathematical Theory of Non-Uniform Gases*. 1939 Cambridge: Cambridge University Press.
109. Hirschfelder, J.O., C.F. Curtiss, and R.B. Bird, *Molecular theory of gases and liquids*. 1954 New York: John Wiley.

110. Zhdanov, V., Y. Kagan, and A. Sazykin, *Effect of Viscous Transfer of Momentum on Diffusion in a Gas Mixture.* Journal of Experimental and Theoretical Physics, 1962. **15**(3): p. 596–602.
111. Mason, E.A., A.P. Malinauskas, and R.B. Evans, *Flow and Diffusion of Gases in Porous Media.* The Journal of Chemical Physics, 1967. **46**(8): p. 3199-3216.
112. Karger, J. and D.M. Ruthven, *Diffusion in Zeolites and Other Microporous Solids*. 1992, New York: John Wiley. 605
113. Nicholson, D. and J.H. Petropoulos, *Calculation of the "surface flow" of a dilute gas in model pores from first principles: II. Molecular gas flow in model pores as a function of gas-solid interaction and pore shape.* Journal of Colloid and Interface Science, 1981. **83**(2): p. 420-427.
114. Nicholson, D., J. Petrou, and J.H. Petropoulos, *Calculation of the "surface flow" of a dilute gas in model pores from first principles. I. Calculation of free molecule flow in an adsorbent force field by two methods.* Journal of Colloid and Interface Science, 1979. **71**(3): p. 570-579.
115. Nicholson, D. and J.H. Petropoulos, *Calculation of the "surface flow" of a dilute gas in model pores from first principles: III. Molecular gas flow in single pores and simple model porous media.* Journal of Colloid and Interface Science, 1985. **106**(2): p. 538-546.
116. Nicholson, D. and J.H. Petropoulos, *A fundamental approach to molecular flow in pore spaces.* Berichte der Bunsengesellschaft für physikalische Chemie, 1975. **79**(9): p. 796-798.
117. Pozhar, L.A. and K.E. Gubbins, *Dense inhomogeneous fluids: Functional perturbation theory, the generalized Langevin equation, and kinetic theory.* The Journal of Chemical Physics, 1991. **94**(2): p. 1367-1384.
118. Guo, Z., T.S. Zhao, and Y. Shi, *Simple kinetic model for fluid flows in the nanometer scale.* Physical Review E, 2005. **71**(3): p. 035301.
119. Guo, Z., et al., *Simulation of fluid flows in the nanometer: kinetic approach and molecular dynamic simulation.* International Journal of Computational Fluid Dynamics, 2006. **20**(6): p. 361-367.
120. Marconi, U.M.B. and S. Melchionna, *Dynamics of fluid mixtures in nanospaces.* The Journal of Chemical Physics, 2011. **134**(6): p. -.
121. Van Den Broeke, L.J.P., S.A. Nuhuis, and R. Krishna, *Monte Carlo simulations of diffusion in zeolites and comparison with the generalized Maxwell-Stefan theory.* Journal of Catalysis, 1992. **136**(2): p. 463-477.
122. Jepps, O.G., S.K. Bhatia, and D.J. Searles, *Wall Mediated Transport in Confined Spaces: Exact Theory for Low Density.* Physical Review Letters, 2003. **91**(12): p. 126102.
123. Bhatia, S.K., O. Jepps, and D. Nicholson, *Tractable molecular theory of transport of Lennard-Jones fluids in nanopores.* The Journal of Chemical Physics, 2004. **120**(9): p. 4472-4485.
124. Jepps, O.G., S.K. Bhatia, and D.J. Searles, *Modeling molecular transport in slit pores.* The Journal of Chemical Physics, 2004. **120**(11): p. 5396-5406.
125. Gubbins, K.E., et al., *The role of molecular modeling in confined systems: impact and prospects.* Physical Chemistry Chemical Physics, 2011. **13**(1): p. 58-85.
126. Fang, H., et al., *Recent developments in first-principles force fields for molecules in nanoporous materials.* Journal of Materials Chemistry A, 2014. **2**(2): p. 274-291.
127. Darkrim, F. and D. Levesque, *Monte Carlo simulations of hydrogen adsorption in single-walled carbon nanotubes.* The Journal of Chemical Physics, 1998. **109**(12): p. 4981-4984.
128. Harris, J.G. and K.H. Yung, *Carbon Dioxide's Liquid-Vapor Coexistence Curve And Critical Properties as Predicted by a Simple Molecular Model.* The Journal of Physical Chemistry, 1995. **99**(31): p. 12021-12024.

129. Mahoney, M.W. and W.L. Jorgensen, *A five-site model for liquid water and the reproduction of the density anomaly by rigid, nonpolarizable potential functions.* The Journal of Chemical Physics, 2000. **112**(20): p. 8910-8922.
130. Berendsen, H.J.C., J.R. Grigera, and T.P. Straatsma, *The missing term in effective pair potentials.* The Journal of Physical Chemistry, 1987. **91**(24): p. 6269-6271.
131. Martin, M.G. and J.I. Siepmann, *Novel Configurational-Bias Monte Carlo Method for Branched Molecules. Transferable Potentials for Phase Equilibria. 2. United-Atom Description of Branched Alkanes.* The Journal of Physical Chemistry B, 1999. **103**(21): p. 4508-4517.
132. Martin, M.G. and J.I. Siepmann, *Transferable Potentials for Phase Equilibria. 1. United-Atom Description of n-Alkanes.* The Journal of Physical Chemistry B, 1998. **102**(14): p. 2569-2577.
133. Wick, C.D., M.G. Martin, and J.I. Siepmann, *Transferable Potentials for Phase Equilibria. 4. United-Atom Description of Linear and Branched Alkenes and Alkylbenzenes.* The Journal of Physical Chemistry B, 2000. **104**(33): p. 8008-8016.
134. Chen, B., J.J. Potoff, and J.I. Siepmann, *Monte Carlo Calculations for Alcohols and Their Mixtures with Alkanes. Transferable Potentials for Phase Equilibria. 5. United-Atom Description of Primary, Secondary, and Tertiary Alcohols.* The Journal of Physical Chemistry B, 2001. **105**(15): p. 3093-3104.
135. Nicholas, J.B., et al., *Molecular modeling of zeolite structure. 2. Structure and dynamics of silica sodalite and silicate force field.* Journal of the American Chemical Society, 1991. **113**(13): p. 4792-4800.
136. Hill, J.-R. and J. Sauer, *Molecular Mechanics Potential for Silica and Zeolite Catalysts Based on ab Initio Calculations. 2. Aluminosilicates.* The Journal of Physical Chemistry, 1995. **99**(23): p. 9536-9550.
137. Tafipolsky, M., S. Amirjalayer, and R. Schmid, *Ab initio parametrized MM3 force field for the metal-organic framework MOF-5.* Journal of Computational Chemistry, 2007. **28**(7): p. 1169-1176.
138. Dubbeldam, D., et al., *Exceptional Negative Thermal Expansion in Isoreticular Metal–Organic Frameworks.* Angewandte Chemie International Edition, 2007. **46**(24): p. 4496-4499.
139. Vanduyfhuys, L., et al., *Ab Initio Parametrized Force Field for the Flexible Metal–Organic Framework MIL-53(Al).* Journal of Chemical Theory and Computation, 2012. **8**(9): p. 3217-3231.
140. Schmid, R. and M. Tafipolsky, *An Accurate Force Field Model for the Strain Energy Analysis of the Covalent Organic Framework COF-102.* Journal of the American Chemical Society, 2008. **130**(38): p. 12600-12601.
141. Amirjalayer, S., R.Q. Snurr, and R. Schmid, *Prediction of Structure and Properties of Boron-Based Covalent Organic Frameworks by a First-Principles Derived Force Field.* The Journal of Physical Chemistry C, 2012. **116**(7): p. 4921-4929.
142. Hu, Z., L. Zhang, and J. Jiang, *Development of a force field for zeolitic imidazolate framework-8 with structural flexibility.* The Journal of Chemical Physics, 2012. **136**(24): p. 244703-244710.
143. Zhang, L., Z. Hu, and J. Jiang, *Sorption-Induced Structural Transition of Zeolitic Imidazolate Framework-8: A Hybrid Molecular Simulation Study.* Journal of the American Chemical Society, 2013. **135**(9): p. 3722-3728.
144. Rappe, A.K., et al., *UFF, a full periodic table force field for molecular mechanics and molecular dynamics simulations.* Journal of the American Chemical Society, 1992. **114**(25): p. 10024-10035.

145. Mayo, S.L., B.D. Olafson, and W.A. Goddard, *DREIDING: a generic force field for molecular simulations.* The Journal of Physical Chemistry, 1990. **94**(26): p. 8897-8909.
146. Jorgensen, W.L., D.S. Maxwell, and J. Tirado-Rives, *Development and Testing of the OPLS All-Atom Force Field on Conformational Energetics and Properties of Organic Liquids.* Journal of the American Chemical Society, 1996. **118**(45): p. 11225-11236.
147. Yazaydın, A.Ö., et al., *Screening of Metal−Organic Frameworks for Carbon Dioxide Capture from Flue Gas Using a Combined Experimental and Modeling Approach.* Journal of the American Chemical Society, 2009. **131**(51): p. 18198-18199.
148. Garberoglio, G., *Computer Simulation of the Adsorption of Light Gases in Covalent Organic Frameworks.* Langmuir, 2007. **23**(24): p. 12154-12158.
149. Sagara, T., J. Klassen, and E. Ganz, *Computational study of hydrogen binding by metal-organic framework-5.* The Journal of Chemical Physics, 2004. **121**(24): p. 12543-12547.
150. Pérez-Pellitero, J., et al., *Adsorption of CO2, CH4, and N2 on Zeolitic Imidazolate Frameworks: Experiments and Simulations.* Chemistry – A European Journal, 2010. **16**(5): p. 1560-1571.
151. Jee, S.E. and D.S. Sholl, *Carbon Dioxide and Methane Transport in DDR Zeolite: Insights from Molecular Simulations into Carbon Dioxide Separations in Small Pore Zeolites.* Journal of the American Chemical Society, 2009. **131**(22): p. 7896-7904.
152. McDaniel, J.G., K. Yu, and J.R. Schmidt, *Ab Initio, Physically Motivated Force Fields for CO2 Adsorption in Zeolitic Imidazolate Frameworks.* The Journal of Physical Chemistry C, 2011. **116**(2): p. 1892-1903.
153. Zang, J., S. Nair, and D.S. Sholl, *Prediction of Water Adsorption in Copper-Based Metal–Organic Frameworks Using Force Fields Derived from Dispersion-Corrected DFT Calculations.* Journal of Physical Chemistry C, 2013. **117**(15): p. 7519-7525.
154. Han, S.S., J.L. Mendoza-Cortes, and W.A. Goddard Iii, *Recent advances on simulation and theory of hydrogen storage in metal-organic frameworks and covalent organic frameworks.* Chemical Society Reviews, 2009. **38**(5): p. 1460-1476.
155. Xiang, Z., et al., *Multiscale simulation and modelling of adsorptive processes for energy gas storage and carbon dioxide capture in porous coordination frameworks.* Energy & Environmental Science, 2010. **3**(10): p. 1469-1487.
156. Getman, R.B., et al., *Review and Analysis of Molecular Simulations of Methane, Hydrogen, and Acetylene Storage in Metal–Organic Frameworks.* Chemical Reviews (Washington, DC, United States), 2011. **112**(2): p. 703-723.
157. Yang, Q., et al., *Development of Computational Methodologies for Metal–Organic Frameworks and Their Application in Gas Separations.* Chemical Reviews (Washington, DC, United States), 2013. **113**(10): p. 8261-8323.
158. Riley, K.E., et al., *Stabilization and Structure Calculations for Noncovalent Interactions in Extended Molecular Systems Based on Wave Function and Density Functional Theories.* Chemical Reviews (Washington, DC, United States), 2010. **110**(9): p. 5023-5063.
159. Bartlett, R.J. and M. Musiał, *Coupled-cluster theory in quantum chemistry.* Reviews of Modern Physics, 2007. **79**(1): p. 291-352.
160. Han, S.S., W.-Q. Deng, and W.A. Goddard, *Improved Designs of Metal–Organic Frameworks for Hydrogen Storage.* Angewandte Chemie International Edition, 2007. **46**(33): p. 6289-6292.
161. Han, S.S., S.-H. Choi, and W.A. Goddard, *Improved H2 Storage in Zeolitic Imidazolate Frameworks Using Li+, Na+, and K+ Dopants, with an Emphasis on Delivery H2 Uptake.* The Journal of Physical Chemistry C, 2011. **115**(8): p. 3507-3512.
162. Jeziorski, B., R. Moszynski, and K. Szalewicz, *Perturbation Theory Approach to Intermolecular Potential Energy Surfaces of van der Waals Complexes.* Chemical Reviews (Washington, DC, United States), 1994. **94**(7): p. 1887-1930.

163. Hohenberg, P. and W. Kohn, *Inhomogeneous Electron Gas.* Physical Review, 1964. **136**(3B): p. B864-B871.
164. Kohn, W. and L.J. Sham, *Self-Consistent Equations Including Exchange and Correlation Effects.* Physical Review, 1965. **140**(4A): p. A1133-A1138.
165. Klimeš, J. and A. Michaelides, *Perspective: Advances and challenges in treating van der Waals dispersion forces in density functional theory.* The Journal of Chemical Physics, 2012. **137**(12): p. 120901-120913.
166. Sholl, D. and J.A. Steckel, *Density Functional Theory : A Practical Introduction*. 2009, Hoboken, NJ: Wiley.
167. Grimme, S., *Accurate description of van der Waals complexes by density functional theory including empirical corrections.* Journal of Computational Chemistry, 2004. **25**(12): p. 1463-1473.
168. Grimme, S., *Semiempirical GGA-type density functional constructed with a long-range dispersion correction.* Journal of Computational Chemistry, 2006. **27**(15): p. 1787-1799.
169. Grimme, S., et al., *A consistent and accurate ab initio parametrization of density functional dispersion correction (DFT-D) for the 94 elements H-Pu.* The Journal of Chemical Physics, 2010. **132**(15): p. 154104-154123.
170. Dion, M., et al., *Van der Waals Density Functional for General Geometries.* Physical Review Letters, 2004. **92**(24): p. 246401.
171. Lee, K., et al., *Higher-accuracy van der Waals density functional.* Physical Review B, 2010. **82**(8): p. 081101.
172. Jiří, K., R.B. David, and M. Angelos, *Chemical accuracy for the van der Waals density functional.* Journal of Physics: Condensed Matter, 2010. **22**(2): p. 022201.
173. Klimeš, J., D.R. Bowler, and A. Michaelides, *Van der Waals density functionals applied to solids.* Physical Review B, 2011. **83**(19): p. 195131.
174. Vydrov, O.A. and T. Van Voorhis, *Nonlocal van der Waals density functional: The simpler the better.* The Journal of Chemical Physics, 2010. **133**(24): p. -.
175. Fang, H., et al., *Prediction of CO2 Adsorption Properties in Zeolites Using Force Fields Derived from Periodic Dispersion-Corrected DFT Calculations.* Journal of Physical Chemistry C, 2012. **116**(19): p. 10692-10701.
176. Zhang, Y. and W. Yang, *Comment on "Generalized Gradient Approximation Made Simple".* Physical Review Letters, 1998. **80**(4): p. 890-890.
177. Bae, Y.-S. and R.Q. Snurr, *Development and Evaluation of Porous Materials for Carbon Dioxide Separation and Capture.* Angewandte Chemie International Edition, 2011. **50**(49): p. 11586-11596.
178. Cavenati, S., C.A. Grande, and A.E. Rodrigues, *Adsorption Equilibrium of Methane, Carbon Dioxide, and Nitrogen on Zeolite 13X at High Pressures.* Journal of Chemical & Engineering Data, 2004. **49**(4): p. 1095-1101.
179. Rochelle, G.T., *Amine Scrubbing for CO2 Capture.* Science, 2009. **325**(5948): p. 1652-1654.
180. Yu, C., C. Huang, and C. Tan, *A Review of CO2 Capture by Absorption and Adsorption.* Aerosol and Air Quality Research, 2012. **12**(5): p. 745-769.
181. Choi, S., J.H. Drese, and C.W. Jones, *Adsorbent Materials for Carbon Dioxide Capture from Large Anthropogenic Point Sources.* ChemSusChem, 2009. **2**(9): p. 796-854.
182. Khatri, R.A., et al., *Carbon Dioxide Capture by Diamine-Grafted SBA-15: A Combined Fourier Transform Infrared and Mass Spectrometry Study.* Industrial & Engineering Chemistry Research, 2005. **44**(10): p. 3702-3708.
183. Sayari, A., Y. Belmabkhout, and R. Serna-Guerrero, *Flue gas treatment via CO2 adsorption.* Chemical Engineering Journal (Lausanne), 2011. **171**(3): p. 760-774.

184. D'Alessandro, D.M., B. Smit, and J.R. Long, *Carbon Dioxide Capture: Prospects for New Materials.* Angewandte Chemie International Edition, 2010. **49**(35): p. 6058-6082.
185. Ferey, G., *Hybrid porous solids: past, present, future.* Chemical Society Reviews, 2008. **37**(1): p. 191-214.
186. Mueller, U., et al., *Metal-organic frameworks-prospective industrial applications.* Journal of Materials Chemistry, 2006. **16**(7): p. 626-636.
187. Davini, P., *Flue gas treatment by activated carbon obtained from oil-fired fly ash.* Carbon, 2002. **40**(11): p. 1973-1979.
188. Rodríguez-Reinoso, F. and M. Molina-Sabio, *Activated carbons from lignocellulosic materials by chemical and/or physical activation: an overview.* Carbon, 1992. **30**(7): p. 1111-1118.
189. Lagorsse, S., F.D. Magalhães, and A. Mendes, *Carbon molecular sieve membranes: Sorption, kinetic and structural characterization.* Journal of Membrane Science, 2004. **241**(2): p. 275-287.
190. Nakashima, M., et al., *On the adsorption of CO2 by molecular sieve carbons—Volumetric and gravimetric studies.* Carbon, 1995. **33**(9): p. 1301-1306.
191. Vyas, S.N., et al., *Adsorption of Gases on Carbon Molecular Sieves.* Journal of Colloid and Interface Science, 1994. **168**(2): p. 275-280.
192. Gogotsi, Y., *Carbon Nanomaterials*. 2006, Boca Raton, FL Taylor & Francis. 326
193. Chmiola, J., et al., *Anomalous Increase in Carbon Capacitance at Pore Sizes Less Than 1 Nanometer*. Science, 2006. **313**(5794): p. 1760-1763.
194. Marsh, H., *Activated Carbon Compendium*. First ed. 2001: Elsevier Science Ltd. 320.
195. Gogotsi, Y., et al., *Tailoring of Nanoscale Porosity in Carbide-Derived Carbons for Hydrogen Storage.* Journal of the American Chemical Society, 2005. **127**(46): p. 16006-16007.
196. Gong, R. and T.C. Keener, *A Qualitative Analysis of the Effects of Water Vapor on Multi-Component Vapor-Phase Carbon Adsorption.* Air & Waste, 1993. **43**(6): p. 864-872.
197. Bourdin, V., P. Grenier, and A. Malka-Edery. *Fundamentals of Adsorption*. in *Proceedings of the Sixth Conference on Fundamentals of Adsorption*. 1998. Presqu'ile de Giens, France: Elsevier.
198. Dawson, R., et al., *Impact of Water Coadsorption for Carbon Dioxide Capture in Microporous Polymer Sorbents.* Journal of the American Chemical Society, 2012. **134**(26): p. 10741-10744.
199. Marx, D., et al., *The Role of Water in Adsorption-based CO2 Capture Systems.* Energy Procedia, 2013. **37**(0): p. 107-114.
200. Brennan, J.K., et al., *Water in porous carbons.* Colloids and Surfaces, A: Physicochemical and Engineering Aspects, 2001. **187-188**: p. 539-568.
201. Liu, L. and S.K. Bhatia, *Molecular Simulation of CO2 Adsorption in the Presence of Water in Single-Walled Carbon Nanotubes.* Journal of Physical Chemistry C, 2013. **117**(26): p. 13479-13491.
202. Gregg, S.J. and K.S.W. Sing, *Adsorption, Surface Area and Porosity*. 2nd ed. ed. 1982, New York: Academic Press. 303.
203. Dubinin, M.M., *Water vapor adsorption and the microporous structures of carbonaceous adsorbents.* Carbon, 1980. **18**(5): p. 355-364.
204. Ohba, T., H. Kanoh, and K. Kaneko, *Affinity Transformation from Hydrophilicity to Hydrophobicity of Water Molecules on the Basis of Adsorption of Water in Graphitic Nanopores.* Journal of the American Chemical Society, 2004. **126**(5): p. 1560-1562.
205. Kimura, T., et al., *Cluster-Associated Filling of Water in Hydrophobic Carbon Micropores.* Journal of Physical Chemistry B, 2004. **108**(37): p. 14043-14048.

206. Müller, E.A. and K.E. Gubbins, *Molecular simulation study of hydrophilic and hydrophobic behavior of activated carbon surfaces.* Carbon, 1998. **36**(10): p. 1433-1438.
207. Müller, E.A., et al., *Adsorption of Water on Activated Carbons: A Molecular Simulation Study.* Journal of Physical Chemistry, 1996. **100**(4): p. 1189-1196.
208. Easton, E.B. and W.D. Machin, *Adsorption of Water Vapor on a Graphitized Carbon Black.* Journal of Colloid and Interface Science, 2000. **231**(1): p. 204-206.
209. Hummer, G., J.C. Rasaiah, and J.P. Noworyta, *Water conduction through the hydrophobic channel of a carbon nanotube.* Nature, 2001. **414**(6860): p. 188-190.
210. Dubinin, M.M. and V.V. Serpinsky, *Isotherm equation for water vapor adsorption by microporous carbonaceous adsorbents.* Carbon, 1981. **19**(5): p. 402-403.
211. D'Arcy, R.L. and I.C. Watt, *Analysis of sorption isotherms of non-homogeneous sorbents.* Transactions of the Faraday Society, 1970. **66**(0): p. 1236-1245.
212. Evans, M.J.B., *The adsorption of water by oxidised microporous carbon.* Carbon, 1987. **25**(1): p. 81-83.
213. Talu, O. and F. Meunier, *Adsorption of associating molecules in micropores and application to water on carbon.* AIChE Journal, 1996. **42**(3): p. 809-819.
214. Stoeckli, F., et al., *Water adsorption in carbons described by the dubinin-astakhov and dubinin-serpinski equations.* Journal of the Chemical Society, Faraday Transactions, 1994. **90**(24): p. 3689-3691.
215. Lodewyckx, P. and E.F. Vansant, *Water isotherms of activated carbons with small amounts of surface oxygen.* Carbon, 1999. **37**(10): p. 1647-1649.
216. Striolo, A., et al., *Simulated water adsorption isotherms in carbon nanopores.* Molecular Physics, 2004. **102**(3): p. 243-251.
217. Liu, J.C. and P.A. Monson, *Does Water Condense in Carbon Pores?†.* Langmuir, 2005. **21**(22): p. 10219-10225.
218. Liu, J.C. and P.A. Monson, *Monte Carlo Simulation Study of Water Adsorption in Activated Carbon.* Industrial & Engineering Chemistry Research, 2006. **45**(16): p. 5649-5656.
219. Brennan, J.K., K.T. Thomson, and K.E. Gubbins, *Adsorption of Water in Activated Carbons: Effects of Pore Blocking and Connectivity.* Langmuir, 2002. **18**(14): p. 5438-5447.
220. Nguyen, T.X. and S.K. Bhatia, *How Water Adsorbs in Hydrophobic Nanospaces.* Journal of Physical Chemistry C, 2011: p. 16606–16612.
221. Nguyen, T.X. and S.K. Bhatia, *Some Anomalies in the Self-Diffusion of Water in Disordered Carbons.* Journal of Physical Chemistry C, 2012. **116**(5): p. 3667-3676.
222. Ma, X., X. Wang, and C. Song, *"Molecular Basket" Sorbents for Separation of CO2 and H2S from Various Gas Streams.* Journal of the American Chemical Society, 2009. **131**(16): p. 5777-5783.
223. Wang, D., et al., *Development of Carbon-Based "Molecular Basket" Sorbent for CO2 Capture.* Industrial & Engineering Chemistry Research, 2012. **51**(7): p. 3048-3057.
224. Wang, X., et al., *Nanoporous molecular basket sorbent for NO2 and SO2 capture based on a polyethylene glycol-loaded mesoporous molecular sieve.* Energy & Environmental Science, 2009. **2**(8): p. 878-882.
225. Xu, X., et al., *Novel Polyethylenimine-Modified Mesoporous Molecular Sieve of MCM-41 Type as High-Capacity Adsorbent for CO2 Capture.* Energy & Fuels, 2002. **16**(6): p. 1463-1469.
226. Xu, X., et al., *Preparation and characterization of novel CO2 "molecular basket" adsorbents based on polymer-modified mesoporous molecular sieve MCM-41.* Microporous and Mesoporous Materials, 2003. **62**(1–2): p. 29-45.

227. Wang, X., et al., *A solid molecular basket sorbent for CO2 capture from gas streams with low CO2 concentration under ambient conditions.* Physical Chemistry Chemical Physics, 2012. **14**(4): p. 1485-1492.
228. Wang, D., et al., *High-Capacity and Low-Cost Carbon-Based "Molecular Basket" Sorbent for CO2 Capture from Flue Gas.* Energy & Fuels, 2010. **25**(1): p. 456-458.
229. Bishnoi, S. and G. Rochelle, T. , *Absorption of carbon dioxide in aqueous piperazine/methyldiethanolamine.* AIChE Journal, 2002b. **48**(12): p. 2788-2799.
230. Bishnoi, S. and G.T. Rochelle, *Thermodynamics of piperazine/methyldiethanolamine/water/carbon dioxide.* Industrial & Engineering Chemistry Research, 2002a. **41**(3).
231. Derks, P.W.J., *Carbon dioxide absorption in piperazine activated N-methyldiethanolamine*. 2006, University of Twente: Enschede. p. iv,4,46,48,105-111,.
232. Farmahini, A.H., B. Kvamme, and T. Kuznetsova, *Molecular dynamics simulation studies of absorption in piperazine activated MDEA solution.* Physical Chemistry Chemical Physics, 2011. **13**(28): p. 13070-13081.
233. Wang, X., et al., *A nanoporous polymeric sorbent for deep removal of H2S from gas mixtures for hydrogen purification.* Green Chemistry, 2007. **9**(6): p. 695-702.
234. Wang, X., et al., *Mesoporous-molecular-sieve-supported Polymer Sorbents for Removing H2S from Hydrogen Gas Streams.* Topics in Catalysis, 2008. **49**(1): p. 108-117.
235. Si, X., et al., *High and selective CO2 uptake, H2 storage and methanol sensing on the amine-decorated 12-connected MOF CAU-1*. Energy & Environmental Science, 2011. **4**(11): p. 4522-4527.
236. Xiang, Z., S. Leng, and D. Cao, *Functional Group Modification of Metal–Organic Frameworks for CO2 Capture*. The Journal of Physical Chemistry C, 2012.
237. Sumida, K., et al., *Carbon Dioxide Capture in Metal–Organic Frameworks.* Chemical Reviews, 2011. **112**(2): p. 724-781.
238. Paraknowitsch, J.P. and A. Thomas, *Doping carbons beyond nitrogen: an overview of advanced heteroatom doped carbons with boron, sulphur and phosphorus for energy applications.* Energy & Environmental Science, 2013. **6**(10): p. 2839-2855.
239. Chen, L.-F., et al., *Three-Dimensional Heteroatom-Doped Carbon Nanofiber Networks Derived from Bacterial Cellulose for Supercapacitors.* Advanced Functional Materials, 2014. **24**(32): p. 5104-5111.
240. Yang, S., et al., *Efficient Synthesis of Heteroatom (N or S)-Doped Graphene Based on Ultrathin Graphene Oxide-Porous Silica Sheets for Oxygen Reduction Reactions.* Advanced Functional Materials, 2012. **22**(17): p. 3634-3640.
241. Li, G., et al., *Water Rejective Nature of Fluorinated Microporous Carbon Fibers.* Langmuir, 1995. **11**(3): p. 716-717.
242. Wang, X., et al., *Heteroatom-doped graphene materials: syntheses, properties and applications.* Chemical Society Reviews, 2014. **43**(20): p. 7067-7098.
243. Touhara, H. and F. Okino, *Property control of carbon materials by fluorination.* Carbon, 2000. **38**(2): p. 241-267.
244. Ruff, O. and O. Bretschneider, *Die Reaktionsprodukte der verschiedenen Kohlenstoffformen mit Fluor II (Kohlenstoff-monofluorid).* Zeitschrift fuer Anorganische und Allgemeine Chemie, 1934. **217**(1): p. 1-18.
245. Rüdorff, W. and G. Rüdorff, *Zur Konstitution des Kohlenstoff-Monofluorids.* Zeitschrift für anorganische Chemie, 1947. **253**(5-6): p. 281-296.
246. Wood, J.L., et al., *Heat of formation of poly(carbon monofluoride).* Journal of Physical Chemistry, 1969. **73**(9): p. 3139-3142.
247. Hamwi, A., et al., *Fluorination of carbon nanotubes.* Carbon, 1997. **35**(6): p. 723-728.

248. Mickelson, E.T., et al., *Fluorination of single-wall carbon nanotubes.* Chemical Physics Letters, 1998. **296**(1–2): p. 188-194.
249. Shen, B., et al., *Synthesis of fluorine-doped multi-layered graphene sheets by arc-discharge.* RSC Advances, 2012. **2**(17): p. 6761-6764.
250. Charlier, J.C., X. Gonze, and J.P. Michenaud, *First-principles study of graphite monofluoride* Physical Review B, 1993. **47**(24): p. 16162-16168.
251. Nakajima, T., S. Kasamatsu, and Y. Matsuo, *Synthesis and characterization of fluorinated carbon nanotube.* European Journal of Solid State and Inorganic Chemistry, 1996. **33**(9): p. 831-840.
252. Lebedev, N.G., I.V. Zaporotskova, and L.A. Chernozatonskii, *Fluorination of carbon nanotubes: Quantum chemical investigation within MNDO approximation.* International Journal of Quantum Chemistry, 2004. **96**(2): p. 142-148.
253. Bulusheva, L.G., et al., *Fluorine Effect on the Binding Energy of Nitrogen Atoms Incorporated into Multiwall CNx Nanotubes.* AIP Conference Proceedings, 2004. **723**(1): p. 595-598.
254. Touhara, H., et al., *Property control of new forms of carbon materials by fluorination.* Journal of Fluorine Chemistry, 2002. **114**(2): p. 181-188.
255. Lee, Y.S., et al., *Surface properties of fluorinated single-walled carbon nanotubes.* Journal of Fluorine Chemistry, 2003. **120**(2): p. 99-104.
256. Valentini, L., et al., *Modification of fluorinated single-walled carbon nanotubes with aminosilane molecules.* Carbon, 2006. **44**(11): p. 2196-2201.
257. Dettlaff-Weglikowska, U., et al., *Effect of fluorination on electrical properties of single walled carbon nanotubes and C60 peapods in networks.* Current Applied Physics, 2007. **7**(1): p. 42-46.
258. Muramatsu, H., et al., *Fluorination of double-walled carbon nanotubes.* Chemical Communications (Cambridge, United Kingdom), 2005(15): p. 2002-2004.
259. Jaffe, R.L., *Quantum Chemistry Study of Fullerene and Carbon Nanotube Fluorination.* The Journal of Physical Chemistry B, 2003. **107**(38): p. 10378-10388.
260. Setoyama, N., et al., *Nitrogen adsorption on fluorinated activated carbon fiber.* Adsorption, 1996. **2**(4): p. 293-297.
261. Li, G., et al., *Adsorption Behavior of Polar Molecules in Fluorinated Micropores.* Journal of Colloid and Interface Science, 1995. **172**(2): p. 539-540.
262. Lee, Y.S., et al., *The adsorption properties of surface modified activated carbon fibers for hydrogen storages.* Catalysis Today, 2007. **120**(3–4): p. 420-425.
263. Parmentier, J., et al., *Structural/textural properties and water reactivity of fluorinated activated carbons.* Carbon, 2012. **50**(14): p. 5135-5147.
264. Wang, Z., et al., *Synthesis of fluorinated graphene with tunable degree of fluorination.* Carbon, 2012. **50**(15): p. 5403-5410.
265. Schrier, J., *Fluorinated and Nanoporous Graphene Materials As Sorbents for Gas Separations.* ACS Applied Materials & Interfaces, 2011. **3**(11): p. 4451-4458.
266. Costa Gomes, M.F. and A.A.H. Pádua, *Interactions of Carbon Dioxide with Liquid Fluorocarbons.* Journal of Physical Chemistry B, 2003. **107**(50): p. 14020-14024.
267. Watkins, E.K. and W.L. Jorgensen, *Perfluoroalkanes: Conformational Analysis and Liquid-State Properties from ab Initio and Monte Carlo Calculations.* The Journal of Physical Chemistry A, 2001. **105**(16): p. 4118-4125.
268. Wang, P., H. Wang, and W. Yang, *Anomalous high adsorption energy of H2O on fluorinated graphenes: a first principles study.* Physical Chemistry Chemical Physics, 2014. **16**(38): p. 20464-20470.

269. Murugan, L., S. Lakshmipathi, and S.K. Bhatia, *Influence of in-plane Stone-Thrower-Wales defects and edge functionalisation on the adsorption of CO2 and H2O on graphene.* RSC Advances, 2014. **4**(74): p. 39576-39587.
270. Ho, T.A., et al., *Liquid water can slip on a hydrophilic surface.* Proceedings of the National Academy of Sciences, 2011. **108**(39): p. 16170-16175.
271. Godawat, R., S.N. Jamadagni, and S. Garde, *Characterizing hydrophobicity of interfaces by using cavity formation, solute binding, and water correlations.* Proceedings of the National Academy of Sciences, 2009. **106**(36): p. 15119-15124.

3. Structural Modelling of Silicon Carbide-Derived Nanoporous Carbon by Hybrid Reverse Monte Carlo Simulation

Amir H. Farmahini[1], *George Opletal*[2], *Suresh K. Bhatia*[1]*

J. Phys. Chem. C, 2013, 117 (27), pp 14081–14094

DOI: 10.1021/jp403929r

Accepted: June 13, 2013 - Published: July 11, 2013

[1]School of Chemical Engineering, The University of Queensland, QLD 4072, Australia

[2]Department of Applied Physics, RMIT University, Melbourne, VIC 3001, Australia

3.1. Abstract

An atomistic model of the nano-particle size Silicon Carbide Derived Carbon (SiC-CDC) is constructed using the Hybrid Reverse Monte Carlo (HRMC) technique through a two-step modeling procedure. Pore volume and 3-member ring constraints were utilized in addition to the commonly used structure factor and energy constraints in the HRMC modeling to overcome the challenges arising from uncertainties involved in determining the structure. The final model is characterized for its important structural features including pore volume, surface area, pore size distribution, physical pore accessibility and structural defects. It is shown that the microporous structure of SiC-CDC 800 possesses a high pore volume and surface area, making it potentially a good candidate for gas adsorption applications. The HRMC model reveals the SiC-CDC 800 structure to be highly amorphous, largely comprising twisted graphene sheets. It is found that these distorted graphene-like carbon sheets comprising the carbon structure present a higher value for the solid-fluid potential strength compared to that of graphite, which is crucial in correct interpretation of experimental adsorption data. Furthermore, the constructed model is validated by comparing predictions of Argon, CO_2 and CH_4 adsorption against experimental data over a wide range of temperatures and pressures. It is demonstrated that our model is able to predict the experimental isotherms of different simple gases over various thermodynamic conditions with acceptable accuracy. The model also suggests the presence of ultra-microporosity that is accessible to CO_2 but only partially accessible to CH_4.

Keywords: Microporous carbon; Adsorption; Small angle scattering; Structure factor; Radial distribution function.

3.2. Introduction

Carbide-Derived Carbons (CDC) form an attractive class of microporous materials which hold promise for a wide range of applications such as adsorptive separation of volatile gases, gas storage, water/air purification and as materials for molecular sieves, battery electrodes and super capacitors [1, 2]. Such a broad range of functionality comes from the unique structural properties of this type of carbon, which combine high capacity and high surface area with tuneability of the pore size distribution [1]. This, in turn, gives the required flexibility to tailor the porous structure suitable for specific applications. Hitherto, a wide range of metal carbides including SiC, TiC, ZrC, TaC, Ti_3SiC_2 have been utilized for the synthesis of different CDC carbons, with the aim of synthesizing high capacity-high surface area porous structures[3-9]. This can be attained through a range of controlled chemical and physical metal extraction techniques such as acid etching, reactions with inorganic salts, halogenation, hydrothermal treatment and vacuum decomposition during which metals or metalloids are eliminated from the main carbide precursor framework [1, 2]. In parallel with experimental studies, atomistic modeling and theoretical characterization of porous structures for this class of materials and activated carbons have seen significant advances [7, 10-16]. Theoretical investigations have been able to provide essential insight into the topology and morphology of the carbon structure at the microscopic scale, which is usually unavailable directly from experiment. Such detailed information is necessary to relate transport properties of adsorptive fluids inside the porous structure with that of observable behavior such as uptake kinetics or fluxes in membrane. Silicon carbide derived microporous carbon (SiC-CDC) is one of the important CDCs, having a narrow pore size distribution, while makes it attractive for adsorption and gas storage applications. However, the atomistic structure of this CDC has hitherto not been investigated, and understanding this will provide information critical for assessing its potential in such applications.

In this work, the nano-structure of a 50 nm particle size silicon carbide derived carbon (SiC-CDC), previously synthesized in our laboratory by chlorination of ßSiC precursor at 1073 K [7], is constructed using the Hybrid Reverse Monte Carlo (HRMC) technique [10, 12]. The experimental sample has previously been characterized in detail using a series of techniques including gas adsorption, helium pycnometery, high resolution transmission electron microscopy (HRTEM) and

Small Angle Neutron Scattering (SANS) [7, 17], as well as Raman spectroscopy[4]. The experimental characterization of the SiC-CDC 800 sample revealed a highly disordered microporous structure with the structure being partially inaccessible for some gases [7]. Besides the modeling of this disordered structure, detailed characterization of the HRMC constructed model in terms of pore volume, accessible surface area, pore size distribution (PSD), as well as molecular pore accessibility of the HRMC constructed model is conducted using a combination of computational and empirical characterization tools. These provide critical insight for the understanding of the topology and morphology of the microporous structure. In addition, the structural modeling is validated by comparison of predicted low pressure argon and CO_2 isotherms, as well as those for high pressure CH_4 and CO_2, with experiment.

3.3. Theoretical background

Although the development of reconstructive modeling techniques based on matching experimental correlation functions with those of molecular simulations obtained from stochastic sampling of amorphous materials was initiated in the mid-1960s [18], major advances were achieved only in the late 1980s when McGreevy and Pusztai introduced their Reverse Monte Carlo (RMC) simulation algorithm [19]. The RMC method constructs a three dimensional model of an experimental sample by matching diffraction data calculated from simulation with its experimental counterpart. The technique employs a variation of Metropolis Monte Carlo (MMC) sampling in which a chosen error norm is minimized instead of the internal energy of the system [19]. The error can be written for the discrepancy of either the experimental structure factor (SF), the radial distribution function (RDF) or both, with simulation at every MC trial move. For example, the error based on RDF of the system for any MC move is given by [20]

$$\chi^2 = \sum_{i=1}^{n_{exp.}} \left(g_{sim.}(r_i) - g_{exp.}(r_i) \right)^2 / \sigma_{exp}^2(r_i) \tag{3-1}$$

where $n_{exp.}$ is the number of experimental data point, σ_{exp} is the experimental error and $g(r)$ is the radial distribution function (RDF). The experimental structure factor (SF), usually obtained from diffraction experiments, can be converted into its corresponding experimental RDF using [20]

$$S(q) = 1 + \frac{4\pi\rho}{q} \int r(g(r) - 1) \sin(qr)\, dr \tag{3-2}$$

here, ρ is the number of atoms per unit volume and q is the magnitude of the scattering vector, which is a function of the scattering angle θ, and the scattering radiation wavelength λ, following [20]

$$q = \frac{4\pi . sin(\frac{\theta}{2})}{\lambda} \tag{3-3}$$

The simulation scheme employs conventional trial MC moves to minimize χ^2 using the acceptance probability [10]

$$P = min\left\{1, exp\left[-\frac{x_{new}^2 - x_{old}^2}{2}\right]\right\} \tag{3-4}$$

The RMC algorithm progresses through sequential MC trial moves, using equation (3-4) to accept moves and thereby generate new configurations. It terminates when χ^2 is converged [19], while overlooking changes in potential energy of the atomistic configuration [21]. However, evolution of the system based on such an energetically unconstrained algorithm may give rise to the generation of highly strained configurations having several unphysical features such as unrealistic 3-member carbon rings [10, 22]. To overcome this pitfall and thereby achieve a realistic structure of the amorphous material, a combination of the conventional RMC method and the energy minimizing Metropolis Monte Carlo scheme has been introduced [10, 12, 23]. The new Hybride Reverse Monte Carlo (HRMC) approach makes use of an energy-based constraint in addition to the initially introduced RMC constraint on the structure factor of the system. The final configurations obtained from HRMC-based algorithms are energetically more stable and physically more meaningful, while at the same time satisfying the experimental structural criteria. The error norm for a HRMC algorithm follows the relation [10]

$$\chi_{total}^2 = \frac{\chi_{g(r)}^2}{2} + \frac{E}{k_B T} \tag{3-5}$$

where we note that each term has been scaled by its own order of magnitude (σ_{exp}^2 in the case of the error in $g(r)$, as given in equation (3-1), and k_BT for energy), so that both relative errors are given equal weight. The acceptance probability follows

$$P = min\left\{1, e^{-\Delta\chi^2_{g(r)}/2}.\, e^{-\Delta E/k_B T}\right\} \quad (3\text{-}6)$$

where $\Delta\chi_{g(r)}$ represents the change in the experimental cost function for $g(r)$, ΔE is the change in the potential energy of the system due to the Monte Carlo moves and $1/k_B T$ is the Boltzmann weighting factor. Theoretically, the modeling procedure can start from any arbitrary initial configuration, usually at a high temperature, so that the structure is initially melted and gradually quenched down to the real temperature of the experimental sample using a simulated annealing method [10, 12, 14, 23, 24].

3.4. Computational details

Our HRMC simulation reconstructs the nanostructure of microporous carbon (SiC-CDC 800) synthesized in our laboratory by chlorination of 50 nm size βSiC particles at 1073 K. The microporous nature of this structure is evident from the pore size distribution (PSD) of the sample determined [7] using the Finite Wall Thickness Density Functional Theory (FWT-DFT) developed in this laboratory [25, 26]. The results from XRD and HRTEM characterization also demonstrate the disordered nature of the carbon structure in the SiC-CDC 800 sample [7]. The main difficulty in the HRMC modeling of such amorphous materials is the 3D reconstruction of the atomistic structure based on only 1D diffraction data, as is available from experiment, an intrinsic pitfall of the RMC algorithms family highlighted by various authors [19, 21, 27]. The other drawback of this method is that the overall structure factor data obtained from neutron or x-ray scattering cannot uniquely resolve all the local structural features of an experimental sample; thus the structure factor or the radial pair distribution function used as target functions in RMC simulation lack sufficient information for the construction of an exact representative model. Extra constraints are therefore required in order to improve the modeling procedure and to narrow down the atomic configurations from the family of possible solutions.

In the current study, the static structure factor (SF) of the disordered SiC-CDC 800 sample was obtained over a wave vector range $0.2 < q < 50$ Å^{-1} (~ 0.13 Å < distance < 31.4 Å) using the SANDALS small angle neutron diffractometer at ISIS - Rutherford Appleton Laboratory, U.K. Inverse Fourier transformation of the experimental structure factor data, following the equation (3-2) was used, to determine its corresponding redial distribution function (RDF). Our HRMC algorithm employs two additional constraints, while minimizing the total error norm. The first is a 3-member ring constraint, implemented in order to prevent formation of unphysical 3-member

carbon rings [28], which are an "inherent by-product" of the unrealistic RMC pathways in fitting $g(r)$ [20]. This constraint rejects any MC move which leads to the formation of a 3-member carbon ring. Although, application of an appropriate potential function for the energy minimization scheme of the HRMC will naturally inhibit formation of most of unphysical carbon rings, some such rings may be obtained as a result of inappropriate compromise between the fit of $g(r)$ and the system energy, as shown by Jain et al. [12]. The implementation of a 3-member ring constraint ensures a physically more meaningful configuration at the end of the simulation, avoiding the inappropriate compromise. Another constraint employed in this study is a pore volume constraint [28] implemented to guarantee that the pore volume of the final structure does not deviate significantly from the experimental pore volume of the actual sample (e.g. based on the helium and bulk densities). For this constraint, the simulation cell is divided into a porosity grid containing $(\frac{\text{cell length}}{grid\ resolution})^3$ cells [28]. The pore volume constraint determines the porosity of the system by tracking the occupancy of these grids by carbon atoms using the following associated error

$$\chi_V^2 = [(f_o - \alpha)^2]/W_V^2 \tag{3-7}$$

where f_o is the fraction of occupied cells, χ_V is the error term representing discrepancy between the experimental and simulation skeletal volume fractions, and the parameter α defines the desired occupancy of the grid cells (i.e. $a = 1 - porosity$). Further, W_V is the volume constraint weighting factor, taken here as 0.001.

The pore volume of the actual sample is a key parameter in the HRMC modeling procedure. The bulk density of the fully converted SiC-CDC 800 is theoretically estimated as 0.951 g/cm^3, based on the density of the silicon carbide precursor (3.17 g/cc), assuming a conformal transformation. The experimental skeletal helium density of our sample is 2.52 g/cc solid [7]; somewhat higher than that of graphite, possibly inherited from the diamond-like structure of the SiC-CDC precursor. The pore volume of the particle is then estimated as 0.655 cc/g solid, following the relation

$$V_p = \frac{1}{\rho_{bulk}} - \frac{1}{\rho_{He}} \tag{3-8}$$

where V_p is the total specific pore volume of the particle, ρ_{bulk} and ρ_{He} are the bulk density and experimental helium density of the sample respectively. Nevertheless, the value of 0.655 cc/g solid should be only considered as an upper limit of the range of possible estimations for the pore volume

of the SiC-CDC 800 sample. This is due to the accessibility problem in the SiC-CDC 800 sample as reported by Bonilla et al. [4], which can affect the experimental estimation. Thus for example, this pore volume is marginally higher than the volume 0.6 cc/g solid, estimated from the argon isotherm using DFT [4]. The difference may be attributable to the finite size of the argon atom and related accessibility effects.

3.5. Modelling procedure

3.5.1. Two-stage modeling approach

A two-stage modeling procedure was employed to reconstruct an atomistic model for the SiC-CDC 800 sample using the HRMC technique; each stage having a slightly different strategy. The two modeling stages make use of the same set of experimental structural data (structure factor or RDF), as well as the same size of the simulation cells. The main difference concerns their initial configurations in addition to the RMC constraints which were employed during each stage, as discussed below. It should be noted here that structure factor and RDF provides the same information, however to make sure no information is lost during inverse Fourier transformation of the structure factor data; we examine both RDF and structure factor as structural constraint.

3.5.1.1. Stage 1: Reconstruction of an approximate but energetically stable structure

The main purpose of this step was to search for a deep local minimum on the Potential Energy Surface (PES), and to generate an energetically stable configuration which can also approximately represent the structural features of the real system. Therefore, a very lengthy HRMC simulation was performed using a 40 Å cubic simulation cell containing 3052 carbon atoms, with a FCC lattice initial configuration. The structure factor (SF) data obtained from neutron scattering was used as the target function to construct a closely matched atomic configuration for the real carbonaceous sample. In order to minimize the energy of the system, the Environment-Dependent Interatomic Potential (EDIP) for carbon was employed to calculate interatomic carbon-carbon potentials [29, 30], while employing periodic boundary conditions (PBC) in all three dimensions. This potential determines the energy, E, as the sum of the energies of individual carbon atoms, U_i, given by

$$U_i = \sum_j U_2(r_{ij}, Z_i) + \sum_{j<k} U_3(r_{ij}, r_{ik}, \theta_{jik}, Z_i) \tag{3-9}$$

here U_2 *and* U_3 are pair and three body interaction potentials, respectively, and are dependent upon not only inter-atomic distance and bond angle but also the generalized coordination number, Z_i.

The latter comprises a spherical coordination component, defined as the sum of distance-based weight functions of all the first nearest neighbors of the centered atom, *i*, and non spherical terms representing local geometrical constraints consisting of dihedral rotation and repulsions between π orbitals at twofold and threefold sites. The potential has the advantage of covering a longer range for the carbon-carbon interaction (3.2 Å) than the Reactive Bond Order potential (2.0 Å) of Brenner and co-workers [31, 32]. Full details of the potential are available elsewhere [29, 30]. The 3-member ring constraint discussed earlier was utilized at this stage, while the pore volume constraint was switched off until start of the second modeling stage. An exponential quenching scheme was designed to simultaneously minimize energy and SF weighting factors ($1/k_BT$ and $\sigma_{exp.}$respectively) by adjusting the temperature and σ_{exp} as the simulation progressed, while fitting the target structural data (in this case SF instead of *g(r)*), according to the equation (3-1). The quenching equations are given by

$$T_n = T_s \times {q_r}^{step} \tag{3-10}$$

$$\sigma_n = \sigma_s \times {q_r}^{step/2} \tag{3-11}$$

where subscript s and n represent the initial and any arbitrary state of the system respectively, $q_r$is the quench rate and "$step$" refers to the simulation step number in millions. Both *T* and *σ* decay to zero, while the ratio of the error weighting terms for the energy and diffraction data remain constant (T/σ^2 = constant). In this first stage, σ_s was chosen to be equal 0.0334. An initial temperature of 5500 K was applied to melt the structure above the carbon boiling point. Subsequently, the temperature (along with the structural weighting factor σ_n) was quenched down using a very slow quenching rate q_r = 0.9995. This leads to a very lengthy simulation run of about 5830 million Monte Carlo steps before the system is quenched to the ambient temperature. As a result of such a slow quenching, the system reaches below the carbon boiling point after almost 590 million steps, which enhances the chance of attaining a deep local minimum on the potential energy surface (PES) and therefore a stable configuration. By the end of this stage, the system was equilibrated at 297.9 K after 5830 million steps, where its final structure factor (SF) function was in good agreement with the experimental target function. Figure 3-1 and Figure 3-2 compare experimental and simulated structure factors (SF) and radial pair distribution functions (RDF) of the system.

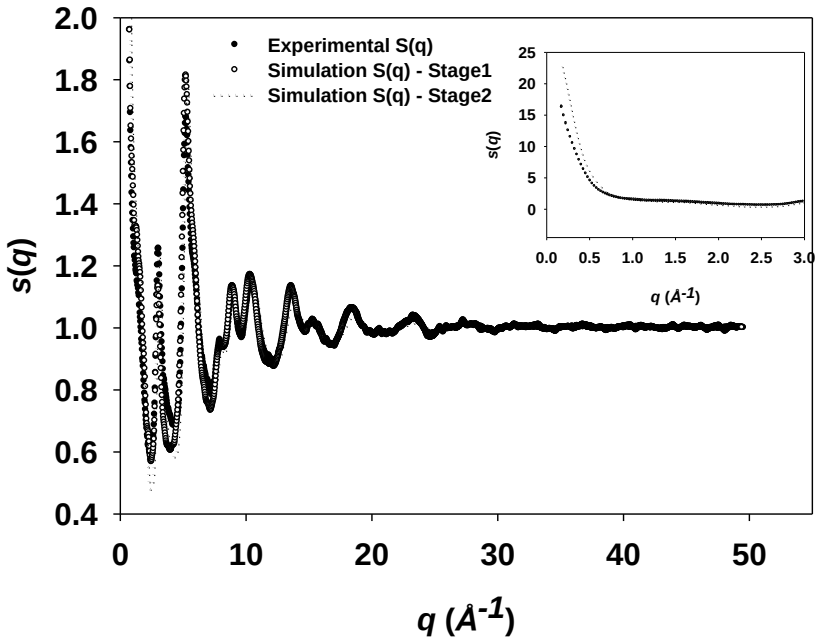

Figure 3-1. Simulation-based structure factor compared to that from experiment.

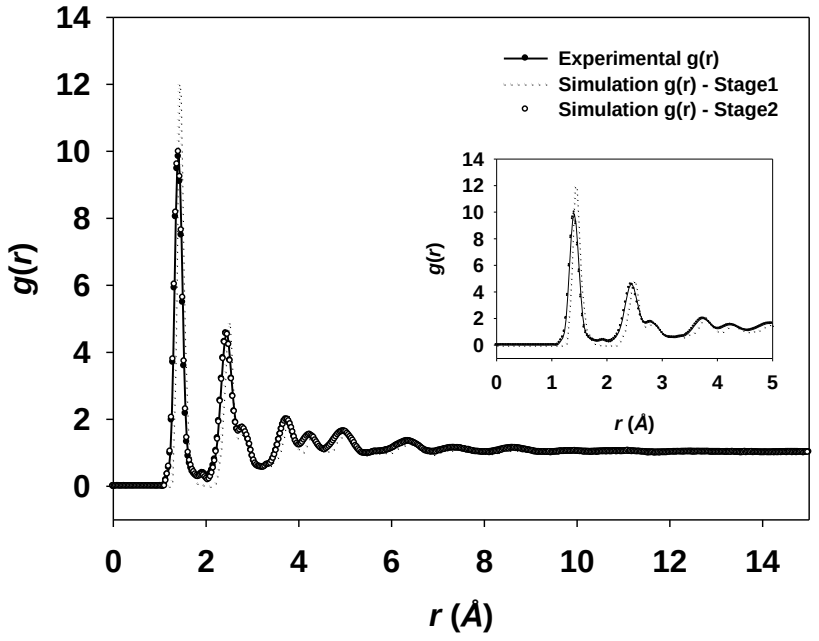

Figure 3-2. Simulation-based radial pair distribution function compared to its experimental counterpart.

As illustrated by Figure 3-1, the simulated structure factor data agrees well with that of experiment obtained from neutron scattering. Moreover, although the radial pair distribution function was not controlled by any constraint during this modeling stage, the final simulation RDF still shows reasonable agreement with the experimental RDF obtained on inversion of the experimental SF.

Geometric determination of total pore volume for the "Stage 1 model", following the method of Gelb and Gubbins [33, 34], revealed that the pore volume is equal to 0.59 cc/g solid, which is slightly lower than the empirical value of 0.6 cc/g solid obtained from Density Functional Theory (DFT) interpretation of argon adsorption data [4] At the same time, estimation of the argon adsorption isotherm on the constructed model using Grand Canonical Monte Carlo (GCMC) simulation suggested that a higher pore volume will be required for the HRMC constructed model in order to match the experimental adsorption isotherm accurately. Figure 3-3 depicts a comparison between the experimental argon adsorption isotherm at 87 K with that from simulation in the constructed model.

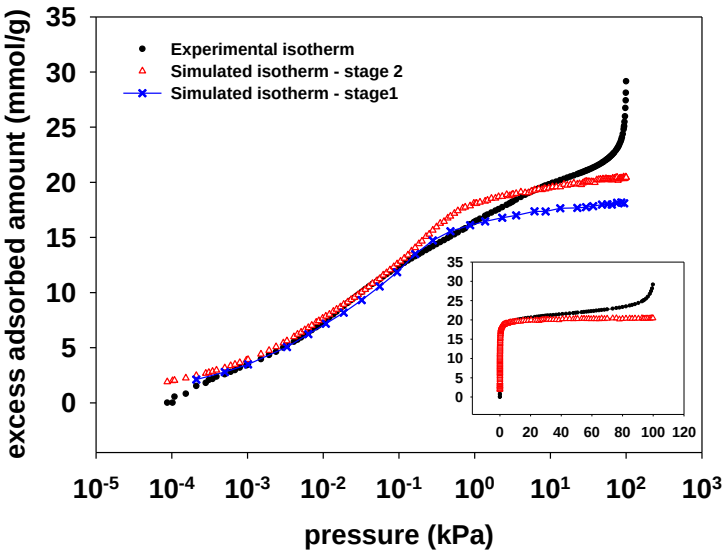

Figure 3-3. Comparison of the predicted argon adsorption isotherm at 87 K with that of experiment.

As can be seen, the "Stage 1" isotherm underpredicts the experimental data in the high loading region. This indicates under-determination of pore volume in the constructed HRMC model, as a result of which the model is unable to accommodate enough of the adsorbate molecules within its porous structure at elevated pressures. Therefore, it was concluded that an additional HRMC

attempt was required with the pore volume constraint applied, in order to increase the current value of the pore volume in the constructed model.

The fluid-fluid and solid-fluid Lennard-Jones parameters for the GCMC simulation are given in Table 3-1, using the value of σ_{cc} = 3.4 Å and $\varepsilon_{cc}/\kappa_B$ = 36.5 K for the solid structure.

Table 3-1. Molecular models and interaction parameters employed for GCMC simulation of adsorption isotherms [35-38]

Fluid Molecule	Atom	Fluid-Fluid Interactions		Solid-Fluid interactions		Molecular Model			
		σ_{ff}(Å)	$\varepsilon_{ff}/\kappa_B$ (K)	ε_{cf} (Å)	$\varepsilon_{cf}/\kappa_B$ (K)	X (Å)	Y (Å)	Z (Å)	Charge (e)
Argon	**Ar**	3.41	120.00	3.38	66.18	0.000	0.000	0.000	0.000
CO_2	**C**	2.82	28.68	3.112	32.36	0.000	0.000	0.000	+0.664
	O	3.03	82.00	3.215	54.71	0.000	0.000	±1.162	-0.332
CH_4	**C**	3.4	73.082	3.4	51.65	-1.9571	+0.8401	-0.0029	-0.66
	H	2.65	7.905	3.025	16.99	-1.9168	+1.2608	-1.0098	+0.165
						-2.8337	+1.2289	+0.5193	+0.165
						-1.0542	+1.1186	+0.5443	+0.165
						-2.0238	-0.2480	-0.0655	+0.165

We note here that the value of $\varepsilon_{cc}/\kappa_B$ = 36.5 K is somewhat higher than the graphite potential well-depth ($\varepsilon^{graphite}/\kappa_B$ = 28 K), due to the effect of the curvature of the highly distorted carbon sheets in the structure of the SiC-CDC 800. It has been shown that the curvature of carbon surfaces enhances the interaction potential strength of disordered carbon in comparison with that of planar graphite

[11, 13, 39]. The value of $\varepsilon_{cc}/\kappa_B$ = 36.5 K in this work was obtained by fitting the simulated and experimental argon isotherms. Calculation of $\varepsilon_{cf}/\kappa_B$ from this value results in a scaling factor of 1.14 for $(\varepsilon_{cf}/\kappa_B)^{-CDC}/(\varepsilon_{cf}/\kappa_B)^{Graphite}$, which is indeed very close to the scaling factor of 1.1 computed from ab-initio simulations for C_{60} fullerene by Klauda et al [39]. A similar value (1.134) is also reported for the scaling factor of ACF-15 activated carbon by Nguyen et al [11] based on isotherm fits. The value of $\varepsilon_{cc}/\kappa_B$ = 36.5 K was used here for all adsorption simulations.

3.5.1.2. Stage 2: Structural improvement of the Stage 1 model

In the second stage, a new HRMC simulation run was performed, in which the final configuration of "Stage1" was used as the initial configuration. Therefore, the second stage simulation was initiated from a low energy level, while at the same time its atomic configuration was initially close enough to that of a realistic model corresponding to the experimental diffraction data of the sample. This is because the final configuration from the previous modeling stage (the stage 1 model) was already a good approximation of the real carbonaceous structure, as a result of achieving the reasonable RDF match illustrated in Figure 3-2.

During the second stage, the pore volume constraint was switched on using porosity value of 0.622 for calculation of the parameter α (cf. equation (3-7)), based on the need for having a higher pore volume in the constructed model of SiC-CDC 800. This porosity value is calculated based on the theoretical bulk density of 0.951 g/cc solid, as well as the experimental skeletal density of 2.52 g/cc. In this stage, the experimental radial pair distribution function was controlled instead of the structure factor by minimizing the objective in equation (3-1). The use of the energy and 3-member ring constraints however, remained unchanged during this stage.

In order for the pore volume constraint to be effective, the carbon structure should be melted again and some degrees of freedom should be given to carbon atoms in terms of the σ_s value in the HRMC modeling procedure. This will enable rearrangement of the carbon atoms beyond the initial configuration of the system. To this end, the initial temperature of the system was raised to 5200 K and a new value equal to 0.0324 was set for σ_s. The system was then requenched using a much faster quench rate (0.9985) over 1910 Monte Carlo steps, following eqs (3-10) and (3-11). Figure 3-4 depicts the variation of the $g(r)$ error, $\sum\left(g_{sim.}(r_i) - g_{exp.}(r_i)\right)^2$, with the number of Monte Carlo steps as the system evolves.

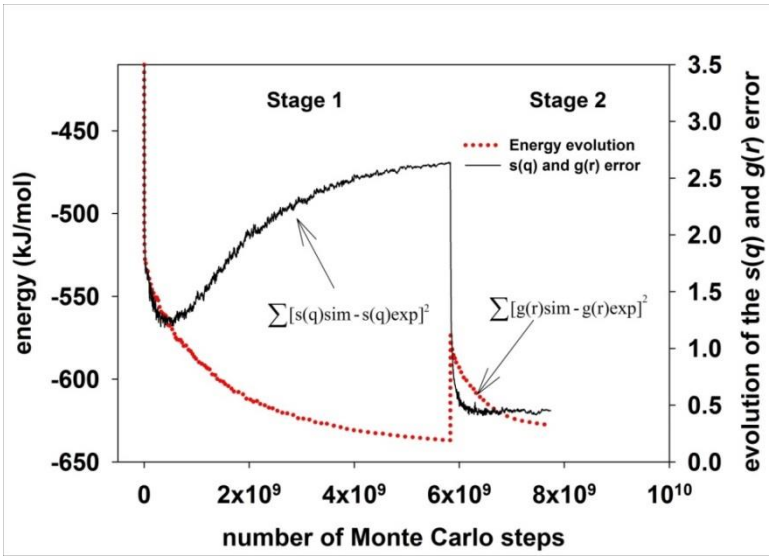

Figure 3-4. Energy evolution and variation of the $s(q) - g(r)$ error terms for the entire simulation (Stage1 and Stage 2)

As illustrated by this figure, the discrepancy between the simulation and experimental *g(r)* becomes nearly constant after 500 million Monte Carlo steps after the start of stage 2, and there is no further significant fluctuation in the error. This is another indication of the fact that the initial configuration used for the 2nd stage modeling was a close approximation of the target experimental data[1]. Therefore, the simulation radial pair distribution function of the system rapidly converged to the experimental $g(r)$. Comparison between the rapid convergence of $g(r)$ - which takes only 500 million MC steps to be achieved - with that of energy occurring over the whole 1910 million MC steps (Figure 3-4) suggests that the system continues to evolve with minor changes in configuration that do not significantly affect the RDF, while still reducing the energy even after 500 million steps. This clearly demonstrates that a number of atomic configurations can be associated with a unique radial distribution function, as has been previously acknowledged by several authors [19, 21, 27]. Figure 3-4 also depicts the energy evolution of the entire system over 7.740 billion Monte Carlo steps, including both modeling stages (Stage 1: 5830 million MC steps – Stage 2: 1910 million MC steps). As can be observed from this figure, the quenching process in the second stage starts from a lower energy level (-573.51 kJ/mol) compared to the starting energy level of the first stage (-407.87 kJ/mol), despite being melted again at the start of the second stage. This suggests that the final configuration of the Stage 1 model is already trapped in the vicinity of a deep local potential

[1] This is further discussed in Chapter 4.

minimum on the PES surface, so that the new quenching procedure is unable to cause dramatic structural changes; instead it only gives rise to small configurational rearrangements. It will be subsequently demonstrated in this paper that even such small atomic rearrangements can improve structural features of the model (such as pore volume and pore size distribution) in line with its overall adsorption performance. The quenching procedure finally terminates at 295.68 K at the end of the Stage 2, when the atomic configuration of the system reaches equilibrium at the energy level of -627.69 kJ/mol. The simulated radial pair distribution function obtained from the final model matches that of experiment more accurately compared to the results at the end of the Stage 1, evident from Figure 3-2. The total geometric pore volume of the final reconstructed model is 0.62 cc/g solid, showing that the new pore volume constraint implemented has been successful to increase pore volume of the model by 0.03 cc/g solid (5%) after 1910 million MC steps. For additional insight into the difference between the final and the Stage 1 models, the pore size distributions (PSDs) of the two structures were determined using the spherical probe geometric approximation technique developed initially by Gelb and Gubbins [33, 34]. Figure 3-5 compares the PSD result for the two HRMC structures (Stage 1 and 2).

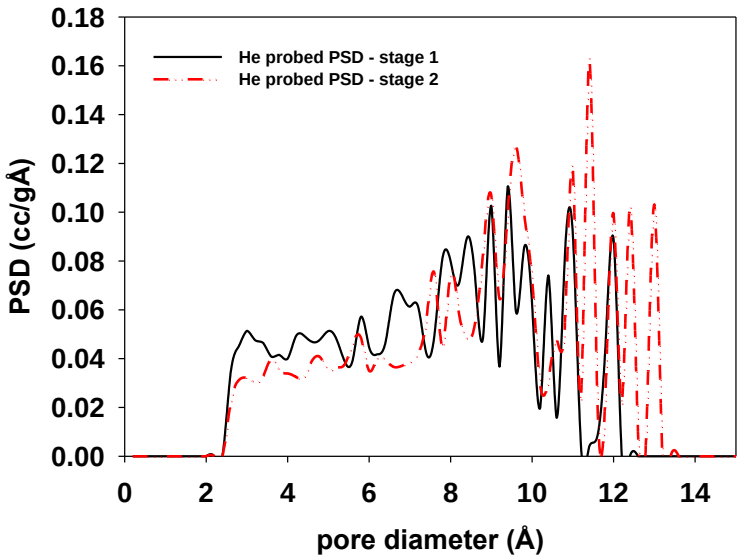

Figure 3-5. Geometric PSD of the stage 1 structure compared to that of the final HRMC model from Stage 2.

It is clear that the final Stage 2 model possesses a higher total pore volume compared to the "Stage 1" model. While this model has a smaller fraction of micropores up to 8.6 Å, it encompasses a higher fraction of large pores between 8.6 – 13.0 Å. In addition, our final model contains a small fraction of pores larger than 12.2 Å that do not exist in the Stage 1 model. These not only

compensate for the lower volume in the small pore size region, but also give rise to increase of the total pore volume by 5% in the final model. This, in turn, improves the adsorption performance of the HRMC model at high loadings, as seen in Figure 3-3. Figure 3-6 illustrates snapshots of the final HRMC constructed model.

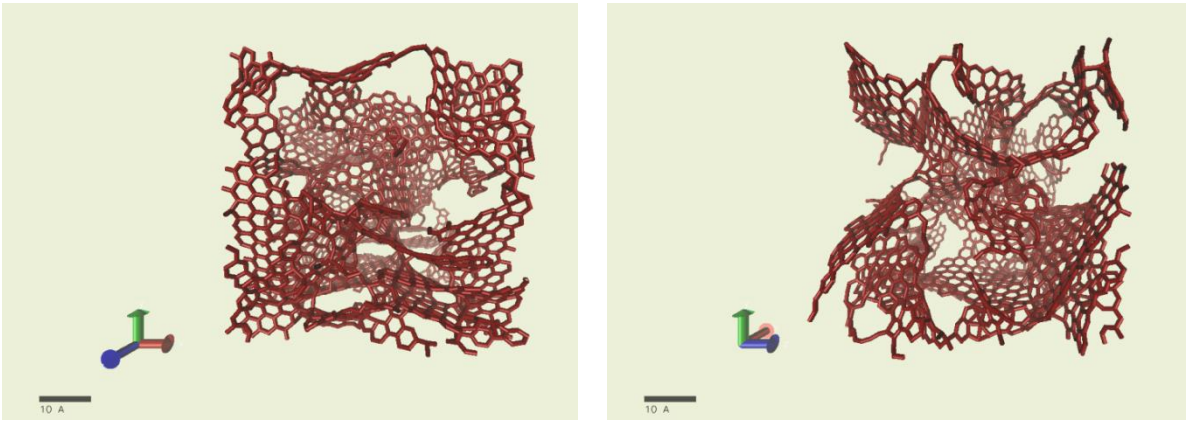

Figure 3-6. Disordered structure of the HRMC constructed model, illustrating formation of highly tortuous carbon sheets.

As seen in this figure, the atomistic structure of the HRMC constructed model is highly disordered, comprising highly curved and twisted graphene sheets resembling a microporous carbon structure, consistent with previous experimental characterizations on the same sample [4, 7].

3.6. Results and discussion

3.6.1. Characterization of the HRMC constructed model

This section characterises the pore volume, surface area, pore size distribution, pore accessibility, atomic coordination and structural defects of the HRMC model, properties which have a strong influence on fluid adsorption and transport properties of the system.

3.6.1.1. Total pore volume

The total pore volume, defined as the total available void space confined within the porous structure, is a key factor in modeling gas adsorption. The determination of pore volume is subject to a variety of uncertainties depending on the employed method. This includes technical limitations in experimental measurements of pore volume, as well as modeling assumptions in theoretical determination of this parameter. Here, the total specific pore volume (V_p) of the final model is determined using two different approaches. First, the helium-accessible volume is estimated using

the second virial approach, which is based on calculation of the mean density of helium in the simulation cell, while neglecting its adsorption [40].

$$V_p = \frac{1}{m_s}\int e^{-\phi(\boldsymbol{r})/k_B.T} d\boldsymbol{r} \tag{3-12}$$

where ϕ is the helium-carbon potential energy for a single helium molecule, m_s is mass of the solid adsorbent (the carbon network) in the simulation box, κ_B is the Boltzmann constant and T is temperature. The total pore volume Vp calculated from the second virial approach at 298 K for the final HRMC model is equal to 0.674 cc/g solid. For comparison, the geometric pore size distribution was also calculated using different probe molecules. The method uses Metropolis Monte Carlo integration to determine the pore volume, following Gelb and Gubbins [33, 34]. The results for argon, helium and a small hypothetical molecule of diameter 0.1 Å are shown in Figure 3-7.

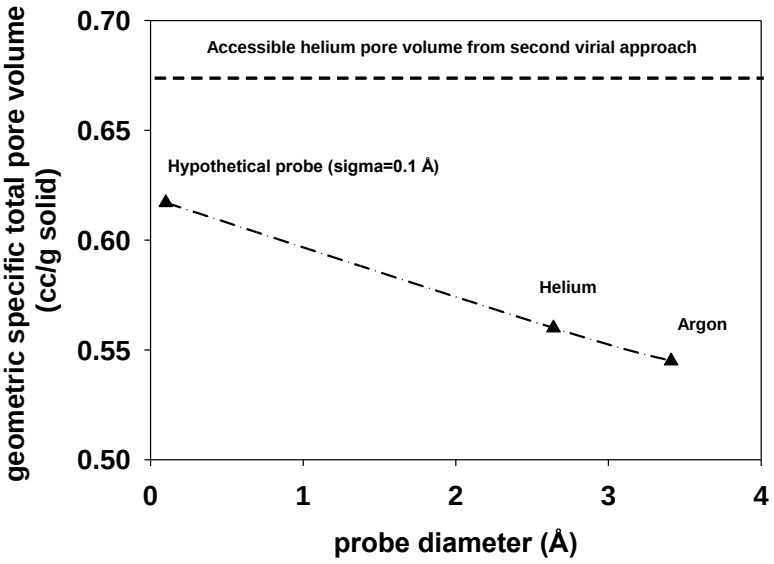

Figure 3-7. Variation of total pore volume with diameter of the probe molecule

The helium accessible pore volume calculated here is larger than the maximum geometric V_p, because the attractive part of the L-J interactions for the helium atoms leads to potential wells in very narrow spaces that are otherwise repulsive to hard sphere probes. Therefore, the pore volume of 0.674 cc/g solid is an overestimation of the actual pore volume. Moreover, in earlier sections we showed that the pore volume of the system obtained from helium pycnometry cannot be experimentally larger than 0.655 cc/g solid. On the other hand, using a reasonably small probe of

0.1 Å diameter, we are able to closely trace the accessible surface on the actual pore walls. Thus, the estimated geometric pore volume of 0.62 cc/g-solid from this method is more reliable and probably closer to the pore volume of the actual sample.

3.6.1.2. Accessible surface area (SA)

Most commonly, the accessible surface is considered to be the locus of the points of the center of a rolling probe molecule on the atomic pore wall (Connolly surface) in such a way that the center of the probe molecule is always located one probe-solid collision diameter ($\sigma^{s\text{-}f}$) away from the center of the wall atoms [33, 41]. The accessible surface area of the final model was calculated based on the above definition utilizing a Monte Carlo protocol [41]. In addition, in order to obtain a correlation between this computed surface area with that experimentally determined using BET theory [42], the accessible surface area was also computed based on the minimum potential distance ($2^{1/6}\sigma$) of the probe-solid atoms instead of the collision diameter [41]. The computed surface area of the HRMC model using argon and helium probes are listed in Table 3-2.

Table 3-2. Experimental and computed surface area of the SiC-CDC 800 obtained from different characterization techniques

Probe	Hard sphere accessible surface area (m^2/g solid)	Minimum potential accessible surface area (m^2/g solid)	DFT surface area (m^2/g solid)	BET surface area (m^2/g solid)
Argon	1581	1309	1912	1556
Helium	1866	1621	- - -	- - -

In this table, the result for the argon surface area is compared to that obtained from FWT-DFT interpretation of argon adsorption, as well as the result from the BET method. As seen in this table, the hard sphere surface area where the solid-probe interatomic distance is equal to σ is always larger than that calculated from the use of the minimum potential distance ($2^{1/6}\sigma$), and this is apparently because the accessible surface in the former case is located closer to the Connolly surface compared to the latter case. One may argue that the minimum potential distance on carbon surface should be calculated from the 10-4-3 potential [43]; however in this case the minimum potential distance will

be very close to the hard sphere case ($\sigma_{min.pot.}^{10-4-3} \cong 0.99\sigma$), therefore no significant difference will be seen in the value of surface area.

The surface area obtained from FWT-DFT using interpretation of argon adsorption overestimates the surface area obtained from the other methods. This is largely due to the idealistic model assumptions in the calculation of pore size distribution using DFT, in particular that of slit-pore geometry. Moreover, the inter-particle adsorption, which gives rise to higher adsorbed amounts of argon at high pressures (as evident in Figure 3-3) can also contribute to overestimation of the surface area by the FWT-DFT method, in which experimental argon adsorption data is used for the determination of pore size distribution and surface area.

The BET interpretation of argon adsorption for determination of the surface area of the SiC-CDC 800 sample gives a fairly close estimation compared to the value obtained geometrically from the hard sphere accessible approach (given in Table 3-2). However, the accuracy of the BET theory for estimation of surface area in heterogeneous solids is usually in question, as this method neglects the surface energy heterogeneity. Generally, the disagreement between the BET surface area and the geometric surface should be more prominent in microporous disordered materials, in which highly narrow non-uniform pore spaces dominate the microporous structure of the system, giving rise to a high surface energy heterogeneity [33]. This is essential because the first monolayer density of the adsorbed fluid in very small pores increases due to the surface curvature [33]. Nevertheless, it is remarkable that the BET surface area can be sometimes comparable with the geometric estimations obtained from molecular simulation techniques [13, 44]. As reported by Coasne et al, a "constricted cylindrical pore" possessing both negative and positive surface curvatures has a closer BET surface area to the geometric surface area in comparison with a planar surface or a conventional cylindrical pore [44]. As a case in point, Palmer et al. have also obtained very close estimates of the Connolly and BET surface areas for their HRMC constructed model of BPL activated carbon [13]. Such carbons, as well as the present HRMC model of SiC-CDC, possess both negative and positive surface curvatures, as evident in Figure 3-6, and may therefore be expected to yield a close match between the BET and Connolly surface areas. As explained by Coasne et al., the negative curvatures can somehow pay the penalty for the excess adsorbed molecules in the positive surfaces, thus giving rise to a more reasonable estimation of geometric surface area from the BET method [44]. Considering the above different results obtained from various experimental and computational techniques for estimation of the SiC-CDC 800 surface area, a realistic estimation of this property would appear to be a value between the hard sphere (Connolly) and the minimum potential accessible surface area, as reported in

3.6.1.3. Pore size distribution

The spherical probe geometric approximation technique [33] was employed in this work to explore the pore size distribution of the HRMC model and the result is compared with that of other methods, as depicted in Figure 3-8.

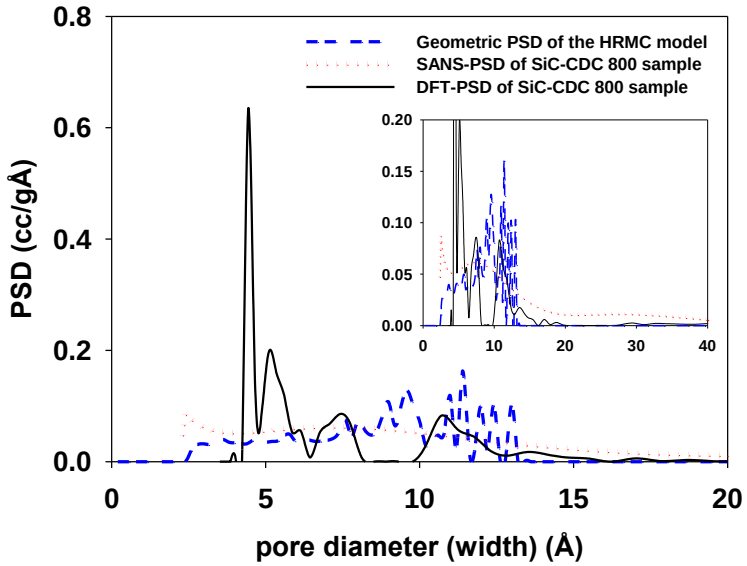

Figure 3-8. He probed geometric PSD of the HRMC constructed model compared to the PSDs obtained from SANS and FWT-DFT using interpretation of argon adsorption

Here, the geometric helium-probed PSD is compared with that obtained from FWT-DFT using interpretation of experimental argon adsorption at 87 K, and also the PSD obtained from Small Angle Neutron Scattering (SANS) reported by Nguyen and Bhatia [17]. It is seen that there is a small fraction of pores lying between 13.0 Å and 15.0 Å in the pore size distribution obtained from FWT- DFT and SANS, which is not predicted by the HRMC model. This is largely because the experimental radial pair distribution function $g(r)$ used for construction of the HRMC model has not been able to capture any distinct structural feature beyond 14.5 Å, and fully decays beyond this distance (Figure 3-2). The existence of pores larger than 15 Å - in both SANS and DFT results, however, is most likely an indication of meso-scale inter-particle spaces in the nano-sized SiC powder, which are probed in the small angle neutron scattering experiment or are filled during argon adsorption. There is also a small fraction of ultra-micropores smaller than 4.0 Å which are present in the HRMC and SANS-PSD results, but not in the DFT-based PSD, most likely due to slow diffusion of argon adsorption through the micropores entries [45]. Indeed, apart from the large

inter-particle pores detected by SANS (>15Å), the geometric PSD of the HRMC constructed model and the SANS-PSD data demonstrate very good agreement, including the ultra-microporous region.

3.6.1.4. Physical pore accessibility

Pore accessibility is a significant issue in the adsorption and diffusion of fluid molecules in the disordered structure of highly amorphous materials such as SiC-CDC 800 [45]. Pore inaccessibility arises from the formation of physical and energy barriers inside the microporous structure, which can hinder diffusion of the adsorbate molecules in the structure. Pore accessibility issues are responsible for uncertainties in the experimental determinations of pore volume, pore size distribution and surface area. Therefore, pore accessibility screening of the target porous structure is of great significance for understanding transport properties of the nano-structure.

For physical accessibility, following Sarkisov and Harrison [41], the porous network is considered physically accessible with respect to a spherical probe of a particular size, if for this probe a continuous trajectory can be constructed from one side of the simulation cell to the opposite side without any physical overlap between the probe particle and the atomic network [41]. The HRMC constructed model of SiC-CDC 800 was explored for the largest spherical probe which can traverse the system in any direction. Details of the computational characterization technique employed here are discussed by Sarkisov and Harrison [41]. We found that a spherical probe of 7.43 Å size is the largest probe which can traverse the SiC-CDC 800 structure, although its percolation occurs only in two dimensions. Nevertheless, with a slightly smaller spherical probe of 6.81 Å the system can be percolated in all three dimensions. Figure 3-9 illustrates the percolation trajectories of this largest percolating spherical probe (6.81 Å) in all three dimensions, within the HRMC constructed framework.

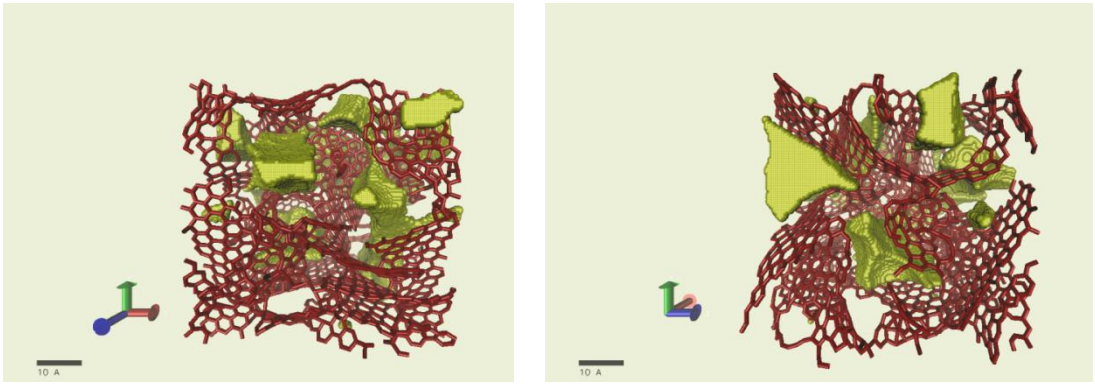

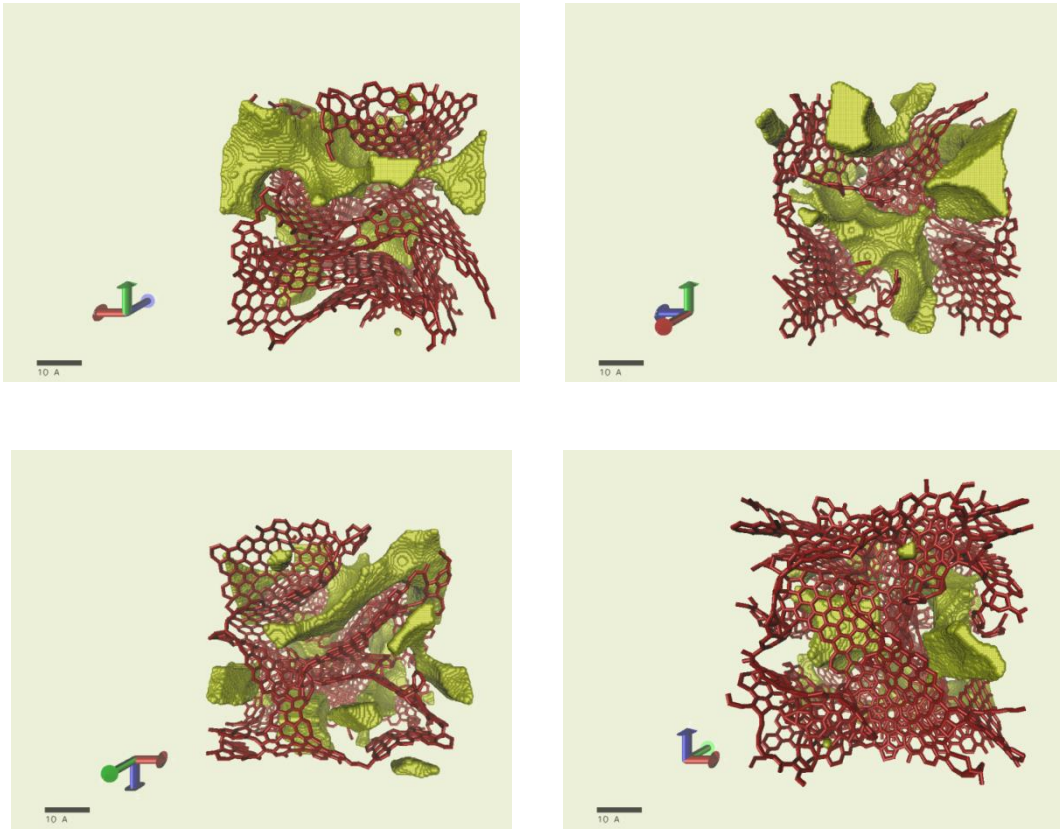

Figure 3-9. Various views of physical percolation paths of the largest spherical probe through the HRMC model.

The pore accessibility screening of the HRMC model indicates that there are narrow but physically accessible channels, percolated stochastically in the system. These channels are large enough to allow physical diffusion of most important simple gases such as carbon dioxide, methane and water vapor through the microporous system; however this investigation of accessibility as being purely related to probe molecular size is approximate. At sufficiently high temperatures the kinetic energy can be adequate to overcome repulsive energy barriers at pore entrances, leading to accessibility enhancement [45].

The constructed model of SiC-CDC 800 was also examined for the percolation of 3-site and 5-site rigid models of CO_2 and CH_4 respectively (with the geometry given in Table 3-1), taking into consideration their molecular geometry with different orientations inside the pore network. It was found that there is at least one three-dimensionally percolated path for each of these molecules, which allows them to travel from one side of the simulation cell to the opposite side. Of course, it is to be noted that this analysis is purely geometric, based on hard-body probes, and does not consider the possibility of overcoming finite energetic barriers (as would arise from more realistic soft interactions) at the pore entries within the structure. Nevertheless, this approach provides useful

insight into percolation properties of the disordered system. Table 3-3 summarizes some useful characteristics of the SiC-CDC 800 porous network, showing the mean pore size of the system to be comparable to that of the largest percolating particle.

Table 3-3. Pore characterization data for the HRMC constructed model

Pore limiting diameter in 2D (Å)	Pore limiting diameter in 3D (Å)	Largest Pore size (Å)	Average Pore Size (Å) *	Average Weighted Pore Size (Å) **
7.43	6.81	13	7.8	8.5

$*\frac{\sum H_n}{N_H}$; where H_n is any pore size and N_H is the total number of pore sizes.

** $\frac{\sum H_n \times i_{H_n}}{\sum i_{H_n}}$; where i_{Hn} is intensity of the any pore size in the PSD histogram.

3.6.1.5. Atomic coordination

The atomic structure of the HRMC model was also scrutinized in terms of the atomic coordination of the carbon atoms. The atomic configuration of the final model consists of 79.82% 3-fold coordinated and 18.22% 2-fold coordinated carbon atoms suggesting the carbonaceous structure to be predominantly occupied by sp^2 carbons, since 3-fold coordinated configuration arises from the sp^2 hybridization of carbon atoms [46]. There is also a very small fraction of 4-fold coordinated atoms (1.9%), which can be interpreted as a population of sp^3 hybridized carbon possibly inherited from sp^3 Si-C bonds in the SiC-CDC 800 precursor [7]. Apart from the tortuous nature of the carbon sheets in the HRMC model (illustrated in Figure 3-6), the main differences between the atomic configuration of carbon atoms in this model with that of graphene are the existence of a considerable fraction of sp bonding (2-fold coordinated carbons), as well as the presence of Stone-Thrower-Wales-like defects. For sp^2-bonded carbons, the Stone-Thrower-Wales (STW) defect is manifested as rearrangement of four six-member rings into a (5-7)-(7-5) conformation [47-49], resulting in a 90° rotation of two carbon atoms with respect to the midpoint of the C-C bond [50]. Our visual observations do not confirm formation of exact STW defects in the structure; however there are noticeable similarities between detected topological defects in our model with those of a STW defect. Adjacent 5- and 7-member carbon rings are widely found in the HRMC model but they are never representing the exact configuration of a STW defect. Considering that STW defects could thermally form at high temperatures [51], this kind of defect can potentially occur during the

halogenation process of the CDC synthesis. Nevertheless, it seems further conformational changes during the synthesis process distort the exact atomic arrangement of possible STW defects giving rise to separation of corresponding heptagonal rings. Figure 3-10 depicts one example of a STW-like defect observed in the HRMC constructed model.

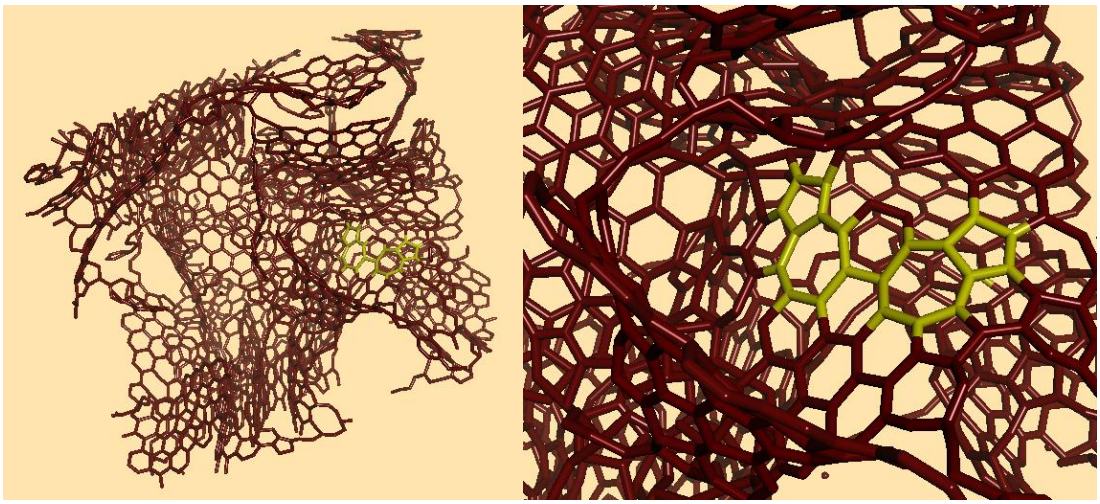

Figure 3-10. Illustration of a STW-like topological defect in the HRMC structure.

It was observed that in this structure, the formation of a large fraction of sp carbon bonds resulted in octagonal and larger multi-member carbon rings; however STW-like defects introduce topological defects that are largely related to the formation of pentagon-heptagon ring pairs.

The above bond analysis is supported by the earlier Raman spectroscopy result for the SiC-CDC [4], showing the presence of prominent sp^2 (G-band) and defect induced [52, 53] (D-band) Raman peaks in the spectrum; this is consistent with our finding of a large (79.82%) fraction of sp^2 carbon, and the distorted nature of the carbon sheets in the HRMC structure. Further, the absence of the sp^3 diamond peak (at 1333 cm^{-1}) in the Raman spectrum is consistent with the finding of a very small (1.9%) fraction of sp^3 carbon.

Further information regarding the local ordering of atomic configuration in carbon sheets can be obtained from interpretation of the radial pair distribution function (Figure 3-2). The first two sharp peaks in the $g(r)$ function suggest some degree of local ordering within the first and second neighboring shells. The first and second neighboring atomic populations in SiC-CDC 800 are compared with those of graphite and BPL activated carbon reported by Palmer et al. [13] in Table 3-4.

Table 3-4. Neighborhood atomic populations of the SiC-CDC 800C compared to those of Graphite and BPL activated carbon

Substance	Coordination numbers n_1, n_2	Neighbourhood distance l_1, l_2 (Å)
SiC-CDC 800C Sample	2.69, 8.29	1.41, 2.43
SiC-CDC 800C HRMC model	2.79, 8.33	1.41, 2.44
Graphite	3.0, 6.0	1.42, 2.46
BPL HRMC model	2.91, 6.34	1.45, 2.53

The coordination number as well as first neighbor distance of the SiC-CDC 800 is very close to those of graphite and BPL carbon, suggesting that the carbon atoms reside in graphene-like carbon sheets in the SiC-CDC sample. This is consistent with the high fraction of sp^2 carbon obtained from our HRMC model and can be easily confirmed by visual inspections of the model. In contrast, for the second neighbor shell, SiC-CDC and BPL possess higher atomic populations compared to graphite with the SiC-CDC's value being even higher. This is suggestive of distortion of graphene sheets in the BPL and SiC-CDC structure, which occurs during their synthesis process [13]. This also suggests that the structure of SiC-CDC 800 is more disordered compared to the BPL carbon, consistent with the formation of highly tortuous graphene-like carbon sheets clearly evident in Figure 3-6.

3.6.2. Validation of the HRMC constructed model

In order to ensure that the HRMC constructed model can correctly predict experimental adsorption data, the conventional Grand Canonical Monte Carlo (GCMC) simulation technique was employed to validate the rigid HRMC model against experimental adsorption isotherms of simple gases including Ar, CO_2 and CH_4 at different pressures and temperatures. A Lennard-Jones (LJ) potential model was used for argon, while multi-site models with partial electrostatic charges were utilized for CO_2 (3-site) and CH_4 (5-site), with parameters given in Table 3-1. To confirm that the fluid-fluid potential well depths obtained from the literature are applicable at the thermodynamic

conditions of interest in this work, fluid bulk densities were examined against experimental bulk densities, as well as the bulk densities calculated from the Bender equation of state [54]. With the exception of methane, all molecular models extracted from literature (according to the references given in Table 3-1) could consistently reproduce the experimental bulk densities. In this table a new potential strength value of the LJ potential well depth, ε_{ff}, for the central carbon atom of the 5-site methane model is suggested, based on matching the simulated bulk density of methane obtained from GCMC with that of experiment and the data calculated from the Bender equation of state (EOS). The bulk density of methane obtained from the use of this new value showed excellent agreement with experiment and the Bender EOS at 313 K, 323 K and 333 K, illustrated in the Supporting Information. ε_{cf} in Table 3-1 is obtained from application of the Lorentz-Berthelot mixing rules using the value of $\varepsilon_{cc}/\kappa_B$ equal 36.5 K, as discussed earlier.

We note, while we have shown here the results of a HRMC model started from a fcc initial structure, other initial structures (random, slit-like and zinc blend) were also attempted, and yielded $g(r)$ fitting error and final energy comparable to the results in Figure 3-4. In principle, the final configuration is expected to be independent of the initial structure, since the combination of melting of the initial structure and large simulation run length largely erases memory effects related to this structure. Indeed, it was soon found that the HRMC result from various initial structures gave comparable agreement of the various adsorption isotherms (Ar, CO_2 and CH_4), after fitting the value of $\varepsilon_{cc}/\kappa_B$ (= 36.5 K), as discussed earlier. The results presented earlier and all adsorption predictions discussed here are based on the HRMC structure derived from the FCC initial structure, as its adsorption predictions were marginally better than those using other initial configurations. The experimental adsorption data used here for validation of our simulation results and details of the experimental procedures have been published earlier [4].

3.6.2.1. Argon adsorption

GCMC simulation was performed (with 50 million Monte Carlo configurations at each pressure point, used for all GCMC simulations in this work) to predict the adsorption isotherm of argon in the HRMC constructed model of SiC-CDC 800 at 87 K. Figure 3-3 depicts comparison of the simulated argon isotherm with that of experiment at 87 K using both logarithmic and standard scales. As expected, a type I isotherm is observed which is a typical isotherm type for microporous materials. It is clear that the simulated isotherm reproduces the experimental one with acceptable degree of accuracy. As one can observe, the simulated isotherm slightly overpredicts the experimental isotherm at very low pressures (up to 0.015 kPa). This is due to the very slow

diffusion of argon adsorption in micropore region of the experimental sample. This observation is supported by the absence of pores smaller than 4.2 Å in the DFT-PSD based on interpretation of argon adsorption (Figure 3-8), indicating the experimental isotherm requires longer time in order to reach equilibrium.

Further, at higher pressures between 0.095 kPa and 5.12 kPa, slight overprediction is detected which is more visible in the logarithmic view of the simulated isotherm. Such behavior is also detected in the simulated argon isotherm in the HRMC constructed model of ACF15 activated carbon reported by Nguyen et al. [11], and is most probably an HRMC modeling defect due to wrong distribution of volume over certain pore sizes. From the standard scale view of the simulated isotherm it is clear that argon molecules fill up almost all the pores very quickly, so that the simulated isotherm reaches its maximum close to 6.17 kPa and no further increase can be observed at higher pressures. Such rapid adsorption at low pressures is an indication of a highly microporous structure, supported by our PSD results depicted in Figure 3-8. In contrast to the simulated isotherm, the experimental isotherm ascends gradually, followed by a steep increase close to the saturation pressure, as seen in the logarithmic scale view, which is due to the contribution of the inter-particle spaces. Such spaces are not pertinent to the calculation of total pore volume for the HRMC constructed model.

3.6.2.2. Sub-atmospheric adsorption of carbon dioxide

Sub-atmospheric adsorption of carbon dioxide was investigated using GCMC simulation sampling 50 million Monte Carlo configurations at each pressure point. A rigid carbon dioxide model possessing three distinct Lennard-Jones and Columbic sites was used, with model parameters given in Table 3-1. As depicted in Figure 3-11, the simulation isotherm matches that of experiment very well, with effect of inter-particle adsorption being negligible due to very low relative pressure of carbon dioxide.

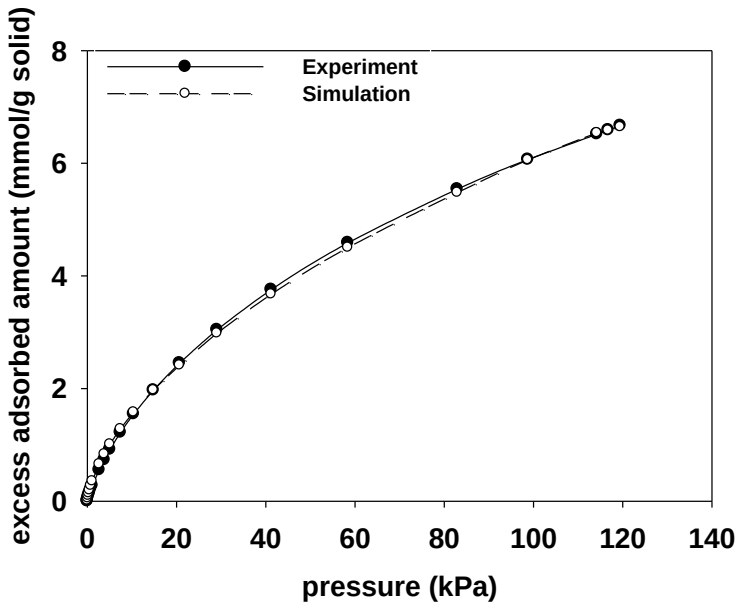

Figure 3-11. Compariso of predicted and experimental sub-atmospheric adsorption isotherms of CO_2 at 273 K.

The zero loading isosteric heat of adsorption, calculated from GCMC using the fluctuation formula is 35 kJ/mole, which is comparable to but somewhat higher than the value calculated for a 4.2 Å size slit pore (the smallest size accessed by Ar, c.f. Figure 3-8), which is equal to 30.43 kJ/mol, On the other hand, for the case of argon adsorption, the isosteric heat at zero loading obtained from GCMC for the HRMC structure is 17 kJ/mole, which is very close to that obtained for the 4.2 Å slit pore (18.55 kJ/mole). This would suggest that there exists an ultra-microporous region in the HRMC model which can be accessed by the 3-site CO_2 molecule due to its linear geometry, giving rise to adsorption of CO_2 in these ultranarrow pores, and this results in a higher heat of adsorption at low loading compared to the smallest micropore size of about 4.2 Å accessed by argon. In contrast, the ultra-microporous region is largely inaccessible to the argon atoms due to their larger effective molecular size.

3.6.2.3. High pressure adsorption of carbon dioxide

The high pressure adsorption of carbon dioxide, increasingly gaining importance, was also examined in the microporous structure of the SiC-CDC 800 at three different temperatures. Figure 3-12 compares experimental [4] high pressure adsorption isotherms of carbon dioxide at 313, 323 and 333 K with those predicted by GCMC simulation, showing good agreement.

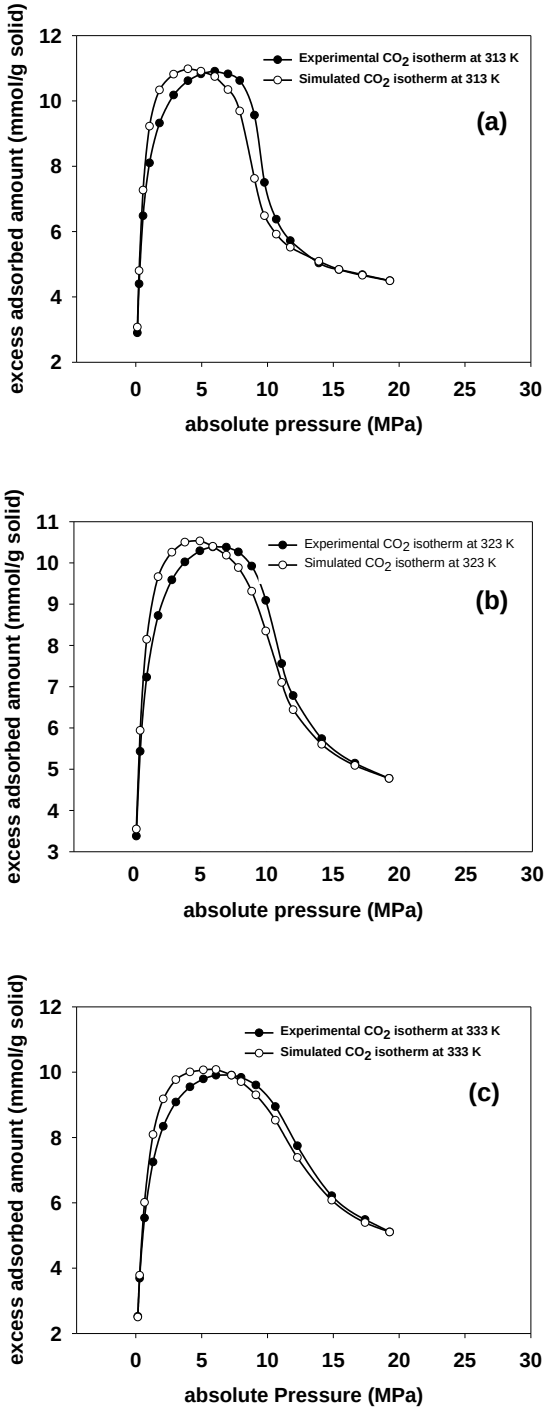

Figure 3-12. Predicted high pressure adsorption isotherms of CO_2 compared to the experimental isotherms at (a) 313 K, (b) 323 K and (c) 333 K.

We note here that the experimental 323 K data used here had been obtained by Bonilla et al. [4] in this laboratory along with the 313 K and 333 K data, though it was not included in the earlier

publication [4]. For all the three different temperatures, the adsorbed amount sharply increases over the left isotherm branch due to rapid growth of the adsorbed phase, while it drops at higher pressures after reaching its peak due to the greater compressibility of the bulk fluid at these conditions. For the predicted excess adsorbed amount in Figure 3-12, we used the formulation [7]

$$m_{excess}^{fluid} = m_{absolute}^{f} - \frac{m_{absolute}^{He}}{\rho^{He}} \cdot \rho_{bulk}^{fluid} - \Delta V_{max} \cdot \rho_{bulk}^{fluid} \qquad (3\text{-}13)$$

In this equation, m, ρ and ΔV_{max} are the adsorbed quantity, density and maximum excess adsorbent volume respectively. We note that the adsorbent pore volume at high pressure is ill-defined [7], the reason being rigidity of the constructed adsorbent model employed in GCMC simulation, while in reality the microporous structure of the carbon solid is flexible and experiences shrinkage or swelling deformations at very high pressures [7]. Such deformations account for the existence of the parameter ΔV_{max} in equation (3-13). The maximum excess volume should be used to take into account the loss or excess of available volume due to shrinkage or swelling deformations to which the fluid is exposed. Here $\Delta V_{max}$is calculated by adjusting the maximum simulated excess adsorbed amount with its corresponding value from experiment using equation (3-13). From our simulation we found out that the maximum excess adsorbent volumes of high pressure CO_2 at 313 K, 323 K and 333 K are -0.186, -0.183 and -0.183 cc/g solid respectively, indicative of shrinkage.

3.6.2.4. High-pressure adsorption of methane

For additional validation of the HRMC structure, the high pressure adsorption of methane was predicted using GCMC simulation at 313, 323 and 333 K. Figure 3-13 depicts the comparison of the high pressure methane adsorption isotherms predicted at three different temperatures with those obtained from experiment.

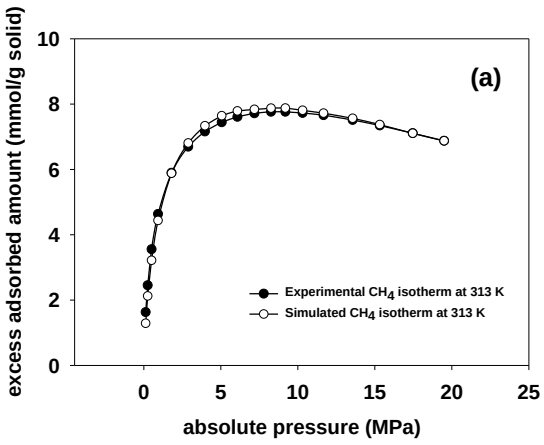

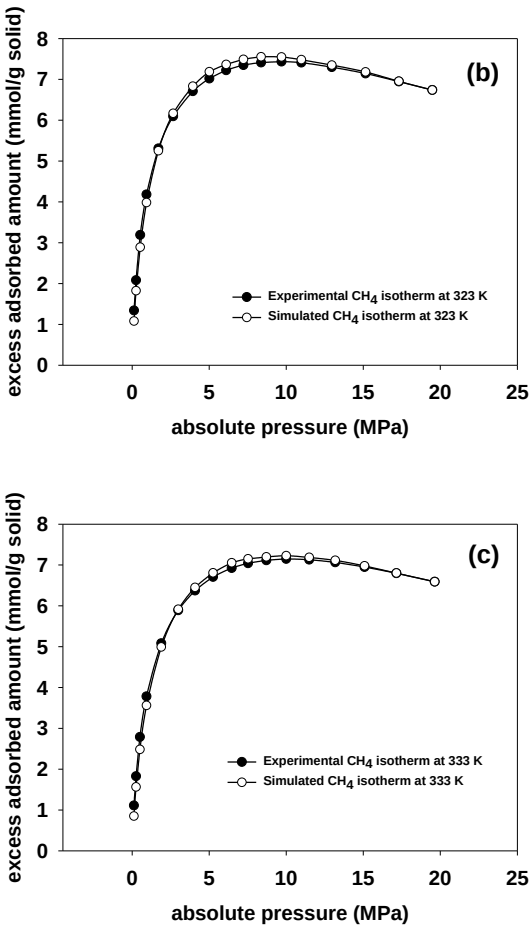

Figure 3-13. Predicted high pressure adsorption isotherms of CH_4 compared to the experimental isotherms at (a) 313, (b) 323 and (c) 333 K.

As for CO_2, we note here that the experimental 323 K data used here had been obtained by Bonilla et al.[4] in this laboratory along with the 313 K and 333 K data, though it was not included in the earlier publication [4]. We also note here that the CH_4 isotherms were plotted as wt% CH_4 in the work of Bonilla et al. [4], but erroneously labeled as mmol/g. The conversion to mmol/g has been made here. As illustrated in Figure 3-13, very good agreement can be seen between experimental and predicted isotherms over each temperature. It was found from the fit of equation (3-13) that the maximum excess adsorbent volumes are -0.197 cc/g solid, -0.195 cc/g solid and -0.194 cc/g solid at 313 K, 323 K and 333 K respectively. As illustrated in Figure 3-14, the maximum deformation (shrinkage) of the solid structure is stronger for high pressure CH_4 adsorption than for CO_2. This is due to filling of ultra-micro pores by CO_2, while these pores are inaccessible to CH_4 due to its larger size. At high methane pressures, the empty ultra-micropores can shrink under the high solvation pressure in the surrounding pores. This observation is consistent with DFT analysis for high

pressure CH_4 and CO_2 adsorption in the same SiC-CDC 800 sample [7]. Furthermore, as seen in Figure 3-14, the maximum excess adsorbent volume is only weakly sensitive to variation of temperature; however it does depend on the adsorbate molecule.

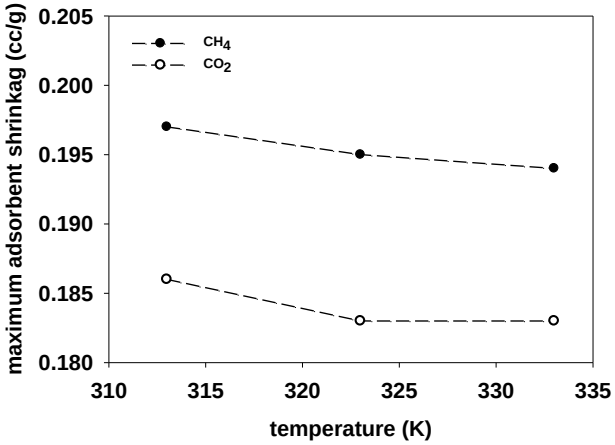

Figure 3-14. Maximum excess adsorbent volume for high pressure adsorption of CH_4 and CO_2 at 313, 323 and 333 K.

3.7. Conclusion

A realistic model of microporous silicon carbide derived carbon has been obtained through a two-step modeling procedure using the Hybrid Reverse Monte Carlo (HRMC) reconstruction technique. It is demonstrated that quantitatively small but effectively significant structural modifications can be made through application of multistage simulations, with different constraints in each stage. We have employed a new constraint on pore volume of the system to control volumetric changes of the pore space during the modeling procedure. Additionally, a 3-member ring constraint was utilized to fully inhibit formation of unphysical 3-member carbon rings. We showed that application of these new constraints in addition to the other constraints commonly used on energy and structure factor of the system can be very effective for construction of structural features of a highly amorphous microporous sample. The final HRMC model has been characterized for its important structural features including pore volume, surface area, pore size distribution, physical pore accessibility and structural defects, which were compared with those of experiment wherever possible. It is shown that the microporous structure of SiC-CDC 800 has a fairly high pore volume and surface area, making it potentially a good candidate for the adsorption of volatile gases. The final constructed model has been also validated against experimental adsorption data of simple gases over a wide

range of temperatures and pressures, showing that our model is able to provide accurate prediction for the available set of experimental data. Comparison of the low-density isosteric heats for CO_2 and Ar with the corresponding values at the smallest slit pore size of 4.2 Å, obtained using DFT, suggests the presence of ultra-microporosity that is accessible to CO_2 at 273 K but not to Ar at 87 K. Further, the larger empirically determined shrinkage of the structure during high pressures CH_4 adsorption in comparison to CO_2 suggests such that there exists some ultra-microporosity that is inaccessible to CH_4 as well.

3.8. Acknowledgement

This research has been supported by the Australian Research Council (ARC), under the Discovery Scheme. It was undertaken with the assistance of resources provided at the NCI NF Fujitsu Primergy, Sun Constellation VAYU and SGI XE Cluster (SU) and NCI NF Nearline Data (GB) through the National Computational Merit Allocation Scheme supported by the Australian Government.

We thank Dr. Lev Sarkisov for his assistance with the structural characterization tools for disordered porous materials. We also acknowledge Prof. Apparao Rao for his assistance with the Raman spectra measurements and Dr. Thanh Nguyen for determination of the structure factor data at the ISIS - Rutherford Appleton Laboratory, U.K.

This article is dedicated to the memory of Professor Ian K. Snook of RMIT University, Melbourne, who sadly passed away on April 7, 2013. Ian was one of the pioneers in the advancement of Hybrid Reverse Monte Carlo simulation for modeling the structure of carbons, and will be remembered for his many outstanding contributions to Physical Chemistry.

3.9. Supporting information

Fits of the GCMC isotherms for the 5-site model of methane to bulk density data from the Bender equation of state are reported in the Supporting Information. This information is available free of charge via the Internet at http://pubs.acs.org.

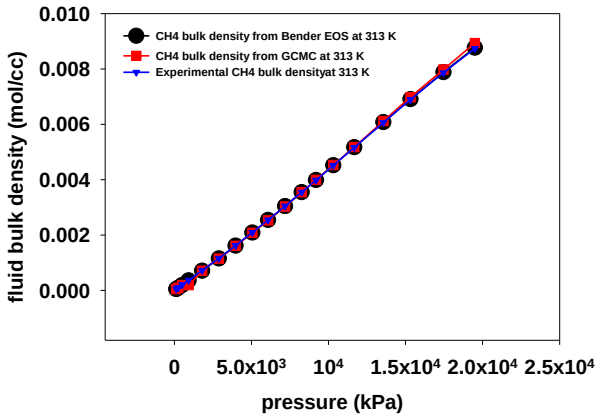

Figure 3-S1. Fitted simulated bulk density data for a 5-site CH_4 model at 313 K compare to the results obtained from experiment and Bender EOS.

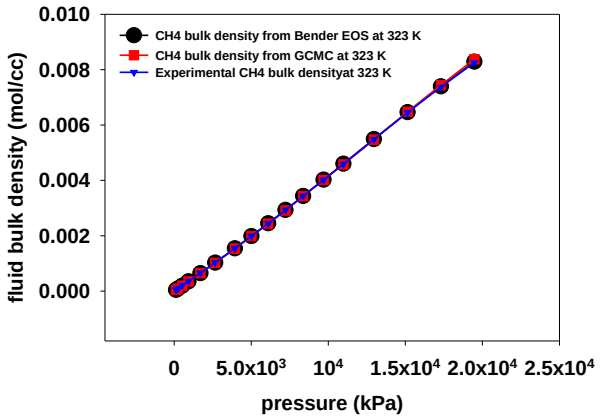

Figure 3-S2. Fitted simulated bulk density data for a 5-site CH_4 model at 323 K compare to the results obtained from experiment and Bender EOS.

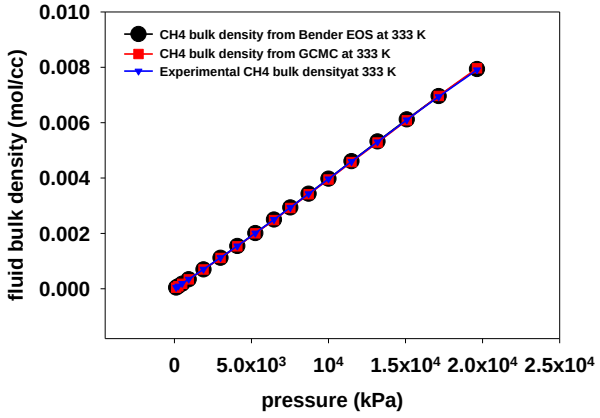

Figure 3-S3. Fitted simulated bulk density data for a 5-site CH_4 model at 333 K compare to the results obtained from experiment and Bender EOS.

3.10. References

1. Gogotsi, Y., et al., *Nanoporous carbide-derived carbon with tunable pore size.* Nature Materials, 2003. **2**(9): p. 591-594.
2. Presser, V., M. Heon, and Y. Gogotsi, *Carbide-Derived Carbons – From Porous Networks to Nanotubes and Graphene.* Advanced Functional Materials, 2011. **21**(5): p. 810-833.
3. Bae, J.-S., T.X. Nguyen, and S.K. Bhatia, *Influence of Synthesis Conditions and Heat Treatment on the Structure of Ti3SiC2-Derived Carbons.* Journal of Physical Chemistry C, 2009. **114**(2): p. 1046-1056.
4. Bonilla, M.R.n., et al., *Heat Treatment-Induced Structural Changes in SiC-Derived Carbons and their Impact on Gas Storage Potential.* Journal of Physical Chemistry C, 2010. **114**(39): p. 16562-16575.
5. Dash, R., et al., *Titanium carbide derived nanoporous carbon for energy-related applications.* Carbon, 2006. **44**(12): p. 2489-2497.
6. Dash, R.K., A. Nikitin, and Y. Gogotsi, *Microporous carbon derived from boron carbide.* Microporous and Mesoporous Materials, 2004. **72**(1-3): p. 203-208.
7. Nguyen, T.X., J.S. Bae, and S.K. Bhatia, *Characterization and Adsorption Modeling of Silicon Carbide-Derived Carbons.* Langmuir, 2009. **25**(4): p. 2121-2132.
8. Yushin, G., et al., *Carbide-Derived Carbons: Effect of Pore Size on Hydrogen Uptake and Heat of Adsorption.* Advanced Functional Materials, 2006. **16**(17): p. 2288-2293.
9. Urbonaite, S., et al., *EELS studies of carbide derived carbons.* Carbon, 2007. **45**(10): p. 2047-2053.
10. Opletal, G., et al., *Hybrid approach for generating realistic amorphous carbon structure using metropolis and reverse Monte Carlo.* Molecular Simulation, 2002. **28**(10-11): p. 927-938.
11. Nguyen, T.X., et al., *New Method for Atomistic Modeling of the Microstructure of Activated Carbons Using Hybrid Reverse Monte Carlo Simulation.* Langmuir, 2008. **24**(15): p. 7912-7922.
12. Jain, S.K., et al., *Molecular Modeling of Porous Carbons Using the Hybrid Reverse Monte Carlo Method.* Langmuir, 2006. **22**(24): p. 9942-9948.
13. Palmer, J.C., et al., *Detailed structural models for activated carbons from molecular simulation.* Carbon, 2009. **47**(12): p. 2904-2913.
14. Pikunic, J., et al., *Structural Modeling of Porous Carbons: Constrained Reverse Monte Carlo Method.* Langmuir, 2003. **19**(20): p. 8565-8582.
15. Palmer, J.C., et al., *Modeling the structural evolution of carbide-derived carbons using quenched molecular dynamics.* Carbon, 2010. **48**(4): p. 1116-1123.
16. Palmer, J.C. and K.E. Gubbins, *Atomistic models for disordered nanoporous carbons using reactive force fields.* Microporous and Mesoporous Materials, 2012. **154**(0): p. 24-37.
17. Nguyen, T.X. and S.K. Bhatia, *Characterization of accessible and inaccessible pores in microporous carbons by a combination of adsorption and small angle neutron scattering.* Carbon, 2012. **50**(8): p. 3045-3054.
18. Kaplow, R., T.A. Rowe, and B.L. Averbach, *Atomic Arrangement in Vitreous Selenium.* Physical Review, 1968. **168**(3): p. 1068-1079.
19. McGreevy, R.L. and L. Pusztai, *Reverse Monte Carlo Simulation: A New Technique for the Determination of Disordered Structures.* Molecular Simulation, 1988. **1**(6): p. 359-367.
20. Opletal, G., et al., *HRMC: Hybrid Reverse Monte Carlo method with silicon and carbon potentials.* Computer Physics Communications, 2008. **178**(10): p. 777-787.

21. O'Malley, B., I. Snook, and D. McCulloch, *Reverse Monte Carlo analysis of the structure of glassy carbon using electron-microscopy data.* Physical Review B, 1998. **57**(22): p. 14148-14157.
22. Rigden, J.S. and R.J. Newport, *A Reverse Monte Carlo Modeling Study of Diamond-like Carbon.* Journal of The Electrochemical Society, 1996. **143**(1): p. 292-296.
23. Nguyen, T.X., et al., *Structure of saccharose-based carbon and transport of confined fluids: hybrid reverse Monte Carlo reconstruction and simulation studies.* Molecular Simulation, 2006. **32**(7): p. 567-577.
24. Kirkpatrick, S., C.D. Gelatt, and M.P. Vecchi, *Optimization by Simulated Annealing.* Science, 1983. **220**(4598): p. 671-680.
25. Bhatia, S.K., *Density Functional Theory Analysis of the Influence of Pore Wall Heterogeneity on Adsorption in Carbons.* Langmuir, 2002. **18**(18): p. 6845-6856.
26. Nguyen, T.X. and S.K. Bhatia, *Probing the Pore Wall Structure of Nanoporous Carbons Using Adsorption.* Langmuir, 2004. **20**(9): p. 3532-3535.
27. Pikunic, J., et al., *Realistic molecular models for saccharose-based carbons.* Applied Surface Science, 2002. **196**(1–4): p. 98-104.
28. Opletal, G., et al., *HRMC_2.0: Hybrid Reverse Monte Carlo method with silicon, carbon and germanium potentials.* Computer Physics Communications, 2013. 184(8): p. 1946-1957.
29. Marks, N.A., *Generalizing the environment-dependent interaction potential for carbon.* Physical Review B, 2000. **63**(3): p. 035401.
30. Nigel, M., *Modelling diamond-like carbon with the environment-dependent interaction potential.* Journal of Physics: Condensed Matter, 2002. **14**(11): p. 2901.
31. Brenner, D.W., *Empirical potential for hydrocarbons for use in simulating the chemical vapor deposition of diamond films.* Physical Review B, 1990. **42**(15): p. 9458.
32. Donald, W.B. and et al., *A second-generation reactive empirical bond order (REBO) potential energy expression for hydrocarbons.* Journal of Physics: Condensed Matter, 2002. **14**(4): p. 783.
33. Gelb, L.D. and K.E. Gubbins, *Characterization of Porous Glasses: Simulation Models, Adsorption Isotherms, and the Brunauer−Emmett−Teller Analysis Method.* Langmuir, 1998. **14**(8): p. 2097-2111.
34. Gelb, L.D. and K.E. Gubbins, *Pore Size Distributions in Porous Glasses: A Computer Simulation Study.* Langmuir, 1998. **15**(2): p. 305-308.
35. Vishnyakov, A., P.I. Ravikovitch, and A.V. Neimark, *Molecular Level Models for CO2 Sorption in Nanopores.* Langmuir, 1999. **15**(25): p. 8736-8742.
36. Steele, W.A., *The interaction of rare gas atoms with graphitized carbon black.* Journal of Physical Chemistry, 1978. **82**(7): p. 817-821.
37. Nguyen, T.X., S.K. Bhatia, and D. Nicholson, *Prediction of High-Pressure Adsorption Equilibrium of Supercritical Gases Using Density Functional Theory.* Langmuir, 2005. **21**(7): p. 3187-3197.
38. Bhatia, S.K. and D. Nicholson, *Adsorption and Diffusion of Methane in Silica Nanopores: A Comparison of Single-Site and Five-Site Models.* Journal of Physical Chemistry C, 2011. **116**(3): p. 2344-2355.
39. Klauda, J.B., J. Jiang, and S.I. Sandler, *An ab Initio Study on the Effect of Carbon Surface Curvature and Ring Structure on N2(O2)−Carbon Intermolecular Potentials.* Journal of Physical Chemistry B, 2004. **108**(28): p. 9842-9851.
40. Talu, O. and A.L. Myers, *Reference potentials for adsorption of helium, argon, methane, and krypton in high-silica zeolites.* Colloids and Surfaces A, 2001. **187–188**(0): p. 83-93.

41. Sarkisov, L. and A. Harrison, *Computational structure characterisation tools in application to ordered and disordered porous materials.* Molecular Simulation, 2011. **37**(15): p. 1248-1257.
42. Brunauer, S., P.H. Emmett, and E. Teller, *Adsorption of Gases in Multimolecular Layers.* Journal of the American Chemical Society, 1938. **60**(2): p. 309-319.
43. Steele, W.A., *The physical interaction of gases with crystalline solids: I. Gas-solid energies and properties of isolated adsorbed atoms.* Surface Science, 1973. **36**(1): p. 317-352.
44. Coasne, B., K.E. Gubbins, and R.J.M. Pellenq, *A Grand Canonical Monte Carlo Study of Adsorption and Capillary Phenomena in Nanopores of Various Morphologies and Topologies: Testing the BET and BJH Characterization Methods.* Particle & Particle Systems Characterization, 2004. **21**(2): p. 149-160.
45. Nguyen, T.X. and S.K. Bhatia, *Kinetic Restriction of Simple Gases in Porous Carbons: Transition-State Theory Study.* Langmuir, 2007. **24**(1): p. 146-154.
46. Lopez, M.J., I. Cabria, and J.A. Alonso, *Simulated porosity and electronic structure of nanoporous carbons.* Journal of Chemical Physics, 2011. **135**(10): p. 104706-9.
47. Thrower, P.A., *The Study of Defects in Graphite by Transmission Electron Microscopy*, in *Chemistry and Physics of Carbon*, P.J. Walker, Editor. 1969, Marcel-Dekker: New York. p. 217– 320.
48. Mauter, M.S. and M. Elimelech, *Environmental Applications of Carbon-Based Nanomaterials.* Environmental Science & Technology, 2008. **42**(16): p. 5843-5859.
49. Stone, A.J. and D.J. Wales, *Theoretical studies of icosahedral C60 and some related species.* Chemical Physics Letters, 1986. **128**(5–6): p. 501-503.
50. Kim, G., J. Park, and S. Hong, *First-principles study of substitutional carbon pair and Stone–Wales defect complexes in boron nitride nanotubes.* Chemical Physics Letters, 2012. **522**(0): p. 79-82.
51. Zhou, L.G., F.Y. Meng, and S.Q. Shi, *Effects of Stone-Wales Defect on Adsorption & Insertion Capacity of Nanotubes.* Nanotech 2003. **3**: p. 3.
52. Pimenta, M.A., et al., *Studying disorder in graphite-based systems by Raman spectroscopy.* Physical Chemistry Chemical Physics, 2007. **9**(11): p. 1276-1290.
53. Costa, S., et al., *Characterization of Carbon Nanotubes by Raman spectroscopy.* Materials Science-Poland, 2008. **26**(2): p. 8.
54. Bender, E. *Equation of State Exactly Representing The Phase Behavior of Pure Substances*. in *Proceedings of the 5th Symposium On Thermophysical Properties*. 1970: ASME.

4. Hybrid Reverse Monte Carlo Simulation of Amorphous Carbon: Distinguishing Between Competing Structures Obtained Using Different Modeling Protocols

Amir H. Farmahini and Suresh K. Bhatia

CARBON, 2015, 83 (0), pp 53–70

DOI:10.1016/j.carbon.2014.11.013

Accepted: November 6, 2014 - Published: March, 2015

School of Chemical Engineering, The University of Queensland, Brisbane, QLD 4072, Australia

4.1. Abstract

We explore different multi-stage and multi-constraint modelling strategies using the Hybrid Reverse Monte Carlo (HRMC) technique to develop realistic models for the amorphous structure of silicon carbide derived-carbon, and investigate the effect of modelling parameters on the development of nano-structural features of the constructed models. It is shown that application of long simulations with slow thermal quench rate is essential for modelling of amorphous structures. Nevertheless, very slow quenching rates are shown to lead to the formation of configurations with large fraction of sp^2 carbon, lacking the level of disorder required to match structure-related experimental data. The predicted gas adsorption isotherms are very sensitive to the pore size distribution (PSD), thus the final structure must reasonably reproduce the total pore volume and pore size distribution of the experimental sample. The frequently-observed strong first peak of the DFT-based PSD obtained from argon adsorption is shown to be an artifact of argon inaccessibility. Pore accessibility analysis of the constructed models, as well as MD simulations of gas transport demonstrate that the HRMC constructed structures contain short-range structural anisotropy, however the models are successful in capturing the long range internal energy barriers of amorphous carbon for methane.

4.2. Introduction

The realistic modeling and computational characterization of amorphous materials is a major challenge for theoreticians interested in the prediction of transport properties of such materials, with fluid transport being strongly controlled by the topology and morphology of the adsorbent structure

[1]. The inapplicability of conventional transport models for materials with nanoscale confinement is now well established [2-4]. Further, for amorphous materials, the geometry of the pore wall, as well as morphology of the solid-fluid interface is highly irregular at microscopic scales, so that the complexity of the boundary conditions makes the established theoretical analysis of the particle motion and fluid transport essentially intractable [5]. In principle, molecular dynamics (MD) simulation can provide exact results for the prediction of fluid transport in such disordered confined spaces; however the reliability of the results obtained from MD depends on the use of realistic adsorbent models and potentials. Such models should represent the topology and morphology of the solid structure with sufficient accuracy to reasonably reproduce the surface heterogeneity and internal energy barriers of the system. Lattice abnormalities including surface roughness and corrugation of the pore walls in addition to interconnectivity of pore spaces, play an important role in the adsorption and diffusion of fluid molecules in amorphous materials, which therefore should be realistically represented.

During the last two decades two major modeling approaches have been employed for atomistic modeling of disordered porous media: the constructive modelling techniques and the mimetic approach. Reverse Monte Carlo modeling (RMC) is the major development in the former class of modelling techniques, which is based on matching experimental correlation functions of the sample obtained from diffraction data with those generated from molecular simulations by stochastic sampling of the amorphous material. The idea of matching experimental distribution function of the actual sample with that of an atomistic model using Monte Carlo methods was first examined by Kaplow et al. as early as mid-1960s [6]. They matched radial distribution functions of amorphous and hexagonal selenium obtained from X-ray diffraction with that of the perturbed atomic configuration of the model. Nevertheless, major advance was not achieved until late 1980s, when McGreevy and Pusztai introduced their Reverse Monte Carlo (RMC) algorithm [7]. In their method, a 3D model of the experimental sample is constructed in such a way that the atomic configuration of the model is consistent with the experimental structure factor (SF) and radial distribution function (RDF). Here, the atomic configuration of the model is stochastically generated using the Metropolis Monte Carlo (MMC) technique with Markov chain sampling, while the RDF or SF of the model is matched with corresponding experimental data, as the target function. The matching procedure is performed based on minimization of an error norm written for the discrepancy of either the experimental SF or the RDF with simulation in every MC trial move, given by

$$\chi^2 = \sum_{i=1}^{n_{exp.}} \left(g_{sim.}(r_i) - g_{exp.}(r_i) \right)^2 / \sigma^2_{exp.}(r_i) \quad (4\text{-}1)$$

where n_{exp} is the number of experimental data points, σ_{exp} is the experimental error and $g(r)$ is the radial distribution function. Nevertheless, RMC suffers from a well-known problem, in that the solution to the 3D reconstruction of the disordered material is not unique due to the large number of degrees of freedom of the system. This drawback was originally acknowledged by McGreevy [7]. The other pitfall associated with the RMC algorithm is that this method makes no assumption regarding interatomic potentials, as the configuration of the system evolves through consecutive MC moves, which often leads to the generation of unphysical configurations [8]. For amorphous carbon this can lead to the formation of highly strained 3-member or 4-member carbon rings [9, 10]. Some authors attempted to address this drawback by using extra structural constraints on the main RMC algorithm. In 1996, Rigden and Newport [10] developed a variation of the constrained RMC algorithm (CRMC) for the modeling of diamond-like amorphous hydrogenated carbon with unusual properties. Their modified version of the RMC algorithm constrains the formation of unphysical 3-membered carbon rings, as well as carbon atoms that are bonded to more than four atoms in their vicinity. Shortly after, O'Malley and co-workers [11] introduced a CRMC algorithm for modeling of the structure of glassy carbon by controlling the atomic coordination number of the system following

$$X^2_{coord.} = (f_{RMC} - f_{req.})^2 / w^2_{coord.} \quad (4\text{-}2)$$

where f_{RMC} is the fraction of properly coordinated atoms in the RMC configuration, f_{req} is the target fraction of properly coordinated atoms and w_c is the weighting factor. Further applications of the CRMC algorithm by Walters et al. [12], Thomson and Gubbins [13] and Pikunic et al. [14, 15] yielded some success, while still demonstrating the presence of unphysical configurations in constructed models of disordered carbon, which appeared to be an intrinsic byproduct of the RMC algorithm [8, 9]. The major improvement in this regard was the development of the Hybrid Reverse Monte Carlo (HRMC) technique [9, 16-18]. The new algorithm performs conventional CRMC simulation, while simultaneously implementing an energy minimization scheme using reactive force fields. Therefore, the final configurations obtained from HRMC-based algorithms are energetically stable and physically more meaningful, while at the same time mimicking experimental structural factor data.

Another approach in atomistic modeling of amorphous materials is based on mimetic methods, which are designed to simulate the actual synthesis process of the porous structure without using any empirical structural parameter. Nevertheless, this approach is still at early stages, since our knowledge of the mechanisms active during the synthesis process at the atomistic level is limited, and the actual experimental synthesis time is well-beyond the capability of current computational resources [19]. Recently, pseudo-mimetic modelling techniques such as Quench Molecular Dynamics (QMD) have been proposed to alleviate general pitfalls of the mimetic approach [19-21], in which the topology and morphology of the porous structure is reproduced using conventional molecular dynamics simulation with reactive force fields. The simulation starts from a high temperature vapor or liquid phase and employs a thermal quenching procedure to finally cool down the system at ambient temperature [19, 20]. Several authors have reported qualitative agreement of pore structure (pore size, pore volume and surface area) with experimental values using such quenching protocols [19-24]. Nevertheless, despite moderate success, this method is unable to satisfactorily capture topological and morphological characteristics of the experimental sample. In contrast, it is well-demonstrated that realistic modeling of disordered porous materials is better achieved using the Hybrid Reverse Monte Carlo modeling (HRMC) technique, so that the final constructed model can reproduce many characteristic properties of the experimental sample including structural features, equilibrium gas adsorption and transport properties of the fluid in the target material [18, 25-29].

While more successful, accurate modeling of amorphous materials using the HRMC method is still a daunting task due to the intrinsic difficulty of solving inverse problems, which are in general ill-posed. The major drawback is the lack of adequate structural data obtained from experiment, based on which reconstructive modeling techniques strive to reconstruct the actual structure of the experimental sample. Towards overcoming this drawback, we demonstrate here that a comprehensive range of experimental data needs to be used during and after the modelling to ensure that the final constructed model is able to capture the properties of the experimental sample that are of interest, specially gas adsorption and fluid transport at different thermodynamic conditions. Importantly, the structural properties of the final model are greatly influenced by the constraints and the modeling parameters employed during the HRMC simulation. This includes choice of the quenching scheme in the simulated annealing process [30], application of structural constraints and use of important weighting factors for each constraint. In this work, we study the effects of such

modeling parameters on the quality and performance of the final constructed structure. We construct the atomistic structure of the silicon carbide derived carbon (SiC-DC) based on diffraction data obtained from neutron scattering experiments. Three different models are constructed using different structural constraints and quenching schemes based on the same set of diffraction data. We study the structural characteristics and transport properties of the constructed models and demonstrate that for reliability of an atomistic model it is necessary to perform a wide range of validations, including investigations of structural properties, as well as the adsorption equilibrium and transport properties of the model.

4.3. Theoretical background

The HRMC algorithm makes use of an energy-based constraint, while at the same time matching the experimental error norm given by equation (4-1). Similar to the RMC algorithm, the simulation scheme employs conventional trial MC moves to minimize a total error χ^2 [9]

$$\chi^2_{total} = \frac{\chi^2_{g(r)}}{2} + \frac{E}{k_B T} \tag{4-3}$$

here, the structural error norm $\chi^2_{g(r)}$ is scaled by σ^2_{exp}, which is the RMC weighting factor for the *ith* data point. Similarly, the energy constraint E is scaled by the Boltzmann weighting factor $k_B.T$, which is in fact a weighting factor for the conventional Monte Carlo part of the algorithm. Any extra constraint can also be introduced to the main RMC algorithm to better reproduce structural features of the experimental sample. In this case, for every additional constraint a new error term will be added to the total error norm along with its corresponding weighting factor. Thus, the total error can be rewritten as the "sum of individual cost functions" following [31]

$$\chi^{old}_{total} = \sum_i \sum_j \frac{({A_{ij}}^{exp} - {A_{ij}}^{old})^2}{W_i} + \frac{E^{old}}{k_B T} \tag{4-4}$$

where, the sum i is calculated over the number of constraints and j over the number of fitted data points within the *ith* constraint. Every cost function is a squared difference between the experimental or target value of ${A_{ij}}^{exp}$. and the simulation value of ${A_{ij}}^{old}$, scaled by weighting factor W_i, as described by Opletal et. al [31].

In our study, in addition to the SF and RDF constraints, we have employed a "3-member ring elimination constraint" [31] to restrict formation of unphysical 3-membered carbon rings, by rejecting the trial moves which lead to formation of such structural defects. Additionally, we have

made use of a porosity (pore volume) constraint developed by Opletal et al. [31]. This constraint controls the pore volume of the model by mimicking the experimental porosity of the target experimental sample through grid occupancy of the simulation cell, with associated error [27, 31]

$$\chi_v^2 = [(f_0 - \alpha)^2]/W_V^2 \tag{4-5}$$

where f_0 is the current fraction of occupied cells by at least one atom; χ_V is the error norm representing the discrepancy between the experimental and simulation skeletal volume fractions; and the parameter α defines the desired occupancy of the grid cells (i.e., α = 1 – porosity). W_V is the volume constraint weighting factor. The pore volume of the sample is calculated based on the equation given below

$$V_p = \frac{1}{\rho_{bulk}} - \frac{1}{\rho_{He}} \tag{4-6}$$

here ρ_{bulk} and $\rho_{He}$are the bulk density and the experimental skeletal density of the sample respectively. The pore volume V_p is required to calculate desired occupancy α, in equation (4-5). In principle, the simulation evolves by minimizing the total error term χ_{total}^{old} given by equation (4-4), so that trial moves are always accepted when χ_{total}^{new} is smaller than χ_{total}^{old}. If MC moves lead to situations, where $\chi_{total}^{new}$is larger than χ_{total}^{old}, trial moves will be only accepted through an acceptance probability following [31]

$$P = e^{(\chi_{total}^{old} - \chi_{total}^{new})} \tag{4-7}$$

The minimization is performed via the simulation annealing procedure [30] in such a way that the initial configuration of the system is first melted at high temperatures and then gradually quenched down until the total error norm, χ_{total}, is converged within a small stopping criterion [8, 9, 16]. The quenching scheme can be designed in different ways. In general, a linear quenching procedure, where the temperature is linearly decreased with the number of trial MC moves may be used, however for more amorphous structures application of exponential functions with very slow quenching rate is advisable [27]. Here the key point is the use of an appropriate reactive force field, which should be able to capture interatomic interactions at different length scales. Among the large variety of potentials available in the literature for carbonaceous materials [22, 32, 33], we have utilized the Environment-Dependent Interatomic Potential (EDIP) of Marks [34, 35], shown to provide a sufficient physical description of disordered carbonaceous structures [16]. It can capture atomic interactions over distances approaching the interlayer spacing distance of graphite, which

makes it more suitable for modelling disorder of carbon structures compared to short-range interatomic potentials [25]. The EDIP potential determines the potential energy of the carbon model as a sum of a two-body pair energy term (U_2) and a three-body angular penalty (U_3) following [34]

$$U_i = \sum_j U_2(r_{ij}, Z_i) + \sum_{j<k} U_3(r_{ij}, r_{ik}, \theta_{jik}, Z_i) \quad (4\text{-}8)$$

The two-body pair energy U_2, as well as the three-body angular potential U_3 is a function of interatomic distance (r_{ij}), bond angle (θ_{jik}) and generalized atomic coordination (Z_i) given by

$$Z_i = z_i + \pi_3(z_i)X_i^{dih} + \pi_3(z_i)X_i^{rep3} + \pi_2(z_i)X_i^{rep2} \quad (4\text{-}9)$$

where z_i is the spherical coordination component, π_2 and π_3 are switching functions identifying two and three coordinated atoms, X_i describes dihedral rotation, π-repulsion at a threefold site, and π-repulsion at a twofold site [34].

4.4. Computational details

We have developed three different atomistic models (namely models A, B and C) using the HRMC technique for the microporous structure of silicon carbide derived carbon (SiC-DC) synthesized in our laboratory by chlorination of 50 nm size βSiC particles at 800 °C. The models are constructed based on a unique set of static structure factor data obtained from neutron scattering experiment with the sample, covering a wave vector range 0.2 < q < 50 $Å^{-1}$ using the SANDALS small angle neutron diffractometer at ISIS - Rutherford Appleton Laboratory, U.K. Details of the synthesis process of the carbon sample, as well as the diffraction experiment at ISIS are given elsewhere [27, 29, 36]. The radial distribution function of the sample is obtained by the Fourier inverse transform of the experimental structure factor data [8]:

$$S(q) = 1 + \frac{4\pi\rho}{q}\int r(g(r) - 1)\sin(qr)\,dr \quad (4\text{-}10)$$

here, ρ is the number of atoms per unit volume and q is the magnitude of the scattering vector as a function of the scattering angle θ, and the scattering radiation wavelength λ, given by [8]

$$q = \frac{4\pi.sin(\frac{\theta}{2})}{\lambda} \quad (4\text{-}11)$$

The simulation procedure for the three models is different in terms of their initial configurations, initial temperatures, quenching schemes and rates, number of modelling stages, as well as type of the structural constraints that have been employed for each model. A 3-member ring elimination constraint and an energy constraint have been used for all three models; however the RDF, SF and porosity constraints have been utilized differently for different cases. For all models, the bulk density is set equal to the experimental bulk density of the carbon sample (0.951 g/cc of solid), which is the bulk density of the fully converted SiC-DC, estimated based on the density of the silicon carbide precursor (3.17 g/cc). A 40 Å cubic unit cell has been used for all HRMC models. Here, we note that the unit cell dimension should be at least twice the size of the largest structural feature detected in the experimental radial distribution function (RDF) to accommodate different structural features of the sample. For the reconstruction of the highly disordered SiC-DC structure we found that, while application of simulation unit cells larger than 40 Å is computationally extremely expensive using the HRMC method, they did not lead to any significant improvement in accuracy of isotherm prediction. Thus, a 40 Å unit cell is adequate for the present study, which is supported by the fact that the measured RDF, to be subsequently discussed, showed no features beyond about 10 Å. Linear or exponential quenching schemes were employed to cool down the system to an equilibrated temperature of 300 K, which is close to that of room temperature for the actual sample. In the linear scheme initial and final temperatures of the system were defined and the temperature was quenched down over consecutive MC steps linearly between the two pre-defined temperatures. For an exponential quenching scheme, temperature and SF/RDF weighting factors were scaled down according to

$$T_n = T_i \times {q_r}^{step} \tag{4-12}$$

$$\sigma_n = \sigma_i \times {q_r}^{step/2} \tag{4-13}$$

here, subscripts *i* and *n* denotes the initial and any arbitrary state of the system respectively; q_r represents the quench rate; and "*step*" refers to the simulation step number in millions. Every simulation run consists of two parts, a main and a data part, following Opletal et al [31]. During the main part, scaling factors of the modeling constraints are in effect, and atomic configurations of the system are allowed to change. However, during the data part, the system is assumed to be in equilibrium, so that the weighting factors of the modelling constraints do not change any more. In this part statistical data of the system is collected. The modeling parameters and procedures for each

HRMC-constructed model are discussed in the sections 4.4.1 to 4.4.3 and a useful summary is provided in Table 4-1.

Table 4-1. HRMC simulation parameters of the constructed models

Modelling details	Model A	Model B.S1	Model B.S2	Model C.S1	Model C.S2
Initial Configuration	FCC	FCC	Model B - Stage 1	FCC	Model C - Stage 1
Initial Temperature (K)	10000	5000	5200	5500	5200
Simulation length (MC configurations)	1.167×10^9	2.010×10^9	1.430×10^9	5.830×10^9	1.910×10^9
Constraint type*	RDF (0.045), Energy, 3-membered ring	RDF (0.0318), SF (0.0318), Energy, 3-membered ring	RDF (0.0324), SF (0.0324), Energy, 3-membered ring	SF (0.0334), Energy, 3-membered ring	RDF (0.0324), Energy, 3-membered ring, Porosity (0.001)
Thermal quenching scheme**	Exponential (0.9970)	Linear	Exponential (0.9980)	Exponential (0.9995)	Exponential (0.9985)
σ_{exp} quenching scheme**	Exponential (0.9970)	Exponential (0.9986) / linear	Exponential (0.9980)	Exponential (0.9995)	Exponential (0.9985)

* Scaling factors of the structural constraints are given within parenthesis.

** Exponential quench rates are given within parenthesis.

The detailed reasons for choice of the modeling procedures and associated parameters are thoroughly discussed in Sections 4.5.1 and 4.5.2. Figure 4-1 illustrates snapshots of the HRMC constructed models discussed here.

4.4.1. Model A

Model A was started from a FCC lattice initial configuration. The RDF is the only structural constraint that was imposed on the system, in addition to the 3-member rings elimination constraint. Initial temperature and initial scaling factor of the RDF constraint ($\sigma_{exp.}$) were set to 10,000 K and 0.045 respectively. Both energy and RDF constraints were scaled down using an exponential quenching scheme with a quench rate equal to 0.997. The simulation was performed for 1.167×10^{9} MC steps to reach equilibrium and the statistical data was collected over an additional 10^{7} MC steps.

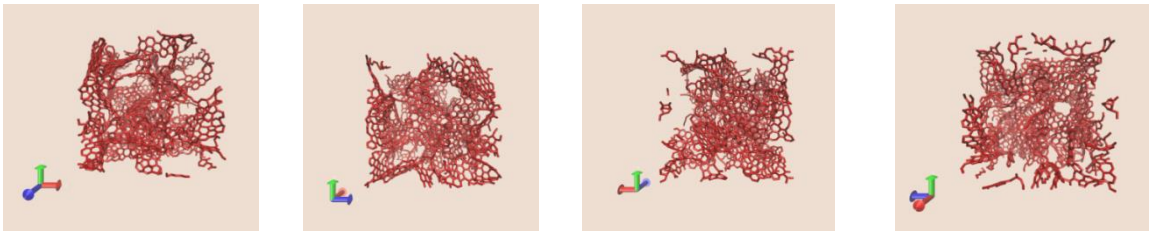

(a)

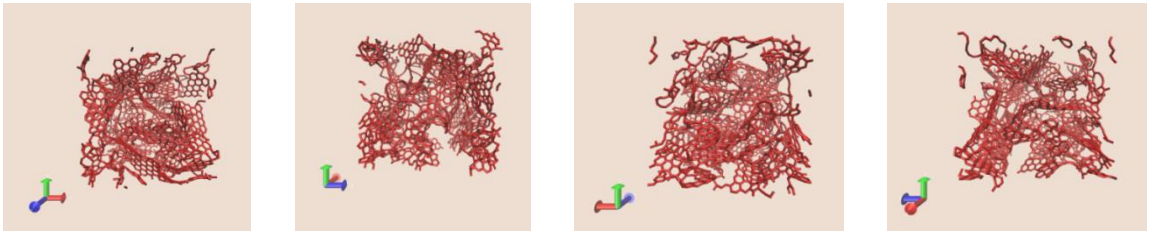

(b)

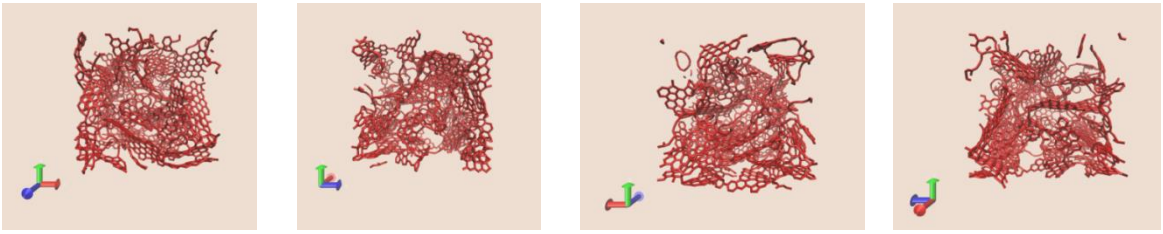

(c)

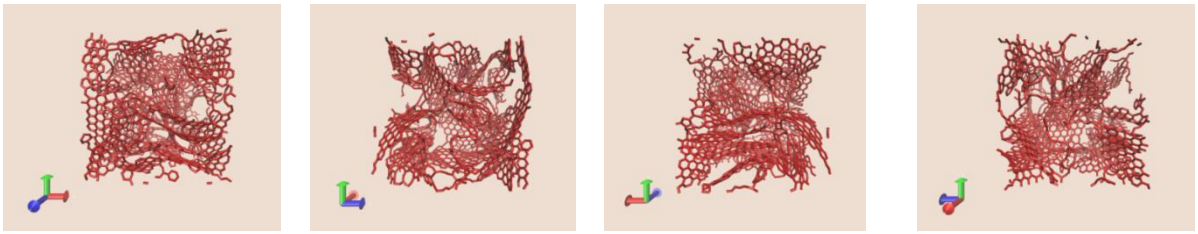

(d)

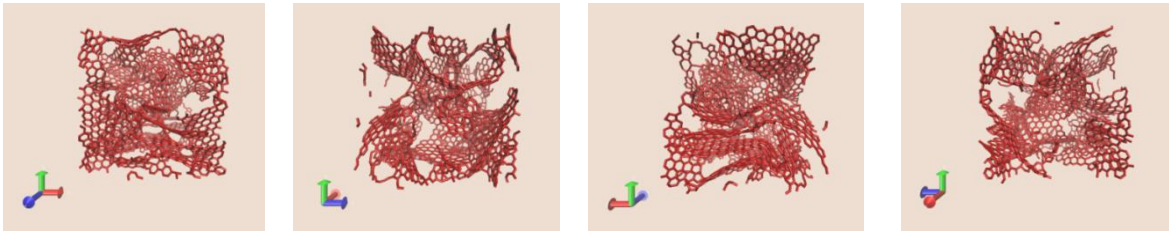

(e)

Figure 4-1. Snapshots of the HRMC constructed models (a) A, (b) B.S1, (c) B.S2, (d) C.S1 and (e) C.S2

4.4.2. Model B

This model was constructed through a two-stage modeling procedure, similar to what we originally used in our previous publication for HRMC modeling of SiC-DC [27]. Both SF and RDF constraints were used for model B. For the first stage (Model B – Stage 1, abbreviated as B.S1) a FCC lattice of carbon atom was melted at 5,000 K and linearly quenched down over three consecutive steps to 4,700 K, 3,300 K and 300 K, so that overall, the simulation was performed for 2.01×10^9 MC steps in this stage. During the first 1.4453×10^9 MC steps of this stage, scaling factors of the structural constraints ($\sigma_{exp.}$ of both RDF and SF) were exponentially quenched down from an initial value of 0.0318 using a quench rate equal 0.9986. For the next 5.647×10^8 MC steps of stage 1, $\sigma_{exp.}$ was kept constant at the value of 0.01153. During the 2nd stage (Model BS.2), the final configuration of the stage1 model (B.S1) was used as the initial configuration. The carbon structure was melted again, this time at 5,200 K and quenched down using an exponential scheme with quench rate equal to 0.998. The $\sigma_{exp.}$ of SF and RDF constraints were scaled down using an initial scaling factor of 0.0324 and a similar quench rate. The second modelling stage was performed for 1.430×10^9 MC steps with the same set of structural constraints (RDF, SF and 3-member rings

elimination). Statistical data was finally collected over 2×10^8 MC steps after the system was equilibrated at the end of stage 2.

4.4.3. Model C[1]

This model is identical to that constructed in our recent work [27] explained in Chapter 3 of this thesis, which has been chosen here as a "reference" model, given that it is broadly validated against experimental structural characterization data, equilibrium gas adsorption isotherms of different gases and dynamic uptake experiments [27, 28]. Although details of the procedure for this model are thoroughly discussed in our previous publication for HRMC modeling of SiC-DC carbon [27], we briefly present it here for sake of clarity. We note that our previous publication on structural modeling of model SiC-DC [27] does not discuss the effect of modeling parameters and their influence on construction of an accurate model, while the principal aim of this work is to investigate such effects and compare them with other models constructed using different modeling procedures.

Model C was constructed using a lengthy two-stage modeling procedure. For the first modeling stage (Model C.S1) the simulation started from a FCC lattice initial configuration, which was melted at an initial temperature of 5,500 K. The simulation was conducted with initial $\sigma_{exp.}$ of 0.0334 and an exponential quenching scheme, in which the quench rate equal to 0.9995 was employed for both temperature and $\sigma_{exp.}$. During this stage only SF and 3-member ring elimination constraints were applied. Due to the use of a very slow quenching rate, the simulation reached equilibrium only after 5.830×10^9 MC steps. For the 2nd modeling stage (C.S2), the RDF was utilized instead of the SF. The use of the 3-member ring elimination constraint and energy constraint remained unchanged. An additional porosity constraint (equation (4-5)) was also imposed on the system during this stage to control the pore volume of the model structure. Model C.S2 was melted initially at 5,200 K, and obtained with initial $\sigma_{exp.}$ of 0.0324 and a fixed value of W_v equal to 0.001. The quench rate for temperate and $\sigma_{exp.}$ was set to 0.9985, while W_v was kept constant. The C.S2 model was run for 1.910×10^9 MC steps to reach equilibrium and statistical data was collected over an additional 200×10^6 MC steps.

[1] The modeling procedure for model C is thoroughly described in Chapter 3 of this thesis.

4.5. Results and discussion

4.5.1. Balancing the effect of individual constraints

One of the critical challenges in HRMC modelling of highly disordered structures is to perform the simulation in such a way that the effect of any constraint is not overshadowed by others, so as to avoid ending up with a structure that is predominantly influenced by one or some of the constraints. For instance, the use of very small scaling factors σ_{exp} for RDF or SF will impose a tight constraint on the system, so that the simulation only accepts trial moves when the simulation pair correlation function of the system strictly matches that of the experiment. This will eventually lead to the formation of atomic configurations that are very well matched with the experimental RDF/SF, but are not energetically favoured or physically meaningful. Such systems are essentially very similar to those obtained from conventional RMC in the past, where no energy constraint was employed. To deal with this situation, the use of somewhat equivalent weighting factors for all constraints are advisable, nevertheless according to our experience this can be sometimes very complex to implement, since there is no established prescription. In principle, the main strategy should be to control the limit to which structural and the energy constraints influence the system separately. One way to control effect of individual constraints on the final structure is to keep the T/σ_{exp}^2 ratio constant, when using an exponential quenching scheme [27, 31]. This ratio dictates how the constraints influence the system. However, this will be inefficient when additional structural constraints (besides SF/RDF based constraints) are in use. This is simply because the total error norm in this case is more complex, so that several competing factors are involved in the evolution of the total error function. A good example of this situation is the procedure for model C.S2 in this work, where an additional porosity constraint is used.

Figure 4-2 (a) and (b) illustrate how diffraction data weighting factors are scaled down for models A, B and C, while the temperature of the system is quenched down.

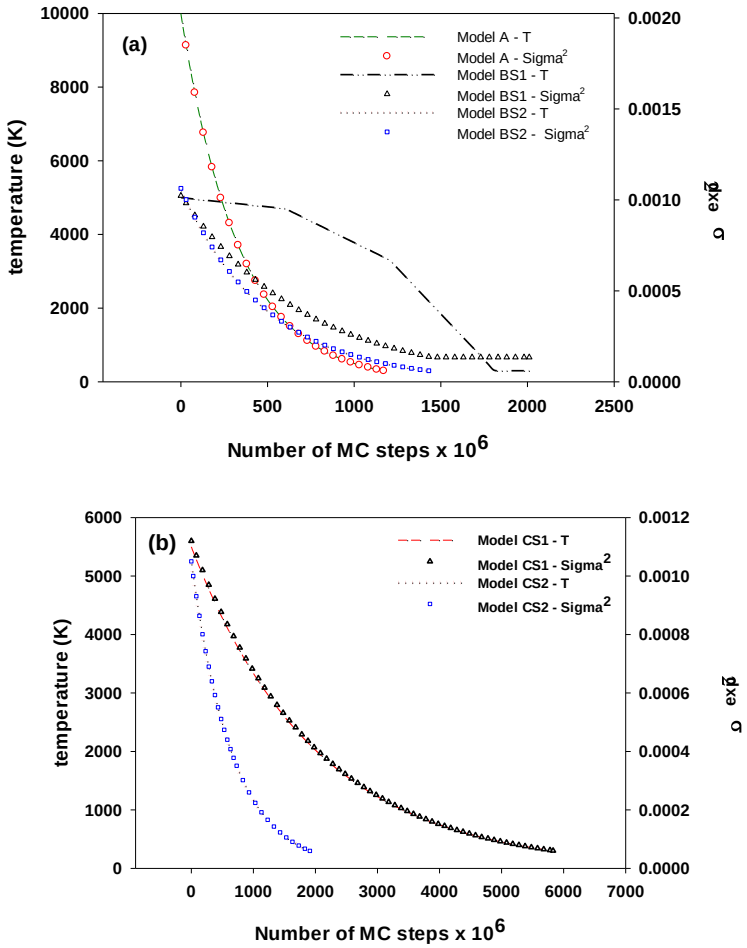

Figure 4-2. Quenching procedure of the energy and structural constraints weighting factors for models (a) A, B.S1, B.S2 and (b) C.S1, C.S2

As illustrated here, except for model B.S1, where a linear quenching scheme is used for temperature, in all other cases simultaneous scaling procedures are employed for both diffraction data and energy based weighting factors. This approach usually provides a more convenient way to control influence of these constraints. Figure 4-2 (b) depicts the use of a very slow quench rate for both modelling stages of the "reference" model (C.S2).

We find that slow annealing processes are very beneficial for modelling of highly disordered structures. This is because the modelling of amorphous materials requires several structural constraints to be used, and this in turn needs adequately long simulation runs to explore the phase space sufficiently and to provide statistically acceptable results. We note that, when performing such lengthy simulation runs, one must ensure that important structural defects, which should be

present in the final realistic model are not annealed off, leading to the formation of configurations with unrealistic perfect graphitic carbon sheets. This is because structural features of the system can be easily dominated by the energy minimization procedure during long simulations. Usually, models with such perfect graphitic structures equilibrate at a level of energy close to that of ideal graphene and are no longer representative of the experimental sample. Figure 4-3 depicts the energy evolutions of the constructed models A, B and C.

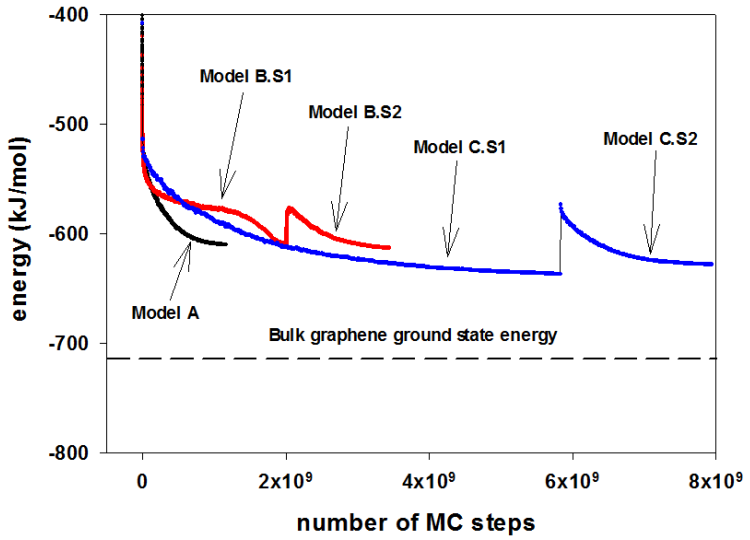

Figure 4-3. Energy evolution of the HRMC constructed models

As shown here, the final configurations of models A, B.S1 and B.S2 are attained on reaching equilibrium at energies of -610.07, -609.13 and -612.87 kJ/mol respectively. However, energy levels of the final configurations of C.S1 and C.S2 models are even lower, which are equal to -636.85 and -627.69 kJ/mol respectively. Systems with energy levels close to that of the graphene ground state will essentially possess structural features analogous to that of graphene, such as having a large fraction of sp^2-carbon atoms. Lopez and co-workers have shown that the formation of graphitic configurations develops as the annealing process progresses during the simulation [24]. In Figure 4-4, we demonstrate that systems with lower level of energy show a higher degree of graphitization.

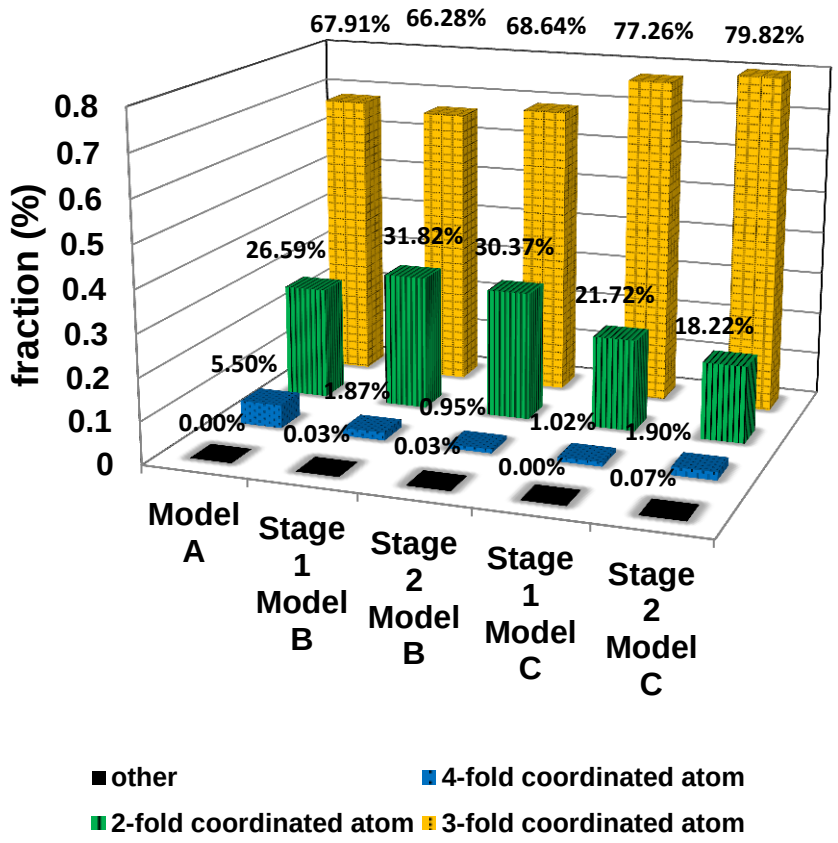

Figure 4-4. Atomic coordination of carbon in different HRMC constructed models

It is evident from this figure that models C.S1 and C.S2 contain the largest fraction of 3-fold coordinated carbons, an indication of highly graphitized structure [24], while at the same time having the lowest energy level, as seen in Figure 4-3. Bhatia and co-workers have shown the existence of non-graphitic structures in SiC-DC using TEM and Raman spectroscopy experiments [36, 37], with the TEM images revealing a rather amorphous atomic configuration. In our previous HRMC study of SiC-DC [27], we also show that the atomic structure of this material possesses a large fraction of sp carbon bonds, as well as other structural defects including Stone–Thrower–Wales (STW) defects. These structural features are consistent with the observation of a prominent defect-induced (D-band) peak in the Raman spectroscopy experiment [27, 37]. Therefore, in constructing atomistic models it is important to ensure that structures that are too graphitic, and thus lack such structural defects, are not attained.

We have also found that using very small scaling factors for diffraction data ($\sigma_{exp.}$) can freeze the atomic configuration of the system attained at the very beginning of the simulation, and prevent

appropriate energy minimization of the system. This is because most of the trial moves leading to minimization of the energy will be rejected by applying a very restrict acceptance criterion for minimization of the structural constraint error terms. In fact, another advantage of slow annealing is to avoid such a scenario. This is evident in our comparison of $\sigma^2_{exp.}$ from Model C with those of two other models shown in Figure 4-2. As illustrated here, $\sigma^2_{exp.}$ is equal to 0.0001 and 0.00025 after 1000 million MC steps for models A and B.S1 respectively, however $\sigma^2_{exp.}$ is equal to 0.0007 for model C.S1 at the same simulation time. Since the diffraction data weighting factor of model C.S1 is somewhat larger than others in its very early stage of evolution, the probability of acceptance (equation (4-7)) for the trial MC moves, which leads to the formation of atomic configurations with lower energy level remains higher. This makes it more likely for the energy constraint to explore the phase space successfully and minimize the system energy by seeking a deeper local minimum on the potential energy surface. In summary, it is apparent that implementation of a simultaneous quenching scheme with an accurately chosen quench rate is critical for the construction of atomistic models which can realistically represent structural properties of the experimental sample. However, the best practice still remains to be the trial and error approach, so that for every simulation run the final structure needs to be validated against suitable experimental data, and this procedure should be repeated iteratively until the best representative configuration is constructed.

4.5.2. Importance of multi-stage and multi-constraint simulations

In theory, HRMC simulation can start from any arbitrary configuration, nevertheless the effect of the initial configuration is retained if simulation is performed for a limited number of steps. This is evident from the HRMC modelling work of Nguyen et al. [25] on atomistic modelling of activated carbon fibre, in which a graphitic-like initial configuration followed by a short simulation run was employed. However, the use of such short simulation runs is only feasible when a reasonable guess for initial configuration of the system is known. In the case of activated carbon fibre for instance, Nguyen et al. [25] successfully use a graphitic slit-like pore configuration based on the pore size distribution (PSD) and pore wall thickness distribution obtained from interpretation of argon adsorption data [25, 38]. On the other hand the use of a highly disordered initial configuration was much less successful for this carbon. Using the appropriate initial configuration from slit-pore characterization, it was shown that their simulation could converge within a fairly short simulation run. However, this strategy is not effective for highly amorphous carbon structures such as that of SiC-DC, which are highly disordered, so that a physically meaningful initial configuration cannot be constructed using the slit-like pore model. This is evident from the simulation snapshots of the

constructed models illustrated in Figure 4-1. As seen here, none of the constructed models represents a graphitic slit-like structure, as opposed to the activated carbon fibre model developed by Nguyen et al. [25].

To address the above limitation, we suggest performing multi-stage simulations, whereby the final configuration of the preceding stage is used as the initial configuration of the following stage. In this strategy, it is usually better to perform a somewhat lengthy simulation run for the first modelling stage to find a metastable configuration, which is equilibrated in the vicinity of a deep local PES minimum. This initial configuration has already captured key structural features of the target sample due to the use of SF/RDF constraints during the first stage. In contrast, the second modelling stage is solely performed for final refinement of the atomic configuration, and should be accompanied by the use of extra structural constraints such as the porosity constraint that we have used for model C.S2 in this work. Therefore, during the second modelling stage, the simulation starts from an approximate initial configuration with low energy, which is gradually treated to improve structural features, that are not correctly constructed during the first stage. In principle, the initial temperature and initial weighting factors of the diffraction data ($\sigma_{exp.}$) constraints should be only slightly increased at the beginning of stage 2 to facilitate easier movement of atoms during this stage by enhancing the acceptance probability. This, however, does not bring the structure back to its initial energy level at the beginning of stage 1. As depicted in Figure 4-3, the initial energy of the following stages always starts from an energy level slightly higher than the final energy level of the preceding stage, but lower in comparison with the starting energy level of stage 1. This "re-melting" process is an inevitable part of a two-stage modelling procedure also shown in our previous publication [27].

4.5.3. Structural characterization of the HRMC constructed models

Comparisons of structural characteristics of the constructed models with those of the actual sample allows us to examine whether or not the final models are good candidates for modelling gas adsorption and fluid transport in the target experimental sample. Nevertheless, final confirmation is always subject to validation of the structures against gas adsorption and uptake-based kinetic data.

In this section, we examine simulation-based diffraction data, as well as other structural features of the constructed models such as pore volume, surface area and pore size distribution, for comparison with experiment. The simulated radial pair distribution function and structure factor of the HRMC constructed models are compared with the corresponding experimental data in in Figure 4-5.

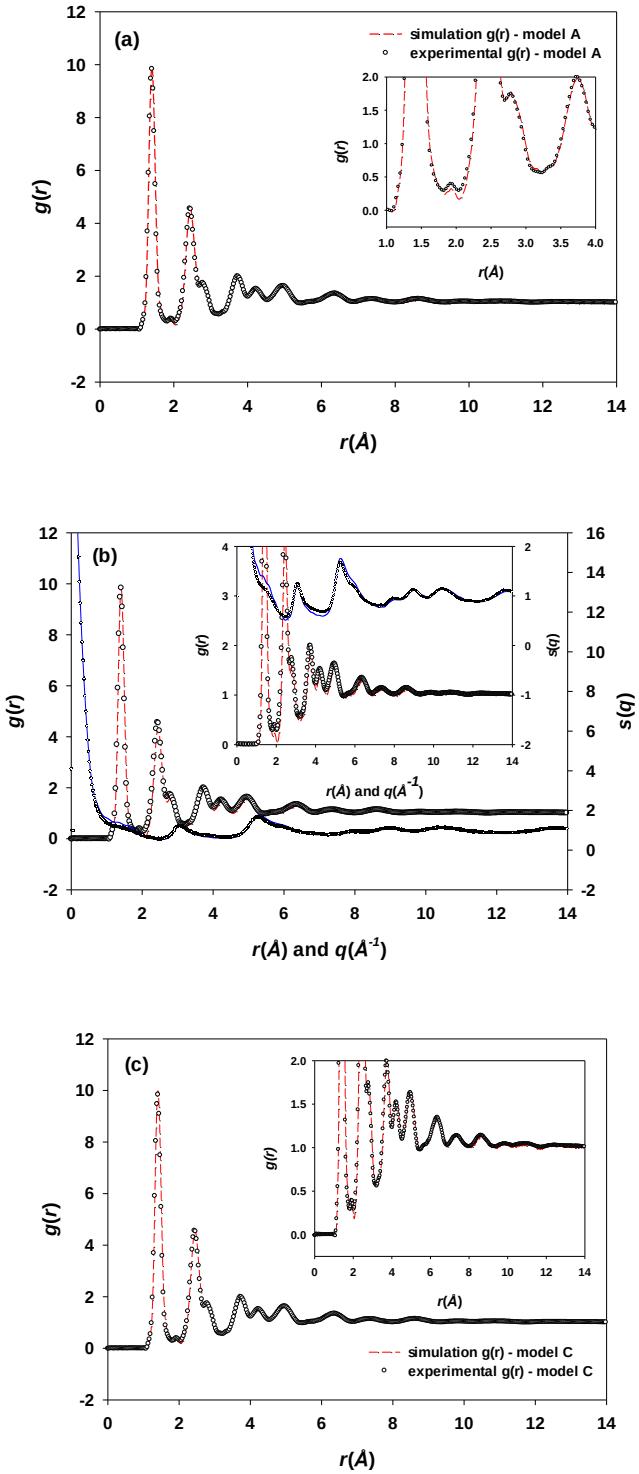

Figure 4-5. Simulation-based radial distribution function and structure factor of the models (a) A, (b) B.S2 and (c) C.S2, compared to those of experiment.

As illustrated in the inset of Figure 4-5 (a), the simulation-based RDF of model A does not capture the first minimum very well; however there is very good agreement between simulated and experimental RDF at larger distances. For model B.S2, depicted in Figure 4-5 (b), the agreement between simulation-based and experimental RDF and SF is poor, especially at short range. This is most likely due to unsuccessful matching of the simulated and experimental diffraction data during the mixed linear-exponential quenching procedure, which was employed for model B. It is apparent that a linear quenching protocol is not a suitable choice for energy minimization, and at the same time reproducing diffraction data in amorphous materials. This is evident from Figure 4-3, where the final energy level of model B.S1 is almost equal to that of model A, although the former model is obtained from a simulation which is more than 840 million MC steps longer than the latter model, an indication of poor minimization obtained from a linear quenching scheme. Additionally, due to the asynchronous quenching of temperature and $\sigma_{exp.}$, the latter weighting factor holds smaller values during the modelling of B.S1structure. Thus, structural constraints unfavourably dominate the system for this model and energy minimization remains imperfect. Contrary to models A and B.S2, the agreement between the simulated and experimental RDF is excellent for model C.S2, as illustrated in Figure 4-5 (c). We can further demonstrate superiority of models A and C.S2 by comparing the variation of $s(q)$ and $g(r)$ errors for the models under study. These error terms are defined by

$$\chi^2_{\mathrm{s(q)}}.\,\sigma^2_{\mathrm{exp.}} = \sum[\mathrm{s(q)_{sim.}} - \mathrm{s(q)_{exp.}}]^2 \tag{4-14}$$

$$\chi^2_{g(r)}.\,\sigma^2_{exp.} = \sum[g(r)_{sim.} - g(r)_{exp.}]^2 \tag{4-15}$$

As depicted in Figure 4-6, the final discrepancies between the simulation-based $s(q)$ and $g(r)$ of the B.S2 model, and their corresponding experimental counterparts, are equal to 3.3258 and 3.4792.

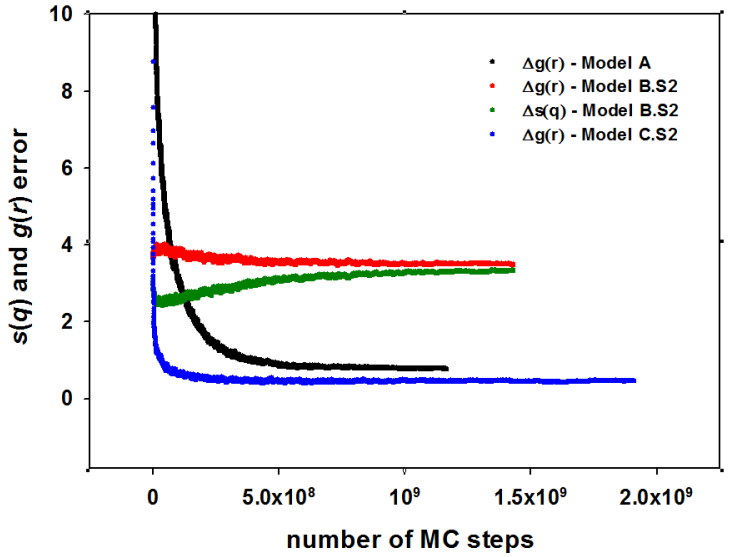

Figure 4-6. Variation of the error in $s(q)$ and $g(r)$ for models A, B.S2 and C.S2

However, this discrepancy for $g(r)$ of models A and C.S2 are 0.7616 and 0.4523 respectively, showing closer agreement of simulation and experimental diffraction data for model C.S2. We also note that for model B.S2, the $s(q)$ error is in fact negatively contributing to minimization of the total error term by showing an increasing trend during the simulation. Moreover, the contribution of the $g(r)$ error in the minimization of the total error in model B.S2 appears to be very small, considering that the difference between initial and final values of the $g(r)$ error is only 0.2082 for this model. Overall, the $s(q)$ and $g(r)$ constraints in model B.S2 neutralize each other's effect, so that both error terms converge to nearly the same number (~3.4). This shows why model B.S2 does not reproduce experimental diffraction data very well, as illustrated in Figure 4-5 5(b). This behaviour can be compared with significant improvement of the $g(r)$ error term for models A and C.S2 during the simulation, with model C.S2 showing even more successful minimization. Therefore, as demonstrated in this argument, model C.S2 is not only an energetically well-converged structure, but it also matches the structural diffraction data with minimum error.

To further investigate structural properties of the constructed models, we also report on the total pore volume (V_p), surface area (SA) and PSD of each model. Table **4-2** summarizes the pore volume and geometric surface area of the HRMC constructed models using helium and argon probes respectively.

Table 4-2. Helium pore volume and geometric argon surface area of the HRMC constructed models compared with experimental data

	Model A	Model B.S1	Model B.S2	Model C.S1	Model C.S2	Experiment
V^t_{He} (cc/g solid)	0.64	0.57	0.59	0.60	0.67	0.66[2]
SA (m^2/g solid)	1711	1548	1558	1483	1581	1556[3]

The total helium-accessible pore volume is a key factor in modelling gas adsorption, and is estimated from the mean density of helium in the simulation cell, based on its second virial coefficient, while neglecting its adsorption, following [39]

$$V_p = \frac{1}{m_s}\int e^{-\phi(\boldsymbol{r})/k_B.T} d\boldsymbol{r} \tag{4-16}$$

where ϕ is the helium-carbon potential energy for a single helium molecule, m_s is mass of the carbon network in the simulation box, κ_B is the Boltzmann constant and T is temperature. The geometric surface area is determined using the computational method of Sarkisov and Harrison with an argon probe [40]. The results are compared with the experimental total pore volume obtained from helium pycnometry, as well as BET surface area based on interpretation of argon adsorption. As can be seen in Table 4-2, models A and C.S2 are the most successful models in predicting total helium pore volumes. The surface area for all models is close to that of BET except for model A, which is higher than the BET surface area but below that of Density Functional Theory (DFT) reported by Bonilla et. al based on interpretation of argon adsorption [37]. One may expect that the relatively large fraction of 4-fold coordinated carbon atoms (sp^3 hybridization) and smaller fraction of 3-fold coordinated carbons (sp^2-hybridization), as illustrated in Figure 4-4, introduces a higher level of structural disorder into the atomistic structure of model A. This higher level of disorder may be giving rise to the higher surface area of model A compared to the other models. In a similar vein, Table 4-3 compares the geometric pore volume distribution of models A, B.S2 and C.S2 using

[2] Total pore volume obtained from helium pycnometry.

[3] BET surface area obtained from interpretation of argon adsorption.

a small probe of 0.1 Å with the experimental data obtained from Small Angle Neutron Scattering (SANS) [41].

Table 4-3. Pore volumes distribution of the HRMC constructed models obtained from geometric spherical probe approximation technique using small probe of 0.1 Å compared to SANS data

	0.1 Å < H_{in} < 3.4 Å (cc/g solid)	**3.4 Å < H_{in} < 16.6 Å (cc/g solid)**	**16.6 Å < H_{in} < 42 Å (cc/g solid)**	**V_t (cc/g solid)**
Model A	0.084	0.527	- - -	0.611
Model B.S1	0.120	0.469	- - -	0.590
Model B.S2	0.114	0.479	- - -	0.593
Model C.S1	0.11	0.478	- - -	0.589
Model C.S2	0.080	0.536	- - -	0.617
SANS	0.070	0.599	0.240	0.909

Again, models A and C.S2 provide the best agreements with the experimental pore volume distribution. We note here that, the HRMC models do not predict pores larger than 15 Å, largely because the experimental redial pair distribution $g(r)$ used for construction of the HRMC models rapidly decays beyond this distance, as illustrated in Figure 4-5. Nevertheless, the existence of pores larger than 15 Å, as observed through SANS is likely to be an indication of mesoscale interparticle spaces in the nanosized SiC powder.

Figure 4-7 compares the He-probed PSD of models A, B.S2 and C.S2 using the spherical probe geometric approximation technique developed by Gelb and Gubbins [42, 43], with that from SANS [41].

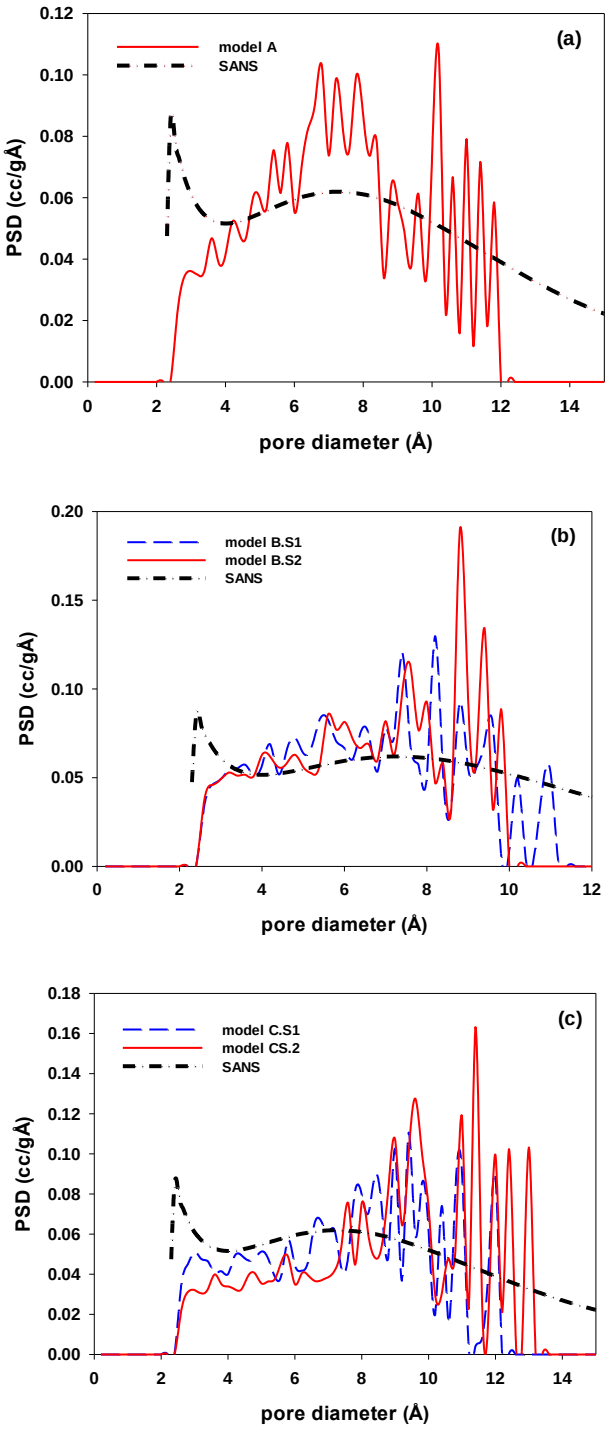

Figure 4-7. Helium-probed geometric PSD of the HRMC constructed models (a) A, (b) B.S1, B.S2 and (c) C.S1, C.S2

As illustrated in this figure, model C.S2 is the most successful in reproducing the pores larger than about 10 Å, which is due to the use of the porosity constraint during the second modelling stage, after the structure initially converged to a deep local PES minimum during stage 1. A comparison between the PSDs of different models reveals that B.S2 model fails to capture pores larger than 10 Å; however it maintains a higher capacity in the ultra-micropore region below 4 Å. In contrast, model C.S2, which is constructed using a porosity constraint contains pores up to 13 Å, nevertheless it accommodates a smaller fraction of pores within the region below 4 Å. For Model A, although it has reproduced pores up to 12 Å, it captures a relatively small volume in the region with pores larger than 10 Å.

To provide further insight, we employed the Finite Wall Thickness Density Functional Theory (FWT-DFT) developed in this laboratory [38, 44] to determine the PSD of the HRMC constructed models based on interpretation of simulated argon adsorption isotherm. The results are then compared with the DFT-based PSD obtained from interpretation of experimental argon isotherm. The argon isotherms are initially simulated for every model using the GCMC method, as illustrated in Figure 4-8. Subsequently, these isotherms were utilized for calculation of PSD using the FWT-DFT technique.

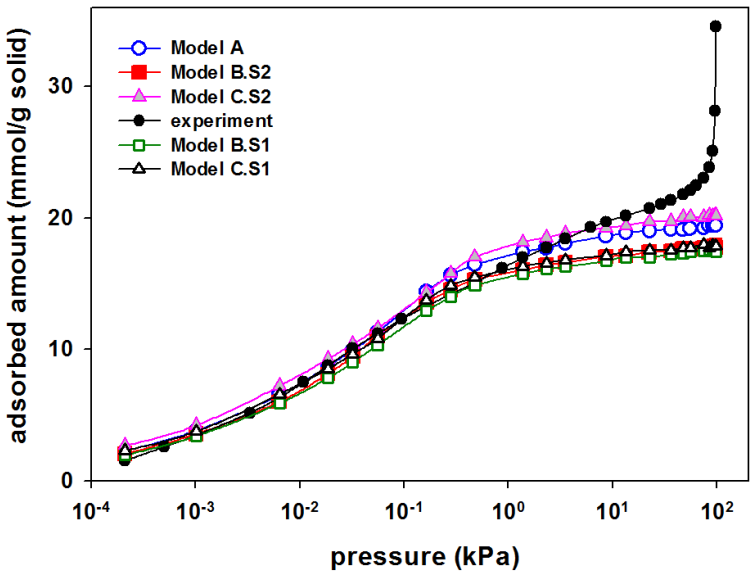

Figure 4-8. Comparison of the predicted argon adsorption isotherms for models A, B.S2 and C.S2 at 87 K with that of experiment

Figure 4-9 depicts comparison of PSDs obtained from the experimental isotherm with the simulated isotherms.

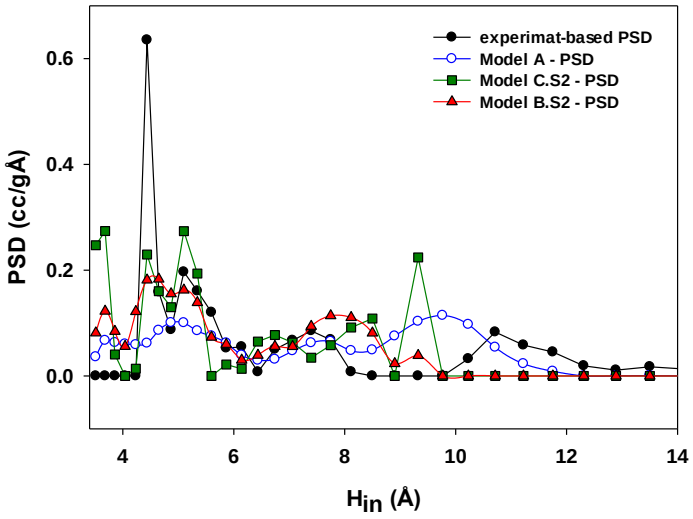

Figure 4-9. DFT-based pore size distribution of the HRMC constructed models compared with experiment-based PSD

It is evident from this figure that the experiment-based PSD cannot detect the ultra-microporous region, which is observed by the geometric method and SANS, however the simulation-based PSDs of all constructed models detect a small pore region of < 4.2 Å. For the experiment-based PSD, this is due to the accessibility problem during argon adsorption, where the diffusion of argon at 87 K is very slow in molecularly narrow pores [27, 37]. Inaccessibility of the internal pore structure at low temperature is previously reported for major characterization gases including argon in Ti_3SiC_2-DCs, SiC-DC and different activated carbons [27, 29, 37, 41, 45-47]. In contrast, the simulated adsorption isotherm does not exhibit this limitation, as the GCMC results are not affected by the inaccessibility issue. This behavior is also supported by slightly lower experimental adsorption of argon compared to the simulated isotherms at low pressures, as illustrated in Figure 4-8. Further, the simulation-based PSDs of the HRMC constructed models obtained from FWT-DFT seem to follow the trends of SANS and helium-probed geometric PSDs which do not possess the very strong peak at 4.4 Å, as opposed to the experiment-based PSD from DFT. This peak is repeatedly detected in PSDs obtained from DFT based on interpretation of experimental argon adsorption for similar materials [25, 36, 37, 45, 48-51]. However, our simulation-based PSDs from FWT-DFT suggest that this strong first peak is an artifact of inaccessibility to argon at 87 K. Thus, an exaggerated first peak at ~4.5 Å is observed in the experimental Ar isotherm-based PSD, and this occurs when smaller ultra-micropores that are inaccessible at low pressures on the experimental time scale are rapidly filled at

higher than true equilibrium pressures. However, these pores are detected in the PSD extracted from the simulation-based isotherms since the inaccessibility, which has an inherently kinetic nature related to pore entry barriers [46, 47], does not influence the simulation results. Other evidence from literature also supports this finding. For example, PSDs obtained from DFT based on interpretation of CO_2 and H_2 do not show a strong first peak, because these gases can pass through the pore mouths that are inaccessible to argon due to their smaller molecular size [29, 45, 52].

Our discussion in this section shows that models A and C.S2 are the most promising candidates for a reliable SiC-DC constructed model, given that they most closely reproduce several important structural features of the target material. However, to further discriminate between these models and to confirm their validity, it is necessary to investigate the adsorption and diffusion performance of these models separately.

4.5.4. Modelling gas adsorption and simulation of internal energy barriers

We employed GCMC and MD simulation techniques for modeling the equilibrium and kinetics of gas adsorption in the HRMC constructed models of microporous SiC-DC. Sub-atmospheric adsorption of argon (87 K), CO_2 (273 K) and high pressure adsorption of methane (323 K) were studied using GCMC simulation. Simulation runs were performed for 10 million MC steps in the equilibration phase followed by 40 million MC steps in the production phase.

To calculate the self-diffusivity of CH_4, equilibrium Molecular Dynamics (EMD) simulations were performed over different temperatures using the LAMMPS simulation package [53]. The simulations were performed in the canonical (NVT) ensemble, in which translational and rotational degrees of freedom of rigid bodies were both thermostated using the Nose-Hoover algorithm with chains, as described by Hoover [54] and Martyna et al. [55, 56]; the rigid-body algorithm for NVT integration is explained elsewhere [57]. A Verlet time integrator was utilized with time step equal to 1 fs. Short range intermolecular interactions were modeled using the 12-6 Lennard-Jones potential with a cut-off distance of 18 Å. The standard Ewald summation was utilized for electrostatic interactions with cut-off distance of 18 Å, so that pairwise interactions within this distance were computed directly and those outside this distance were calculated in reciprocal space. The self-diffusivity of CH_4 was calculated using mean-squared displacements (MSDs) of the center of mass of the molecules following

$$D_s = \frac{1}{2Nd} \lim_{t \to \infty} \frac{1}{t} \langle \sum_{i=1}^{N} |r_i(t) - r_i(0)|^2 \rangle \quad (4\text{-}17)$$

where $r_i(t)$ is the center of mass position vector of molecule *i* at time *t*, *N* is the number of molecules and *d* is dimensionality of the system. To calculate the activation energy barrier of methane in each constructed model, the Arrhenius formula was employed, following

$$D = D_0 . e^{-E_a/RT} \quad (4\text{-}18)$$

where, *D* and D_0 are the diffusivity and temperature-independent pre-exponential factor respectively. Molecular models and force-field parameters for all GCMC and MD simulations are given in our recent publication [27].

Figure 4-8 compares the argon adsorption isotherm at 87 K for all the HRMC constructed models. As illustrated here, models B.S1, B.S2 and C.S1 show the largest deviation from the experimental isotherm, and the predicted isotherms using these three models are almost identical. The underestimation of amount adsorbed based on these models compared to experimental values, is clearly due to their small pore volume. It is interesting to see that lack of pores larger than 10 Å in model B.S2 does not affect its adsorption isotherm compared to the other two models. Given the similar pore volume distribution of these three models (Table 4-3), it is not surprising that they lead to very similar adsorption isotherms. Figure 4-8 also shows that models A and C.S2, whose total pore volume is higher than 0.6 cc/g solid, are more successful in matching the experimental argon isotherm, with model C.S2 to be even slightly better at higher pressures. This is likely due to model C.S2 having pores larger than 12 Å, which are missing in model A. We also note that the higher surface area of model A, seen in Table 4-2, does not improve the adsorption isotherm of this model in comparison with model C.S2, which has a smaller SA; thus the total pore volume appears to be the governing factor here.

Figure 4-10 and Figure 4-11compare simulated CO_2 and CH_4 adsorption isotherms for models A, BS.2 and C.S2 with the experimental isotherms.

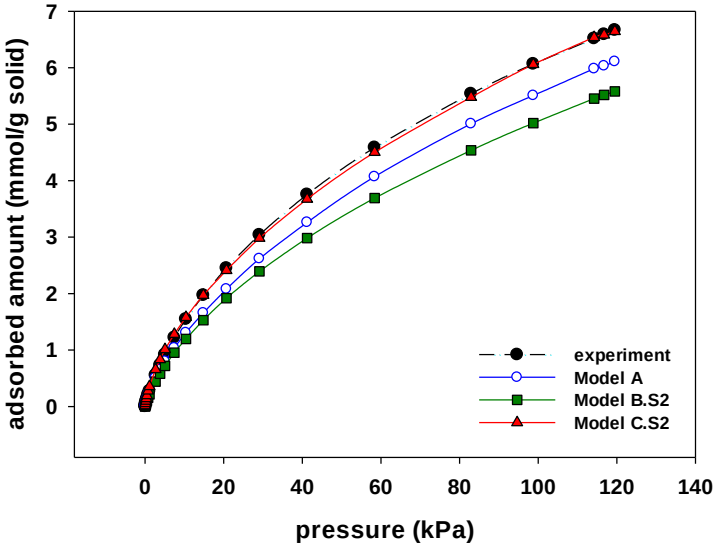

Figure 4-10. Comparison of the predicted sub-atmospheric CO_2 adsorption isotherms for models A, B.S2 and C.S2 at 273 K with that of experiment

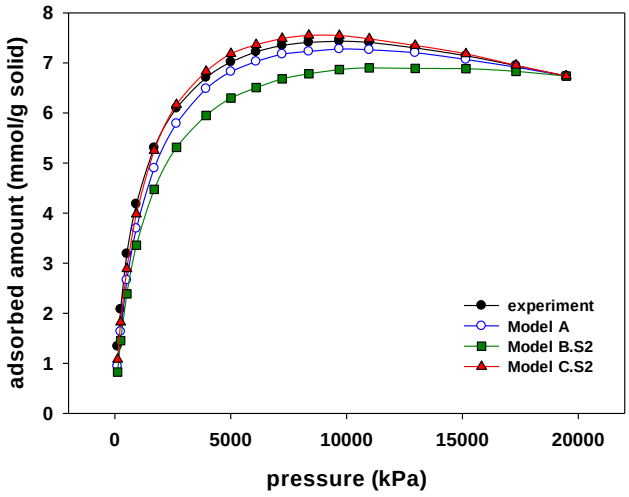

Figure 4-11. Comparison of the predicted high pressure CH_4 adsorption isotherms for models A, B.S2 and C.S2 at 323 K with that of experiment

As shown in these figures, model C.S2 provides excellent match with the experimental adsorption isotherms of carbon dioxide and methane; however model A is only successful in reproducing the

adsorption isotherm of methane. We note that model C.S2 shows significantly better agreement with the CO_2 experimental isotherm compared to model A, however its pore volume is only slightly higher than that of model A, which is an indication of sensitivity of the simulated isotherms to variation the total pore volume of the HRMC models. Further, similar to argon adsorption, the higher surface area of model A does not have any obvious effect on enhancing carbon dioxide adsorption based on this model. From these comparisons is evident that total pore volume and PSD are the key factors dictating adsorption behavior of the models, while the role of SA in modeling adsorption isotherms appears to be less significant. Therefore, one important strategy for modeling gas adsorption in HRMC constructed models is the use of pore volume-based constraints, to accurately capture the experimental pore volume, as for model C.S2 in this paper.

We have also investigated structural and diffusional isotropy of the HRMC constructed models using different methods. Although the disordered macroscopic structure of amorphous materials is considered isotropic, this study suggests that in microscopically constructed models, such as those investigated here, the atomistic structure can possess short-range anisotropy. Such local structural anisotropy is expected due to unidirectional transport of the chlorine and metal chloride at the reaction interface during chlorination process, which is strongly influenced by particle size of the sample [29]. As noted by Shahtalebi et al. [29], smaller particles give rise to higher chlorine partial pressures and lower metal chloride partial pressures at the carbide-carbon interface, thus faster chlorination is expected. Considering the experimental SiC-DC sample under investigation in this study is obtained from nano-size βSiC particles [36], faster conversion and greater structural distortions of the final synthesized sample compared to micron size particles is not unexpected. Structural anisotropy of the HRMC constructed models is evident through the percolation path analysis of these models, using the “pore space accessibility” method of Sarkisov [40]. In this method, accessibility of the pore space is examined by exploring the unit cell using the largest geometric spherical probe (with limiting pore diameter), which can traverse the system in different directions. The system is called percolated in one direction, if the probe molecule can traverse the unit cell from one side to the other side without overlapping the atomic network. Table 4-4 summarizes the data for percolation path analysis of the HRMC constructed models, as defined here.

Table 4-4. Percolation path analysis of the HRMC constructed models

Model	Limiting pore diameter (Å)	Maximum pore size (Å)	Pore space percolation
Model A	6.2	11.78	1D – Channel
Model B.S1	5.99	11.00	1D – Channel
Model B.S2	5.78	9.86	3D – 3D pores
Model C.S1	6.64	12.03	1D – Channel
Model C.S2	7.43	13.05	2D – Slit

According to this information, it is clear that the pore space is percolated differently for models A, B.S2 and C.S2, so that they are percolated in 1, 3 and 2 dimensions respectively. It is also noted that percolation path of the unit cell can change during a multi-stage modelling procedure, as seen for models B and C.

To further study isotropicity of the constructed models, we have examined the self-diffusion and internal energy barriers of methane in different directions of the unit cell. Figure 4-12 illustrates the temperature variation of the *X*, *Y* and *Z* components of methane self-diffusivity at infinite dilution for models A, B.S2 and C.S2.

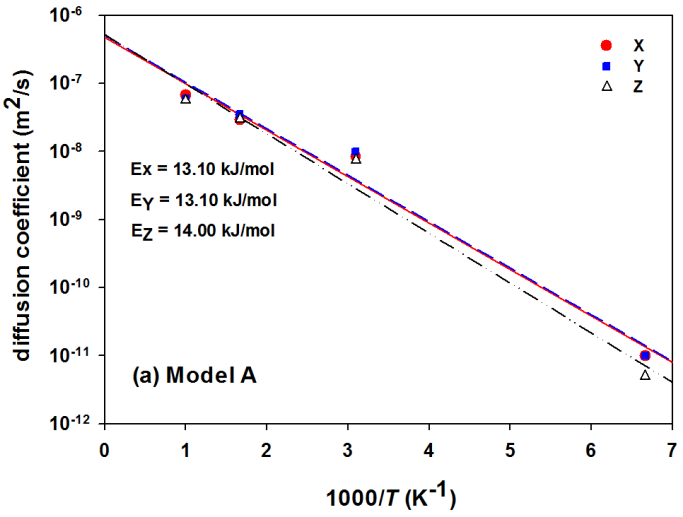

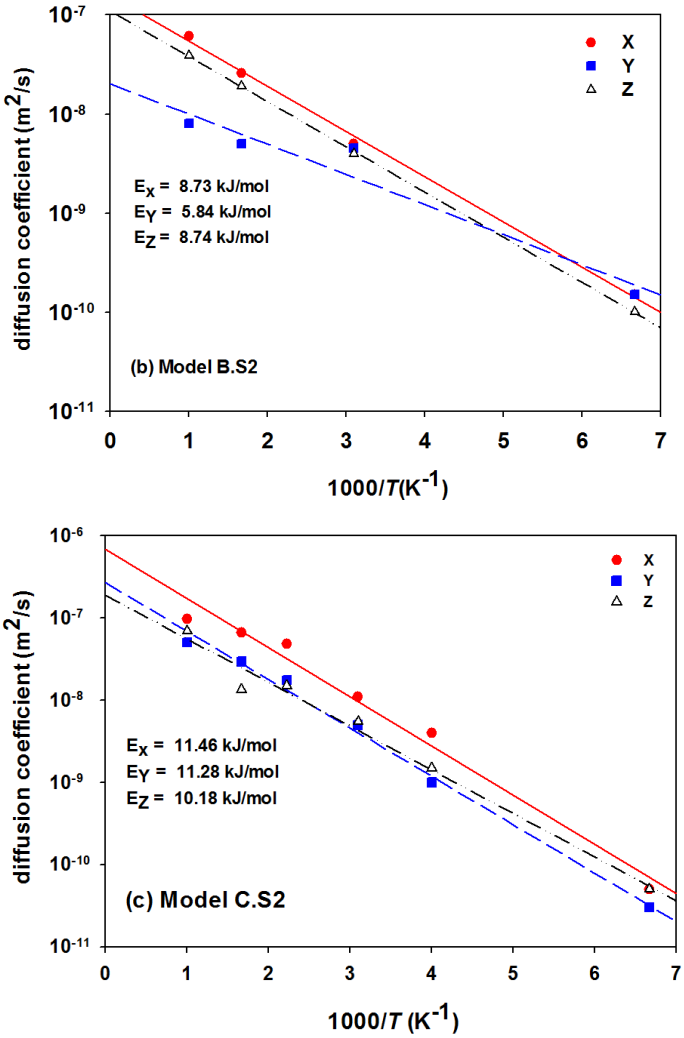

Figure 4-12. Arrhenius plots of the infinite dilution self-diffusivity of methane in X, Y and Z directions, for models (a) A, (b) B.S2 and (c) C.S2

As seen here, while the variation of the self-diffusivity of CH_4 with respect to the unit cell direction is very small for all models at temperatures below 600 K, the significant differences in the diffusivities in the three directions at temperatures above 323 K suggest diffusional anisotropy for models B.S2 and C.S2. In particular model B.S2 shows significantly smaller activation energy in the *Y*-direction compared to the *X* and *Z* directions. Only model A (Figure 4-12 (a)) appears to show diffusional isotropy over the entire temperature range investigated, with activation energy barriers and magnitudes of diffusivities in all there directions being very similar. This finding suggests differences in the spatial distribution of bottle-necks and energy barriers in the models, although they have been constructed based the same diffraction data. The anisotropic distribution of energy

barriers is supported by different activation energy barriers estimated from the self-diffusivity of methane in each direction for the HRMC constructed models using equation (4-18), as shown in Figure 4-12.

To provide more insight into internal energy barriers of the constructed models, we have also calculated total activation energy barriers of models A, B.S2 and C.S2[4] using equation (4-18) from the dimensionally averaged self-diffusivity of methane at infinite dilution. The reported diffusion coefficients are obtained within 43% standard deviation. The infinite dilution diffusion coefficient of methane for these models are compared with the experimental values [29] obtained from macroscopic uptake-based kinetics data in Figure 4-13.

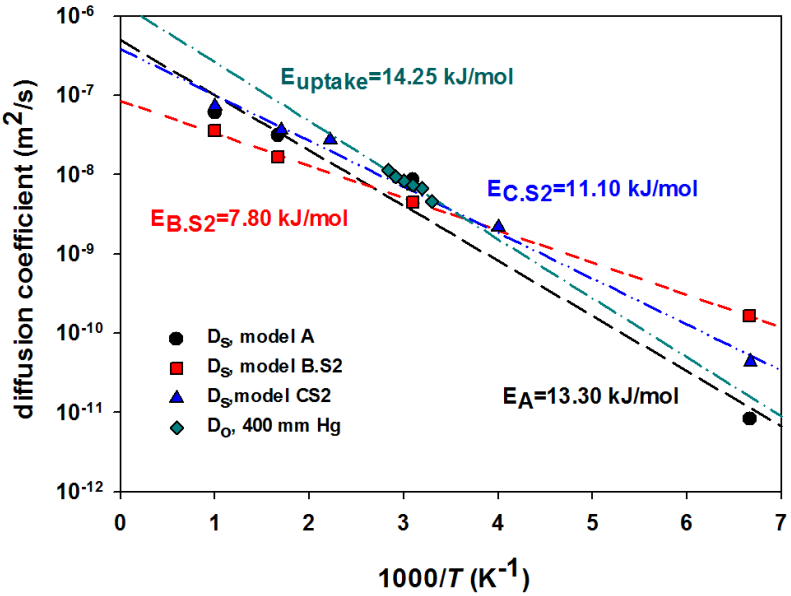

Figure 4-13. Comparison of temperature dependence of EMD diffusion coefficient of different HRMC models with uptake-based data for CH_4 at 400 mmHg

Details of the experimental measurement are given in our previous publication [29]. The experimental results obtained from macroscopic uptake represent collective diffusivities, and are based on measurements at 400 mm Hg bulk pressure. These were essentially constant for pressures below 400 mm Hg and may therefore be meaningfully compared with simulation self-diffusivities at infinite dilution. As depicted in Figure 4-13, activation energy barriers of the HRMC constructed models of A and C.S2 are in remarkable agreement with the experimental results, with model A providing even better prediction; however model B.S2 predicts a much smaller activation energy

[4] Activation energy barriers of different gases and their molecular origin for model C.S2 are thoroughly discussed in chapter 5 and 6.

barrier for methane. This information, in addition to that illustrated in Figure 4-12, demonstrates that model A contains somewhat more restricted pore spaces that impose a larger energy barrier on diffusing molecules in comparison to model C.S2. Such structural constrictions are experimentally and theoretically shown to have significant influence on transport properties of different gases in porous materials [28, 58, 59], therefore it is very important that they are taken into consideration for realistic modeling of amorphous materials. Although no direct relation between modeling parameters of the HRMC technique with internal energy barriers of the constructed models is evident, it is critical that the final constructed model is validated against diffusion data obtained from experiment, as demonstrated here.

Taking into account the results obtained from the wide range of validation examinations, specially performance of the constructed models in modeling equilibrium gas adsorption and uptake-based kinetic data, model C.S2 appears to be the most promising structure, although the performance of model A would appear to be slightly better in reproducing the activation energy barrier of methane. Finally, we note that from our modeling studies it appears that the HRMC technique is capable of capturing the long range internal energy barriers of amorphous carbon materials with very good level of accuracy, at least for some gases. In general, macroscopic diffusivities are often several orders of magnitude smaller than microscopic diffusivities calculated by molecular dynamics simulation in crystalline or other ordered systems such as zeolites, largely because of the presence of defects and related energy barriers [58, 60]; however our studies demonstrate that accurately constructed HRMC models are able to decrease this gap to within a small factor.

4.6. Conclusions

We have developed three different atomistic models for amorphous structure of SiC-DC carbon using the HRMC modelling technique. The models were constructed using different modeling strategies involving implementation of various structural constraints and application of different thermal quenching protocols. Structural characterization of the constructed models demonstrates how the modelling parameters influence development of nano-structural features of the carbon models through the process of HRMC simulation. It is shown that implementing multi-stage and multi-constraint algorithms, in which influence of different constraints are accurately adjusted in a controlled process, is essential for successful modelling of amorphous carbon. In this procedure, the main purpose of the first modelling stage is to develop a model which is energetically stable, while at same time mimicking structural features of the experimental sample approximately. On the other

hand, the second modelling stage is mainly designed to improve important structural features of the model such as pore volume by means of extra constraints. We find that application of long simulation runs with slow thermal quench rate is essential for modelling of highly disordered structures. Nevertheless through calculation of the atomic coordination number of the system, it is shown that application of very slow quenching rates can lead to the formation of configurations with graphene-like carbon sheets which have a large fraction of sp^2 carbon. Energy level of such structures are very close to the ground state energy level of perfect graphene, thus lacking the level of disorder required to correctly reproduce experimental adsorption isotherm data. Finally, it is stressed that there is no universal prescription for the choice of the modeling parameters in the HRMC modeling technique, and the use of a systematic trial and error approach remains the most useful option. The choice of modelling parameters can be initially made based on the values used for other carbons in the literature; however, how successful these choices might be strongly depends on the complexity, level of disorder of the target structure, and the number of constraints employed in the simulation. We expect that this finding applies in modeling of similar micro and mesoporous systems (which will require larger unit cell sizes), however one will nevertheless need to adjust the parameters for the new system size, level of disorder, and existence of heteroatoms.

Comparison of the predicted adsorption isotherms with experimental results for different gases shows that simulated isotherms are very sensitive to the choice of pore volume distribution, and the final constructed models must reasonably reproduce the total pore volume, as well as PSD of the experimental sample. Therefore, application of a pore volume-based constraint is highly advisable here.

It is found that existence of the exaggerated first peak in experiment-based PSD of amorphous carbons is an artifact of argon inaccessibility to ultra-micropores. This finding was shown to be supported by PSDs obtained from DFT based on interpretation of CO_2 and H_2 adsorption isotherms, as reported in literature.

Pore accessibility analysis of the constructed models and molecular dynamics simulation studies of gas transport demonstrate that disordered structures obtained from the HRMC method contain short-range structural and diffusional anisotropy, however these models are capable of capturing the long range internal energy barriers of amorphous carbon with very good level of accuracy, at least for some gases.

Overall, comparison of the predicted gas adsorption isotherms in addition to the simulated diffusivities of different gases with experimental results shows that a comprehensive range of experimental data needs to be used during and after the modelling to ensure that the final constructed model is able to capture the properties of the experimental sample that are of interest. It is demonstrated that constructed models may very well reproduce nano-structural features of the experimental sample including pore volume, surface area and pore size distribution, but remain unable to accurately predict equilibrium gas adsorption and transport properties of fluid molecules in the pore network. Therefore, we stress the importance of model validation against experimental data for both gas adsorption and transport properties, which should include comparison of activation energy barriers of the constructed models obtained from simulation with that of uptake-based experiment. This has been hitherto overlooked in structural modeling of amorphous carbon and is proposed for the first time in this paper.

4.7. Acknowledgement

This research has been supported by a grant from the Australian Research Council under the Discovery Scheme, and undertaken with the assistance of the computational resources provided by the NCI National Facility systems at the Australian National University (ANU) through the National Computational Merit Allocation Scheme.

4.8. References

1. Sahimi, M., G.R. Gavalas, and T.T. Tsotsis, *Statistical and continuum models of fluid-solid reactions in porous media.* Chemical Engineering Science, 1990. **45**(6): p. 1443-1502.
2. Bhatia, S.K. and D. Nicholson, *Friction based modeling of multicomponent transport at the nanoscale.* Journal of Chemical Physics, 2008. **129**(16): p. 164709- 164721.
3. Bhatia, S.K. and D. Nicholson, *Modeling Mixture Transport at the Nanoscale: Departure from Existing Paradigms.* Physical Review Letters, 2008. **100**(23): p. 236103.
4. Jepps, O.G., S.K. Bhatia, and D.J. Searles, *Wall Mediated Transport in Confined Spaces: Exact Theory for Low Density.* Physical Review Letters, 2003. **91**(12): p. 126102.
5. Sahimi, M., *Flow and transport in porous media and fractured rock : from classical methods to modern approaches*. 1995, Weinheim, Germany: Wiley-VCH. 482.
6. Kaplow, R., T.A. Rowe, and B.L. Averbach, *Atomic Arrangement in Vitreous Selenium.* Physical Review, 1968. **168**(3): p. 1068-1079.
7. McGreevy, R.L. and L. Pusztai, *Reverse Monte Carlo Simulation: A New Technique for the Determination of Disordered Structures.* Molecular Simulation, 1988. **1**(6): p. 359-367.
8. Opletal, G., et al., *HRMC: Hybrid Reverse Monte Carlo method with silicon and carbon potentials.* Computer Physics Communications, 2008. **178**(10): p. 777-787.
9. Opletal, G., et al., *Hybrid approach for generating realistic amorphous carbon structure using metropolis and reverse Monte Carlo.* Molecular Simulation, 2002. **28**(10-11): p. 927-938.
10. Rigden, J.S. and R.J. Newport, *A Reverse Monte Carlo Modeling Study of Diamond-like Carbon.* Journal of The Electrochemical Society, 1996. **143**(1): p. 292-296.
11. O'Malley, B., I. Snook, and D. McCulloch, *Reverse Monte Carlo analysis of the structure of glassy carbon using electron-microscopy data.* Physical Review B, 1998. **57**(22): p. 14148-14157.
12. Walters, J.K., et al., *Progress in modeling the chemical bonding in tetrahedral amorphous carbon.* Physical Review B, 1998. **58**(13): p. 8267-8276.
13. Thomson, K.T. and K.E. Gubbins, *Modeling Structural Morphology of Microporous Carbons by Reverse Monte Carlo.* Langmuir, 2000. **16**(13): p. 5761-5773.
14. Pikunic, J., et al., *Realistic molecular models for saccharose-based carbons.* Applied Surface Science, 2002. **196**(1–4): p. 98-104.
15. Pikunic, J., et al., *Structural Modeling of Porous Carbons: Constrained Reverse Monte Carlo Method.* Langmuir, 2003. **19**(20): p. 8565-8582.
16. Opletal, G., et al., *The structure of disordered carbon solids studied using a hybrid reverse Monte Carlo algorithm.* Journal of Physics: Condensed Matter, 2005. **17**(17): p. 2605.
17. Jain, S.K., et al., *Molecular Modeling of Porous Carbons Using the Hybrid Reverse Monte Carlo Method.* Langmuir, 2006. **22**(24): p. 9942-9948.
18. Nguyen, T.X., et al., *Structure of saccharose-based carbon and transport of confined fluids: hybrid reverse Monte Carlo reconstruction and simulation studies.* Molecular Simulation, 2006. **32**(7): p. 567-577.
19. Palmer, J.C. and K.E. Gubbins, *Atomistic models for disordered nanoporous carbons using reactive force fields.* Microporous and Mesoporous Materials, 2012. **154**(0): p. 24-37.
20. Palmer, J.C., et al., *Modeling the structural evolution of carbide-derived carbons using quenched molecular dynamics.* Carbon, 2010. **48**(4): p. 1116-1123.
21. Shi, Y., *A mimetic porous carbon model by quench molecular dynamics simulation.* Journal of Chemical Physics, 2008. **128**(23).
22. Tersoff, J., *Empirical Interatomic Potential for Carbon, with Applications to Amorphous Carbon.* Physical Review Letters, 1988. **61**(25): p. 2879-2882.

23. Stephan, U. and M. Haase, *A molecular dynamics study and the electronic properties of amorphous carbon using the Tersoff potential.* Journal of Physics: Condensed Matter, 1993. **5**(49): p. 9157.
24. Lopez, M.J., I. Cabria, and J.A. Alonso, *Simulated porosity and electronic structure of nanoporous carbons.* Journal of Chemical Physics, 2011. **135**(10): p. 104706-9.
25. Nguyen, T.X., et al., *New Method for Atomistic Modeling of the Microstructure of Activated Carbons Using Hybrid Reverse Monte Carlo Simulation.* Langmuir, 2008. **24**(15): p. 7912-7922.
26. Palmer, J.C., et al., *Detailed structural models for activated carbons from molecular simulation.* Carbon, 2009. **47**(12): p. 2904-2913.
27. Farmahini, A.H., G. Opletal, and S.K. Bhatia, *Structural Modelling of Silicon Carbide-Derived Nanoporous Carbon by Hybrid Reverse Monte Carlo Simulation.* Journal of Physical Chemistry C, 2013. **117**(27): p. 14081-14094.
28. Farmahini, A.H., et al., *Influence of Structural Heterogeneity on Diffusion of CH4 and CO2 in Silicon Carbide-Derived Nanoporous Carbon.* Journal of Physical Chemistry C, 2014. **118**(22): p. 11784-11798.
29. Shahtalebi, A., et al., *Slow diffusion of methane in ultra-micropores of silicon carbide-derived carbon.* Carbon, 2014. **77**(0): p. 560-576.
30. Kirkpatrick, S., C.D. Gelatt, and M.P. Vecchi, *Optimization by Simulated Annealing.* Science, 1983. **220**(4598): p. 671-680.
31. Opletal, G., et al., *HRMC_2.0: Hybrid Reverse Monte Carlo method with silicon, carbon and germanium potentials.* Computer Physics Communications, 2013. **184**(8): p. 1946-1957.
32. Brenner, D.W., *Empirical potential for hydrocarbons for use in simulating the chemical vapor deposition of diamond films.* Physical Review B, 1990. **42**(15): p. 9458.
33. Donald, W.B. and et al., *A second-generation reactive empirical bond order (REBO) potential energy expression for hydrocarbons.* Journal of Physics: Condensed Matter, 2002. **14**(4): p. 783.
34. Marks, N.A., *Generalizing the environment-dependent interaction potential for carbon.* Physical Review B, 2000. **63**(3): p. 035401.
35. Nigel, M., *Modelling diamond-like carbon with the environment-dependent interaction potential.* Journal of Physics: Condensed Matter, 2002. **14**(11): p. 2901.
36. Nguyen, T.X., J.S. Bae, and S.K. Bhatia, *Characterization and Adsorption Modeling of Silicon Carbide-Derived Carbons.* Langmuir, 2009. **25**(4): p. 2121-2132.
37. Bonilla, M.R.n., et al., *Heat Treatment-Induced Structural Changes in SiC-Derived Carbons and their Impact on Gas Storage Potential.* Journal of Physical Chemistry C, 2010. **114**(39): p. 16562-16575.
38. Nguyen, T.X. and S.K. Bhatia, *Probing the Pore Wall Structure of Nanoporous Carbons Using Adsorption.* Langmuir, 2004. **20**(9): p. 3532-3535.
39. Talu, O. and A.L. Myers, *Reference potentials for adsorption of helium, argon, methane, and krypton in high-silica zeolites.* Colloids and Surfaces A: Physicochemical and Engineering Aspects, 2001. **187–188**(0): p. 83-93.
40. Sarkisov, L. and A. Harrison, *Computational structure characterisation tools in application to ordered and disordered porous materials.* Molecular Simulation, 2011. **37**(15): p. 1248-1257.
41. Nguyen, T.X. and S.K. Bhatia, *Characterization of accessible and inaccessible pores in microporous carbons by a combination of adsorption and small angle neutron scattering.* Carbon, 2012. **50**(8): p. 3045-3054.

42. Gelb, L.D. and K.E. Gubbins, *Characterization of Porous Glasses: Simulation Models, Adsorption Isotherms, and the Brunauer−Emmett−Teller Analysis Method.* Langmuir, 1998. **14**(8): p. 2097-2111.
43. Gelb, L.D. and K.E. Gubbins, *Pore Size Distributions in Porous Glasses: A Computer Simulation Study*. Langmuir, 1998. **15**(2): p. 305-308.
44. Bhatia, S.K., *Density Functional Theory Analysis of the Influence of Pore Wall Heterogeneity on Adsorption in Carbons.* Langmuir, 2002. **18**(18): p. 6845-6856.
45. Bae, J.-S., T.X. Nguyen, and S.K. Bhatia, *Pore accessibility of Ti3SiC2-derived carbons.* Carbon, 2014. **68**(0): p. 531-541.
46. Nguyen, T.X. and S.K. Bhatia, *Determination of Pore Accessibility in Disordered Nanoporous Materials.* Journal of Physical Chemistry C, 2007. **111**(5): p. 2212-2222.
47. Nguyen, T.X. and S.K. Bhatia, *Kinetic Restriction of Simple Gases in Porous Carbons: Transition-State Theory Study.* Langmuir, 2007. **24**(1): p. 146-154.
48. Nguyen, T.X. and S.K. Bhatia, *Characterization of heat-treated porous carbons using argon adsorption.* Carbon, 2006. **44**(4): p. 646-652.
49. Nguyen, T.X. and S.K. Bhatia, *Characterization of activated carbon fibers using argon adsorption.* Carbon, 2005. **43**(4): p. 775-785.
50. Bae, J.-S., T.X. Nguyen, and S.K. Bhatia, *Influence of Synthesis Conditions and Heat Treatment on the Structure of Ti3SiC2-Derived Carbons.* Journal of Physical Chemistry C, 2009. **114**(2): p. 1046-1056.
51. Nguyen, T.X. and S.K. Bhatia, *Characterization of Pore Wall Heterogeneity in Nanoporous Carbons Using Adsorption: the Slit Pore Model Revisited.* Journal of Physical Chemistry B, 2004. **108**(37): p. 14032-14042.
52. Jagiello, J. and M. Thommes, *Comparison of DFT characterization methods based on N2, Ar, CO2, and H2 adsorption applied to carbons with various pore size distributions.* Carbon, 2004. **42**(7): p. 1227-1232.
53. Plimpton, S., *Fast Parallel Algorithms for Short-Range Molecular Dynamics.* Journal of Computational Physics, 1995. **117**(1): p. 1-19.
54. Hoover, W.G., *Canonical dynamics: Equilibrium phase-space distributions.* Physical Review A, 1985. **31**(3): p. 1695-1697.
55. Martyna, G.J., et al., *Explicit reversible integrators for extended systems dynamics.* Molecular Physics, 1996. **87**(5): p. 1117-1157.
56. Martyna, G.J., M.L. Klein, and M. Tuckerman, *Nosé–Hoover chains: The canonical ensemble via continuous dynamics.* Journal of Chemical Physics, 1992. **97**(4): p. 2635-2643.
57. Kamberaj, H., R.J. Low, and M.P. Neal, *Time reversible and symplectic integrators for molecular dynamics simulations of rigid molecules.* Journal of Chemical Physics, 2005. **122**(22): p. 224114.
58. Feldhoff, A., et al., *Intracrystalline Transport Resistances in Nanoporous Zeolite X.* Chemical Physics and Physical Chemistry, 2009. **10**(14): p. 2429-2433.
59. Jobic, H., et al., *PFG NMR and QENS diffusion study of n-alkane homologues in MFI-type zeolites.* Microporous and Mesoporous Materials, 2006. **90**(1–3): p. 299-306.
60. Jobic, H., *Molecular dynamics of n-pentane in NaX zeolite studied by quasi-elastic neutron scattering.* Physical Chemistry Chemical Physics, 1999. **1**(4): p. 525-530.

5. Influence of Structural Heterogeneity on Diffusion of CH_4 and CO_2 in Silicon Carbide-Derived Nanoporous Carbon

Amir H. Farmahini[†], *Ali Shahtalebi*[†], *Hervé Jobic*[‡] *and Suresh K. Bhatia*[*,†]

J. Phys. Chem. C, 2014, 118 (22), pp 11784–11798

DOI: 10.1021/jp502929k

Accepted: May 8, 2014 - Published: June 5, 2014

[†]School of Chemical Engineering, The University of Queensland, QLD 4072, Australia

[‡]Institut de Recherches sur la Catalyse et l'Environnement de Lyon, CNRS, Université Lyon 1, 2 Ave. Albert Einstein, 69626 Villeurbanne, France

5.1. Abstract

We investigate the influence of structural heterogeneity on the transport properties of simple gases in a Hybrid Reverse Monte Carlo (HRMC) constructed model of Silicon Carbide-Derived Carbon (SiC-DC). The energy landscape of the system is determined based on free energy analysis of the atomistic model. The overall energy barriers of the system for different gases are computed along with important properties such as Henry constant and differential enthalpy of adsorption at infinite dilution, and indicate hydrophobicity of the SiC-DC structure and its affinity for CO_2 and CH_4 adsorption. We also study the effect of molecular geometry, pore structure and energy heterogeneity considering different hopping scenarios for diffusion of CO_2 and CH_4 through ultra-micropores using the Nudged Elastic Band (NEB) method. It is shown that the energy barrier of a hopping molecule is very sensitive to the shape of the pore entry. We provide evidence for the influence of structural heterogeneity on self-diffusivity of methane and carbon dioxide using molecular dynamics simulation, based on a maximum in the variation of self-diffusivity with loading. A comparison of the MD simulation results with self-diffusivities from quasi-elastic neutron scattering (QENS) measurements, and with macroscopic uptake-based low-density transport coefficients, reveals the existence of internal barriers not captured in MD simulation and QENS experiments. Nevertheless, the simulation and macroscopic uptake-based diffusion coefficients agree within a factor of 2-3, indicating that our HRMC model structure captures most of the important energy barriers affecting the transport of CH_4 in the nanostructure of SiC-DC.

Keywords: Self-Diffusion; Hybrid Reverse Monte Carlo Simulation; Activation Energy Barrier; Molecular Dynamics; Nudged Elastic Band; Quasi-elastic neutron scattering.

5.2. Introduction

Understanding transport properties of fluid molecules in microporous materials is of great importance due to intriguing features of fluidic phenomena at the nano-scale [1-3]. Many industrial and scientific applications such as gas storage and separation, petroleum refining, electrochemical energy storage, nanofluidics and materials screening require fundamental understanding of fluid properties in confined spaces. In recent years, there has been rapid development of a variety of new microporous materials such as Carbide Derived Carbons (CDC) [4-7], carbon nanotubes [8, 9] and Metal-Organic Frameworks (MOF) [10-13], leading to interest in the complexity of the fluid dynamics in such nano-structures [1-3, 14-17]. Nevertheless, the transport properties of fluid molecules in such tight confinements are not very well understood. Established approaches such as the dusty gas model (DGM) [18] or Knudsen model have limited applications in nanoscale confinements [19, 20], while Maxwell-Stefan type models [21, 22] disregard effect of fluid inhomogeneities in mixture adsorptions [23] and more rigorous models based on the Boltzman equation rely on approximations [24] that may not be accurate in narrow nanopores [15]. On the other hand, molecular dynamics simulation can in principle provide exact results for prediction of fluid properties in confined spaces based on the potential models used to corroborate theoretical models. Nevertheless, this type of simulation can potentially suffer from inadequacy of the force field used, lack of a realistic adsorbent model and requirement of large computational resources for capturing slow diffusion processes. This is particularly true in the case of disordered microporous materials, where diffusion of gas molecules takes place at considerably slow rates. The use of realistic structures is, however, now within reach, with the development of the hybrid reverse Monte Carlo (HRMC) simulation method [25-31].

There are relatively few diffusion studies based on realistic disordered adsorbent models in the literature. Notable among these is the work of Moore el al. who studied diffusion of argon in a disordered BPL carbon model [26] and those reported earlier by Gubbins and co-workers [27, 28, 30, 32] on diffusion of argon and nitrogen in structural model of saccharose based porous carbons, as well as a more recent study conducted by Nguyen and Bhatia on anomalies of water self-diffusion in the disordered structure of activated carbon [33]. A key advance achieved by using realistically constructed models of disordered materials – as opposed to idealised slit pore or crystalline models – for diffusion studies of fluid molecules is to address the significant influence of

surface and structural heterogeneity on transport properties of adsorbed molecules. The effect of energy distribution arising from the micropore size distribution is already shown to be the source of system heterogeneity in activated carbon materials [34, 35]. Moreover, the surface roughness of the adsorbent is known to have influence on surface diffusion of microporous solids [36]. Both of these features, i.e. surface roughness and micropore size distribution have been found to exist in the amorphous structure of silicon carbide derived carbon (SiC-DC) [25][1], and may be expected to be inherent to carbide-derived carbons in general. It is therefore important that effects of structural heterogeneities on transport properties of fluid molecules be examined in new studies of this class of adsorbents. In very narrow pores frictional resistance arises from both intermolecular and wall-molecule collisions, with the wall-fluid events dominating transport of adsorbate molecules [3, 23]. However, due to lattice abnormalities including surface roughness and corrugation of pore walls, existence of dead-ends and bottle necks, as well as other structural defects in disordered microporous materials, fluid molecules experience a very heterogeneous potential energy surface (PES) and a variety of different energy barriers along their diffusion paths within the solid matrix. Therefore, investigation of structural heterogeneity, and the significance of the associated energy barriers is critical to the understanding of fluid transport in microporous materials.

Here, we use an experimentally validated atomistic model of disordered microporous SiC-DC developed in this laboratory [25], to perform lengthy molecular dynamics simulations and to determine self-diffusivities of different gases over a broad range of loadings at various temperatures. The results are important to the understanding of transport properties of industrially important gases including carbon dioxide and methane in the disordered structure of SiC-DC, suggested to be promising for adsorption and gas storage applications due to its narrow pore size distribution and high pore volume [25, 37, 38]. We investigate the effect of structural heterogeneity on the internal resistances to the diffusion of methane and carbon dioxide in the microporous structure of SiC-DC, comparing the results from MD simulation with experimental measurements of gas diffusion using both microscopic quasi elastic neutron scattering (QENS) and macroscopic volumetric adsorption methods. We also investigate heterogeneity of the energy landscape in our carbon model, which is an important consequence of structural disorder and internal resistances, impacting diffusion rates and molecular accessibility in the system [39, 40]. In addition to the use of molecular dynamics simulation and experimental methods for calculation of molecular diffusion, we analyze the free energy landscape of the system based on the computational method of Sarkisov

[1] Reference 25 forms Chapter 3 of this thesis.

[41, 42] to provide more insights into structural heterogeneity and internal constrictions in the SiC-DC carbon, which have rate limiting effects on gas diffusion. We also employ the Nudged-Elastic Band (NEB) technique [43-45] to case study anomalies of molecular transition through ultra-narrow pores.

5.3. Computational details

We have employed an atomistic model of silicon carbide-derived carbon, developed in our laboratory [25], based on experimental structure factor data obtained from neutron scattering using 50 nm particle size SiC-derived carbon, using the Hybrid Reverse Monte Carlo modeling technique [31, 46, 47]. The model (illustrated in Figure 5-1(a-c)) provides the spatial positions of 3052 carbon atoms in a 40 Å cubic simulation cell representing the disordered structure of SiC-DC. Details of the modeling technique, as well as validation procedure of the HRMC constructed model is discussed in our recent publication [25] and Chapter 3 of this thesis.

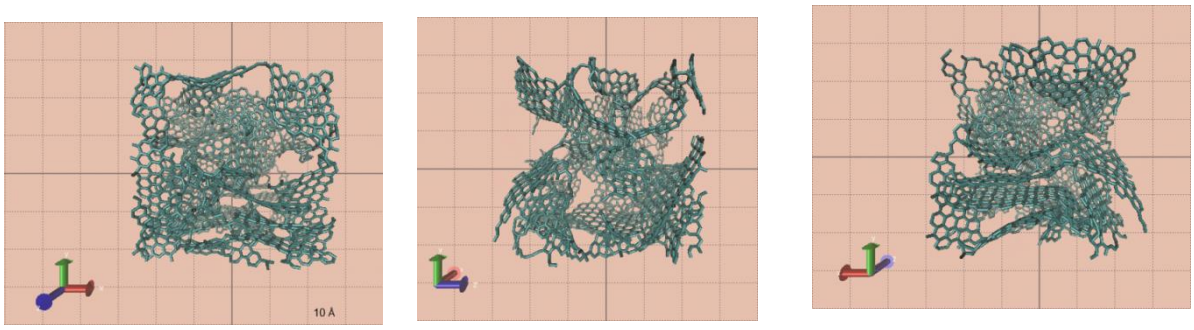

(a) **(b)** **(c)**

Figure 5-1. Illustration of atomistic structure of HRMC constructed model of SiC-DC

This model provides a solid matrix with topology and morphology consistent with that of the experimental sample and has been used for the entire simulations reported in this paper. All simulations performed for this study have made use of all-atom molecular models and force field parameters, detailed in the supporting information, as well as our recent work on HRMC modelling of SiC-DC structure [25].

5.3.1. Free Energy Landscape of Disordered System

Investigation of the energy landscape of a microporous system is crucial for understanding fluid transport properties in this class of materials. In very narrow pores, frictional resistance arises from

both intermolecular and wall-molecule collisions, however due to tight confinement, diffusion of fluid molecules is predominantly affected by wall-fluid interactions [3]. Under this condition, significantly narrow pores provide highly energetic adsorption sites, which can potentially act as restrictive energy barriers during fluid diffusion. Distribution of such barriers is dictated by steric restrictions of the system associated with geometry and interconnectivity of its pore network. Hitherto, different computational methods have been employed to elucidate transport properties and diffusion behavior of fluid molecules in a variety of Zeolites and MOFs, based on determination of the local or overall energy landscape of the system [39, 41, 48-51], nevertheless this type of calculations is overwhelmingly limited to non-carbonaceous materials. Here, we have employed the Helmholtz free energy analysis method of Sarkisov [41, 42] to determine energy heterogeneity of the disordered SiC-DC carbon and to estimate important properties such as overall energy barriers of the system for different adsorbate molecules, as well as their Henry constant at infinite dilution. This method is a direct extension of the method developed earlier by Haldoupis, et al., which performs its calculation based on determination of potential energy surface rather than Helmholtz free energy of binding [52].

Assuming the simulation is performed at infinite dilution, atomic interactions are reduced to solid-fluid interactions. Under such conditions, one can relate the Henry constant with "the Helmholtz free energy changes associated with transferring a single molecule of adsorbate from the ideal gas system of volume V_s to a sample of porous structure of the same volume", as described by Sarkisov [42].

$$\begin{aligned} -RTln(RT\rho_s K_H) &= -RTlnZ_s(1,T,V_s) + RTlnZ_{i.g.}(1,T,V_s) \\ &= A_s(1,T,V_s) - A_{i.g.}(1,T,V_s) \end{aligned} \tag{5-1}$$

In this equation R and T are gas constant and temperature, ρ_s is the density of porous solid, K_H is the Henry constant, A is the Helmholtz free energy of binding and Z is the configurational integral of a single adsorbate molecule in the porous structure, while *s* and *i.g.* subscripts stand for solid and ideal gas states. The configurational integral Z_s follows [42]

$$Z_s(1,T,V_s) = \iint e^{-U_s(\theta,r)/kT} d\theta . dr \tag{5-2}$$

where, k is the Boltzmann's constant and U_s is the interaction potential energy between a fluid molecule and the solid structure. The integral is over all possible orientations and positions of the

center of mass of the molecule within the adsorbent matrix. In practice, the simulation cell is divided into a large number of cubelets and the configurational integral is calculated for each cubelet. If the cubelet is small enough, the calculation is reduced to an integration taken solely over orientational configurations of the molecule. We have used 0.5 Å size cubelets to construct the grid network for calculation of free energy. The calculation is performed at every cubelet allowing us to obtain the free energy map of the solid structure. This approach also facilitates calculation of local properties such as local Henry constant or selectivity at different parts of the adsorbent model. To construct a plausible percolation path based on the energy map obtained from computation of free energy of bindings at every individual cubelet (A_i), we need to seek the threshold energy, at which one single molecule can traverse the system. This is in fact a combination of percolation path analysis [53] and free energy calculation. For a molecule travelling from one side of the simulation cell to the other side through a pattern of interlaced cubelets, interaction energies vary at every different spots. Thus, an estimation of "limiting free energy barrier" can be obtained from difference of the energy of the most attractive site along this path with the "percolating free energy threshold" explained above [41, 42].

5.3.2. Nudged-Elastic Band (NEB) Calculations

A central problem in diffusion studies of adsorbate molecules through confined spaces is estimation of transition rate (hopping rate) between two sides of an energy barrier within harmonic approximation of the transition state theory (hTST) [54, 55]. This cannot be achieved unless the activation energy barrier of the system is already known, following [56]

$$k^{hTST} = \frac{\pi_i^{3N}.\nu_i^{init}}{\pi_i^{3N-1}.\nu_i^{sdl}} \times e^{-(E^{sdl}-E^{init})/k_BT} \qquad (5\text{-}3)$$

where $k^{hTST}$is the transition rate constant, $E^{sdl}$is the energy of the saddle point, $E^{init}$is the local potential energy minimum corresponding to the initial state and $\nu_i$are the corresponding normal mode frequencies. The determination of the potential energy maximum (E^{sdl}) along the Minimum Energy Path (MEP) - the lowest energy pathway between two stable configurations - is important for calculation of transition rates of rare events. It also provides interesting information on magnitude of local energy barriers, as well as roughness and heterogeneity of the transition pathway.

Several computational techniques have been developed to accurately determine the activation energy barrier of a system or, in other words, to determine the highest saddle points along the MEP

[45, 57]. One of the most promising approaches is the so-called Nudged Elastic Band (NEB) technique, a class of "chain of states" methods, in which a chain of several connected intermediate states are defined between two end points of a transition path, which are located at two local minima of the potential energy surface (PES). Spring interactions are imposed between neighboring images to generate a continuous path. These intermediate replica are then simultaneously optimized during simulation in such a way that the forces acting on the replica are minimized [45]. This algorithm employs a "force projection" or "nudging" feature to guarantee no competition between "true forces" and "spring forces", as explained by Henkelman and Jonsson [55]. Although the NEB method is able to properly estimate position and magnitude of the saddle point between two given initial and final stable configurations, the method is likely to fail in search for the highest saddle point along MEP, considering there might be several minima and saddle points due to heterogeneity of the energy surface. As emphasized by Henkelman and co-workers [56], in order for the NEB method to find the highest saddle point, it is essential to have an accurate estimate of the shape of the MEP. To address this issue, they have slightly modified the NEB algorithm, so that after regular NEB has converged to its MEP, the image with highest energy is selected to climb up to the top of the barrier in such a way that "the climbing image moves up the potential energy surface along the elastic band and down the potential surface perpendicular to the band" [56].

In this work, transition path and saddle-points of two ultra-narrow pore entries in the rigid HRMC constructed model of SiC-DC have been investigated using implementation of NEB in LAMMPS (Large-scale Atomic/Molecular Massively Parallel Simulator) package [58] based on the discussion and improvements of the algorithm by Henkelman et al. [56], Henkelman and Jonsson [55] and Nakano [59]. The minimization procedure has been performed using the "*fire*" style damped dynamics method, as described by Bitzek et al. [60] and implemented in LAMMPS. Except initial configurations of initial and final replica at the two ends of the transition path, which are explicitly defined, initial configurations of the intermediate replica are linearly interpolated between the first and the last replica. The initial configurations of the initial and final replica at the two ends of the transition path, in addition to the configurations of non-NEB fluid molecules have been obtained using Grand Canonical Monte Carlo (GCMC) simulation. The non-NEB fluid molecules have been considered as fixed molecular bodies merely to provide an appropriate background force field for the NEB molecule, while it crosses the barrier.

5.3.3. Molecular Dynamics Simulation

We have performed Equilibrium Molecular Dynamics (EMD) simulations for CO_2 at CH_4 in a periodic system of SiC-DC model over a wide range of loadings at 323 K, 600 K and 1000 K using LAMMPS simulation package [58]. The simulations were performed in the canonical (NVT) ensemble, in which translational and rotational degrees of freedom of rigid bodies were both thermostated using the Nose-Hoover algorithm with chains, as originally described by Hoover [61] and Martyna et al. [62, 63]; the rigid-body algorithm for NVT integration is explained elsewhere [64]. A Verlet time integrator was used with time step equal to 1 fs. Short term intermolecular interactions were modeled using the 12-6 Lennard-Jones potential with a cut-off distance of 18 Å. The standard Ewald formalism was employed for electrostatic interactions with cut-off distance of 18 Å in such a way that pairwise interactions within this distance were computed directly and those outside this distance were calculated in reciprocal space. This way the cut-off distance became effectively infinite. Depending on the loading, MD simulations were run for 30 ns in average in the production phase so that displacement of the center of mass of the molecules was a multiple of the simulation cell dimension.

To calculate self-diffusivity of CO_2 and CH_4, mean-squared displacements (MSDs) of the center of mass of the molecules were collected in the Fickian regime, in which log-log dependence of MSD with time is linear. Self-diffusivity was then obtained using the well-known Einstein equation:

$$D_s = \frac{1}{2Nd} \lim_{t \to \infty} \frac{1}{t} \langle \sum_{i=1}^{N} |r_i(t) - r_i(0)|^2 \rangle \tag{5-4}$$

where $r_i(t)$ is the center of mass position vector of molecule i at time t, N is the number of molecules and d is dimensionality of the system. From the self-diffusion coefficients obtained at various temperatures, we have also estimated the Arrhenius activation energy following

$$D = D_0 . e^{[-\frac{E_a}{RT}]} \tag{5-5}$$

where, D and D_0 are diffusivity and temperature-independent pre-exponential factor respectively.

5.4. Results and discussion

5.4.1. Free Energy Analysis of Disordered SiC-DC

As briefly discussed in the previous section, the free energy landscape of a disordered system can be obtained at certain temperatures through calculation of the free energy of binding of a guest

molecule inserted in every cubelet of a fine grid network, superimposed on a three dimensional atomistic model of the adsorbent structure. The most useful information that can be extracted from this type of calculation is the percolating free energy threshold and limiting free energy barrier of diffusing molecules. This information is summarized in Table 5-1 for different adsorbate molecules in the HRMC constructed model of SiC-DC at 300 K.

Table 5-1. Characterization of percolation path based on analysis of the free energy of binding at infinite dilution and 300 K

Adsorbate	Minimum free energy (kJ/mol)	Percolating free energy threshold (kJ/mol)	Limiting free energy barrier (kJ/mol)
Argon	-27.31	-10.83	16.47
CO_2	-38.83	-17.12	21.71
CH_4	-33.50	-13.76	19.73
H_2O[2]	-20.17	-8.10	12.07

As presented in this table, methane and carbon dioxide are the most favorable adsorbates. These two molecules also experience the highest limiting free energy barrier, when traversing the system. Information given in Table 5-1 is visualized in Figure 5-2 (a) for CO_2 and Figure 5-2 (b) for CH_4, where the percolation paths of adsorbate molecules are compared with most energetically favorable pore-spaces (areas with free energy of binding between -40 kJ/mol and -20 kJ/mol).

Figure 5-2. Percolation path of (a) CO_2 and (b) CH_4 compared to high energy pore-spaces at 300 K. Dotted blue area represents percolation path of each molecule, while solid volumes (red or gold) refer to the high energy pore spaces

[2] SPC/E water model has been used for water in this calculation.

As illustrated here, the most favorable pore spaces are widely scattered across the system and do not span a continuous percolation path. This implies that molecules adsorbed in these regions, cannot easily leave the cavity to diffuse through the system unless they overcome the corresponding activation energy barriers for diffusion. Based on the information obtained from analysis of free energy landscape of the system, the position and strength of most favorable and unfavorable pore spaces for the adsorption of a particular molecule can be identified. This information can be linked to the geometry of the pore space to provide further insight on the adsorption behavior of fluid molecules in confined spaces. Figure 5-3 (a) – (c) visualize repulsive and attractive pore spaces for a CO_2 probe molecule across the model based on free energy of binding at 300 K.

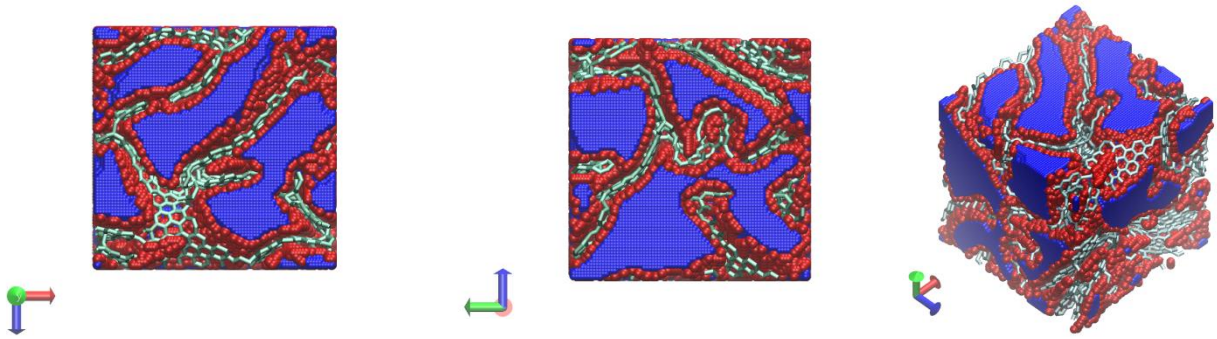

(a) **(b)** **(c)**

Figure 5-3. Visualization of repulsive and attractive pore spaces for CO_2 at 300 K, with the red volumes representing repulsive area (having free energy of binding between +1000 to +1766.8 kJ/mol), and the blue volumes representing pore spaces with negative free energy of binding (attractive interactions)

As depicted here, visual observation reveals that repulsive regions (pore spaces with very high positive energy values) consist of either extremely confined spaces inside highly narrow pores or the areas which are very close to the pore walls. On the contrary, attractive regions, which can favorably accommodate guest molecules, mainly occupy the inner part of the pore spaces.

We note here that our analysis has considered a rigid structure, neglecting the effect of vibrations. In the literature there have been conflicting views on the extent of difference on transport properties due to the flexibility of the host lattice. For example, Jakobtorweihen et al. [65, 66] report some reduction of the low-density transport coefficient for CH_4 and C_2H_6 in a carbon nanotube when vibrations are considered through a boundary thermostat, with only small reduction in the value at

high densities. In contrast, Bernardi et al. [67] in their study of couette flow, find that the use of a boundary thermostat leads to larger slip at the wall in comparison to the rigid wall. While not considered here, the effect of such vibrations will be investigated in subsequent studies.

According to the correlation between free energy of binding and the Henry constant given by equation (5-1), the free energy map of the system can also provide useful information on affinity of adosorbate molecules towards disordered carbon structure at infinite dilution. This information can be calculated from the Henry constant of the molecule or from interpretation of differential heat of adsorption, following [42, 68, 69]

$$\Delta\bar{H} = -R\left[\frac{\partial \ln(K_H)}{\partial(\frac{1}{T})}\right]_n \tag{5-6}$$

where ΔH is differential enthalpy of adsorption and n denotes adsorbed quantity. Values of the Henry constant for different adsorbate molecules, as well as corresponding differential heat of adsorption are summarized in Table 5-2.

Table 5-2. Henry constant and differential heat of adsorption for different adsorbate molecules

	Temperature (K)	**K_H (mol/kg.bar), equation (5-1)**	**K_H (mol/kg.bar), GCMC**	**ΔH (kJ/mol), equation (5-6)**	**ΔH (kJ/mol), equation (5-7)**
Ar					
	100	94.92×10^6	31.04×10^6	-26.86	-20.28
	200	26.07	14.45	-24.52	-19.85
	300	0.64	0.45	-18.07	-15.95
	600	0.03	0.03	-14.82	-14.76
CO_2					
	273	65.64	41.02	-38.12	-34.00
	300	16.89	10.71	-33.41	-31.66
	600	0.07	0.058	-25.93	-22.46
	1000	0.01	0.01	-21.20	-22.36
CH_4					
	300	2.70	1.84	-26.07	-22.63
	600	0.05	0.04	-19.59	- 18.41
	1000	0.01	0.01	-17.92	-19.82
H_2O					
	300	0.17	0.15	-10.93	-11.30
	600	0.02	0.02	-10.60	- - -
	1000	0.01	0.01	-11.79	- - -

In this table, we compare the Henry constant and differential heat of adsorption obtained from free energy analysis of the system with the Henry constant and isosteric heat of adsorption calculated from the Widom insertion method [70] and GCMC simulation at infinite dilution. Figure 5-4 illustrates the variation of the Henry constant obtained from analysis of free energy of the system (equation (5-1)) with respect to the reciprocal temperature showing the temperature dependence of this property.

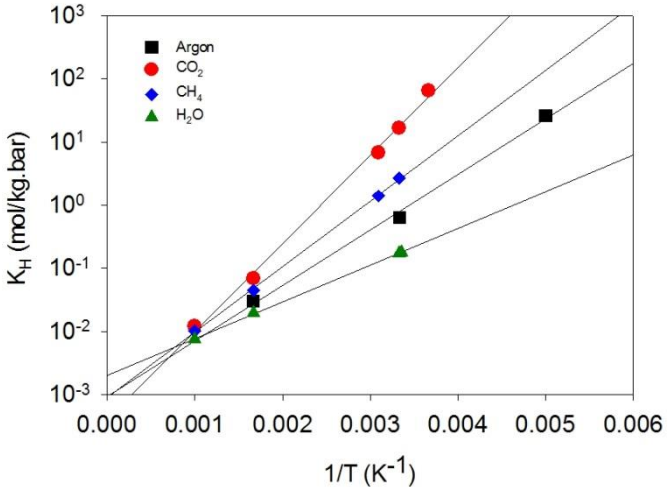

Figure 5-4. Variation of the Henry constant with reciprocal temperature for different adsorbate molecules

Affinities of different adsorbate molecules for the adsorbent structure can be inferred from this plot. As depicted here, carbon dioxide and methane possess the highest affinity for adsorption in the disordered structure of SiC-DC, as the logarithm of their Henry constants is distinctly larger than those of argon and water at the same temperature. It is important to note that CH_4 has a smaller limiting free energy barrier compared to CO_2 despite its somewhat larger geometry. Moreover, adsorption of this molecule over different temperatures is less exothermic compared to carbon dioxide, indicative of lower affinity. These two properties together can potentially facilitate higher mobility of CH_4 compared to CO_2. This is shown to be true in the following sections; where the self-diffusivity of the two adsorbate molecules is calculated using MD simulation. The lowest affinity (the least exothermic adsorption process) according to Figure 5-4 belongs to water. This information in addition to the fact that minimum free energy of binding for water is much higher than other molecules across the system (given in Table 5-1) is an indication of hydrophobicity of the microporous structure of SiC-DC, which is consistently reported in the literature for similar carbonaceous materials [71-74].

5.4.2. Local Energy Barriers and Transition Path

In this section, transition path and position of local saddle points for two nominated pore entries have been studied, solely to demonstrate how heterogeneity of pore structure, as well as molecular geometry can dictate different scenarios for diffusion path of a single molecule independent of its kinetic energy. This information can be used to calculate the local potential energy barrier at each pore entry, as opposed to the overall energy barrier of the system obtained from analysis of the free energy landscape. The former is a local potential energy barrier that an individual adsorbate molecule has to overcome, when it tries to cross a chosen pore entry, although the latter is an estimation of overall free energy barrier that a molecule experience, while traversing the simulation cell from one side to the other. The method for calculation of local energy barrier is the Nudged Elastic Band (NEB) technique, as explained earlier in this paper. Two ultra-narrow pore entries (named Pore entry A and B) were selected for this calculation. Each pore entry provides a limited access to the cavity behind it through a narrow window, as illustrated in Figure 5-5.

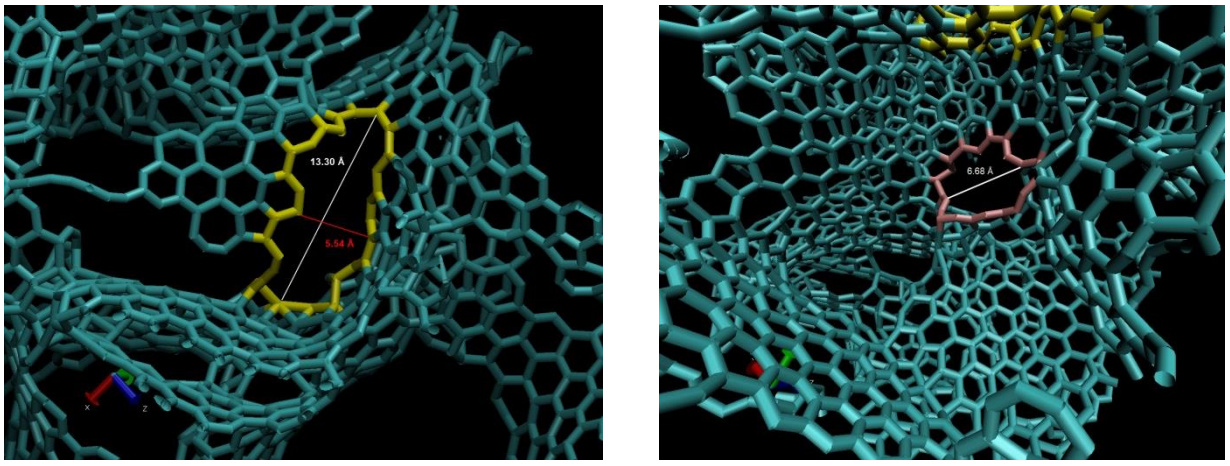

(a) **(b)**

Figure 5-5. Geometry of the pore entry A (a) and B (b) selected for NEB calculations

Pore entry A (Figure 5-5(a)) is a 13.30 Å long and 5.54 Å wide window (center to center distance). Pore entry B (Figure 5-5 (b)) however, has almost a circular geometry with an average diameter of 7.0 Å. To ensure that initial configurations of the transiting molecules are closely located to the mean energy pathway at two ends of the transition path, Grand Canonical Monte Carlo (GCMC) simulation were used at similar thermodynamic conditions (~8.2 mmol/g solid and 323 K) for both CO_2 and CH_4 molecules. The same temperature and pressure were applied to obtain positions of the non-NEB (background) molecules. During the NEB calculation, framework and background

molecules were held fixed and only one NEB molecule at a time was allowed to move. Figure 5-6 depicts energy profiles of individual CO_2 and CH_4 molecules hopping through pore entries A and B.

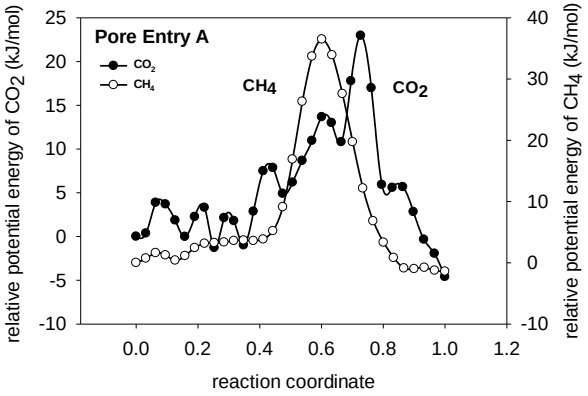

(a)

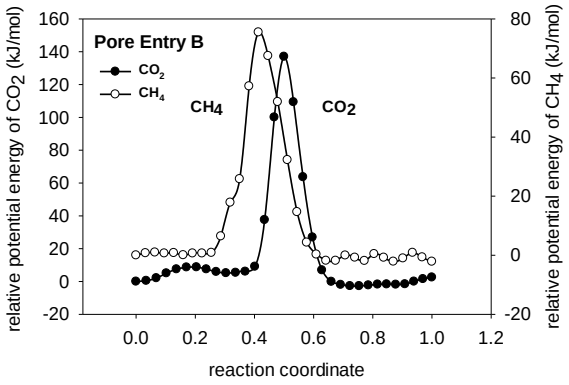

(b)

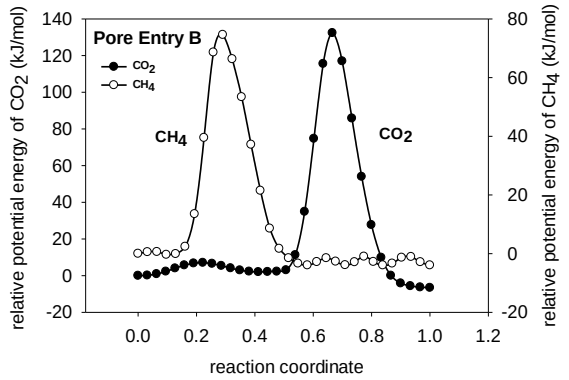

(c)

Figure 5-6. Transition energy profile of CO_2 and CH_4 for Pore entry A and B under the effect of background molecules (a-b), as well as Pore entry B without any background molecule (c)

The potential energy in this figure is relative to the potential energy of the NEB molecule at the start of its transition path. Here, we note that for the non-circular pore entry A, the energy profile of the methane molecule is very smooth compared to that of carbon dioxide, showing only one maximum (Figure 5-6 (a)). This is due to different molecular geometries of CO_2 and CH_4. As indicated earlier a molecule can face multiple saddle-points along its transition path, which is the case for CO_2 here. As a linear molecule, CO_2 is able to adjust itself according to the geometry of the pore mouth by rotating around its symmetry axis, while hopping through the window. This is shown in Figure 5-7, as well as a movie provided in the supporting document of this paper.

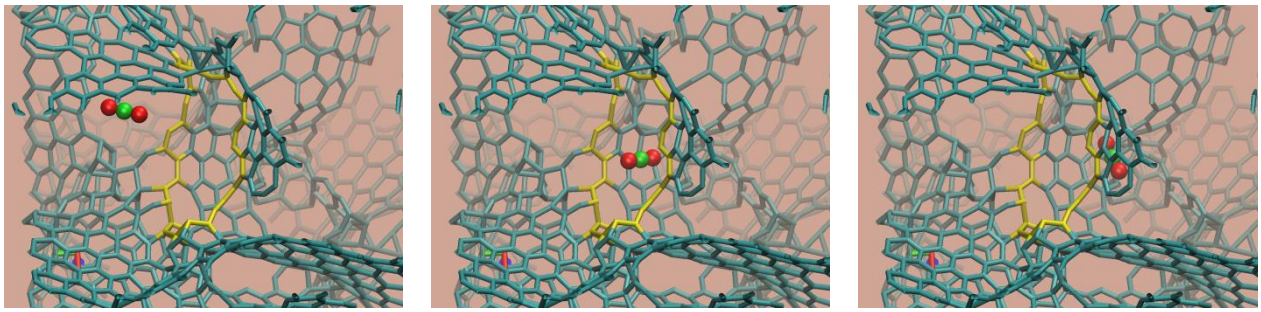

(a) **(b)** **(c)**

Figure 5-7. Transition of CO_2 molecule through pore entry A at reaction coordinate (a) 0, (b) 0.73 and (c) 1. Snapshot (b) illustrates orientation of the linear molecule around its symmetry axis at the highest saddle-point, in order to adjust itself with the limiting geometry of the pore mouth

As shown here, the O-C-O angle is nearly parallel to the pore entry cross-section at the starting and final points of the transition path (Figure 5-7 (a) and (c) respectively), while its orientation is perpendicular to the pore entry at the pore mouth (Figure 5-7 (b)). Such adjusting rotations help the molecule to find a pathway with the smallest energy barrier, which in this case is obtained when the orientation of CO_2 is perpendicular to the pore mouth, as illustrated in the snapshot in Figure 5-7(b). In comparison, the spherical geometry of methane makes no difference among different possible orientational configurations of this molecule, thus leading a less noisy energy profile. A similar comparison for pore entry B is even more insightful (Figure 5-6 (b)). In this case, not only CH_4 holds a smooth diffusion energy profile, but CO_2 also shows analogous behavior. Such similarity can be explained based on circular geometry of pore entry B, so that orientational movements of

CO_2 cause limited differences in the interaction potential energy of the molecule with its surrounding pore wall atoms.

Figure 5-6 reveals further information on the effect of structural heterogeneity on the dynamics of fluid molecules in confined spaces. The local energy barrier for CH_4 is larger than that of CO_2 in pore entry A (Figure 5-6 (a)), as may be expected from the larger molecular size of methane. However, our NEB simulations indicate that this may not be the only possible scenario. According to the energy profiles of CH_4 and CO_2 in pore entry B, CO_2 may experience a larger energy barrier despite its smaller and more adjustable molecular geometry (Figure 5-6 (b)). This suggests the importance of structural heterogeneity more directly. Considering CO_2 adsorbs stronger (compared to CH_4) due to its higher potential strength, a larger repulsive energy will be imposed on the molecule in ultra-narrow pores, where atoms interact over distances smaller than their equilibrium distance, as for pore entry B. Similarly, when CO_2 molecule is inside the cavity and outside the pore mouth, it will be attracted more strongly by the surrounding solid atoms, thus having a lower level of energy compared to CH_4. Consequently, a higher energy barrier for CO_2 molecule is expected, since the difference between energy levels of the molecule inside the cavity and at the pore entry is larger. However, in pore entry A, where the pore mouth is larger, CO_2 will face a less severe repulsive barrier.

Here, it is also important to study effect of the fluid-fluid interaction on the energy barrier. We have repeated our NEB calculations for pore entry B in the absence of background fluid molecules (Figure 5-6 (c)). This way, we have been able to solely investigate interactions of the solid structure with a single NEB molecule without any interruption from surrounding sources. The result signifies no dramatic change in magnitude of the energy barrier, as well as shape of the energy profile, although saddle-points are seen to be slightly shifted along the reaction coordinate axis, as illustrated in Figure 5-6 (c). According to this figure, CO_2 still has to overcome a larger energy barrier compared to CH_4, due to its higher potential strength and tight geometry of the pore entry as postulated above. Consequently, it is evident that in the limit of narrow pores, the magnitude of the energy barrier is largely dictated by the solid atoms at the pore mouth and the effect of fluid-fluid interactions is insignificant.

Our finding of the possibility of CO_2 molecules being hindered more severely by ultra-micropores, together with other evidence from analysis of the limiting free energy barrier at infinite dilution, discussed in the previous section, provides a basic explanation for the question that "why CH_4 can

diffuse faster compared to CO_2 in microporous materials" [75-77], especially since existence of such ultra-micropores has been theoretically and experimentally confirmed in this class of materials [25, 78, 79]. Higher mobility of CH_4 in the microporous structure of SiC-DC is demonstrated in the subsequent section of the current paper, based on the diffusivity results obtained from molecular dynamics simulation. Nevertheless, the implication of our NEB results on this issue should be considered inadequate for a definite conclusion, and need to be further investigated using methods such as Transition Path Sampling (TPS) to obtain hopping rates of the fluid molecules at the pore entry, taking into account effect of entropy on molecular diffusion.

In summary, our NEB simulations indicate that transition behavior of fluid particles including shape of the energy profile, as well as quantity and magnitude of saddle points are very sensitive to the heterogeneity of the pore structure, arrangement of the neighboring atoms, molecular geometry and energetic characteristic of the fluid molecule, among which heterogeneity of the pore structure plays a significant role.

5.4.3. Molecular Diffusion

To investigate dynamics of CO_2 and CH_4 in the disordered structure of SiC-DC, the loading and temperature dependence of self-diffusivities of these gases have been studied by tracing spatial positions of molecular configurations over time trajectories from multiple MD simulations. Starting from initial configurations obtained using GCMC, MD simulations were performed at 323 K, 600 K and 1000 K and self-diffusion coefficients were determined using equation (5-4). The results for the self-diffusivity of CO_2 and CH_4 at these temperatures are shown in Figure 5-8 and Figure 5-9 respectively. Standard deviation of the reported diffusion coefficients is 16% on average so that the error at the highest loading is 11%, while it increases to 20% at low loading.

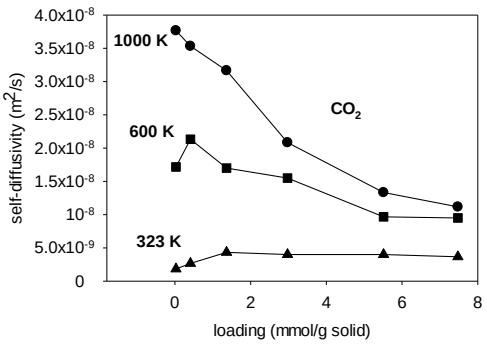

Figure 5-8. Loading dependence of self-diffusivity of CO_2 at three different temperatures

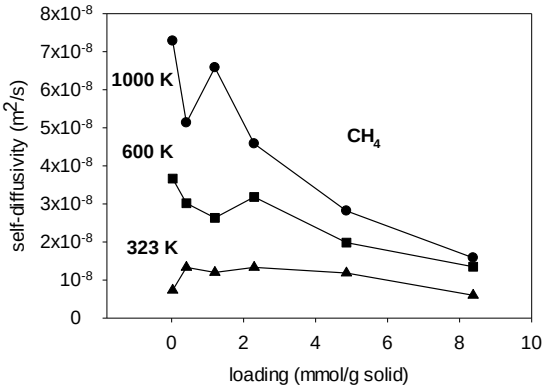

Figure 5-9. Loading dependence of self-diffusivity of CH_4 at three different temperatures

It is known that Fickian diffusion behavior of gases can be only detected in long time runs, when molecules have escaped their initial local environment and traversed the entire lattice length [26, 80]. This is associated with the "residence time", which is the time a particle is moving around inside a "cage-like" confinement before it can leave the cage to the next repeating part of the simulation cell [80]. At very short time scales, on which intermolecular collisions are negligible, molecules are in the ballistic (free-flight) regime with a quadratic time dependence [26, 80]. This regime is hard to detect in microporous materials, requiring MD simulation to be run at very small time steps. This is because of extremely limited spaces, which is available to fluid molecules inside the micropores, so that molecular collisions occur shortly after simulation starts.

An "intermediate regime" is also detectable in nanoporous materials, where fluid molecules start colliding with each other, as well as with the pore wall in a local neighborhood [80]. At longer time steps, fluid molecules experience either a sub-diffusive or a fully diffusive regime depending on the pore size and the level of confinement. A sub-diffusive regime occurs when molecular diffusion is dominated by the confinement effect of a small pore space or by the traffic of molecules passing through a narrow window at high pressures [26]. A slope of 0.5 - 1 is usually measurable on logarithmic coordinates for a single-file sub-diffusive regime, in which the molecules are unable to pass each other [81-83]. However, when molecules enter the diffusive (Fickian) regime, the slope will approach unity. Due to the highly heterogeneous structure of amorphous carbon in the SiC-DC model, lengthy MD simulations were performed to ensure the required residence time is met and the adsorbate molecules have explored the entire lattice length. Moreover, since the Fickian diffusion is at the focus of this study, the calculation of self-diffusivity has been performed in the region in which MSD is linearly related to the simulation time. Hence, MD trajectories were only collected after 1 ps of the simulation time in the production phase to avoid non-linearity, as well as other anomalies associated with the ballistic and intermediate regimes. Nevertheless, as an exception to

this convention, Figure 5-10 depicts the time dependence of the mean square displacement for CO_2 and CH_4 molecules after 0.1 ps of the simulation time at 323 K for both infinite dilution and ~8.0 mmol/g loading.

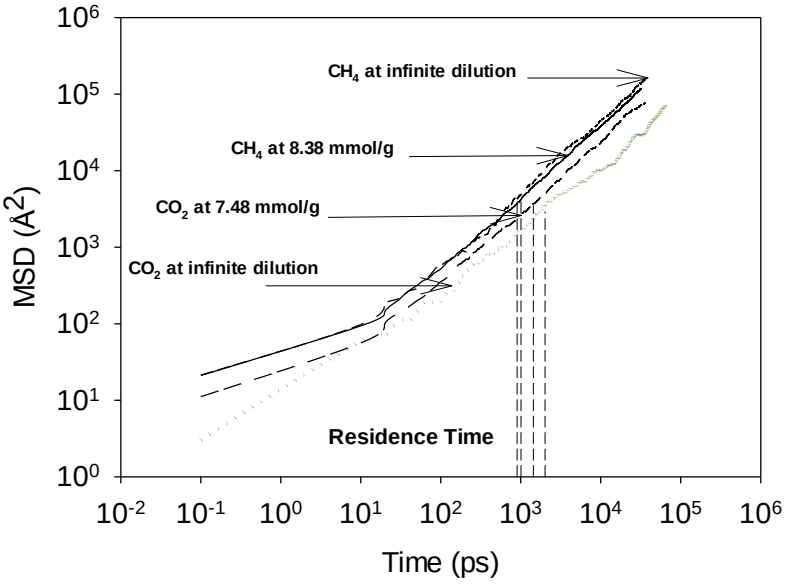

Figure 5-10. Mean-squared displacement of CH_4 and CO_2 as a function of simulation time at 323 K, infinite dilution and ~8.0 mmol/g loading

As illustrated here, a sub-diffusive regime is observed at the beginning of the simulation before the slope of the MSD approaches unity. This has been constantly observed for both gases in this study, indicating the effect of confinement in the microporous structure of SiC-DC. At low loading, tight confinement of small pores dictates the sub-diffusive regime; however occurrence of this phenomenon at higher pressures suggests strong effect of pore confinement in addition to the tight molecular packing after start of the pore filling at intermediate loadings [26].

Our simulation reveals non-monotonic behavior of molecular diffusion with a maximum in the loading dependence of the diffusion coefficient, as shown in Figure 5-8 and Figure 5-9. This behavior is similar to diffusion of argon in disordered bituminous coal-based BPL carbon and ordered carbon replica of Faujasite Zeolite (C-FAU) studied by Gubbins and co-workers [26]. Self-diffusion coefficients of both methane and carbon dioxide are smaller at infinite dilution of lower temperatures; however they increase at slightly higher loadings showing a maximum at intermediate densities. With further increase in the loading the self-diffusivity decreases again. Experimental evidence for diffusion of gases in active carbons and zeolite materials has shown the existence of

such maxima in the concentration dependence of gas diffusivity at the level of pore filling [84, 85]. PFG-NMR studies of disordered nano-porous materials have also confirmed this phenomenon [86]. Two competing mechanisms are postulated to be involved; a site-blocking entropic mechanism, as well as an energetically favored diffusion process. Slow diffusion of fluid molecules at infinite dilution is due to the existence of highly favorable adsorption sites in the amorphous structure of SiC-DC. At slightly higher concentrations most of these high affinity sites are already occupied by adsorbed molecules with increasing contribution from sites of weaker adsorption, where mobility is higher. With further increase in loading, fluid molecules fill up the bulk of the large pores, leading to significant increase in molecular collisions and steric interactions, which in turn leads to the decrease in self-diffusion coefficients.

This is very similar to what Bonilla and Bhatia have recently shown in connection with the effect of pore size distribution on diffusion in pore networks [87]. Moreover, according to Karger and Ruthven [85], intracrystalline self-diffusivities can demonstrate different patterns of concentration dependence, ranging from constantly descending or ascending self-diffusivities to a pattern yielding a self-diffusivity variation with a maximum, which occurs in the presence of heterogeneity. Such diffusion patterns are thoroughly discussed by Keil et al. for Zeolites [86]. Heterogeneity of SiC-DC structure is evident in our simulation results of the isosteric heat of adsorption, shown in Figure 5-11 (a) – (c).

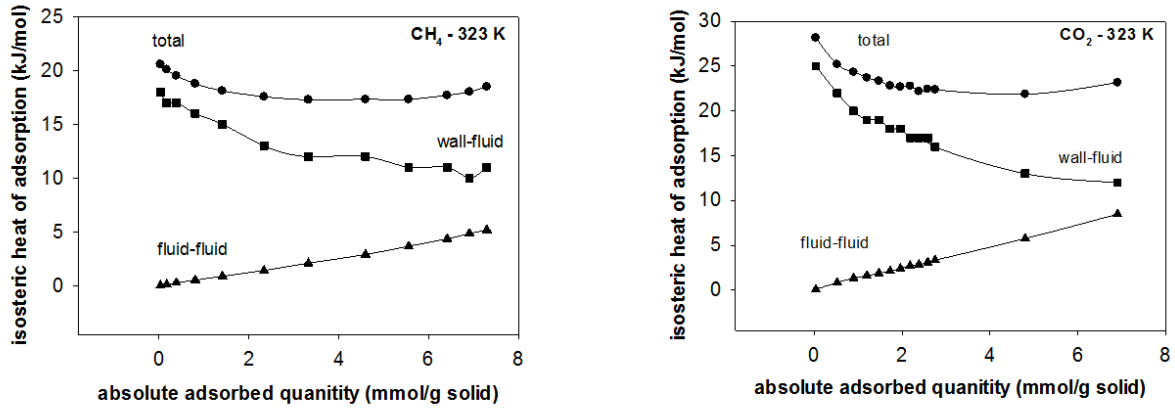

(a)

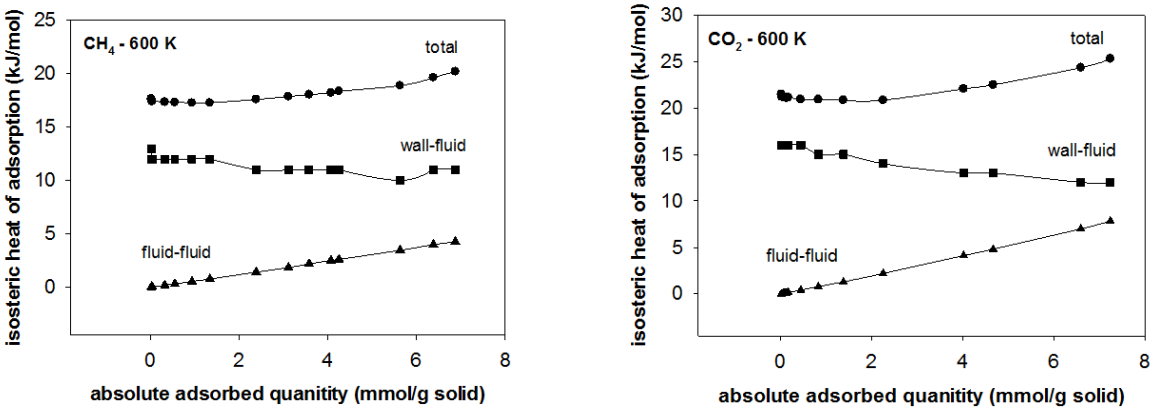

(b)

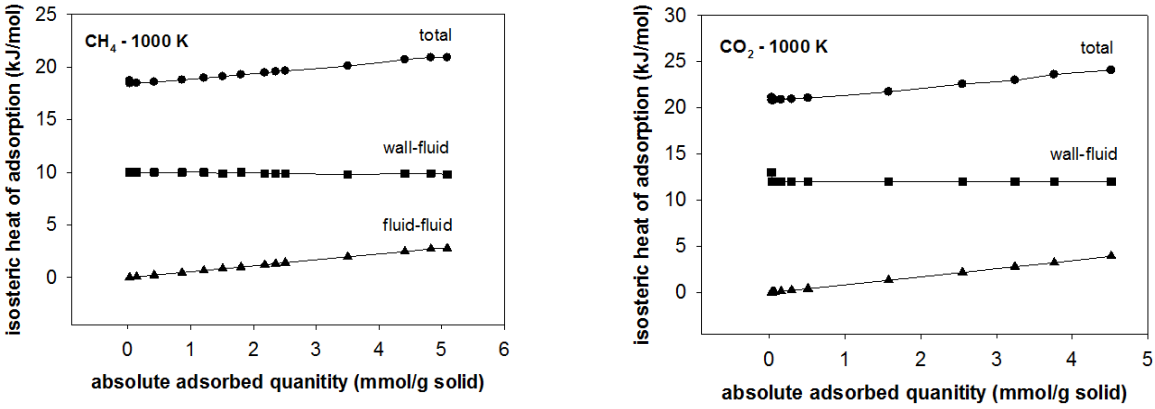

(c)

Figure 5-11. Variation of isosteric heat of adsorption with loading for CH_4 and CO_2 at (a) 323 K, (b) 600 K and (c) 1000 K

here, wall-fluid and fluid-fluid contributions are depicted separately along with the total heat of adsorption calculated using the fluctuation formula

$$Q^{st} = RT - \frac{\langle NU \rangle - \langle N \rangle \langle U \rangle}{\langle N^2 \rangle - \langle N \rangle^2} \tag{5-7}$$

where N refers to the number of molecules, U is the energy and $\langle \cdot \rangle$ indicates the average over the simulation run. As depicted in Figure 5-11 (a) and (b), the total heat of adsorption has a minimum at intermediate loadings at 323 K, and a weaker one at 600 K; this indicates that isosteric heat is higher at infinite dilution due to stronger adsorption of molecules in narrow micropores, where fluid molecules are tightly packed. It is also the low loading region where molecules show smaller mobility (low diffusivity at infinite dilution). The adsorption process becomes less exothermic with

increase in loading, because favorable adsorption sites are progressively occupied as loading increases. This trend for the heat of adsorption continues until it reaches its minimum at intermediate loadings, and then starts to increase again, due to stronger fluid-fluid interactions at elevated pressures, evident from the rising fluid-fluid contribution to the heat of adsorption in Figure 5-11. The effect of heterogeneity becomes less significant at very high temperature (1000 K), as demonstrated by the steadily increasing variation of the isosteric heat (Figure 5-11 (c)) and decreasing trend of self-diffusivity with loading at this temperature (Figure 5-8 and Figure 5-9). At 1000 K, the self-diffusivity does not show a maximum for CO_2. Moreover, the maximum observed for CH_4 at the intermediate loading (Figure 5-9) is still lower than the self-diffusivity of this molecule at infinite dilution, and could also be due to statistical scatter of the MD diffusivity data. This behavior is consistent with the monotonically increasing trend of isosteric heat at this temperature, illustrated in Figure 5-11 (c). It should be noted here that isosteric heat of adsorption is always dominated by the wall-fluid contribution, which is an obvious indication of pore confinement. Fluid-fluid interactions become only slightly significant at higher pressures. Figure 5-8 and Figure 5-9 also demonstrate that while self-diffusion coefficients of both CO_2 and CH_4 increase with temperature as expected, at high loadings the effect of temperature on enhancement of self-diffusivity is much weaker in comparison to that at infinite dilution or intermediate loadings, an indication of tight molecular packing under these conditions.

A series of molecular dynamics simulation studies based on reconstructed models of carbonaceous materials have demonstrated similar behavior in diffusion of simple gases. Moore et al. [26] have shown a similar non-monotonic behavior of the self-diffusion coefficient for the adsorption of argon in BPL carbon. Gubbins and co-workers observed an analogous trend for diffusion of nitrogen and argon in a Reverse Monte Carlo (RMC) constructed model of saccharose-based carbon [27-29]. Finally, Nguyen el al. [30] find similar behavior for their HRMC constructed model of saccharose-based activated carbon, based on the investigation of the self-diffusivity of argon and nitrogen.

The results from our MD simulations demonstrate anisotropic diffusion of fluid molecules within the SiC-DC pore network[3]; so that self-diffusivities of CO_2 and CH_4 in the *X* direction are always larger than those in other directions (Figure 5-12 and Figure 5-13).

[3] This is thoroughly discussed for different HRMC constructed models in Section 4.5.4 from page 124 to 127.

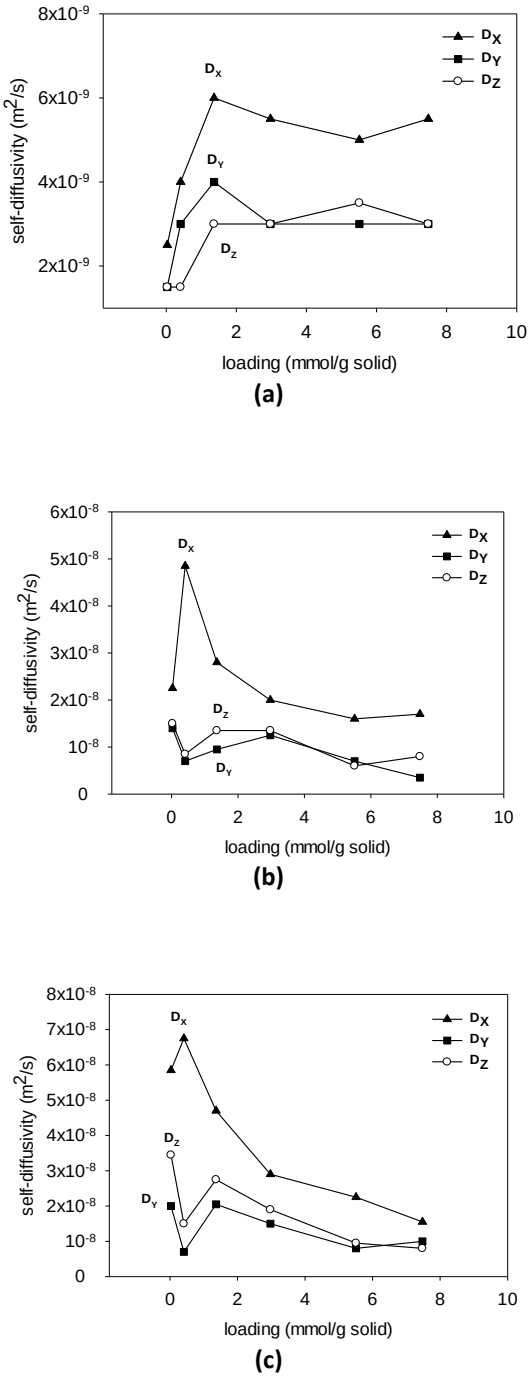

Figure 5-12. Loading dependence of self-diffusivity in different directions for CO_2, at (a) 323 K, (b) 600 K and (c) 1000 K

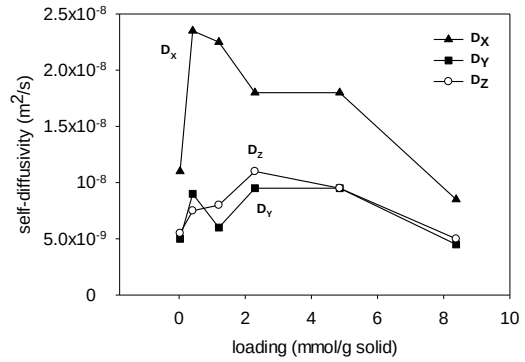

(a)

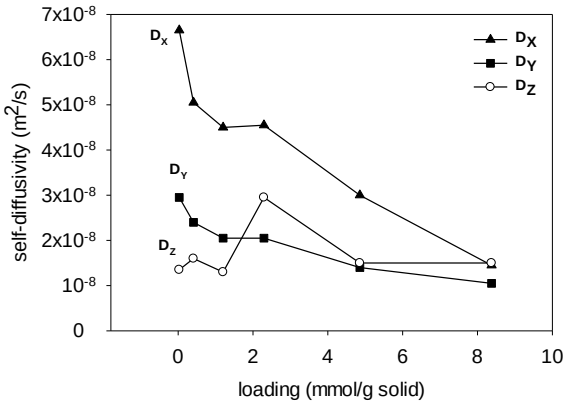

(b)

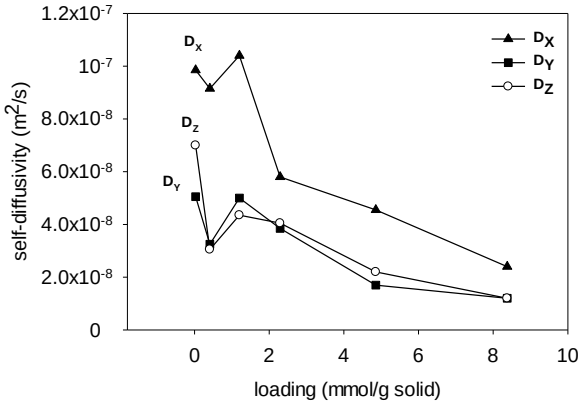

(c)

Figure 5-13. Loading dependence of self-diffusivity in different directions for CH_4, at (a) 323 K, (b) 600 K and (c) 1000 K

On the other hand, the self-diffusivities in the *Y* and *Z* directions are very close. Such behavior is explained by the anisotropic structure of amorphous SiC-DC, which may be a consequence of uni-dimensional propagation of the C-SiC interface during synthesis. Our finding for anisotropic

diffusion of methane and carbon dioxide is in line with our previous studies on structural characterization of silicon carbide-derived carbon, demonstrating a disordered structure with percolation paths propagating anisotropically across the system [25, 37].

5.4.4. Experimental Validation of Molecular Diffusion Coefficient

In this section, we report on our investigations of the diffusion of CH_4 in Silicon Carbide-Derived Carbon (SiCDC), comparing microscopic molecular dynamics simulation with experimental Quasi-Elastic Neutron Scattering (QENS) and macroscopic uptake-based kinetics data at low densities.

Among a variety of experimental techniques suitable for the measurement of different ranges of the mean length of the diffusion path, the Quasi-Elastic Neutron Scattering (QENS) technique is known to be consistent with predictions of MD simulation [88, 89]. While Zero Length Column (ZLC) and uptake-rate measurements can only provide information on long range diffusion[90], Pulsed-Field Gradients-Nuclear Magnetic Resonance (PFG-NMR) offers more flexibility in measuring distances from a few hundreds of nanometers up to a few micrometers [91, 92]. In contrast, the QENS technique is able to measure diffusion distances of the order of a few nanometers [92], similar to MD simulation within current computational capabilities. The results from microscopic measurements such as QENS and molecular dynamics simulation do not account for rate limiting internal resistances and structural defects that are usually observable for the mean diffusion path at larger length scales[90, 92], thus measuring diffusivity that is a few order of magnitudes larger than those from macroscopic or long range methods [90, 92-98].

Volumetric uptake kinetics measurements of CH_4 on the SiC-DC samples have been carried out at different temperatures using a Micromeritics ASAP 2020 adsorption analyzer, in which the transient pressure variation during small uptake steps was monitored. The corresponding uptake-time curve was interpreted using the model of diffusion in a bidisperse solid to yield a particle scale collective diffusivity, and a slow diffusivity in grain-scale ultra-micropores. The details of the experimental study will be provided elsewhere. Here, the low density particle scale diffusion data is compared with the results of QENS and MD simulation, since self and collective diffusivities of gases are identical in the limit of infinite dilution. The diffusivities used here have been obtained from uptake data at 400 mm Hg using 22.8 micron diameter particles and were similar to those at lower pressures. Consequently, they are expected to represent the low density self-diffusivity of methane. In effect, the volumetric uptake-rate method measures the flux through the porous structure of adsorbent material under well-defined boundary conditions, based on the transient pressure change in the sample cell. The diffusivity is then calculated by matching the experimental

flux to the solution of the Fick's law-based diffusion equation [90, 99]. Measurement of self-diffusivity using QENS experiment is however, based on broadening in the elastic peak of the energy distribution of an incident neutron beam [98-100]. In practice, interaction of neutrons with diffusing particles gives rise to the Doppler shift, which in turn accounts for the broadening of the elastic peak [99]. In this study, the QENS experiments were carried out using the time-of-flight spectrometer IN6, at the Institut Laue-Langevin (ILL). The energy of the incident neutron beam was taken as 3.12 meV, corresponding to a wavelength of 5.12 Å. The elastic energy resolution could be fitted by a Gaussian function, whose half-width at half-maximum (HWHM) varies from 40 μeV at small wave vector transfer (Q) to 50 μeV at large Q. The SiC-DC sample was first equilibrated at 480 mbar and 300 K and the actual neutron scattering measurement was performed at constant loading (0.85 mmol/g solid) over a range of temperatures from 150 – 300 K. For methane, one follows the mobility of individual CH_4 molecules, since the scattering is dominated by the large incoherent cross section of hydrogen [98]. Subtraction of the signal of the degassed material modifies the elastic intensity, as shown in Figure 5-14, because of the large small-angle scattering of the carbon.

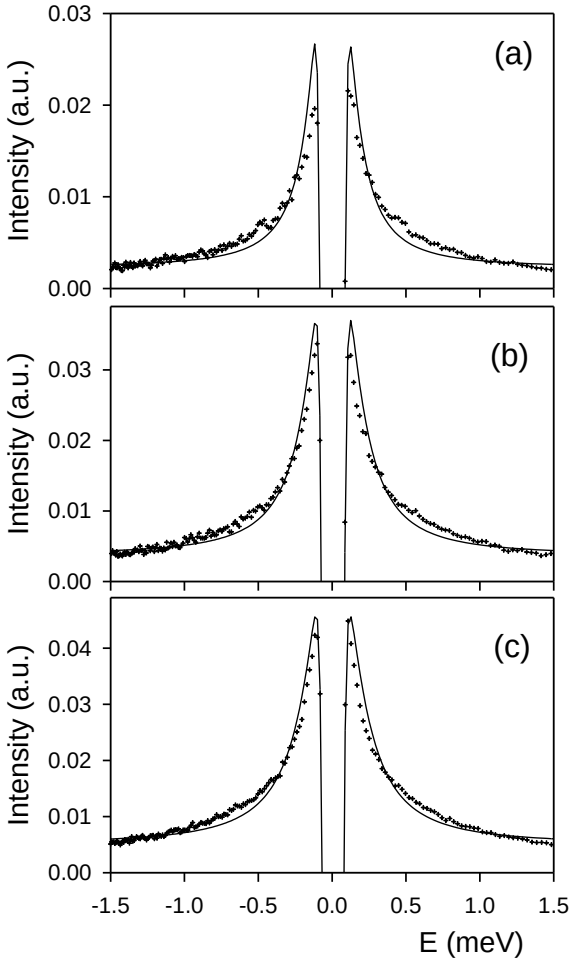

Figure 5-14. Comparison between experimental and fitted QENS spectra obtained for CH_4 at 300 K at different wave vector transfers: (a) 0.29 Å-1, (b) 0.36 Å-1, (c) 0.41 Å-1. The negative elastic intensity is due to the subtraction of the empty SiC-DC.

Spectra obtained at the different *Q* values could be fitted individually with a model consisting of isotropic diffusion, convoluted with isotropic rotation and with the instrumental resolution (Figure 5-14). Several spectra obtained at low *Q* could be fitted simultaneously using a jump diffusion model with a distribution of jump lengths. The error on the self-diffusivities is of 50%. The quality of the data was not sufficient to test anisotropic diffusion models. Figure 5-15 compares the temperature dependence of the diffusion coefficients for CH_4 obtained from MD simulation at a loading of 1.2 mmol/g, with that from QENS at 0.85 mmol/g and macroscopic uptake-based data at low density.

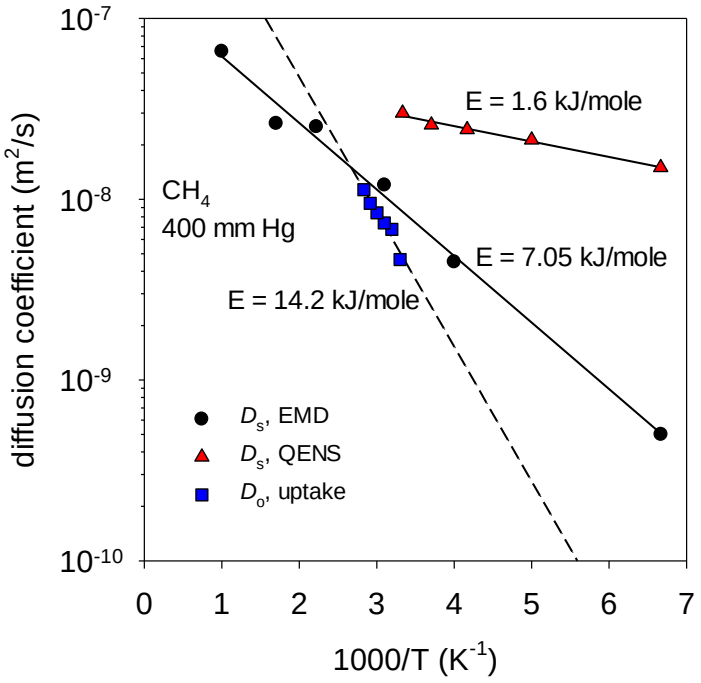

Figure 5-15. Comparison of temperature dependence of EMD diffusion coefficient with QENS and uptake-based data, for CH_4 at 400 mmHg

As seen in this figure, the QENS-based diffusion coefficients are as much as one order of magnitude larger than those based on the MD simulation. This is because the length scale probed by this QENS measurement is not large enough: the lowest Q value, 0.29 $Å^{-1}$, corresponds to a distance in real space of $2\pi/Q \approx 22$ Å. This is smaller than the size of the unit cell used in the MD calculations. However, what is remarkable here is the excellent agreement between predictions of the MD simulation with the macroscopic uptake-based data at low density. Since long-range diffusion of fluid molecules is considerably retarded by internal barriers arising from structural constrictions and disorder, macroscopic diffusivities are almost always several orders of magnitude smaller than microscopic diffusivities, usually measured by molecular dynamics simulation or QENS experiments, which probe much smaller length scales [90, 92-94, 96-98, 101]. Interestingly, our MD results are close to the macroscopic-based diffusivities within a factor of 2-3. This kind of agreement is remarkable and indicative of the ability of our HRMC constructed model of SiC-DC to accurately capture the key internal constrictions and barriers arising from the disorder in this material, so that it can successfully reproduce both equilibrium and dynamics of gas adsorption based on the results provided here and in our previous publication [25]. Nevertheless, the higher activation energy of the macroscopic measurements, of 14.2 kJ/mol, in comparison to that from

simulation, of 7.05 kJ/mol, seen in Figure 5-15 does indicate the presence of additional barriers not captured by the HRMC model. Additionally, the difference between the simulation-based activation energy and that of the uptake experiment may in part be due to the fact that experimental measurements were carried out over a narrow temperature range, while our sampling in MD covers a much broader range. The self-diffusivities of CH_4 and CO_2 obtained from MD simulation are also compared in Figure 5-16, demonstrating the slightly higher activation energy of carbon dioxide (10.28 kJ/mol) compared to methane (7.05 kJ/mol).

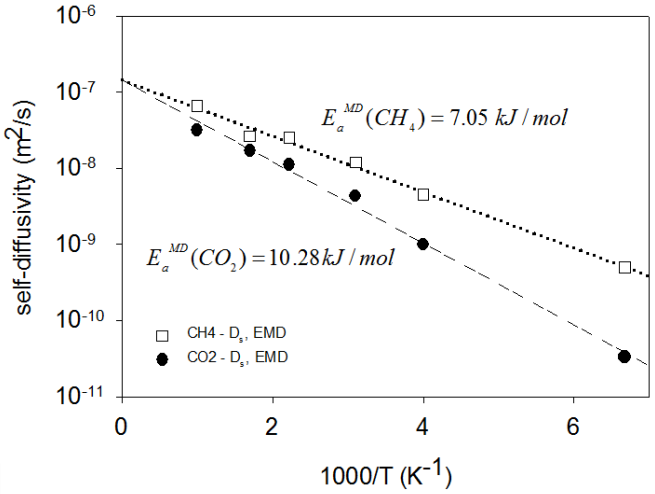

Figure 5-16. Arrhenius plot of self-diffusivities of CH_4 and CO_2, obtained from EMD simulation

5.5. Conclusion

We have investigated the heterogeneity of energy landscape of the system for the amorphous structure of microporous silicon carbide derived carbon using a representative atomistic HRMC model of the SiC-DC. The limiting free energy barrier, the percolating free energy threshold, Henry constant and differential heat of adsorption of water, carbon dioxide, methane and argon have been determined in the limit of infinite dilution using analysis of free energy landscape. Hydrophobicity of carbon structure is shown based on high minimum free energy of binding of water, as well as low heat of adsorption of this molecule compared to other adsorbates. It is shown that both methane and carbon dioxide are more favorably adsorbed compared to water. We have demonstrated how structural heterogeneity of the disordered system generates an inhomogeneous energy landscape, which in turn gives rise to the formation of high energy cluster-like adsorption sites for CH_4 and CO_2. The limiting free energy barrier of the system for each gas was computed from the difference between the most energetic energy sites of such and the percolating free energy threshold. This

barrier is directly related to the existence and distribution of the above mentioned high energy adsorption clusters, which affect mobility and diffusion of fluid molecules.

With the use of Nudged-Elastic Band (NEB) method, we have provided tangible evidence that molecular geometry, surface roughness and structural disorder of the pore wall influence diffusion through ultra-narrow pore entries. Our NEB calculations confirm that the diffusion of single molecules can be quite sensitive to structural heterogeneity and associated barriers. We find that the CO_2 molecule can face a larger energy barrier compared to CH_4 in ultra-micropores, despite its linear and smaller molecular geometry. This is confirmed not only by our NEB calculations, but also by analysis of the free energy map of the system at infinite dilution.

We have also investigated self-diffusion of methane and carbon dioxide over a wide range of densities and temperatures using both simulation and experimental techniques. Anisotropic diffusion of CH_4 and CO_2 is found, and considered to be related to structural heterogeneity and pore size distribution of SiC-DC, arising from uni-dimensional motion of the reaction interface during chlorination of the SiC precursor. The structural heterogeneity and disorder of the SiC-DC is evident from the initial increase of self-diffusivity and decrease of the isosteric heat of adsorption with increase in loading. This observation is shown to be consistent with other investigations on heterogeneous carbonaceous materials. A comparison of our simulation results with experimental QENS and low density macroscopic uptake-based data shows remarkable agreement between MD-based and the macroscopically measured diffusivities. Such agreement indicates adequacy of our HRMC constructed model of SiC-DC in capturing the internal heterogeneity and barriers affecting transport in the structure. Nevertheless, from the difference between the activation energies obtained from MD simulation and QENS with that from macroscopic uptake, we conclude that there are some long range internal barriers and structural constrictions, which are not captured by MD or the QENS experiment. Moreover, the larger discrepancy between QENS and MD-based results is due to the shorter distance probed by QENS measurement compared to MD which is ~ 22 Å vs. 40 Å.

5.6. Acknowledgement

The authors acknowledge financial support from Australian Research Council (ARC) through a grant under the Discovery Scheme. One of us (S.K.B.) acknowledges an Australian Professorial Fellowship from the Australian Researches Council. This research was undertaken with the assistance of the computational resources provided at the NCI National Facility systems at the Australian National University (ANU), through the National Computational Merit Allocation

Scheme supported by the Australian Government, as well as PACE (A Partnership for an Advanced Computing Environment) at the Georgia Institute of Technology, USA. Helpful discussions with members of Prof. David Sholl's group, especially Ph.D. candidates Ambarish Kulkarni and Jason Gee, during A.H.F's stay at GaTech as a research scholar, are gratefully acknowledged. The visit to the Georgia Institute of Technology was supported by a Graduate School International Travel Award (GSITA) from The University of Queensland (UQ). We thank Dr. M. M. Koza for his help during the QENS measurements carried out with the IN6 spectrometer at the Institut Laue-Langevin, Grenoble, France.

5.7. Supporting Information

Force field parameters for the molecular models used in this paper are reported in the Supporting Information. In addition, a movie is provided to show the transition of a CO_2 molecule through pore entry A based on our NEB calculation. This information is available free of charge via the Internet at http://pubs.acs.org.

Force Fields Parameters

All simulations performed for this study have made use of all-atom molecular models and force field parameters, detailed in Table 5-S1.

Table 5-S1. Molecular models and interaction parameters employed for molecular simulations

Fluid Molecule	Atom	Fluid-Fluid Interactions		Solid-Fluid interactions		Molecular Model			
		σ_{ff} (Å)	$\varepsilon_{ff}/\kappa_B$ (K)	σ_{cf} (Å)	$\varepsilon_{cf}/\kappa_B$ (K)	X (Å)	Y (Å)	Z (Å)	Charge (e)
Argon	**Ar**	3.41	120.00	3.38	66.18	0.000	0.000	0.000	0.000
CO_2	**C**	2.82	28.68	3.112	32.36	0.000	0.000	0.000	+0.664
	O	3.03	82.00	3.215	54.71	0.000	0.000	±1.162	-0.332
CH_4	**C**	3.4	73.082	3.4	51.65	-1.9571	+0.8401	-0.0029	-0.66

	H	2.65	7.905	3.025	16.99	-1.9168	+1.2608	-1.0098	+0.165
						-2.8337	+1.2289	+0.5193	+0.165
						-1.0542	+1.1186	+0.5443	+0.165
						-2.0238	-0.2480	-0.0655	+0.165

NEB Calculation

As discussed in the paper, CO_2 face multiple saddle-points along its transition path, while hopping through Pore entry A. As a linear molecule, CO_2 is able to adjust itself according to the geometry of the pore mouth by rotating around its symmetry axis. This behavior helps the molecule to find a pathway with the smallest energy barrier. For CO_2 this is achieved when the symmetry axis of CO_2 is perpendicular to its diffusion path, as shown in a short video clip provided here.

5.8. References

1. Dubbeldam, D. and R.Q. Snurr, *Recent developments in the molecular modeling of diffusion in nanoporous materials.* Molecular Simulation, 2007. **33**(4-5): p. 305-325.
2. Whitby, M. and N. Quirke, *Fluid flow in carbon nanotubes and nanopipes.* Nature Nanotechnology, 2007. **2**(2): p. 87-94.
3. Nicholson, D. and S.K. Bhatia, *Fluid transport in nanospaces.* Molecular Simulation, 2009. **35**(1-2): p. 109-121.
4. Gogotsi, Y., et al., *Nanoporous carbide-derived carbon with tunable pore size.* Nature Materials, 2003. **2**(9): p. 591-594.
5. Presser, V., M. Heon, and Y. Gogotsi, *Carbide-Derived Carbons – From Porous Networks to Nanotubes and Graphene.* Advanced Functional Materials, 2011. **21**(5): p. 810-833.
6. Gogotsi, Y., *Carbon Nanomaterials*. 2006, Boca Raton, FL Taylor & Francis. 326
7. Chen, X., et al., *Carbide-Derived Nanoporous Carbon and Novel Core−Shell Nanowires.* Chemistry of Materials, 2006. **18**(3): p. 753-758.
8. Zhou, W., et al., *Synthesis, Structure, and Properties of Single-Walled Carbon Nanotubes.* Advanced Materials, 2009. **21**(45): p. 4565-4583.
9. Thostenson, E.T., Z. Ren, and T.-W. Chou, *Advances in the science and technology of carbon nanotubes and their composites: a review.* Composites Science and Technology, 2001. **61**(13): p. 1899-1912.
10. Rosi, N.L., et al., *Hydrogen Storage in Microporous Metal-Organic Frameworks.* Science, 2003. **300**(5622): p. 1127-1129.
11. Furukawa, H., et al., *Ultrahigh Porosity in Metal-Organic Frameworks.* Science, 2010. **329**(5990): p. 424-428.
12. Liu, J., et al., *A novel series of isoreticular metal organic frameworks: realizing metastable structures by liquid phase epitaxy.* Scientific Reports, 2012. **2**: p. 921.
13. Falcaro, P., et al., *A new method to position and functionalize metal-organic framework crystals.* Nature Communications, 2011. **2**: p. 237.
14. Beerdsen, E., B. Smit, and D. Dubbeldam, *Molecular Simulation of Loading Dependent Slow Diffusion in Confined Systems.* Physical Review Letters, 2004. **93**(24): p. 248301.
15. Bhatia, S.K. and D. Nicholson, *Modeling Self-Diffusion of Simple Fluids in Nanopores.* Journal of Physical Chemistry B, 2011: p. 11700–11711.
16. Skoulidas, A.I. and D.S. Sholl, *Molecular Dynamics Simulations of Self-Diffusivities, Corrected Diffusivities, and Transport Diffusivities of Light Gases in Four Silica Zeolites To Assess Influences of Pore Shape and Connectivity.* Journal of Physical Chemistry A, 2003. **107**(47): p. 10132-10141.
17. Sholl, D.S., *Understanding Macroscopic Diffusion of Adsorbed Molecules in Crystalline Nanoporous Materials via Atomistic Simulations.* Accounts of Chemical Research, 2006. **39**(6): p. 403-411.
18. Mason, E.A. and A.P. Malinauskas, *Gas Transport in Porous Media: The Dusty-Gas Model*. 1983, Amsterdam: Elsevier.
19. Bhatia, S.K. and D. Nicholson, *Modeling Self-Diffusion of Simple Fluids in Nanopores.* Journal of Physical Chemistry B, 2011. **115**(40): p. 11700-11711.
20. Bhatia, S.K. and D. Nicholson, *Some pitfalls in the use of the Knudsen equation in modelling diffusion in nanoporous materials.* Chemical Engineering Science, 2011. **66**(3): p. 284-293.
21. Krishna, R., *Multicomponent surface diffusion of adsorbed species: a description based on the generalized Maxwell—Stefan equations.* Chemical Engineering Science, 1990. **45**(7): p. 1779-1791.

22. Krishna, R., *Problems and pitfalls in the use of the fick formulation for intraparticle diffusion.* Chemical Engineering Science, 1993. **48**(5): p. 845-861.
23. Bhatia, S.K., M.R. Bonilla, and D. Nicholson, *Molecular transport in nanopores: a theoretical perspective.* Physical Chemistry Chemical Physics, 2011. **13**(34): p. 15350-15383.
24. Bhatnagar, P.L., E.P. Gross, and M. Krook, *A Model for Collision Processes in Gases. I. Small Amplitude Processes in Charged and Neutral One-Component Systems.* Physical Review, 1954. **94**(3): p. 511-525.
25. Farmahini, A.H., G. Opletal, and S.K. Bhatia, *Structural Modelling of Silicon Carbide-Derived Nanoporous Carbon by Hybrid Reverse Monte Carlo Simulation.* Journal of Physical Chemistry C, 2013. **117**(27): p. 14081-14094.
26. Moore, J.D., et al., *Adsorption and diffusion of argon confined in ordered and disordered microporous carbons.* Applied Surface Science, 2010. **256**(17): p. 5131-5136.
27. Coasne, B., S.K. Jain, and K.E. Gubbins, *Adsorption, structure and dynamics of fluids in ordered and disordered models of porous carbons.* Molecular Physics, 2006. **104**(22-24): p. 3491-3499.
28. Coasne, B., S.K. Jain, and K.E. Gubbins, *Adsorption and dynamics of argon in porous carbons.* The European Physical Journal Special Topics, 2007. **141**(1): p. 121-125.
29. Pikunic, J. and K. Gubbins, *Molecular dynamics simulations of simple fluids confined in realistic models of nanoporous carbons.* European Physical Journal E: Soft Matter and Biological Physics, 2003. **12**(1): p. 35-40.
30. Nguyen, T.X., et al., *Structure of saccharose-based carbon and transport of confined fluids: hybrid reverse Monte Carlo reconstruction and simulation studies.* Molecular Simulation, 2006. **32**(7): p. 567-577.
31. Nguyen, T.X., et al., *New Method for Atomistic Modeling of the Microstructure of Activated Carbons Using Hybrid Reverse Monte Carlo Simulation.* Langmuir, 2008. **24**(15): p. 7912-7922.
32. Pikunic, J. and K.E. Gubbins, *Molecular dynamics simulations of simple fluids confined in realistic models of nanoporous carbons.* European Physical Journal E: Soft Matter and Biological Physics, 2003. **12**(1): p. 35-40.
33. Nguyen, T.X. and S.K. Bhatia, *Some Anomalies in the Self-Diffusion of Water in Disordered Carbons.* Journal of Physical Chemistry C, 2012. **116**(5): p. 3667-3676.
34. Hu, X. and D.D. Do, *Effect of Surface Heterogeneity on the Adsorption Kinetics of Gases in Activated Carbon: Pore Size Distribution vs Energy Distribution.* Langmuir, 1994. **10**(9): p. 3296-3302.
35. Do, D.D. and K. Wang, *A new model for the description of adsorption kinetics in heterogeneous activated carbon.* Carbon, 1998. **36**(10): p. 1539-1554.
36. Horiguchi, Y., R.R. Hudgins, and P.L. Silveston, *Effect of surface heterogeneity on surface diffusion in microporous solids.* Canadian Journal of Chemical Engineering, 1971. **49**(1): p. 76-87.
37. Nguyen, T.X., J.S. Bae, and S.K. Bhatia, *Characterization and Adsorption Modeling of Silicon Carbide-Derived Carbons.* Langmuir, 2009. **25**(4): p. 2121-2132.
38. Bhatia, S.K. and T.X. Nguyen, *Potential of Silicon Carbide-Derived Carbon for Carbon Capture.* Industrial & Engineering Chemistry Research, 2011. **50**(17): p. 10380-10383.
39. Nguyen, T.X. and S.K. Bhatia, *Kinetic Restriction of Simple Gases in Porous Carbons: Transition-State Theory Study.* Langmuir, 2007. **24**(1): p. 146-154.
40. Nguyen, T.X. and S.K. Bhatia, *Accessibility of simple gases in disordered carbons: theory and simulation.* Asia-Pacific Journal of Chemical Engineering, 2009. **4**(5): p. 557-562.

41. Sarkisov, L., *Calculation and visualization of free energy barriers for several VOCs and TNT in HKUST-1.* Physical Chemistry Chemical Physics, 2012. **14**(44): p. 15438-15444.
42. Sarkisov, L., *Toward Rational Design of Metal–Organic Frameworks for Sensing Applications: Efficient Calculation of Adsorption Characteristics in Zero Loading Regime.* Journal of Physical Chemistry C, 2012. **116**(4): p. 3025-3033.
43. Mills, G. and H. Jónsson, *Quantum and thermal effects in H2 dissociative adsorption: Evaluation of free energy barriers in multidimensional quantum systems.* Physical Review Letters, 1994. **72**(7): p. 1124-1127.
44. Mills, G., H. Jónsson, and G.K. Schenter, *Reversible work transition state theory: application to dissociative adsorption of hydrogen.* Surface Science, 1995. **324**(2–3): p. 305-337.
45. Jo'nsson, H., G. Mills, and K.W. Jacobsen, *Nudged elastic band method for finding minimum energy paths of transitions*, in *Classical and Quantum Dynamics in Condensed Phase Simulations*, B.J. Berne, G. Ciccotti, and D.F. Coker, Editors. 1998, World Scientific: Singapore. p. 385.
46. Opletal, G., et al., *Hybrid approach for generating realistic amorphous carbon structure using metropolis and reverse Monte Carlo.* Molecular Simulation, 2002. **28**(10-11): p. 927-938.
47. Jain, S.K., et al., *Molecular Modeling of Porous Carbons Using the Hybrid Reverse Monte Carlo Method.* Langmuir, 2006. **22**(24): p. 9942-9948.
48. Dubbeldam, D., et al., *Incommensurate Diffusion in Confined Systems.* Physical Review Letters, 2003. **90**(24): p. 245901.
49. Dubbeldam, D. and B. Smit, *Computer Simulation of Incommensurate Diffusion in Zeolites: Understanding Window Effects.* Journal of Physical Chemistry B, 2003. **107**(44): p. 12138-12152.
50. Maesen, T.L.M., et al., *Understanding cage effects in the n-alkane conversion on zeolites.* Journal of Catalysis, 2006. **237**(2): p. 278-290.
51. Haldoupis, E., S. Nair, and D.S. Sholl, *Pore size analysis of >250 000 hypothetical zeolites.* Physical Chemistry Chemical Physics, 2011. **13**(11): p. 5053-5060.
52. Haldoupis, E., S. Nair, and D.S. Sholl, *Efficient Calculation of Diffusion Limitations in Metal Organic Framework Materials: A Tool for Identifying Materials for Kinetic Separations.* Journal of the American Chemical Society, 2010. **132**(21): p. 7528-7539.
53. Sarkisov, L. and A. Harrison, *Computational structure characterisation tools in application to ordered and disordered porous materials.* Molecular Simulation, 2011. **37**(15): p. 1248-1257.
54. Vineyard, G.H., *Frequency factors and isotope effects in solid state rate processes.* Journal of Physics and Chemistry of Solids, 1957. **3**(1–2): p. 121-127.
55. Henkelman, G. and H. Jonsson, *Improved tangent estimate in the nudged elastic band method for finding minimum energy paths and saddle points.* Journal of Chemical Physics, 2000. **113**(22): p. 9978-9985.
56. Henkelman, G., B.P. Uberuaga, and H. Jonsson, *A climbing image nudged elastic band method for finding saddle points and minimum energy paths.* Journal of Chemical Physics, 2000. **113**(22): p. 9901-9904.
57. Henkelman, G., G. Johannesson, and H. Jonsson, *Methods for finding saddle points and minimum energy paths*, in *Progress on Theoretical Chemistry and Physics*, S.D. Schwartz, Editor. 2000, Kluwer Academic: New York.
58. Plimpton, S., *Fast Parallel Algorithms for Short-Range Molecular Dynamics.* Journal of Computational Physics, 1995. **117**(1): p. 1-19.

59. Nakano, A., *A space–time-ensemble parallel nudged elastic band algorithm for molecular kinetics simulation.* Computer Physics Communications, 2008. **178**(4): p. 280-289.
60. Bitzek, E., et al., *Structural Relaxation Made Simple.* Physical Review Letters, 2006. **97**(17): p. 170201.
61. Hoover, W.G., *Canonical dynamics: Equilibrium phase-space distributions.* Physical Review A, 1985. **31**(3): p. 1695-1697.
62. Martyna, G.J., et al., *Explicit reversible integrators for extended systems dynamics.* Molecular Physics, 1996. **87**(5): p. 1117-1157.
63. Martyna, G.J., M.L. Klein, and M. Tuckerman, *Nosé–Hoover chains: The canonical ensemble via continuous dynamics.* Journal of Chemical Physics, 1992. **97**(4): p. 2635-2643.
64. Kamberaj, H., R.J. Low, and M.P. Neal, *Time reversible and symplectic integrators for molecular dynamics simulations of rigid molecules.* Journal of Chemical Physics, 2005. **122**(22): p. 224114.
65. Jakobtorweihen, S., et al., *Understanding the Loading Dependence of Self-Diffusion in Carbon Nanotubes.* Physical Review Letters, 2005. **95**(4): p. 044501.
66. Jakobtorweihen, S., et al., *Diffusion of chain molecules and mixtures in carbon nanotubes: The effect of host lattice flexibility and theory of diffusion in the Knudsen regime.* Journal of Chemical Physics, 2007. **127**(2): p. -.
67. Bernardi, S., B.D. Todd, and D.J. Searles, *Thermostating highly confined fluids.* Journal of Chemical Physics, 2010. **132**(24): p. 244706.
68. Myers, A.L. and P.A. Monson, *Adsorption in Porous Materials at High Pressure: Theory and Experiment.* Langmuir, 2002. **18**(26): p. 10261-10273.
69. Talu, O. and A.L. Myers, *Molecular simulation of adsorption: Gibbs dividing surface and comparison with experiment.* AIChE Journal, 2001. **47**(5): p. 1160-1168.
70. Widom, B., *Some Topics in the Theory of Fluids.* Journal of Chemical Physics, 1963. **39**(11): p. 2808-2812.
71. Brennan, J.K., et al., *Water in porous carbons.* Colloids and Surfaces, A, 2001. **187-188**: p. 539-568.
72. Kimura, T., et al., *Cluster-Associated Filling of Water in Hydrophobic Carbon Micropores.* Journal of Physical Chemistry B, 2004. **108**(37): p. 14043-14048.
73. Nguyen, T.X. and S.K. Bhatia, *How Water Adsorbs in Hydrophobic Nanospaces.* Journal of Physical Chemistry C, 2011: p. 16606–16612.
74. Liu, L. and S.K. Bhatia, *Molecular Simulation of CO2 Adsorption in the Presence of Water in Single-Walled Carbon Nanotubes.* Journal of Physical Chemistry C, 2013. **117**(26): p. 13479-13491.
75. Ribeiro, R.P., et al., *Adsorption of CO2, CH4, and N2 in Activated Carbon Honeycomb Monolith.* Journal of Chemical & Engineering Data, 2008. **53**(10): p. 2311-2317.
76. Saha, D., et al., *Adsorption of CO2, CH4, N2O, and N2 on MOF-5, MOF-177, and Zeolite 5A.* Environmental Science & Technology, 2010. **44**(5): p. 1820-1826.
77. Skoulidas, A.I. and D.S. Sholl, *Self-Diffusion and Transport Diffusion of Light Gases in Metal-Organic Framework Materials Assessed Using Molecular Dynamics Simulations.* Journal of Physical Chemistry B, 2005. **109**(33): p. 15760-15768.
78. Bae, J.-S., T.X. Nguyen, and S.K. Bhatia, *Pore accessibility of Ti3SiC2-derived carbons.* Carbon, 2014. **68**(0): p. 531-541.
79. Nguyen, T.X. and S.K. Bhatia, *Characterization of accessible and inaccessible pores in microporous carbons by a combination of adsorption and small angle neutron scattering.* Carbon, 2012. **50**(8): p. 3045-3054.
80. Dubbeldam, D., et al., *A new perspective on the order-n algorithm for computing correlation functions.* Molecular Simulation, 2009. **35**(12-13): p. 1084-1097.

81. Hahn, K. and J. Kärger, *Deviations from the Normal Time Regime of Single-File Diffusion.* Journal of Physical Chemistry B, 1998. **102**(30): p. 5766-5771.
82. Hahn, K., J. Kärger, and V. Kukla, *Single-File Diffusion Observation.* Physical Review Letters, 1996. **76**(15): p. 2762-2765.
83. Felderhof, B.U., *Fluctuation theory of single-file diffusion.* Journal of Chemical Physics, 2009. **131**(6): p. 064504
84. Karger, J. and H. Pfeifer, *Molecular self-diffusion in active carbons.* Pure and Applied Chemistry, 1989. **61**(11): p. 1875-1880.
85. Brandani, S., D.M. Ruthven, and J.r. Ka¨rger, *Concentration dependence of self-diffusivity of methanol in NaX zeolite crystals.* Zeolites, 1995. **15**(6): p. 494-495.
86. Valiullin, R., J. Karger, and R. Glaser, *Correlating phase behaviour and diffusion in mesopores: perspectives revealed by pulsed field gradient NMR.* Physical Chemistry Chemical Physics, 2009. **11**(16): p. 2833-2853.
87. Rincon Bonilla, M. and S.K. Bhatia, *Diffusion in Pore Networks: Effective Self-Diffusivity and the Concept of Tortuosity.* Journal of Physical Chemistry C, 2013. **117**(7): p. 3343-3357.
88. Jobic, H., et al., *Influence of Isotherm Inflection on the Loading Dependence of the Diffusivities of n-Hexane and n-Heptane in MFI Zeolite. Quasi-Elastic Neutron Scattering Experiments Supplemented by Molecular Simulations.* Journal of Physical Chemistry B, 2006. **110**(5): p. 2195-2201.
89. Jobic, H. and D.N. Theodorou, *Diffusion of Long n-Alkanes in Silicalite. A Comparison between Neutron Scattering Experiments and Hierarchical Simulation Results.* Journal of Physical Chemistry B, 2006. **110**(5): p. 1964-1967.
90. Karger, J. and D.M. Ruthven, *On the comparison between macroscopic and n.m.r. measurements of intracrystalline diffusion in zeolites.* Zeolites, 1989. **9**(4): p. 267-281.
91. Karger, J. and D.M. Ruthven, *Diffusion in Zeolites and Other Microporous Solids*. 1992, New York: John Wiley. 605
92. Feldhoff, A., et al., *Intracrystalline Transport Resistances in Nanoporous Zeolite X.* Chemical Physics and Physical Chemistry, 2009. **10**(14): p. 2429-2433.
93. Jobic, H., et al., *PFG NMR and QENS diffusion study of n-alkane homologues in MFI-type zeolites.* Microporous and Mesoporous Materials, 2006. **90**(1–3): p. 299-306.
94. Jobic, H., *Molecular dynamics of n-pentane in NaX zeolite studied by quasi-elastic neutron scattering.* Physical Chemistry Chemical Physics, 1999. **1**(4): p. 525-530.
95. Guimarães, A., et al., *Diffusion of linear paraffins in silicalite studied by the ZLC method in the presence of CO2.* Adsorption, 2010. **16**(1-2): p. 29-36.
96. Jobic, H., *Diffusion of linear and branched alkanes in ZSM-5. A quasi-elastic neutron scattering study.* Journal of Molecular Catalysis A: Chemical, 2000. **158**(1): p. 135-142.
97. Jobic, H., A.N. Fitch, and J. Combet, *Diffusion of Benzene in NaX and NaY Zeolites Studied by Quasi-Elastic Neutron Scattering.* Journal of Physical Chemistry B, 2000. **104**(35): p. 8491-8497.
98. Jobic, H. and D.N. Theodorou, *Quasi-elastic neutron scattering and molecular dynamics simulation as complementary techniques for studying diffusion in zeolites.* Microporous and Mesoporous Materials, 2007. **102**(1–3): p. 21-50.
99. Karger, J., S. Vasenkov, and S.M. Auerbach, *Diffusion in Zeolites*, in *Handbook of Zeolite Science and Technology*. 2003, Marcel Dekker, Inc.: New York.
100. Jobic, H., J. Kärger, and M. Bée, *Simultaneous Measurement of Self- and Transport Diffusivities in Zeolites.* Physical Review Letters, 1999. **82**(21): p. 4260-4263.
101. Jobic, H., M. Bée, and S. Pouget, *Diffusion of Benzene in ZSM-5 Measured by the Neutron Spin−Echo Technique.* Journal of Physical Chemistry B, 2000. **104**(30): p. 7130-7133.

6. Differences in the Adsorption and Diffusion Behaviour of Water and Non-polar Gases in Nanoporous Carbon: Role of Cooperative Effects of Pore Confinement and Hydrogen Bonding

Amir H. Farmahini[a], *Suresh K. Bhatia*[a*]

J. Mol. Sim., 2014, 41 (5-6), pp 432-445

DOI: 10.1080/08927022.2014.976640

Accepted: October 8, 2014 - Published: April 13, 2015

[a] School of Chemical Engineering, The University of Queensland, QLD 4072, Australia

6.1. Abstract

We investigate the effect of pore confinement and molecular geometry on the adsorption and self-diffusion of H_2O, CO_2, Ar, CH_4, C_3H_6, SF_6 and C_5H_{12}, in a realistic model of nanoporous silicon carbide derived carbon (SiC-DC), constructed using the hybrid reverse Monte Carlo simulation. Adsorption isotherms, adsorbate-adsorbate and adsorbate-adsorbent contributions to the isosteric heat of adsorption are determined to study the effect of pore confinement, microporosity and molecular geometry on adsorption of these gases. We describe the cooperative effect of pore confinement and hydrogen bonding on the formation of water clusters and anomalous adsorption behaviour of water compared to non-polar gases. We find that, in contrast to literature results based on the slit-pore model, pore-filling does not occur below the saturation pressure in hydrophobic amorphous carbon materials such as SiC-DC and activated carbon fibre. We also compare self-diffusivities and activation energy barriers of water and non-polar gases in the microporous structure of SiC-DC to identify underlying correlations with molecular properties. We demonstrate that the self-diffusivity of water deviates considerably from the correlation between diffusivity and molecular kinetic diameter observed for non-polar gases. This is attributed to the reduced diffusivity of water, and its relatively large energy barrier at high loadings despite its small kinetic diameter, which is due to the blocking effect of water clusters at pore entries.

Keywords: Activation energy barrier, Molecular dynamics, self-diffusion, water cluster

6.2. Introduction

The control and manipulation of fluids under tight confinement are of interest to many applications in nanofluidics including infiltration technologies and transporting molecularly sized pore spaces [1, 2]. A range of novel technologies such as miniaturized screening devices [3] or lab-on-a chip technology (LoC) [4], where exceedingly small amount of fluid is transported through nano-size fluid conduits are being developed, in which the dominating effects of confining walls in nanoscale spaces available for fluid transport leads to large difference from the bulk fluid [2]. A class of well-studied materials, which provide similar conditions for fluid transports are nanoporous materials. With the synthesis of a large variety of new microporous materials over the last few decades, such as carbide derived carbons (CDCs) [5, 6], carbon nanotubes [7, 8] and metal-organic frameworks [9-11], the investigation of fluidic phenomena in nanoporous media has attracted increasing attention.

The description of fluid transport under extremely tight confinements has long been characterized by simplified theoretical models, which rely on the use of idealised pore geometries. Nevertheless, while molecular dynamics (MD) simulations offer a more accurate, albeit computationally demanding, alternative their use has been limited by the lack of realistic adsorbent models. We study here the adsorption and diffusion of different fluid molecules in a realistically constructed model of nanoporous silicon carbide derived carbon (SiC-DC), a highly disordered sub-class of the CDC family with microporosity comprising ultra-micropores smaller than 4 Å to micropores of up to 13 Å [12-14]. SiC-DC is considered to be a promising medium for the adsorption of industrially significant gases such as CO_2, CH_4 and hydrogen [12, 13, 15-17].

Here, we investigate larger molecules, including propene, neopentane and sulphur hexafluoride using molecular simulation techniques. We discuss the effect of adsorbent microporosity and its pore size distribution (PSD), as well as molecular size and geometry of the fluid particles on the diffusion and activation energy barrier of these molecules and compare the results with those for water. We provide insights into the different mechanisms involved in adsorption and diffusion of water and non-polar gases in the nanoporous structure of SiC-DC, highlighting the cooperative effect of pore confinement and hydrogen bonding on water adsorption.

Understanding water adsorption in porous materials is important not only because of its relevance to adsorptive drying technology, but also for adsorptive separations, where the co-adsorption of water vapour has a significant effect on capacity, selectivity and diffusion for other molecules [18, 19]. Microporous carbon materials are known to be hydrophobic structures due to the non-polar nature

of the graphitic carbon sheets inherent to their structure and the weaker carbon-water interactions than the water-water interactions, which are dominated by electrostatic effects. This leads to an unfavourable adsorption isotherm at low loading, with reduced level of electrostatically mediated hydrogen bonding, which can destabilize formation of the adsorbed phase inside the pore [20-24]. Thus, the adsorption of water in such hydrophobic materials is subject to the formation of stable water clusters based on intermolecular hydrogen bonding. Ohba et al. have shown that a single water molecule interacts weakly with the carbon slit pore, nevertheless the potential depths of water clusters are directly related to their size, so that "the greater the cluster size, the deeper the potential depth" [25], leading to stabilisation of the adsorbed phase. Kimura et al. later explained that dipole moment of the water cluster can be reduced due to dipole-dipole interactions between individual water molecules, and this leads to higher affinity of the water cluster towards the hydrophobic carbon wall, giving rise to further molecular ordering within the cluster at the level of pore filling [20]. Experimental and simulation studies have revealed that pore filling can take place at below or above saturation pressure depending on a variety of factors, including the existence of functional groups and activated sites in the carbon sample, topology and morphology of the carbon framework, pore size and type of the water model used in the simulation [20, 21, 26, 27]. Grand canonical Monte Carlo (GCMC) simulation studies of water adsorption in slit-pore models have shown that condensation does not occur below the saturation pressure of water in pores larger than 10 Å [26]. These studies also provide evidence that condensation can occur at pressures below P_o for pore spaces comparable to the molecular size, nevertheless for very small pores (6 Å) condensation will also not occur until pressure is raised beyond P_o [26]. However, the predicted water adsorption in amorphous carbon materials does not simply follow a similar pattern. The disordered topology and morphology of carbons, in addition to their PSD and inter-connectivity of the pore structure, give rise to many anomalies associated with adsorption and diffusion of water in this class of materials. Hitherto there have been only a handful of simulation studies of water adsorption in non-slit pore models considering structural disorder [27-30], despite the need for more comprehensive investigations in this area. Therefore, this study is conducted to address these requirements.

6.3. Computational approaches

6.3.1. Adsorbent model

We have developed a reliable structural model for SiC-DC using the Hybrid Reverse Monte Carlo (HRMC) modelling technique [31-33], as reported in our recent publication [13]. The model has

been successfully validated against both equilibrium adsorption data and dynamic uptake experiments [13, 34]. The HRMC model is reconstructed based on the structure factor data obtained from neutron scattering experiments with SiC-DC synthesized at 1073 K [12]. The model represents the positions of 3052 carbon atoms in a 40 Å cubic unit cell, as illustrated in Figure 6-1.

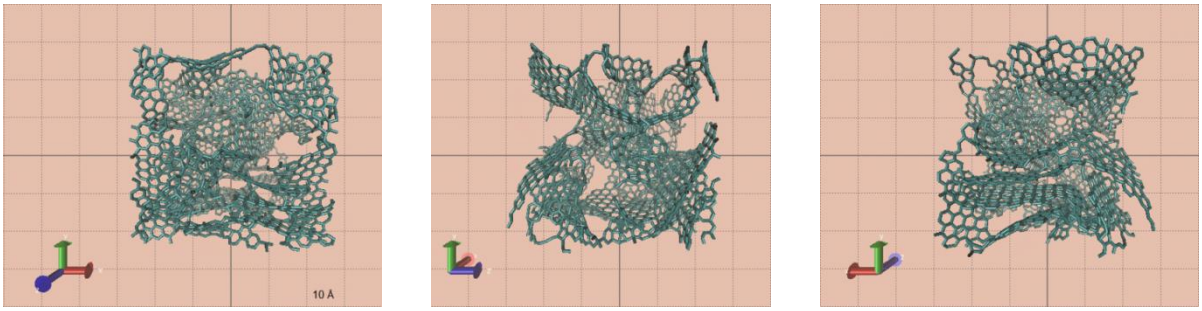

(a) (b) (c)

Figure 6-1. Atomistic structure of HRMC constructed model of SiC-DC

The microporosity of this structure has been demonstrated based on the pore size distribution (PSD) of the sample determined using small angle neutron scattering (SANS) experiments [35] and a spherical probe geometric approximation technique with the HRMC model [36, 37]. The PSD from these techniques are compared in Figure 6-2, and have been thoroughly discussed elsewhere [13].

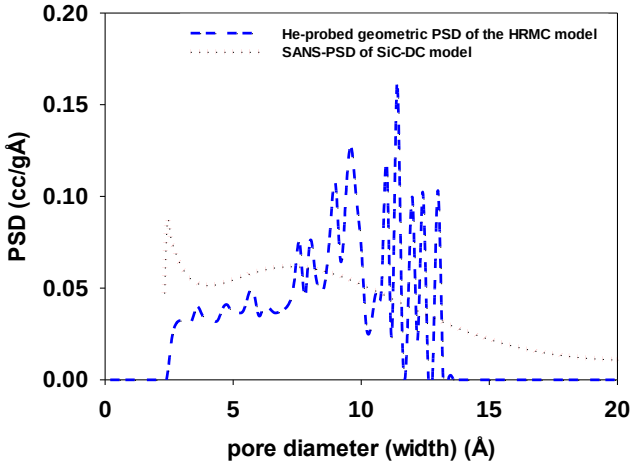

Figure 6-2. PSD of SiC-DC, as determined by the spherical geometric approximation technique and Small Angle Neutron Scattering (SANS)

In the current simulation studies, carbon-carbon Lennard-Jones (LJ) parameters of σ = 3.4 Å and ε/k_B = 36.5 K have been used, following earlier studies [13].

6.3.2. Modelling gas adsorption and self-diffusion

The modelling of gas adsorption is carried out through Grand Canonical Monte Carlo (GCMC) simulation using the RASPA simulation package [38]. Adsorption isotherms were obtained for all gases at 310 K, except for argon and water vapour, which were simulated at 87 K and 298 K respectively. A one-site Lennard-Jones (LJ) potential model was used for argon, while multi-site models with or without partial electrostatic charges (as applicable) were utilized for CO_2, CH_4, C_3H_6, C_5H_{12} (neopentane) and SF_6 with parameters given in Table 6-1.

Table 6-1. Molecular models and interaction parameters employed for GCMC and MD simulations

Fluid Molecule	Atom	Fluid-fluid interactions		Solid-fluid interactions		Partial Charge (e)	Reference
		σ_{ff} (Å)	$\varepsilon_{ff}/\kappa_B$ (K)	σ_{cf} (Å)	$\varepsilon_{cf}/\kappa_B$ (K)		
Ar	**Ar**	3.41	120.00	3.38	66.18	0.000	[39]
CO_2	**C**	2.82	28.68	3.11	32.36	+0.664	[40]
	O	3.03	82.00	3.22	54.71	-0.332	
CH_4	**C**	3.40	73.082	3.40	51.65	-0.66	[13, 41]
	H	2.65	7.905	3.03	16.99	+0.165	
						+0.165	

						+0.165	
						+0.165	
C_3H_6	CH_2	3.69	93.0	3.543	58.26	0.000	[42, 43]
	CH	3.74	53.0	3.57	43.98	0.000	
	CH_3	3.76	108.0	3.58	62.79	0.000	
C_5H_{12}	CH_3	3.75	98.0	3.58	59.81	0.000	[44]
	C	6.4	0.5	4.9	4.27	0.000	
SF_6	S	0.0	0.0	0.0	0.0	0.000	[45]
	F	2.77	73.13	3.085	51.67	0.000	

The simple point charge (SPC) [46] and SPC/E [47] models were employed for water simulation. The isosteric heat of adsorption along with its wall-fluid and fluid-fluid contributions was calculated using the fluctuation formula

$$Q^{st} = RT - \frac{\langle NU \rangle - \langle N \rangle \langle U \rangle}{\langle N^2 \rangle - \langle N \rangle^2} \quad (6\text{-}1)$$

where, R is the ideal gas constant, T is the temperature, N refers to the number of molecules, U is the energy and the brackets indicate an average over the simulation run.

Equilibrium MD simulation was also performed using the LAMMPS simulation package [48] to compute diffusivities of the above molecules through the microporous structure of SiC-DC. The time integration was performed on Nose-Hoover style non-Hamiltonian equations of motion to sample molecular positions from the NVT ensemble. The application of classical statistical mechanics of non-Hamiltonian systems in MD simulation is discussed by Tuckerman et al [49, 50]. A Verlet time integrator with time step equal to 1 fs was used. In the MD simulation, small molecules including water (SPC model), CO_2, CH_4 and propene were modelled as rigid molecular

bodies, while the larger molecules such as neopentane and sulphur hexafluoride were modelled as flexible molecular structures. Intramolecular interaction parameters of the flexible molecules are given in Table 6-2.

Table 6-2. Intra-molecular interaction parameters of flexible molecules investigated

	C_3H_6*		**C_5H_{12}***	**SF_6** [45]
Harmonic bond**	CH_2-CH	CH-CH_3	CH_3-C	S-F
Bond strength (kJ/mol.Å^2)	802.35	802.35	802.35	1386.96
Bond length (Å)	1.33	1.54	1.54	1.565
Harmonic bend**	CH_2-CH-CH_3		CH_3-C-CH_3	F-S-F
Bond strength (kJ/mol.rad^2)	585.50		519.65	614.72
angle (degree)	119.7		109.47	90.00

* TraPPE force field.

****** Harmonic bond: $U_{bond} = \frac{1}{2}K_r(r - r_0)^2$; Harmonic bend: $U_{bend} = \frac{1}{2}K_\theta(\theta - \theta_0)^2$

For rigid molecules, translational and rotational degrees of freedom of rigid bodies were both thermostated. The rigid-body algorithm for NVT integration is explained elsewhere [51]. For dynamic simulation of water and propene, bond stretching and angle bending interactions were frozen using the Shake algorithm [52]. Short-range intermolecular interactions were modelled using the 12-6 Lennard-Jones potential with a cut-off distance of 18 Å. The standard Ewald formalism was utilized for electrostatic interactions with cut-off distance of 18 Å so that pairwise interactions within this distance were computed directly, and those beyond this distance were calculated in the *k*-space. To obtain self-diffusivities of fluid molecules, mean-squared displacements (MSDs) of the centre of mass of the molecules were collected in the Fickian regime, where the dependence of MSD with time is linear. Self-diffusivity was then calculated using the Einstein formula

$$D_s = \frac{1}{2Nd} \lim_{t \to \infty} \frac{1}{t} \langle \sum_{i=1}^{N} |r_i(t) - r_i(0)|^2 \rangle \quad (6\text{-}2)$$

where r_i *(t)* is the centre of mass position vector of molecule *i* at time *t*, *N* is the number of molecules and *d* is dimensionality of the system. We have estimated the activation energy barrier of the molecules using the Arrhenius formalism

$$D = D_o . e^{-E_a/RT} \quad (6\text{-}3)$$

where, *D* and D_o are diffusivity and temperature-independent pre-exponential factor respectively.

6.4. Results and discussion

6.4.1. Modelling gas adsorption

6.4.1.1. Adsorption of non-polar gases

Molecular adsorption in confined spaces of microporous materials is strongly governed by the topology and morphology of the adsorbent structure, as well as geometry and potential strength of adsorbate molecules. We predicted the adsorption isotherms of different gases with various molecular geometries in a rigid HRMC constructed model of SiC-DC using the GCMC simulation technique. Simulated adsorption isotherms of CO_2 and CH_4 at 310 K are shown in Figure 6-3.

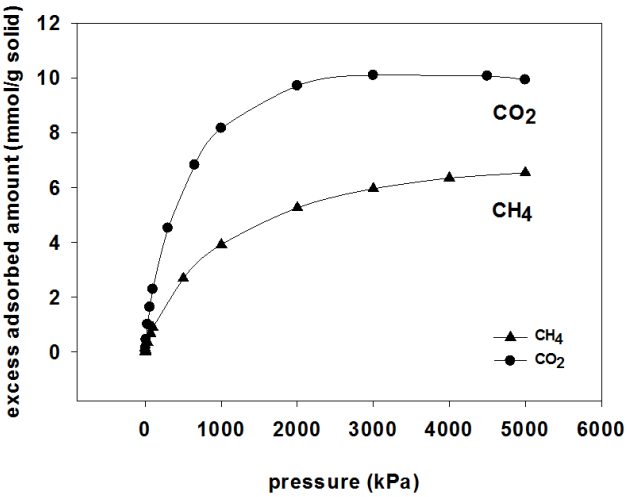

Figure 6-3. Predicted adsorption isotherms of CH_4 and CO_2 at 310 K

As illustrated here, CH_4 and CO_2 behave quite differently under similar thermodynamic conditions. With temperature and pressure kept constant, the adsorption of CO_2 is seen to be 1.5 to 2 times larger than CH_4 at elevated pressures. This is mainly due to higher affinity of CO_2 towards the carbon framework; nevertheless, molecular size and geometry of the molecule also play an important role here. According to this figure, the adsorption of CO_2 is nearly four times that of CH_4 under sub-atmospheric conditions. Besides the higher potential strength of CO_2, this is likely to be related to CO_2 adsorption in ultra-microporous regions of the SiC-DC structure, for which there is simulation and experimental evidence in the literature [13, 14, 53]. The DFT-based PSD of SiC-DC obtained from interpretation of CO_2 adsorption at 273 K reveals that ultra-micropores of 3.2 –3.7 Å are expected to be more accessible to CO_2 than CH_4 due to the smaller kinetic diameter of CO_2 [14]. Integration of the geometric PSD shown in Figure 6-2 demonstrates that 0.04 cc/g of the total pore volume ($V_{tot.}$ = 0.62 cc/g) lies within the ultra-microporous region (2.3 –3.4 Å), which is similar to that based on small angle neutron scattering (SANS) of 0.07 cc/g [35]. In agreement with prediction of the adsorption isotherm, stronger adsorption of CO_2 than CH_4 is evident from its higher heat of adsorption, as shown in Figure 6-4 and Figure 6-5.

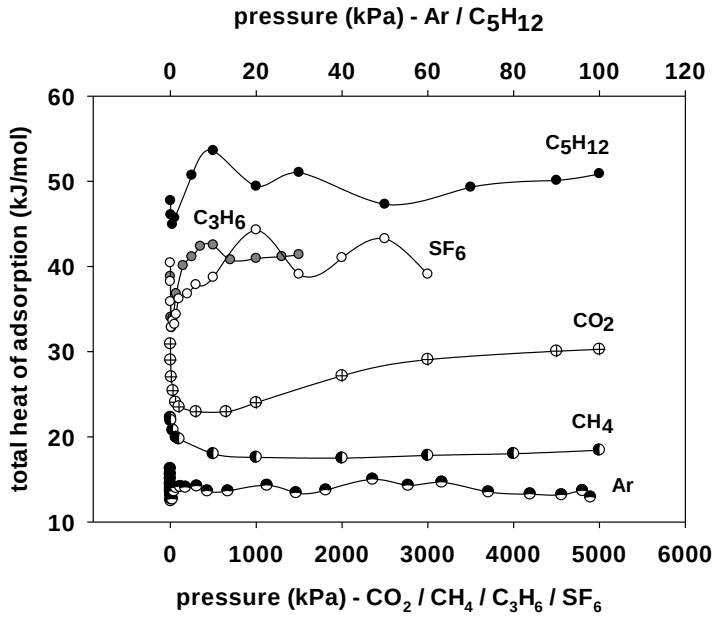

Figure 6-4. Comparison of the predicted total heat of adsorption for different gases at 310 K (Argon at 87 K)

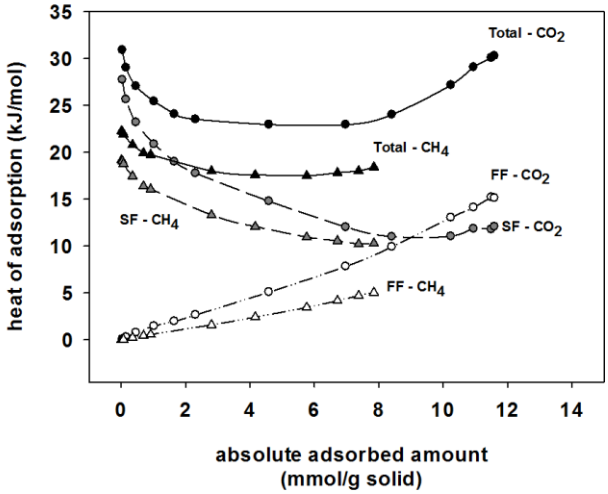

Figure 6-5. Variations of predicted heat of adsorption with loading for CH_4 and CO_2 at 310 K, along with solid-fluid (SF) and fluid-fluid (FF) contributions to heat of adsorption

Figure 6-5 also highlights the significant contribution of the fluid-fluid interactions at elevated pressures in the rising trend of the heat of adsorption, which is due to high density and close packing of adsorbate molecules at these pressures. Figure 6-6 demonstrates the predicted adsorption isotherms of larger molecules including propene, sulphur hexafluoride and neopentane at 310 K.

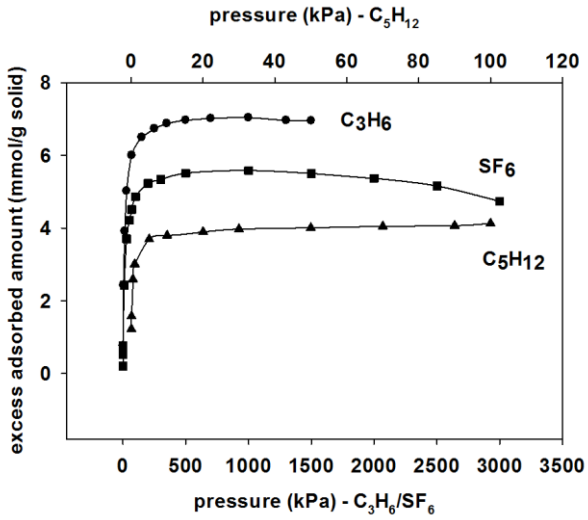

Figure 6-6. Predicted adsorption isotherms of C_3H_6, C_5H_{12} and SF_6 at 310 K

As depicted here, the adsorption of propene is higher than that of the other two gases; however, the adsorption of neopentane is predicted to be less than that of SF_6. This is consistent with kinetic molecular diameters of these molecules (C_3H_6 = 4.5 Å [54], SF_6 = 5.5 Å [55] and C_5H_{12} = 6.2 Å [56]). Although the heats of adsorption of C_3H_6 and SF_6 are very similar in terms of trend and magnitude (illustrated in Figure 6-4 and Figure 6-7), the adsorption of neopentane is much more exothermic.

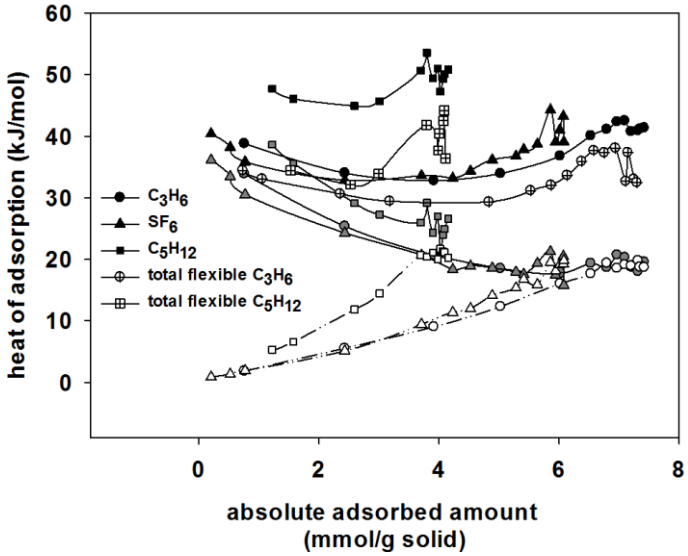

Figure 6-7. Variations of predicted heat of adsorption with loading for C_3H_6, C_5H_{12} and SF_6 at 310 K. Black, gray and white symbols represent total heat, solid-fluid and fluid-fluid contributions respectively

This is because the four methyl groups in the neopentane structure are stronger adsorption agents than fluorines in SF_6 and the alkyl groups of propene. The smaller adsorption of C_5H_{12} can be readily explained based on its larger molecular size. A comparison between solid-fluid and fluid-fluid contributions to the heat of adsorption for these three gases reveals a similar trend, as seen for CO_2 and CH_4, in such a way that the tight molecular packing at higher pressures gives rise to significant increase of the fluid-fluid interactions. The larger slope of the fluid-fluid contribution for C_5H_{12} than for C_3H_6 and SF_6, is an indication of the stronger fluid-fluid interactions. Figure 6-7 also provides some information on the effect of molecular flexibility on total heat of adsorption for C_5H_{12} and C_3H_6, showing that the total heats of adsorption for flexible models are less than those of

rigid molecules. This is because some portion of the released energy during the adsorption process is consumed by the intra-molecular bond stretching and angle bending interactions.

We have also simulated the sub-atmospheric adsorption of argon at 87 K. As seen in Figure 6-8 (a), the adsorption of argon is significantly higher than that of all other gases discussed so far, but this is only because of the lower temperature, at which argon isotherm is simulated.

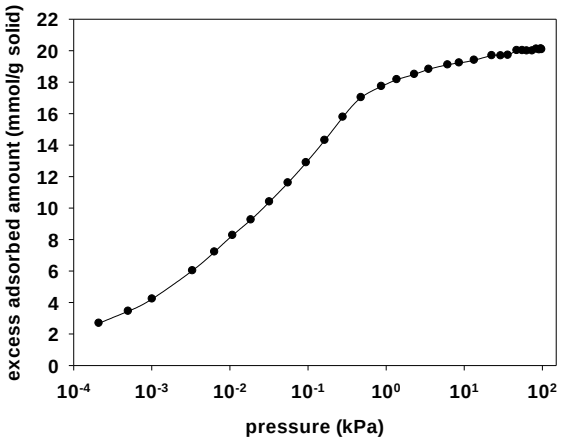

(a)

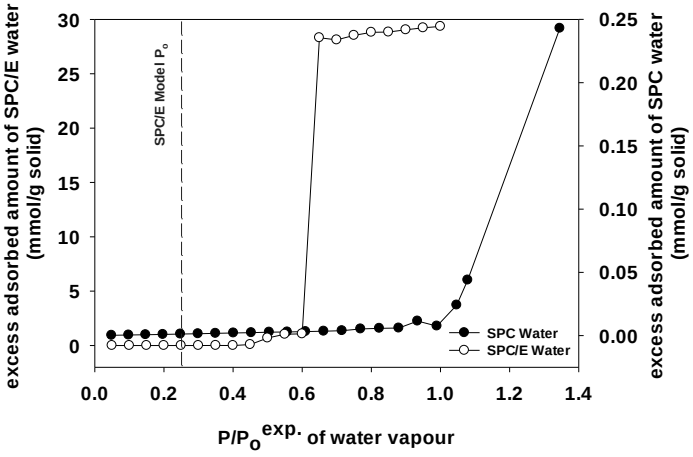

(b)

Figure 6-8. Predicted adsorption isotherms of (a) argon at 87 K and (b) water vapour at 298.15 K

The significantly lower heat of adsorption of argon, as shown in Figure 6-4, implies that argon is the least favoured gas for adsorption in the microporous structure of SiC-DC. The spherical molecular geometry of argon in addition to its relatively small kinetic diameter (3.41 Å) facilitates close molecular packing inside the pore space. From Figure 6-8 (a), it is clear that argon molecules

quickly fill up almost all the pores, so that the isotherm reaches its maximum close to 6.17 kPa and no further increase can be seen at higher pressures. Such rapid adsorption at low pressures is an indication of a highly microporous structure of SiC-DC supported by our experimental and simulated PSDs, as illustrated in Figure 6-2. Finally, a comparison between the total heats of adsorption of all gases discussed so far reveals a steep drop at low pressure (Figure 6-4), indicative of strong heterogeneity of the narrow micropores. We have shown in our previous studies of structural heterogeneity of SiC-DC that narrow pores accommodate strong adsorption sites, which can significantly hinder self-diffusion of fluid particles due to adsorption in highly confined pores [34]. Contrary to the adsorption in narrow pores, the adsorption behaviour of different gases in response to pressure increase varies from molecule to molecule based on their molecular geometries. For instance, isosteric heats of adsorption of argon and CH_4 remain almost invariant with increasing pressure after the initial rapid drop; however the isosteric heat of CO_2 shows a monotonically ascending curve until pressure reaches supercritical conditions. This is likely due to better packing of linear CO_2 molecules. Thus, it is clear that there is a general correlation between molecular geometry of the non-polar fluid molecules and their adsorption behaviour.

6.4.1.2. Adsorption of water vapour

An important topic studied in this work concerns adsorption of water vapour in the hydrophobic microporous structure of SiC-DC. We have employed the SPC model, as well as its extended version (SPC/E) to investigate water adsorption in our HRMC model of SiC-DC. Our GCMC results by the use of the SPC/E model reveal an analogous pattern with that observed in the experiment for activated carbon materials, in which a pore filling mechanism gives rise to a sudden jump in the amount of water adsorbed at $P < P_o$ ($P/P_o \approx 0.65$) [20, 21], when P_o is taken as the experimental value of vapour pressure ($P_o^{exp.}$). Although Nguyen and Bhatia [29] have also observed a similar behaviour for their activated carbon fibre model, we will show here that this similarity for the SPC/E-based isotherms is purely fortuitous. As illustrated in Figure 6-8 (b), the pre-pore filling process starts gradually at $P/P_o^{exp.} \approx 0.45$ by forming water clusters in highly narrow pores of 7.0 – 9.0 Å (centre-to-centre distance), which is shown in Figure 6-9 (a) – (d).

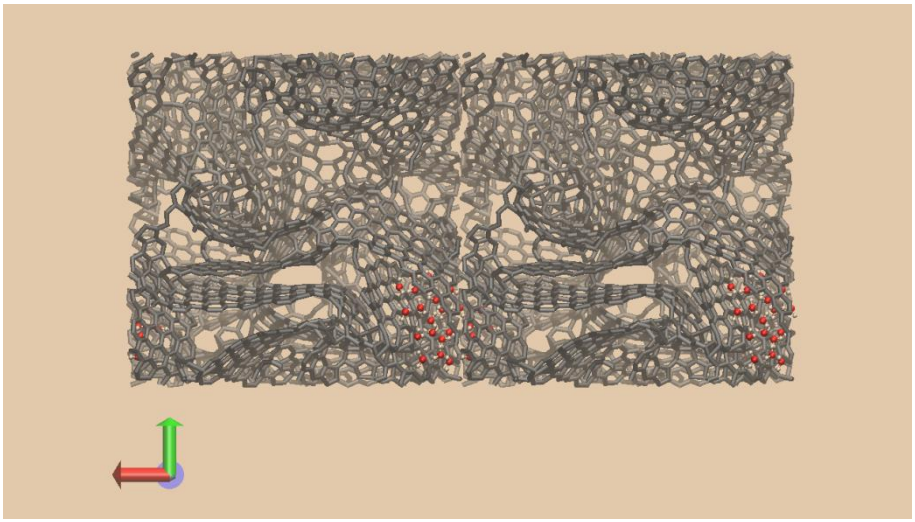

(a)

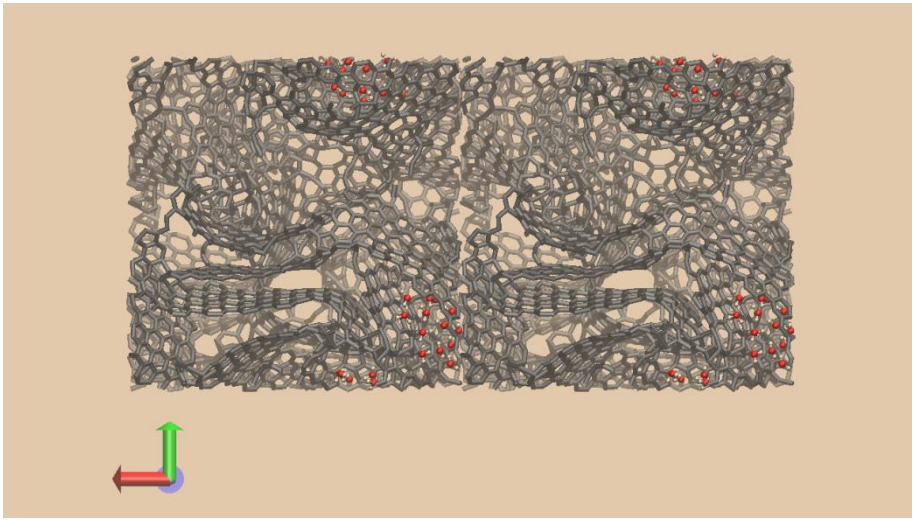

(b)

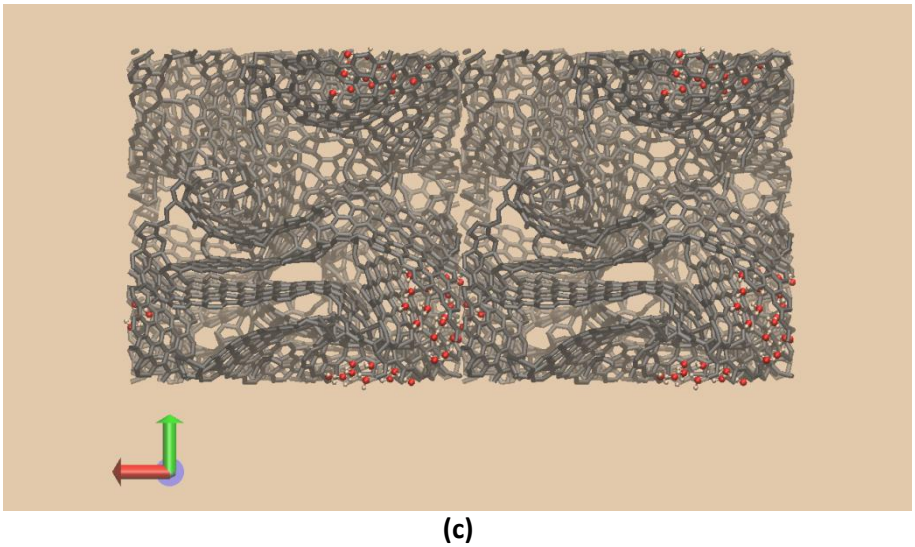

(c)

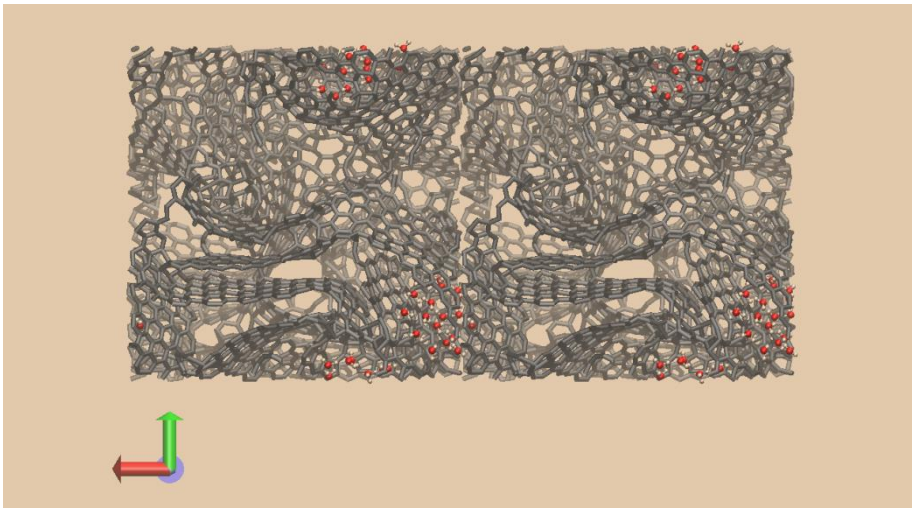

(d)

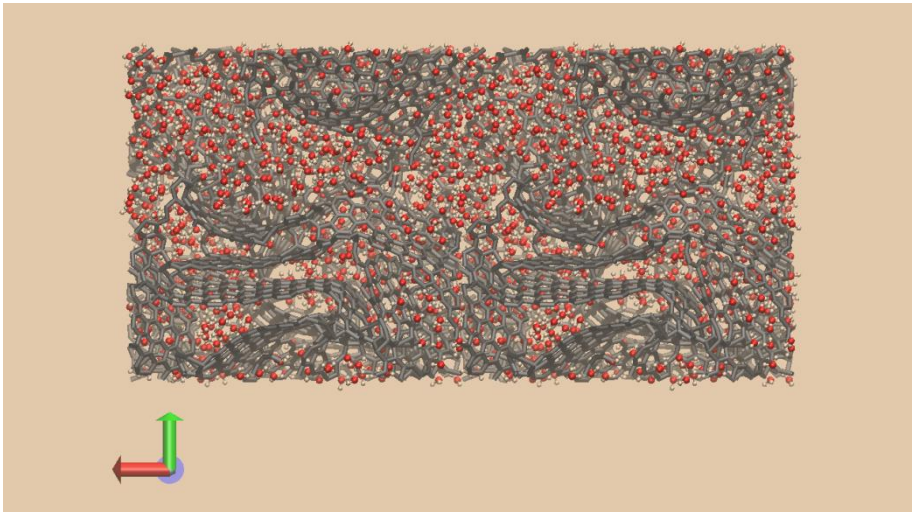

(e)

Figure 6-9. Final snapshot of GCMC configurations at $P/P_o^{exp.}$ of (a) 0.45, (b) 0.5, (c) 0.55, (d) 0.6 and (e) 0.65 using the SPC/E water model

This corresponds to a remarkable increase in the heat of adsorption beyond the latent heat of bulk water, evident in Figure 6-10.

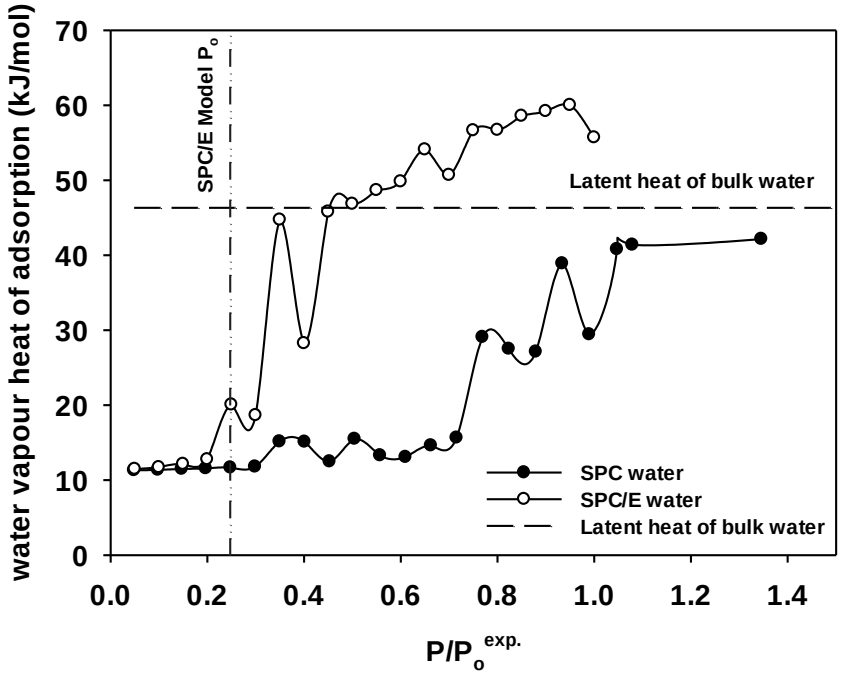

Figure 6-10. Variations of predicted heat of adsorption for water vapour at 298.15 K for two different models

We note the presence of statistical fluctuation in the heats in this figure, which arises due to the sensitivity of the fluctuation formula used (equation (6-1)), but this does not affect the conclusion of unexpected rise in heat of adsorption beyond the latent heat. The mechanism for water adsorption in the HRMC constructed model of SiC-DC appears to be similar to that for activated carbon fibre reported by Nguyen and Bhatia [29] based on the SPC/E model). In both cases, the formation of sufficiently large and stable water clusters in small nanopores, which are connected to larger pore spaces, eventually leads to filling larger pores. Figure 6-9 illustrates this mechanism for $P/P_o^{exp.}$ = 0.45 – 0.65. Striolo et al. have explained how water clusters can be stabilized in narrow slit pores by the strong attractive interactions of water with both opposite pore walls to initiate the whole clustering mechanism [57].

Figure 6-8 (b) also illustrates the adsorption isotherm of water based on the use of the SPC model in our GCMC simulations. Here, the pre-pore filling process does not start until the pressure is at the experimental saturation pressure ($P/P_o^{exp.} \approx 1.0$), similar to the increasing trend of the heat of adsorption, which only starts to rise at pressures close to the saturation pressure, as illustrated in Figure 6-10. For the SPC water model, it is noteworthy that heat of adsorption does not increase beyond the latent heat of water even at $P/P_o^{exp.}$=1.4. Our predictions for the SiC-DC model is in

good agreement with the results from Brennan et al. for adsorption of water in a reverse Monte Carlo (RMC) constructed model of activated carbon, based on the use of SPC model, that adsorption of water in virgin amorphous carbon materials is negligible below the saturation pressure [28]. Based on these observations, we suspect that the similarity between the SPC/E model based isotherms for SiC-DC structure of this work and that of ACF15 of Nguyen and Bhatia [29] with experimental ACF-15 data is fortuitous, and due to two different phenomena. The sudden increase of water adsorption in the experimental sample of ACC-5092-15 activated carbon (ACF15) can be due to the existence of oxygen and nitrogen impurities, evident from X-ray photoelectron spectroscopy of the sample [58]. It is widely known that the oxidized sites can encourage growth of water clusters in nanoporous carbon [59, 60]. Both Brennan et al. and Liu and Monson [27, 28] have also demonstrated that adsorption of water is strongly enhanced in the presence of activated sites. In contrast, the source of adsorption take-off for the SPC/E based isotherm at relative pressures below unity is essentially the use of the experimental P_o value in the calculation of relative pressure. According to Liu and Monson [26], the uncertainty in the saturation pressure of the employed water models can result in erroneous conclusions. Thus, if the relative pressures is based on the experimental saturation vapour pressure of water (3.167 kPa), any difference between the actual saturation pressure of the water model and the experiment value will lead to inconsistencies in our comparisons. Liu and Monson determined saturation activities of the SPC and SPC/E models at bulk vapour-liquid equilibrium and 298.15 K using the Gibbs Ensemble Monte Carlo (GEMC) technique, and showed that saturation pressure of the SPC/E model is more than four times smaller than that of the SPC model at this temperature. This means that saturation pressure point of the SPC/E water in Figure 6-8 (b) is in fact located in the left side of the plot, as shown by the vertical dashed line. However, the saturation pressure of the SPC model is very close to that of the experiment (3.26 kPa versus 3.167 kPa respectively). There is also other evidence that the SPC/E model cannot very well reproduce the vapour pressure of water at various temperatures [61], however the SPC model predicts both saturated vapour pressure and experimental isotherms of water reliably [27]. When the correct model-based saturation pressures are used (instead of the experimental P_o), both SPC/E and SPC based isotherms will show a consistent trend for the adsorption of water in the SiC-DC model with pore-filling only occurring at $P > P_o^{model}$, in agreement with the results of Brennan et al. [28] for water adsorption in activated carbon, as discussed earlier. Thus, we calculate that pore filling by water occurs at $P / P_o^{model} > 1$ in purely hydrophobic carbons, and its occurrence at $P / P_o < 1$ in the experiment with activated carbons [62]

is likely due to the presence of some hydrophilic surface groups and impurities. This is supported by the experimental results of Bhatia and Nguyen [15], showing very little water adsorption in purely hydrophobic SiC-DC at relative pressures up to unity at 298 K, albeit with strong kinetic limitations being noted in this study.

To summarize, it is apparent that adsorption of water in HRMC constructed models of SiC-DC and activated carbon fibre follow the same pattern. In both cases, formation of water clusters does not occur until pressure is increased beyond the model saturation pressure or very close to it. The underlying mechanism is consistent for both microporous models and similar to that proposed by Ohba et al. [25], where the water cluster growth transforms affinity of the water cluster, which leads to stabilization of the adsorbed phase. Cluster stabilization is a key step in starting the adsorption mechanism. According to Vaitheeswaran et al. the smallest stable water cluster in a hydrophobic spherical cavity of 10 Å is a trimer with one hydrogen bond per molecule [63]. They have shown that stability of a water cluster largely depends on the cavity size, as well as strength of the cluster interaction with the pore wall. This is consistent with our observations as depicted in Figure 6-11, where encapsulated water molecules are trapped in pore cavities of 7.0 – 9.0 Å, in such a way that the level of confinement enhances interaction of water molecules with the pore walls.

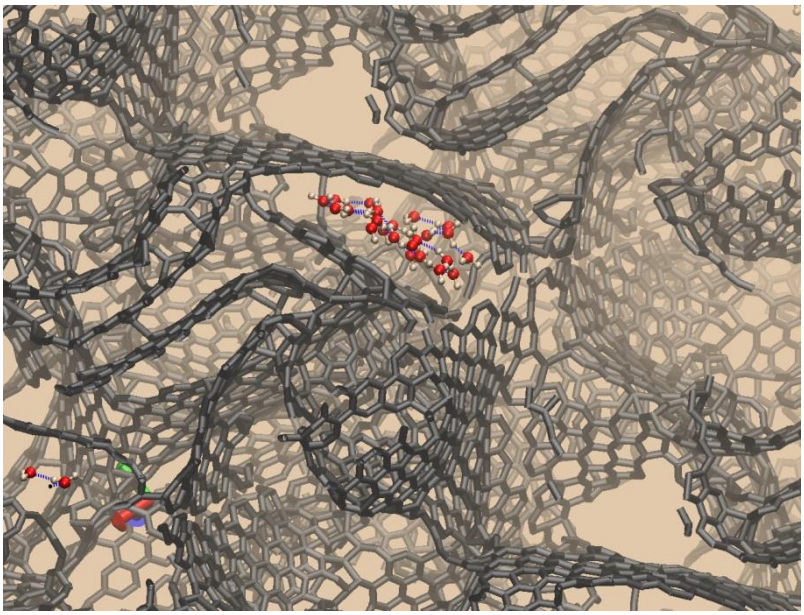

(a)

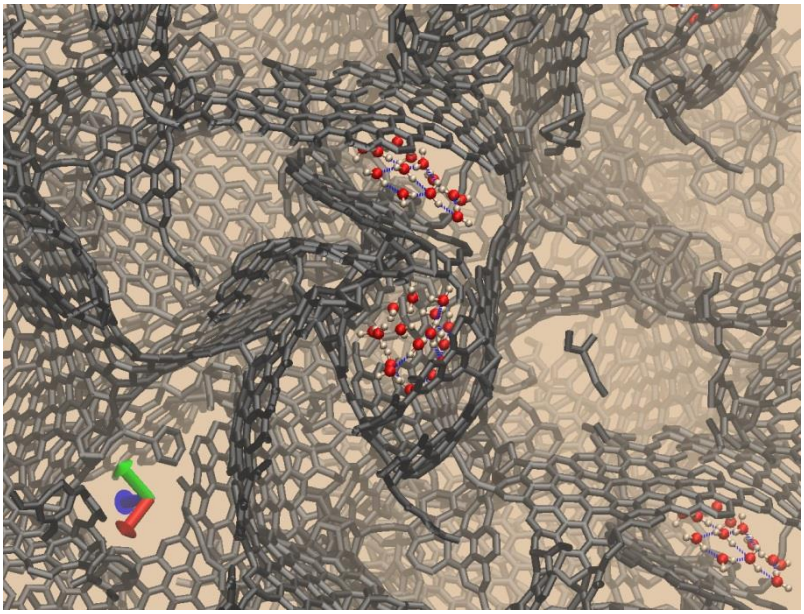

(b)

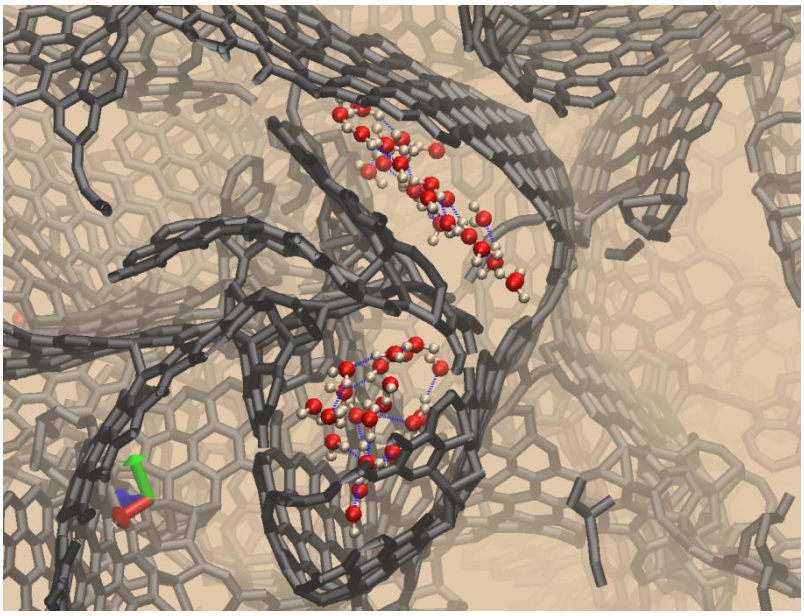

(c)

Figure 6-11. Stable water clusters at small nanopores of 7~ 9 Å at $P/P_o^{exp.}$ equal to (a) 0.45, (b) 0.5 and (c) 0.55 using SPC/E water model. Blue dashed lines represent hydrogen bonds

Here, we also note that dispersion interaction of disordered carbon walls with fluid particles is stronger than that of slit-like graphitic sheets, as demonstrated by several authors [13, 32, 64, 65].

This property imposes a stronger potential field on the water clusters in highly confined spaces of microporous carbon materials such as SiC-DC and activated carbon. As depicted in Figure 6-11, a network of hydrogen bonds stabilizes water clusters. Chen et al. have shown that confinement is able to stabilize hydrogen bonding among water molecules [66]. In our study, the geometric definition of hydrogen bonding is adopted from Luzar and Chandler's work, according to which donor-acceptor intermolecular distance and hydrogen-donor…acceptor angle are considered to be less than 3.5 Å and 30° respectively [67]. The number of hydrogen bonds (NHBs) per water molecule is known to be a good indicator of cluster stability based on intra-cluster hydrogen bond interactions [30, 63]. As depicted in Figure 6-12, the NHBs per molecule in our simulation is very close to the value reported by Nguyen and Bhatia [30] for their HRMC model of activated carbon, which is between 1.99 and 2.48 in unsaturated small pore regions.

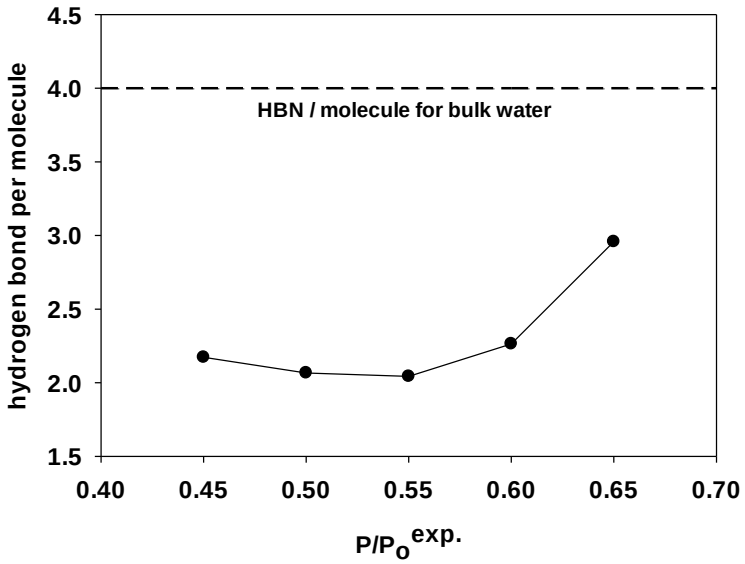

Figure 6-12. Variation of the number of hydrogen bonds (NHB) per molecule in final snapshots of the GCMC simulations (SPC/E model) versus experimental relative pressure

Here, we note that the analysis of water clusters illustrated in Figure 6-9, Figure 6-11 and Figure 6-12 is based on the SPC/E water model, since GCMC simulation based on the use of the SPC model at pressures below saturation pressure shows very weak adsorption, and does not generate sufficient configurations required for cluster analysis. Formation of stable water clusters in small nanopores occurs above or very close to the model saturation pressure, and is the seed for larger accumulation of water molecules occurring at higher pressures. Inter-connectivity of the disordered microporous carbon helps these cluster-like structures to be extended to larger pore

spaces, when pressure is adequately high. The influence of pore connectivity on the mechanism of water transport between small and large pores has been detailed earlier by Nguyen and Bhatia for their ACF-15 activated carbon fibre model [29].

6.4.2. Barrier to diffusion of small molecules

We have previously studied molecular diffusion and activation energy barriers of CO_2 and CH_4 in the amorphous structure of SiC-DC carbon, showing significant influence of structural heterogeneity on transport of these molecules [14, 34]. Here, we compare self-diffusion of water and non-polar gases with various molecular geometries to provide a better understanding of the significance of water clustering on the diffusion of water in the highly amorphous structure of SiC-DC. We also highlight the interplay between the clustering effect and activation energy barrier of water. Figure 6-13 illustrates the temperature dependence of the activation energy barrier for different non-polar molecules and water, at loading ~ 1.0 mmol/g.

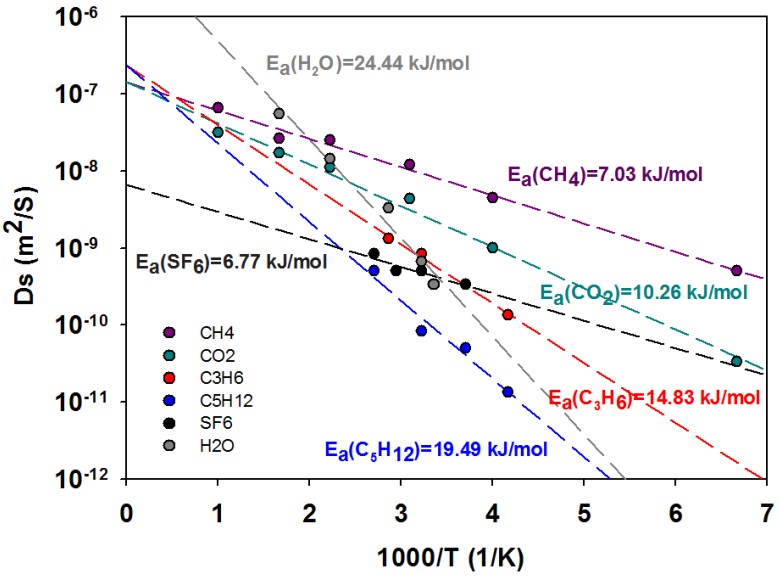

Figure 6-13. Activation energy barrier of different gases at ~ 1.0 mmol/g loading, estimated using the Arrhenius relation (water data are based on the SPC model)

In general, smaller molecules should face less severe energy barriers due to their smaller kinetic diameter, unless other competing factors come into effect. One example here is CO_2, whose molecular geometry overshadows the effect of its molecular size, so that its activation energy is larger than that of CH_4 and SF_6, despite its smaller kinetic diameter (SF_6 = 5.5 Å [55], H_2O = 2.65 Å [68], CO_2 = 3.30 Å [68], CH_4 = 3.8 Å [69]). This is due to unique linear geometry of CO_2, which allows the molecule to penetrate narrower micropores, thus being hindered by more severe energy

barriers. The larger molecules face even greater energy barriers in such micropores, and are unable to penetrate these pores in the MD time scale, and so the effective energy barriers obtained for these molecules are smaller. Yet, the best example for such exceptional behaviour is water, the smallest molecule among those studied here, whose cluster-like adsorption largely slows its molecular diffusion. Figure 6-14 depicts the correlation between self-diffusivities and kinetic diameters of the molecules investigated.

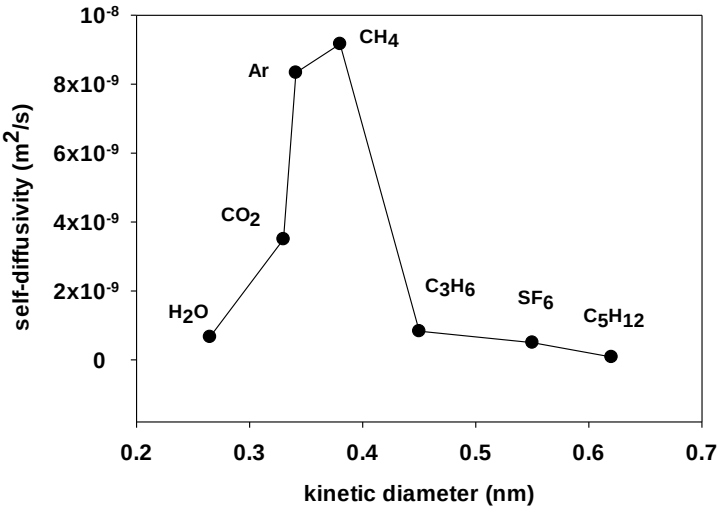

Figure 6-14. Correlation of self-diffusion coefficient with kinetic diameter of various molecules (water data is based on the SPC model)

To further study the anomalous diffusion of water, we report on simulated self-diffusion of SPC water at three different temperatures over a range of loadings from infinite dilution to more than 5 mmol/g solid. MSDs of water at infinite dilution for 298, 450 and 600 K are shown in Figure 6-15.

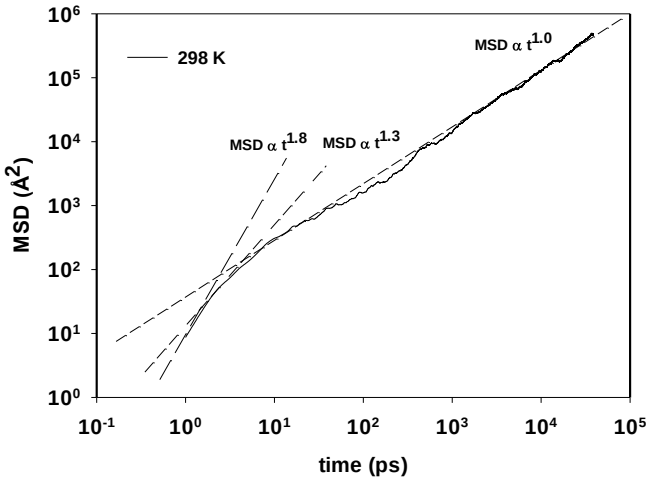

(a)

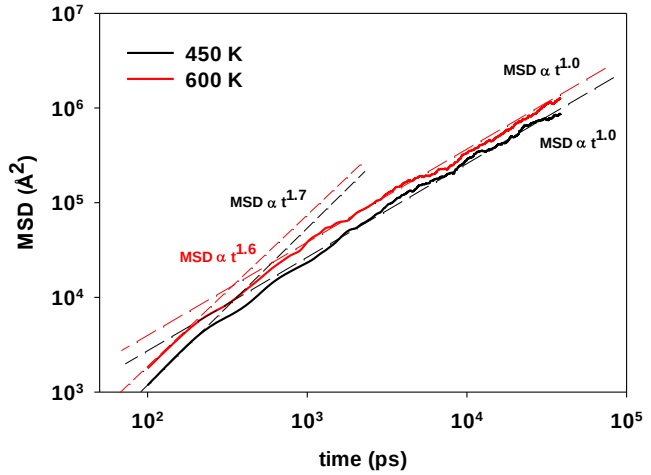

(b)

Figure 6-15. Mean-squared displacement of H_2O as a function of simulation time at infinite dilution and temperatures equal to (a) 298 K; (b) 450 K and 600 K

As seen here, for every temperature, a super-diffusive regime, where the MSD of the diffusant molecule is nearly proportional to $t^{1.5}$, is observed. At infinite dilution, the occurrence of a sub-diffusive regime is an indication of pore confinement [70]. However, we do not detect any single-file type sub-diffusion, where the slope of MSD is proportional to ~ 0.5-1.0 and molecules are unable to pass each other [71-73], over the region of time depicted in Figure 6-15. Molecules are seen to finally enter the diffusive (Fickian) regime, where the MSD slope will approach unity. Figure 6-16 depicts the loading dependence of the self-diffusion of water at 298 – 600 K.

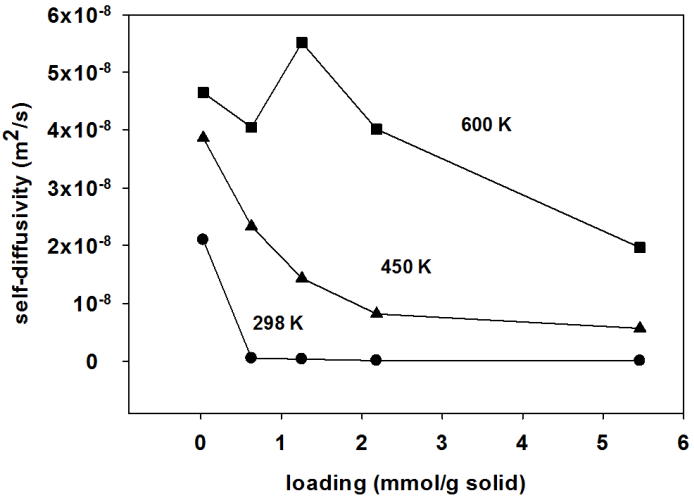

Figure 6-16. Loading dependence of self-diffusivity of SPC water at three different temperatures

The system is assumed to be in equilibrium with a saturated external environment at loadings beyond 0.24 mmol/g. As illustrated here, the diffusivity of water drops quickly as loading increases. This is a similar trend with that for activated carbon reported by Nguyen and Bhatia [30], but different from that of CO_2 and CH_4 in the SiC-DC model [34]. The self-diffusion of CO_2 and CH_4 shows a non-monotonic loading dependence, as reported in our previous publication [34], so that the diffusivity has a maximum at moderate loadings, an indication of structural heterogeneity, demonstrated by different authors [74-77]. Nevertheless, this phenomenon is absent in water diffusion in the SiC-DC structure at 298 K and 450 K, consistent with Nguyen and Bhatia's results for the diffusion of water in their activated carbon fibre model at 298 K [30]. Instead, the diffusivity of water in such microporous carbon structures has a monotonically declining trend with respect to loading, which is most likely due to the clustering effect. As noted earlier, stable water clusters are formed in highly narrow micropores due to strong interactions between water clusters and pore walls. In such tight confinements, water clusters are softer, because water molecules are more strongly influenced by the wall-molecule dispersive forces compared with larger pores, where hydrogen bonding and fluid-fluid electrostatic interactions become overwhelmingly dominant. In Figure 6-12, we showed that NHBs per molecule is higher at pore filling, where the water adsorbed in large pores is essentially in a state similar to that of bulk water (Figure 6-9 (e)). As a result of these effects, water clusters are more aggregated in larger pores allowing them to move as single

entities, as postulated by Nguyen and Bhatia [30]. The formation of such large and firmly aggregated clusters can reduce pore space accessibility and increase energy barriers for crossing pore entries. This in turn leads to the steep decline in self-diffusivity of water with pressure increase, depicted in Figure 6-16. This hypothesis is supported by the significantly higher activation energy barrier (E_a) of water than that of other gases, illustrated in Figure 6-13. The activation energies in this figure have been calculated for adsorption loading of ~ 1.0 mmol/g for all gases. As seen here, the activation energy barrier of water is even larger than that of neopentane, which has considerably larger kinetic diameter. Calculation of the activation energy of water at infinite dilution (0.027 mmol/g) based on the use of the different coefficients at the temperatures given in Figure 6-16 leads to a much lower E_a value of ~ 4.0 kJ/mol, indicating that water molecules (as opposed to clusters) face a much smaller energy barrier, when they are adsorbed in very small pores at low loading, an implication of the lack of the clustering-related pore blockage that is observed at higher loadings. A similar comparison for CH_4 is very insightful. The activation energy barrier of CH_4 at 1.2 mmol/g is smaller than that of infinite dilution by about 4.05 kJ/mol, as shown in our previous studies of gas diffusion in SiC-DC carbon structure [14, 34]; in contrast to the large increase in the E_a of water at higher loading. This is a strong indication of pore blockage due to water clustering during the diffusion of water, showing that the mechanism of water diffusion in disordered nanoporous carbon materials is significantly different from that of non-polar gases, for which the clustering mechanism is absent.

6.5. Conclusion

We have studied the adsorption and self-diffusion of various molecules with different molecular geometries and kinetic diameters in a realistic HRMC constructed model of microporous SiC-DC. The effect of pore confinement and molecular geometry on the adsorption behaviour of non-polar gases was investigated using GCMC simulation. We have shown that gas adsorption in the microporous structure of SiC-DC is sensitive to the changes in size and geometry of fluid molecules. Microporosity of the SiC-DC model is shown based on the steep drop of the total heat of adsorption of gases at low pressures, consistent with our experimental and simulated PSD. It is demonstrated that the rising trend of the heat of adsorption at elevated pressures is caused by tight packing of adsorbate molecules inside micropores leading to higher intermolecular interactions of fluid particles, evident from the stronger adsorbate-adsorbate contribution of the heat of adsorption. Furthermore, we find that molecular flexibility has an observable effect on the total heat of

adsorption; nevertheless its effect on the amount of gas adsorption remains negligible. We have compared our results with those for water adsorption, to better understand the difference from other gases, arising from interplay between the effect of pore confinement and hydrogen bonding on the water isotherm. The adsorption mechanism of water is found to be triggered by clustering of water molecules in highly confined micropores of 7.0 – 9.0 Å, whose formation and growth are driven by the intermolecular hydrogen bonding. We have demonstrated that in the absence of activated hydrophilic sites, pore-filling of amorphous SiC-DC and activated carbon fibre does not occur until pressure exceeds the saturation pressure, which is not always the case in slit-pore models.

We have also estimated the activation energy barrier for water and non-polar molecules based on the Arrhenius formalism, by investigating molecular self-diffusion using MD simulation. It is found that there is a clear correlation between the self-diffusivities and the kinetic molecular diameter for most of the non-polar molecules. Contrary to CO_2 and CH_4, whose self-diffusion is greatly influenced by heterogeneity of the adsorbent structure, the diffusion of water is dominated by the cooperative effect of hydrogen bonding and pore confinement, leading to the formation of stable water clusters with different levels of aggregation. These clusters face greater activation energy barriers at higher loadings, an indication of pore blockage phenomenon. Thus, the diffusion mechanism for water is dictated by different factors compared with non-polar gases, and leads to significant deviation from the general correlation found between diffusivity of non-polar molecules and their kinetic diameter.

6.6. Acknowledgement

Financial support from Australian Research Council (ARC) under the Discovery Scheme is gratefully acknowledged. This research was undertaken with the assistance of the computational resources provided at the NCI Facility systems at the Australian National University (ANU), through the National Computational Merit Allocation Scheme supported by the Australian Government.

6.7. References

1. Bhatia, S.K., M.R. Bonilla, and D. Nicholson, *Molecular transport in nanopores: a theoretical perspective.* Physical Chemistry Chemical Physics, 2011. **13**(34): p. 15350-15383.

2. Nicholson, D. and S.K. Bhatia, *Fluid transport in nanospaces.* Molecular Simulation, 2009. **35**(1-2): p. 109-121.

3. Sheehan, A.D., et al., *The Development of Novel Miniaturized Immuno-sensing Devices: A Review of a Small Technology with a Large Future.* Analytical Letters, 2003. **36**(3): p. 511-537.

4. Herold, K.E.R., Avraham, *Lab on a Chip Technology (Vol. 1): Fabrication and microfluidics*. Vol. 1. 2009, Norfolk: Caister Academic Press.

5. Gogotsi, Y., et al., *Nanoporous carbide-derived carbon with tunable pore size.* Nature Materials, 2003. **2**(9): p. 591-594.

6. Presser, V., M. Heon, and Y. Gogotsi, *Carbide-Derived Carbons – From Porous Networks to Nanotubes and Graphene.* Advanced Functional Materials, 2011. **21**(5): p. 810-833.

7. Zhou, W., et al., *Synthesis, Structure, and Properties of Single-Walled Carbon Nanotubes.* Advanced Materials, 2009. **21**(45): p. 4565-4583.

8. Thostenson, E.T., Z. Ren, and T.-W. Chou, *Advances in the science and technology of carbon nanotubes and their composites: a review.* Composites Science and Technology, 2001. **61**(13): p. 1899-1912.

9. Furukawa, H., et al., *Ultrahigh Porosity in Metal-Organic Frameworks.* Science, 2010. **329**(5990): p. 424-428.

10. Liu, J., et al., *A novel series of isoreticular metal organic frameworks: realizing metastable structures by liquid phase epitaxy.* Scientific Reports, 2012. **2**: p. 921.

11. Li, H., et al., *Design and synthesis of an exceptionally stable and highly porous metal-organic framework.* Nature, 1999. **402**(6759): p. 276-279.

12. Nguyen, T.X., J.S. Bae, and S.K. Bhatia, *Characterization and Adsorption Modeling of Silicon Carbide-Derived Carbons.* Langmuir, 2009. **25**(4): p. 2121-2132.

13. Farmahini, A.H., G. Opletal, and S.K. Bhatia, *Structural Modelling of Silicon Carbide-Derived Nanoporous Carbon by Hybrid Reverse Monte Carlo Simulation.* Journal of Physical Chemistry C, 2013. **117**(27): p. 14081-14094.

14. Shahtalebi, A., et al., *Slow diffusion of methane in ultra-micropores of silicon carbide-derived carbon.* Carbon, 2014. **77**(0): p. 560-576.

15. Bhatia, S.K. and T.X. Nguyen, *Potential of Silicon Carbide-Derived Carbon for Carbon Capture.* Industrial & Engineering Chemistry Research, 2011. **50**(17): p. 10380-10383.

16. Gogotsi, Y., et al., *Tailoring of Nanoscale Porosity in Carbide-Derived Carbons for Hydrogen Storage.* Journal of the American Chemical Society, 2005. **127**(46): p. 16006-16007.

17. Bonilla, M.R.n., et al., *Heat Treatment-Induced Structural Changes in SiC-Derived Carbons and their Impact on Gas Storage Potential.* Journal of Physical Chemistry C, 2010. **114**(39): p. 16562-16575.

18. Gong, R. and T.C. Keener, *A Qualitative Analysis of the Effects of Water Vapor on Multi-Component Vapor-Phase Carbon Adsorption.* Air & Waste, 1993. **43**(6): p. 864-872.

19. Bourdin, V., P. Grenier, and A. Malka-Edery. *Fundamentals of Adsorption*. in *Proceedings of the Sixth Conference on Fundamentals of Adsorption*. 1998. Presqu'ile de Giens, Paris: Elsevier.

20. Kimura, T., et al., *Cluster-Associated Filling of Water in Hydrophobic Carbon Micropores.* Journal of Physical Chemistry B, 2004. **108**(37): p. 14043-14048.

21. Brennan, J.K., et al., *Water in porous carbons.* Colloids and Surfaces, A, 2001. **187–188**(0): p. 539-568.

22. Müller, E.A., et al., *Adsorption of Water on Activated Carbons: A Molecular Simulation Study.* Journal of Physical Chemistry, 1996. **100**(4): p. 1189-1196.

23. Easton, E.B. and W.D. Machin, *Adsorption of Water Vapor on a Graphitized Carbon Black.* Journal of Colloid and Interface Science, 2000. **231**(1): p. 204-206.

24. Hummer, G., J.C. Rasaiah, and J.P. Noworyta, *Water conduction through the hydrophobic channel of a carbon nanotube.* Nature, 2001. **414**(6860): p. 188-190.

25. Ohba, T., H. Kanoh, and K. Kaneko, *Affinity Transformation from Hydrophilicity to Hydrophobicity of Water Molecules on the Basis of Adsorption of Water in Graphitic Nanopores.* Journal of the American Chemical Society, 2004. **126**(5): p. 1560-1562.

26. Liu, J.C. and P.A. Monson, *Does Water Condense in Carbon Pores?.* Langmuir, 2005. **21**(22): p. 10219-10225.

27. Liu, J.C. and P.A. Monson, *Monte Carlo Simulation Study of Water Adsorption in Activated Carbon.* Industrial & Engineering Chemistry Research, 2006. **45**(16): p. 5649-5656.

28. Brennan, J.K., K.T. Thomson, and K.E. Gubbins, *Adsorption of Water in Activated Carbons: Effects of Pore Blocking and Connectivity.* Langmuir, 2002. **18**(14): p. 5438-5447.

29. Nguyen, T.X. and S.K. Bhatia, *How Water Adsorbs in Hydrophobic Nanospaces.* Journal of Physical Chemistry C, 2011: p. 16606–16612.

30. Nguyen, T.X. and S.K. Bhatia, *Some Anomalies in the Self-Diffusion of Water in Disordered Carbons.* Journal of Physical Chemistry C, 2012. **116**(5): p. 3667-3676.

31. Opletal, G., et al., *Hybrid approach for generating realistic amorphous carbon structure using metropolis and reverse Monte Carlo*. Molecular Simulation, 2002. **28**(10-11): p. 927-938.

32. Nguyen, T.X., et al., *New Method for Atomistic Modeling of the Microstructure of Activated Carbons Using Hybrid Reverse Monte Carlo Simulation.* Langmuir, 2008. **24**(15): p. 7912-7922.

33. Jain, S.K., et al., *Molecular Modeling of Porous Carbons Using the Hybrid Reverse Monte Carlo Method.* Langmuir, 2006. **22**(24): p. 9942-9948.

34. Farmahini, A.H., et al., *Influence of Structural Heterogeneity on Diffusion of CH4 and CO2 in Silicon Carbide-Derived Nanoporous Carbon.* Journal of Physical Chemistry C, 2014. **118**(22): p. 11784-11798.

35. Nguyen, T.X. and S.K. Bhatia, *Characterization of accessible and inaccessible pores in microporous carbons by a combination of adsorption and small angle neutron scattering.* Carbon, 2012. **50**(8): p. 3045-3054.

36. Gelb, L.D. and K.E. Gubbins, *Characterization of Porous Glasses: Simulation Models, Adsorption Isotherms, and the Brunauer−Emmett−Teller Analysis Method.* Langmuir, 1998. **14**(8): p. 2097-2111.

37. Gelb, L.D. and K.E. Gubbins, *Pore Size Distributions in Porous Glasses: A Computer Simulation Study.* Langmuir, 1998. **15**(2): p. 305-308.

38. Dubbeldam, D., et al., *RASPA 1.0: Molecular Software Package for Adsorption and Diffusion in (Flexible) Nanoporous Materials*. 2013: Northwestern University: Evanston, IL.

39. Rahman, A., *Correlations in the Motion of Atoms in Liquid Argon.* Physical Review, 1964. **136**(2A): p. A405-A411.

40. Nguyen, T.X., S.K. Bhatia, and D. Nicholson, *Prediction of High-Pressure Adsorption Equilibrium of Supercritical Gases Using Density Functional Theory.* Langmuir, 2005. **21**(7): p. 3187-3197.

41. Bhatia, S.K. and D. Nicholson, *Adsorption and Diffusion of Methane in Silica Nanopores: A Comparison of Single-Site and Five-Site Models.* Journal of Physical Chemistry C, 2011. **116**(3): p. 2344-2355.

42. Liu, B., *Molecular simulation studies of adsorption and diffusion : phenomena of gases in porous materials*, in *Van't Hoff Institute for Molecular Sciences (HIMS)*. 2008, University of Amsterdam Amsterdam p. 134.

43. García-Pérez, E., et al., *Influence of Cation Na/Ca Ratio on Adsorption in LTA 5A: A Systematic Molecular Simulation Study of Alkane Chain Length.* Journal of Physical Chemistry B, 2006. **110**(47): p. 23968-23976.

44. Martin, M.G. and J.I. Siepmann, *Novel Configurational-Bias Monte Carlo Method for Branched Molecules. Transferable Potentials for Phase Equilibria. 2. United-Atom*

Description of Branched Alkanes. Journal of Physical Chemistry B, 1999. **103**(21): p. 4508-4517.

45. Olivet, A. and L.F. Vega, *Optimized molecular force field for sulfur hexafluoride simulations.* Journal of Chemical Physics, 2007. **126**(14): p. 144502.

46. Berendsen, H.J.C., et al. *Interaction models for water in relation to protein hydration*. in *14th Jerusalem symposium on quantum chemistry and biochemistry: "Intermolecular Forces"*. 1981. JERUSALEM: Reidel, Dordrecht

47. Berendsen, H.J.C., J.R. Grigera, and T.P. Straatsma, *The missing term in effective pair potentials.* Journal of Physical Chemistry, 1987. **91**(24): p. 6269-6271.

48. Plimpton, S., *Fast Parallel Algorithms for Short-Range Molecular Dynamics.* Journal of Computational Physics, 1995. **117**(1): p. 1-19.

49. Tuckerman, M.E., C.J. Mundy, and G.J. Martyna, *On the classical statistical mechanics of non-Hamiltonian systems.* EPL (Europhysics Letters), 1999. **45**(2): p. 149.

50. Tuckerman, M.E., et al., *Non-Hamiltonian molecular dynamics: Generalizing Hamiltonian phase space principles to non-Hamiltonian systems.* Journal of Chemical Physics, 2001. **115**(4): p. 1678-1702.

51. Kamberaj, H., R.J. Low, and M.P. Neal, *Time reversible and symplectic integrators for molecular dynamics simulations of rigid molecules.* Journal of Chemical Physics, 2005. **122**(22): p. 224114.

52. Ryckaert, J.-P., G. Ciccotti, and H.J.C. Berendsen, *Numerical integration of the cartesian equations of motion of a system with constraints: molecular dynamics of n-alkanes.* Journal of Computational Physics, 1977. **23**(3): p. 327-341.

53. Bae, J.-S., T.X. Nguyen, and S.K. Bhatia, *Pore accessibility of Ti3SiC2-derived carbons.* Carbon, 2014. **68**(0): p. 531-541.

54. Oikawa, H., et al., *Highly selective conversion of ethene to propene over SAPO-34 as a solid acid catalyst.* Applied Catalysis A: General, 2006. **312**(0): p. 181-185.

55. Senkovska, I., et al., *Adsorptive capturing and storing greenhouse gases such as sulfur hexafluoride and carbon tetrafluoride using metal–organic frameworks.* Microporous and Mesoporous Materials, 2012. **156**(0): p. 115-120.

56. Centeno, T.A. and A.B. Fuertes, *Carbon molecular sieve gas separation membranes based on poly(vinylidene chloride-co-vinyl chloride).* Carbon, 2000. **38**(7): p. 1067-1073.

57. Striolo, A., et al., *Water Adsorption in Carbon-Slit Nanopores.* Langmuir, 2003. **19**(20): p. 8583-8591.

58. Sullivan, P., et al., *Water adsorption with hysteresis effect onto microporous activated carbon fabrics.* Adsorption, 2007. **13**(3-4): p. 173-189.

59. Mowla, D., D.D. Do, and K. Kaneko, *Adsorption of water vapor on activated carbon: A brief overview.* Chemistry and Physics of Carbon, 2003. **28**: p. 229 - 262.

60. Do, D.D. and H.D. Do, *A model for water adsorption in activated carbon.* Carbon, 2000. **38**(5): p. 767-773.

61. Errington, J.R. and A.Z. Panagiotopoulos, *A Fixed Point Charge Model for Water Optimized to the Vapor−Liquid Coexistence Properties.* Journal of Physical Chemistry B, 1998. **102**(38): p. 7470-7475.

62. Tomonori, O. and K. Katsumi, *Initial filling mechanism of predominant water adsorption on hydrophobic slit-shaped carbon nanopores.* Journal of Physics: Conference Series, 2009. **177**(1): p. 012001.

63. Vaitheeswaran, S., et al., *Water clusters in nonpolar cavities.* Proceedings of the National Academy of Sciences of the United States of America, 2004. **101**(49): p. 17002-17005.

64. Palmer, J.C., et al., *Detailed structural models for activated carbons from molecular simulation.* Carbon, 2009. **47**(12): p. 2904-2913.

65. Klauda, J.B., J. Jiang, and S.I. Sandler, *An ab Initio Study on the Effect of Carbon Surface Curvature and Ring Structure on N2(O2)−Carbon Intermolecular Potentials.* Journal of Physical Chemistry B, 2004. **108**(28): p. 9842-9851.

66. Chen, Q., et al., *The effect of hydrogen bonds on diffusion mechanism of water inside single-walled carbon nanotubes.* Journal of Chemical Physics, 2014. **140**(21): p. 214507-214513.

67. Luzar, A. and D. Chandler, *Hydrogen-bond kinetics in liquid water.* Nature, 1996. **379**(6560): p. 55-57.

68. Sumida, K., et al., *Carbon Dioxide Capture in Metal–Organic Frameworks.* Chemical Reviews, 2011. **112**(2): p. 724-781.

69. Mehio, N., S. Dai, and D.-e. Jiang, *Quantum Mechanical Basis for Kinetic Diameters of Small Gaseous Molecules.* Journal of Physical Chemistry A, 2014. **118**(6): p. 1150-1154.

70. Moore, J.D., et al., *Adsorption and diffusion of argon confined in ordered and disordered microporous carbons.* Applied Surface Science, 2010. **256**(17): p. 5131-5136.

71. Hahn, K. and J. Kärger, *Deviations from the Normal Time Regime of Single-File Diffusion.* Journal of Physical Chemistry B, 1998. **102**(30): p. 5766-5771.

72. Hahn, K., J. Kärger, and V. Kukla, *Single-File Diffusion Observation.* Physical Review Letters, 1996. **76**(15): p. 2762-2765.

73. Felderhof, B.U., *Fluctuation theory of single-file diffusion.* Journal of Chemical Physics, 2009. **131**(6): p. 064504

74. Brandani, S., Ruthven, D.M., and Ka¨rger, J., *Concentration dependence of self-diffusivity of methanol in NaX zeolite crystals.* Zeolites, 1995. **15**(6): p. 494-495.

75. Karger, J. and H. Pfeifer, *Molecular self-diffusion in active carbons.* Pure and Applied Chemistry, 1989. **61**(11): p. 1875-1880.

76. Valiullin, R., J. Karger, and R. Glaser, *Correlating phase behaviour and diffusion in mesopores: perspectives revealed by pulsed field gradient NMR.* Physical Chemistry Chemical Physics, 2009. **11**(16): p. 2833-2853.

77. Rincon Bonilla, M. and S.K. Bhatia, *Diffusion in Pore Networks: Effective Self-Diffusivity and the Concept of Tortuosity.* Journal of Physical Chemistry C, 2013. **117**(7): p. 3343-3357.

7. Fluorinated Carbide-Derived Carbon: More Hydrophilic, Yet Apparently More Hydrophobic

*Amir H. Farmahini†, David S. Sholl‡, Suresh K. Bhatia†**

J. Am. Chem. Soc. (JACS), 2015, 137 (18), pp 5969–5979

DOI: 10.1021/jacs.5b01105

Accepted: April 24, 2015 - Published: May 13, 2015

† School of Chemical Engineering, The University of Queensland (UQ), QLD 4072, Australia

‡ School of Chemical and Biomolecular Engineering, Georgia Institute of Technology, Atlanta 30332, USA

7.1. Abstract

We explore the effect of fluorine doping on hydrophobicity of nanoporous silicon carbide-derived carbon (SiCDC), and investigate the underlying barriers for adsorption and diffusion of water vapor and CO_2 in the fluorinated and non-fluorinated structures. We develop atomistic models of fluorine-doped SiCDC at three different levels of fluorination, based on a hybrid reverse Monte Carlo constructed model of SiCDC, and develop a novel first-principles force field for the simulation of adsorption and transport of water and CO_2 in the fluorine-doped carbon materials. We demonstrate an apparent dual effect of fluorination, showing that while fluorination generates more hydrophilic carbon surfaces, they actually act as more hydrophobic structures due to enhanced energy barriers in the disordered network of microporous carbon. While an increase in adsorption energy and in water uptake is seen for fluorine-doped carbon, large internal free energy barriers as well as the results of MD simulations demonstrate that the increased adsorption is kinetically limited and not experimentally observable on practical time scales. We show that an increase in apparent hydrophobicity due to fluorination is mediated by larger free energy barriers arising from stronger binding of fluid molecules inside the pore network, as opposed to repulsion or steric hindrance to the diffusion of molecules through narrow pore entries. For carbon dioxide, adsorption enthalpies and activation energy barriers are both decreased on fluorination, indicating weakened solid-fluid binding energies in the fluorinated systems.

Keywords: water adsorption, carbon dioxide adsorption, fluorine-doped microporous carbon, ab-initio calculations, force field development, diffusion, molecular dynamics simulation, grand canonical Monte Carlo

7.2. Introduction

The engineering of adsorbents to increase hydrophobicity is an area of much current interest, as moisture present in gas streams reduces the efficiency of processes for gas separation and storage. Fluorination of porous carbon has long been known to increase hydrophobicity [1-5], and has found application not only in gas adsorption but also in proton exchange membrane (PEM) fuel cells and microfluidic devices [6-9]. Fluorine-doped graphite (poly carbon monofluoride) has been shown to be super-hydrophobic [10], based on the low sliding angles of water; while observations of high contact angle on fluorine-doped amorphous carbon films with diamond-like structure indicate these to be as hydrophobic as polytetrafluoroethylene (PTFE) [11]. Nevertheless, despite such evidence, fundamental studies of the apparently water-repelling nature of fluorinated microporous carbon are scarce, and mechanistic understanding of the increase in hydrophobicity remains an open question.

Studies have shown that fluorination of activated carbon fibre (ACF) reduces N_2 adsorption, due to reduction in pore volume, surface area and pore size [12-13] and of the surface energy [12]; with the level of fluorination having an inverse relation with pore volume, surface area and average pore width of the sample [13]. Li et al. [14-15] reported significant reduction of N_2 and ethanol adsorption after fluorination of microporous ACF, which they attribute to reduction of micropore volume arising from pore blockage by C-F bonds. On the other hand, for water the observed decrease in adsorption was found to be much greater than that justified by the decrease in micropore volume. This they take to be an indication of increased hydrophobicity on fluorination and repulsive nature of the fluorine atoms [14], since the basic microporous structure of the ACF was considered unaltered by fluorination while the micropore wall structure adapted to the fluorinated state. Li et al. [15] hypothesized that water clusters cannot be formed on the fluorinated surface of F-ACF, while methanol and ethanol do adsorb in the form of molecular clusters due to attractive vdW interactions between their nonpolar functional groups and the hydrophobic surface of F-ACF. An interesting feature of their results is strong adsorption/desorption hysteresis for water, but its complete absence for methanol and ethanol. While the reasons for this were not discussed, the presence of significant energy barriers for water adsorption/desorption would appear likely. More recently, such hysteresis for water adsorption on virgin and mildly fluorinated activated carbon, and a decrease of water adsorption on fluorination has also been noted by Parmentier et al. [16]. While they attribute the

decrease of adsorption on fluorination to increased hydrophobicity, they also noted an increase in water content on the desorption branch for the fluorinated material for relative pressure below 0.5, an indication of increased hydrophilicity.

Thus, it is clear that while there exists experimental evidence for reduced water adsorption on fluorination, its interpretation in terms of the concept of hydrophobicity is tenuous. Fluorine-doped carbon forms a variety of complex covalently bonded substances whose chemical and structural properties are influenced by semi-ionic, ionic and van der Waals interactions [17]. Therefore, understanding the mechanism leading to reduction of water uptake, or increase of "hydrophobicity", requires fundamental knowledge of the adsorption process at molecular scales.

Here, we investigate the mechanisms underlying hydrophobicity of fluorinated microporous carbon to provide a clear description of this concept. The strong structure-dependence of adsorption necessitates access to a realistic representation of the microporous network of carbon atoms, which is non-trivial. To this end, we use a hybrid reverse Monte Carlo simulation-based atomistic model of silicon carbide-derived nanoporous carbon (SiCDC) for modeling fluorinated carbon samples. While this structural model has been extensively validated against adsorption data [18-21], investigation of the effect of fluorination on adsorption, using this as a platform, is unique to this study. Here we design models of fluorinated silicon carbide-derived carbon (F-SiCDC) at three levels of fluorination, based on this virgin model; and investigate mechanisms underlying water adsorption in these materials.

We also report on development of a novel first-principles force field for the adsorption of water vapor and CO_2 in fluorinated microporous carbon structures. Our study demonstrates that while fluorination leads to more hydrophilic carbon surfaces, they actually act as more hydrophobic structures, due to enhanced energy barriers in the disordered microporous carbon network, revealing an apparent dual effect of fluorination.

7.3. Computational details

7.3.1. Development of first-principles force fields

We have developed a new first-principles force field for CO_2 and water vapor adsorption on fluorinated porous carbons. Considerable progress has been made in recent years on development of force fields for adsorption in porous materials, as reviewed by Fang et al [22]. We performed DFT calculations on a 22 × 22 Å sheet of fluorinated graphene containing 150 carbon and 17 fluorine atoms, having a circular defect at the center, of diameter ~9 Å, on whose edge unsaturated carbon

atoms are fluorinated. A 3 × 3 × 3 extended super cell of this structure, with interlayer distance equal to 20 Å, illustrated in Figure 7-1, was used for simulations.

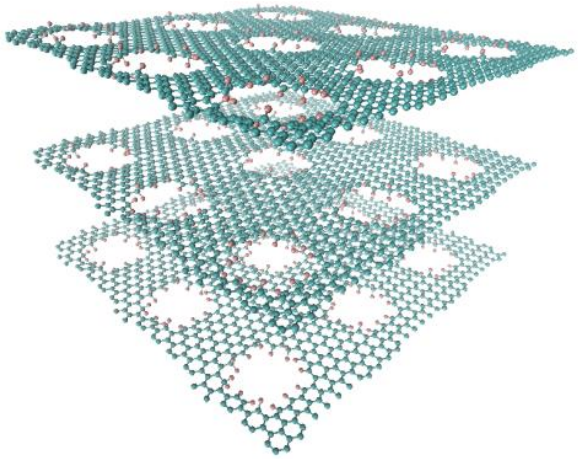

Figure 7-1. Fluorinated sheet of graphene with embedded defects in the form of pores.

We used methods applied by Fang and co-workers to develop force fields for CO_2 adsorption in zeolites [23-25], that have been validated for even smaller systems.

Geometry optimization of the periodic system was performed using the dispersion-corrected DFT method of Grimme (DFT-D2) [26] implemented in VASP [27, 28] following [23, 24]

$$E_{disp.} = -s_6 \sum_{i=1}^{N-1} \sum_{j=i+1}^{N} \frac{C_6^{ij}}{r_{ij}^6} f_{damp}(r_{ij}) \qquad (7\text{-}1)$$

where, s_6 is a global scaling factor for each functional, N is the number of atoms, r_{ij} is the interatomic distance for atoms i and j, and finally C^{ij}_6 represents the dispersion coefficient. Electron-ion interactions were modeled using the projector augmented wave (PAW) formalism [29, 30] with the Perdew-Burke-Ernzerhof (PBE) functional [31] chosen for the generalized gradient approximation (GGA). A plane wave basis set was employed with an energy cutoff of 400 eV for valence electrons. Reciprocal space was sampled at the Γ-point only. Geometry optimization was performed until forces on all atoms were smaller than 0.03 eV/Å.

Point charges on atoms in the fluorinated graphene were assigned using the density-derived electrostatic and chemical (DDEC) charges approach [32-35]. The DDEC method reproduces the electrostatic potential exactly outside the electron distribution by partitioning the electron and spin densities to compute net atomic charges and atomic spin moments [32-35]. The effect of

polarization was investigated by calculating point charges of the fluorinated graphene in the presence of water molecules and comparing the results with charges for the isolated system. Polarization changed the total energy of the system by only 8.6%. Our results show that the mean absolute deviation of the charges in the polarized fluorinated graphene is 0.009e relative to the unpolarized graphene. Also, the mean absolute deviation of charges for polarized water molecules is equal to 0.03e relative to the SPC model used in our GCMC and MD simulations. Thus, polarization mainly affects the water molecules. We also note that the polarization effect is implicitly considered here, since we match the solid-fluid adsorption energy by fitting the parameters of the non-electrostatic part of the force field, while retaining the electrostatic part in the SPC water model as discussed below. A similar approach has previously been adopted by Calero et al. [36], in which effective Lennard-Jones interactions between the solid and weakly polarizable alkanes were used. A much more computationally intensive calculation would explicitly define a polarization term in the developed force field [37], but was not attempted here.

Single point energy calculations (SPE) were performed for individual water and CO_2 molecules interacting with the fluorinated graphene using VASP. A large number of molecular configurations were randomly generated for adsorbate molecules in a simulation box containing the fluorinated graphene, to adequately sample the pore space. This includes both low and high-energy configurations of adsorbate molecules, so that the force field derived from our DFT data appropriately describes different energy states of the system for applications in Grand Canonical Monte Carlo (GCMC) and Molecular Dynamics (MD) simulations. For SPE calculations, relaxation of the electronic degrees of freedom was terminated when variation of the total energy between two consecutive iterations was smaller than 0.0001 eV. The solid-fluid interaction energy of the system obtained from DFT calculations for all configurations was then fitted to the 12-6 LJ potential model augmented by electrostatic interactions [23, 24]:

$$E_{ff}(r_{ij}) = E_{vdW} + E_{Coul} = s_{12}\frac{C_{12}^{ij}}{r_{ij}^{12}} - s_6\frac{C_6^{ij}}{r_{ij}^6} + \frac{q_i q_j}{\varepsilon_o r_{ij}} \tag{7-2}$$

here, r_{ij} represents interatomic distances of ij pairs, C^{ij}_{12} and C^{ij}_6 are repulsive and attractive coefficients respectively, q_i and q_j stand for atomic charges of atoms i and j, and ε_o is the permittivity of free space. s_{12} and s_6 are global scaling factors for force field fitting. In this equation, charges for water were taken from the SPC model [38] and for CO_2 from a model described by Nguyen et al for CO_2 adsorption in microporous carbon [39, 40]. Point charges of the solid fluorinated graphene are obtained from our DFT calculations, as described below. The second term

in the right hand side of equation (7-2) is the Grimme's dispersion-corrected form of attractive interactions without the damping function of equation (7-1), since the repulsive term is explicitly included [23]. The repulsion coefficient C^{ij}_{12} is calculated following

$$\frac{C_{12}^{ij}}{C_{6}^{ij}} = \frac{(R_0^i + R_0^j)^6}{2} \tag{7-3}$$

here the parameters C_6 and R_0 are taken from Grimme's study on the long-range corrected semi-empirical GGA-Type density functional [26]. The attractive and repulsive terms of the vdW energy obtained from equation (7-2) are equivalent to the corresponding terms in the usual 12-6 LJ representation

$$E_{LJ}(r_{ij}) = 4\varepsilon_{ij}\left[\left(\frac{\sigma_{ij}}{r_{ij}}\right)^{12} - \left(\frac{\sigma_{ij}}{r_{ij}}\right)^{6}\right] \tag{7-4}$$

where, ε_{ij} is the minimum-potential well depth, σ_{ij} is the distance, at which interatomic potential energy is zero and r_{ij} is the inter-particle separation. In order to calculate ε and σ from equations (7-2) and (7-4), the distances $(1/r_{ij})^{12}$ and $(1/r_{ij})^{6}$ for each cross-species were measured in an extended periodic cell of 3 × 3 × 3 model (Figure 7-1) to account for vdW contributions of neighboring atoms, beyond which such contributions are negligible, as described by Zang et al [24].

After an initial force field was generated using the DFT data described above, this force field was used to generate a new set of molecular configurations for water and CO_2 using GCMC. DFT-D2 energies of these newly generated configurations were then fitted to equation (7-4) once again to obtain a new set of interaction parameters (ε and σ). This procedure was repeated iteratively until the values obtained for ε and σ were converged [23,25], which is achieved after three iterations here. In this way, a total of 905 and 676 molecular configurations were generated and fitted for water and CO_2 respectively. To ensure that our force field captures a broader range of possible energy states, DFT-D2 energies of all configurations, which were previously used for fitting in every iteration, were combined and again considered for fitting, from which the final LJ parameters (listed in Table S1) were calculated. We note that in this table the value of ε for the F-H pair is equal to zero, which arises from the fitting. This is consistent with the absence of LJ interactions for the hydrogen atom in SPC [38] and SPC/E [41] models of water. Figure 7-2 illustrates the agreement between our fitted potential and the full set of DFT-D2 interaction energies.

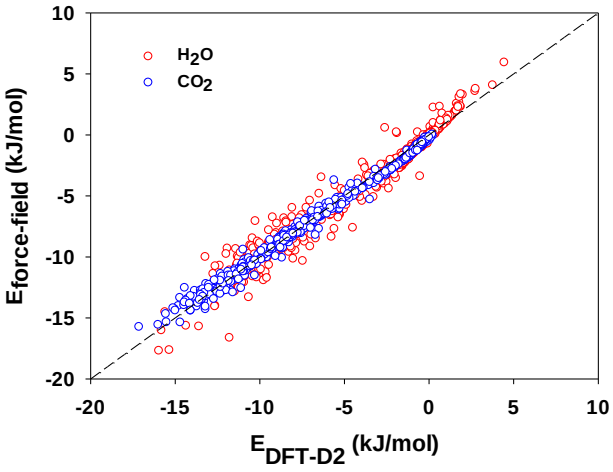

Figure 7-2. Comparison of the DFT-D2 energy with force field energy for H_2O and CO_2.

7.3.2. Modeling Fluorine-doped CDC

We have developed atomistic models of fluorine-doped SiCDC at different levels of fluorination, having F/C atomic ratios of 0.019, 0.053 and 0.1, labeled as F-SiCDC.1, F-SiCDC.2 and F-SiCDC.3 respectively. The skeleton of all three models is based on a hybrid reverse Monte Carlo (HRMC) constructed model of SiCDC, recently developed in our laboratory [18], that has shown good performance against a wide range of structural characterization, equilibrium and experimental kinetic uptake data for different gases [18-21].

The virgin SiCDC model consists of 3052 carbon atoms in a 40 Å cubic unit cell. This model was subjected to fluorination of the carbon structure at the edges of carbon sheets, in addition to the carbon atoms with unsaturated bonding. Such unsaturated carbons are found in the amorphous SiCDC structure in substantial amounts, due to existence of various structural defects in this material [18]. The structure of the fluorinated models was then optimized using the conjugate gradient algorithm in GULP [42, 43]. Bonded carbon-carbon interactions were modeled using the reactive EDIP force field [44, 45]. Bonded F-C interactions consist of two-body and three-body interactions, for which the interaction parameters are given in Table S2. Non-bonded vdW interactions for F-F and F-C pairs applied during geometry optimization are calculated using the 12-6 LJ potential with cut-off distance of 10 Å. Details of LJ parameters used in this section are also provided in Table S2.

Partial charge distributions of the F-SiCDC models were determined based on the pattern derived from the charge distribution of the fluorinated graphene sheet, discussed above, in addition to the

partial charge distribution of a sample fluorinated disordered carbon cluster removed from the original SiCDC model, as shown in Figure 7-3. The reason for including charge distribution of the disordered cluster of carbon atoms in our investigation was to account for the effect of curvature on the distribution of partial charges in the charge pattern derived for the target F-SiCDC models. Details of calculations for DDEC charges obtained from the DFT-D2 energy of the disordered carbon cluster are similar to those discussed for the fluorinated graphene sheet in the previous section.

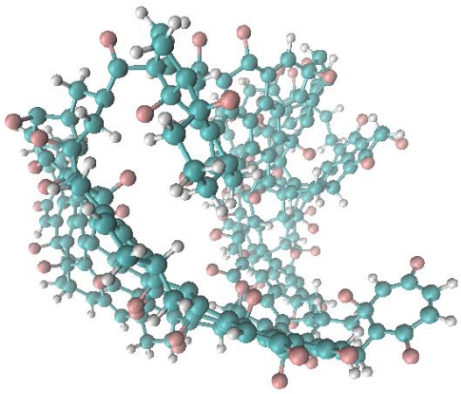

Figure 7-3. Fluorinated disordered cluster of carbon atoms removed from the virgin SiCDC model for charge calculations (non-fluorinated edge atoms saturated with hydrogen).

Our calculations showed that effects of structural curvature on distribution of partial charges are small. The charge distributions of the fluorinated graphene, as well as the disordered carbon cluster are presented in Table S3 and compared with the charge distribution pattern derived for the F-SiCDC models in this work. This table lists average partial charges of the first and second nearest carbon atoms, which are ultimately connected to one or two fluorine atoms in every given structure. For the F-SiCDC.1 model, having low level of fluorination, we have adopted a charge distribution analogous to that of the fluorinated graphene. However for the other two models (F-SiCDC.2 and F-SiCDC.3), where fluorine atoms have stronger effect on the second nearest neighboring carbons (i.e. second nearest carbons can be sometimes polarized by two fluorine atoms in their vicinity), the pattern derived in the current study for charge distribution has been utilized. Except for those atoms detailed in Table S3, other carbon atoms (i.e. carbon atoms beyond second nearest neighbor of fluorine) carry a constant partial charge of 0.004, 0.01 and 0.04 in F-SiCDC models 1 to 3 respectively, determined for electroneutrality of the unit cells. Snapshots of the virgin and fluorinated SiCDC models are illustrated in Figure 7-4.

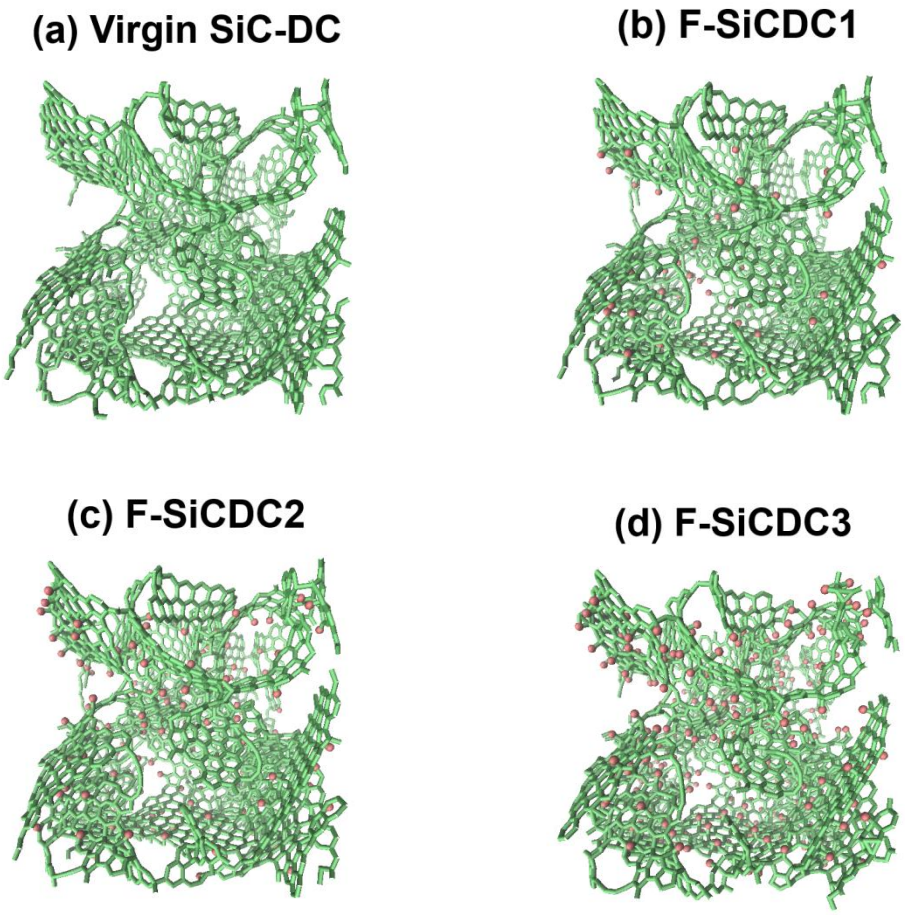

Figure 7-4. Virgin and fluorinated models of SiC-DC.

7.4. Results and discussion

7.4.1. Structural characterization of fluorinated SiCDC

Structural characterization of the models provides insight into simulated adsorption isotherms and transport properties of the system. Pore size distributions (PSDs) of the fluorinated models were determined using the spherical probe geometric approximation technique [46, 47], and are depicted in Figure 7-5. These distributions show a clear trend of pore volume reduction for pores in the range of 8-12 Å. More detailed information regarding structural properties of the models is provided in Table 7-1. The total pore volume (V_p), specific surface area (SA) and mean pore diameter of the SiCDC show slight decrease on fluorination, consistent with experimental results for fluorinated ACFs [12-14].

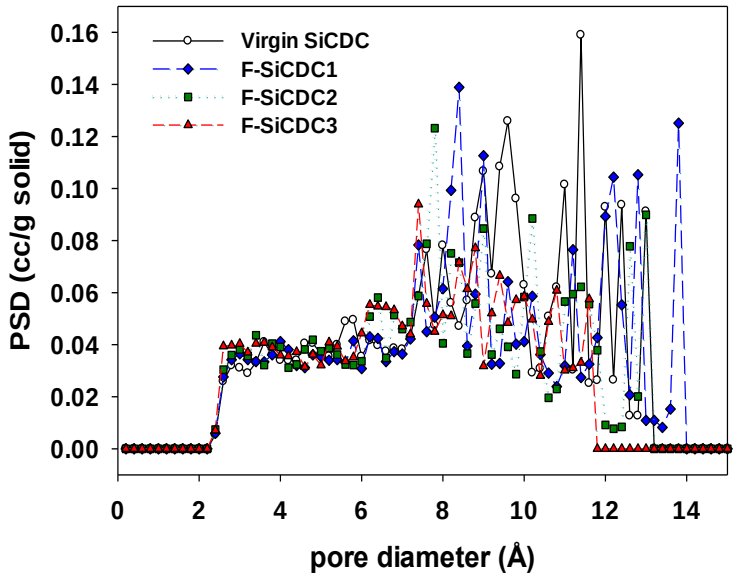

Figure 7-5. PSDs of the fluorinated models compared with that of virgin SiCDC.

The computational techniques for determination of accessible surface area and pore limiting diameter of the virgin and fluorinated models in our study are detailed elsewhere [48]. Here, pore limiting diameter is the diameter of the largest spherical probe that can permeate through the structure [46,49], while the mean pore diameter is defined by 2Vpv/SA.

We note here the formation of large pores at ~14 Å in F-SiCDC.1, and increase in mean pore diameter, despite reduction in pore volume (Table 7-1). This occurs on relaxation following structure optimization of the fluorinated carbon, and is a complex process that depends on the location of the randomly placed F atoms and the internal forces arising from the potential model. Clearly swelling of some parts of the structure along with shrinkage in others occurs. For example, it is seen that the peak at ~9.5 Å in the virgin carbon is substantially lost in the fluorinated structures. This behavior is consistent with published experimental characterization data for fluorinated activated carbons, showing increased average micropore width despite apparent reduction of pore volume on fluorination [14,16]. Nevertheless, the 14 Å peak is however not seen here in the more highly fluorinated structures, F-SiCDC.2 and F-SiCDC.3, because their larger number of F atoms reduce the size of such larger pores, and lower pore volume.

Table 7-1. Structural properties of fluorinated and virgin models

	F/C	Unit density (g/cc)	V_p^v (cc/g)*	V_p^r (cc/g)†	SA (m^2/g)‡	Mean pore diameter (Å) ‡‡	Limiting pore diameter (Å)	Max. pore diameter (Å)
Virgin SiCDC	0.00	0.951	0.674	0.564	1866	7.23	7.44	13.14
F-SiCDC1	0.019	0.995	0.639	0.533	1755	7.28	7.72	13.98
F-SiCDC2	0.053	1.044	0.573	0.487	1682	6.82	7.29	13.04
F-SiCDC3	0.10	1.092	0.485	0.431	1554	6.24	6.99	11.6

* Helium accessible pore volume using the second virial approach [50]: $\mathbf{V_p = \frac{1}{m_s}\int e^{-\phi(r)/k_B.T} dr}$

† Pore volume using geometric approximation technique with hard sphere helium probe

‡ Accessible surface area using hard sphere helium probe

‡‡Mean pore diameter = $2V_p^v/SA$

7.4.2. Equilibrium uptake of water vapor and CO_2 in F-SiCDC models

We have investigated the equilibrium uptake of water vapor and CO_2 in all F-SiCDC models, and have compared the results with that for virgin SiCDC to demonstrate the effect of fluorination on adsorption of these gases. Adsorption isotherms of gases have been predicted by GCMC simulation, using the RASPA simulation package [51]. Water adsorption was predicted at 298 K and pressures up to saturation pressure of the SPC model [38] (3.26 kPa [52]). Sub-atmospheric adsorption of CO_2 was simulated at 273 K using the interaction model described by Nguyen et al. [39, 40]. In both cases, vdW interactions are computed using 12-6 L-J potential with cutoff distance of 34 Å in a simulation box containing a 2×2×2 array of unit cells. Electrostatic interactions are calculated using Ewald formalism with cutoff distance of 38 Å. Periodic boundary conditions are applied for all potential calculations. Several ab-initio and empirical studies have demonstrated that curvature of graphene-like carbon sheets in non-graphitic carbon materials leads to enhanced atomic interactions between solid carbon and adsorbate molecules [18, 53-55]. As suggested by these studies, we have applied a scaling factor of α = 1.1417 to all carbon (solid)-fluid cross-potential

well-depths ($\varepsilon_{c\text{-}f}$) of the force field developed in this study, to account for the effect of carbon sheet curvature on the adsorption strength:

$$\varepsilon_{Carbon}^{c-f} = \alpha . \varepsilon_{Graphite}^{c-f} \quad (7\text{-}5)$$

The scaling factor α is usually applied to modify the value of $\varepsilon^{c\text{-}f}{}_{Graphite}$, which is traditionally obtained using the Lorenz-Berthelot mixing rules with the C-C well-depth of 28 K, originally estimated by Steele for the interaction of adsorbate molecules with graphitized carbon black [56]. However, in this study, we have applied this scaling factor on carbon (solid)-fluid parameters of our own force field to account for the effect of carbon sheet curvature in disordered SiCDC-based structures. The original and scaled parameters are both provided in Table S1.

As depicted in Figure 7-6, fluorination significantly enhances uptake of water, in apparent contrast with experimental observations of decreased water adsorption after fluorination [14, 15], so that the effect of pore volume and surface area reduction is completely overshadowed.

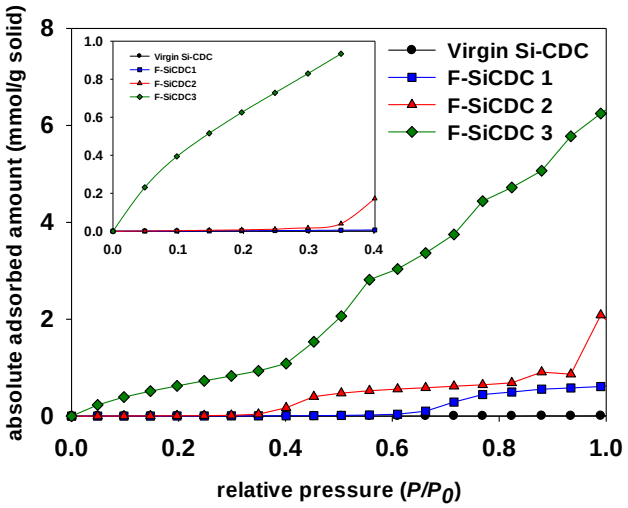

Figure 7-6. Predicted adsorption isotherm of water. Inset shows expanded view of low pressure region, P/Po < 0.4.

As seen in this figure, higher levels of fluorination lead to higher water uptake. We note that the last data point in the water isotherm of F-SiCDC.2, as well as the last 6 data points in the water isotherm of F-SiCDC.3 (i.e. for P/P_o>0.7) are not fully equilibrated, although they are close to equilibration, as shown in the supporting information (Figure S1-S3). The equilibration of water at high relative pressures in the fluorinated systems was extremely time consuming. Nevertheless, this does not affect our finding regarding the increasing trend of water isotherms in the fluorinated systems, since full equilibration will achieve even higher adsorbed amounts. Consequently, we can conclude that fluorination increases hydrophilicity, evident also from the fully equilibrated low

pressure data points reported in Figure 7-6. This is consistent with the experimental observation of enhanced water uptake below P/P_o of 0.5 by Parmentier et al. [16]. In particular, it may be seen that for the most highly fluorinated SiCDC, model 3, $\frac{\partial^2 n}{\partial P^2} < 0$ for $P/P_o < 0.4$ (inset), albeit weakly, a clear indication of hydrophilicity in this region. On the other hand the isotherms are fundamentally different from those of Li et al. [14], suggesting that the covalent F-C bonding arising in their system is not pertinent to our fluorinated structure. Alternately, their isotherms may be different because they are affected by increased internal barriers for water diffusion (demonstrated later in this paper), while our GCMC-based isotherms are not affected by such barriers.

Analysis of the isosteric heat of adsorption and the contributions of adsorbate-adsorbent and adsorbate-adsorbate interactions (Figure 7-7 (a)-(c)) clearly shows that water molecules are more strongly attracted to the pore walls in the fluorinated systems compared to the virgin material.

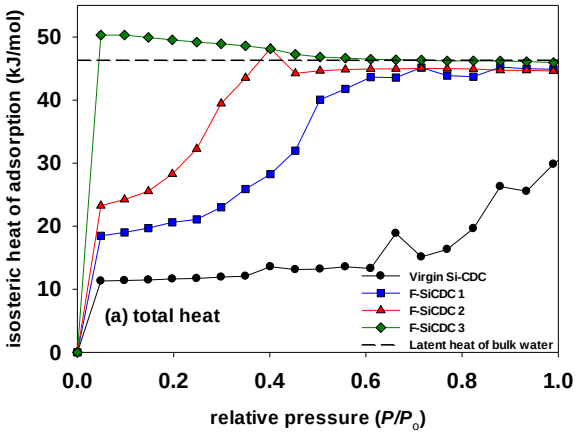

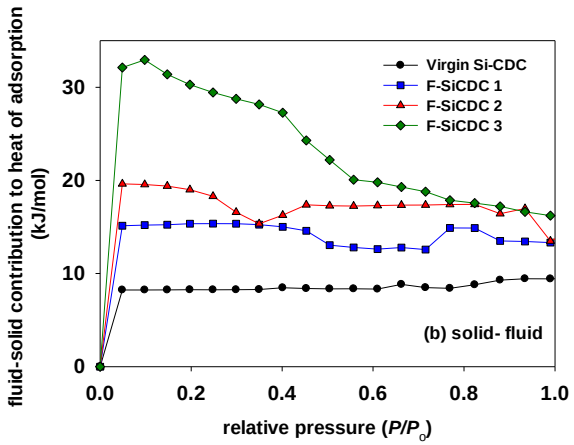

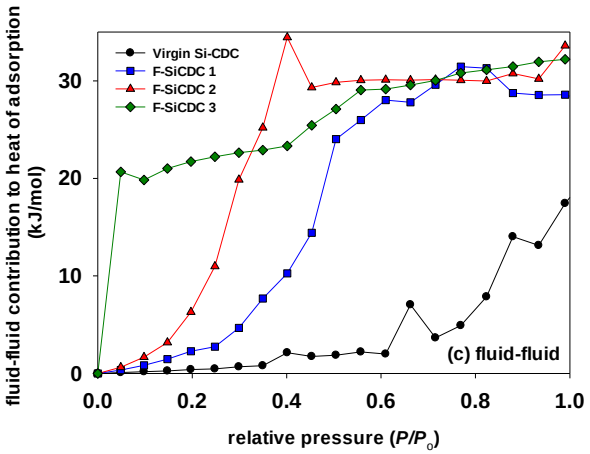

Figure 7-7. (a) Isosteric heat of adsorption of H_2O, and (b) fluid-solid and (c) fluid-fluid interaction contributions.

As depicted in Figure 7-7 (c), F-SiCDC.2 model shows a steep rise of fluid-fluid interactions at relative pressure of about 0.2, an indication of the initiation of pore filling. However, the F-SiCDC.1 model shows more gradual filling, with initiation of pore filling near relative pressure of 0.3. The slope in the fluid-fluid interaction increases with increase in pressure for the fluorinated systems indicating lower hydrophobicity of these systems compared to the virgin material. The F-SiCDC.3 model has a high fluid-fluid interaction energy (magnitude > 20 kJ/mol) even at the lowest pressure sampled. This suggests very early initiation of filling of some part of the pore space at very low pressures not captured in this figure, an indication of much lower hydrophobicity. The dominance of the fluid-fluid contribution to the heat of adsorption shows that inter-adsorbate interactions are more significant at elevated pressures. This is not surprising since hydrogen bonding stabilizes formation of water clusters at pressures close to the saturation pressure of water [57-62]. In our previous studies (Chapter 6) on adsorption of water vapor in the hydrophobic virgin SiCDC, we showed that such clusters barely form below saturation pressure [63]. Nevertheless according to Figure 7-6, pore filling starts well below the saturation pressure for the fluorinated systems. A key question is then what provides the seed for early clustering of water molecules in the fluorinated systems?

To address this question, vdW and Coulombic contributions to fluid-fluid and solid-fluid interactions have been calculated at low pressure points, where hydrogen bonding is not significant. As illustrated in Figure 7-8, solid-fluid vdW interactions are the strongest interatomic interactions at these pressures, which also show an increasing trend with the level of fluorination of the models. In this figure, we have provided the results for the virgin SiCDC, as well as F-SiCDC.1 and F-SiCDC.2. The results from the F-SiCDC.3 model are not provided here as they require extremely

lengthy simulations for convergence. Nevertheless, we do not expect to see any difference in the pattern, which is reported here for the other three porous carbons.

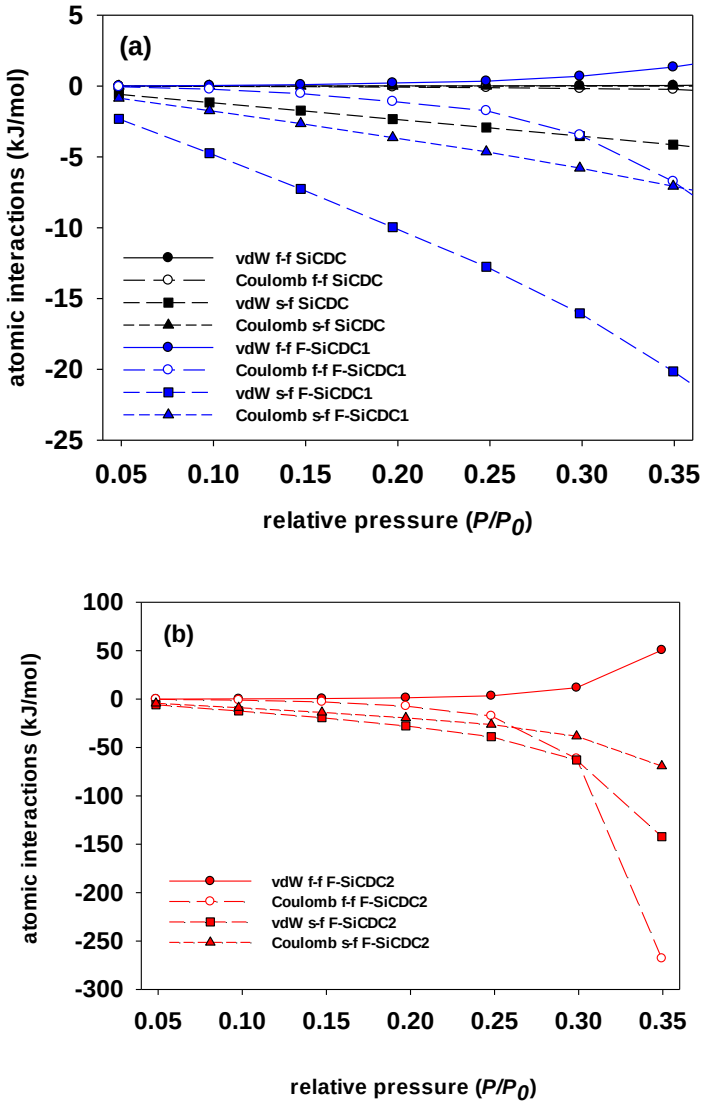

Figure 7-8. Fluid-fluid and solid-fluid contributions of vdW and Coulombic interactions of (a) virgin SiCDC and F-SiCDC.1 and (b) F-SiCDC.2, at low relative pressures.

As seen here, solid-fluid vdW interactions seem to be the main governing interatomic potential at low pressures. The results above suggest that fluorination gives rise to enhancement of vdW interactions between water molecules and the pore walls. Comparison of the potential strengths of F-O and C-O pairs in Table S1 suggests that F-O interactions are more important in this regard than C-O pairs. The radial distribution functions of F-O pairs for different F-SiCDC models at the lowest pressure indicate apparent increase adsorbate multi-layers (or water clustering), as seen in Figure 7-9 (a), considering the magnitude of the second RDF peak relative to the first is larger for

the systems with higher fluorination. The decrease in magnitude of the first RDF peak in Figure 7-9 (a) relates to the presence of water predominantly in the most highly confined (thus more energetic) pore regions which are filled first at the low pressure, P/P_o = 0.05, at which the RDF is determined. On increasing fluorination the decreased hydrophobicity (or increased hydrophilicity) leads to a disproportionately larger amount of water going into the smallest pores (the most confined regions) which provide the most energetic spaces. This increases the water clustering, and reduces the intensity of the first peak after averaging over all F-O pairs in the carbon.

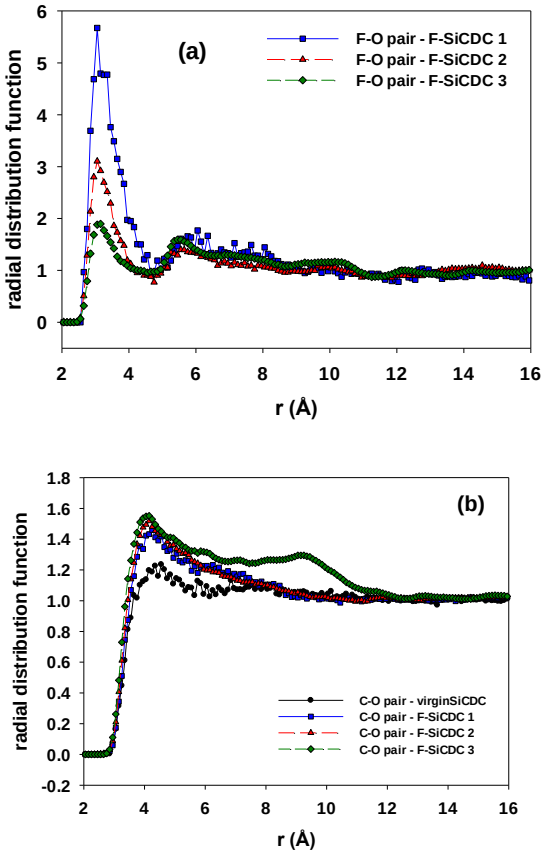

Figure 7-9. RDFs of the (a) F-O and (b) C-O pairs at the lowest pressure (P/P_o = 0.05)

In contrast, Figure 7-9 (b) shows that formation of such multilayer structures is weaker around carbon atoms in the virgin and F-SiCDC.1 as well as F-SiCDC.2 carbons, with the first peak increasing in magnitude relative to the second for F-SiCDC.1 and F-SiCDC.2. Given the abundance of carbon over fluorine, this is an indication of weaker hydrophobicity or improved hydrophilicity, supported by the slight shift of the peak position to smaller C-O distance. The higher relative magnitude of the second peak for F-SiCDC.3 is clearly due to water clustering over the first shell due to much larger amount adsorbed at the same relative pressure of 0.05, evident in Figure 7-6, and

is the case for both the F-O and C-O RDFs. The snapshots in Figure S4 of the supporting information provide evidence of water clustering in the small pore regions of the F-SiCDC.3 model.

Overall, Figure 7-8 and Figure 7-9 together indicate that fluorination encourages formation of the adsorbed phase around fluorine atoms at very low pressure due to stronger F-O vdW interactions in narrow pore regions. In addition, the increasing trend of water adsorption with pressure (Figure 7-6) suggests that once sufficiently large number of water molecules is adsorbed around fluorine atoms at low pressures, water molecules start to progressively evolve into stable molecular clusters, which is expected to be fast growing due to the increased fluid-fluid interactions at elevated pressures (Figure 7-7 (c)). Subsequently, such water clusters grow until they fill the entire pore space, which is generally seen in the pore filling mechanism of microporous carbon materials [63, 64].

Based on the above argument, fluorinated surfaces of carbon appear to be less hydrophobic than the virgin material. The highly fluorinated model 3 could reasonably be described as being hydrophilic. Our finding is further supported by a recent DFT study with the same functional used in our calculation on adsorption of water in C_4F (a stable fluorocarbon derivative of graphene). The study reveals anomalous super-hydrophilicity of the fluorinated graphene [65], although, we note that dispersion-correction is not applied in the DFT-GGA calculations in that study.

Figure 7-10 depicts sub-atmospheric adsorption isotherms of CO_2 at 273 K. As illustrated here, fluorination decreases adsorption of CO_2 considerably even at the lowest level of fluorination. This unusual behavior is explained by the reduction in strongly adsorbing sites, evident from the variation of heat of adsorption with pressure discussed below.

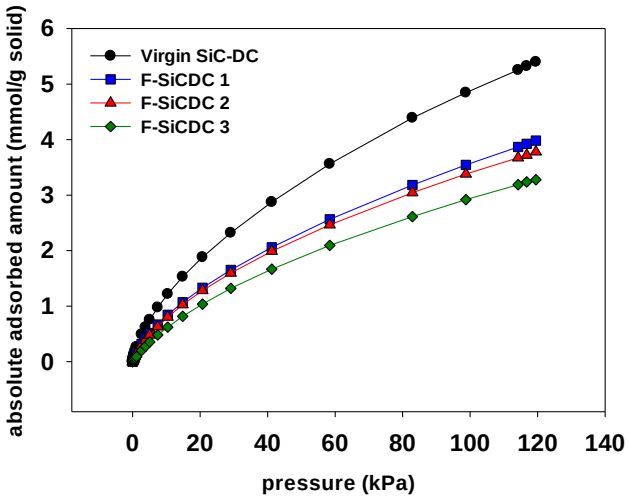

Figure 7-10. sub-atmospheric adsorption isotherm of CO_2 at 273 K.

In Figure 7-11, it is seen that the steep drop in heat of adsorption of CO_2 at low pressure in the virgin SiCDC is absent in the fluorinated materials, indicative of elimination of the most strongly adsorbing sites on fluorination.

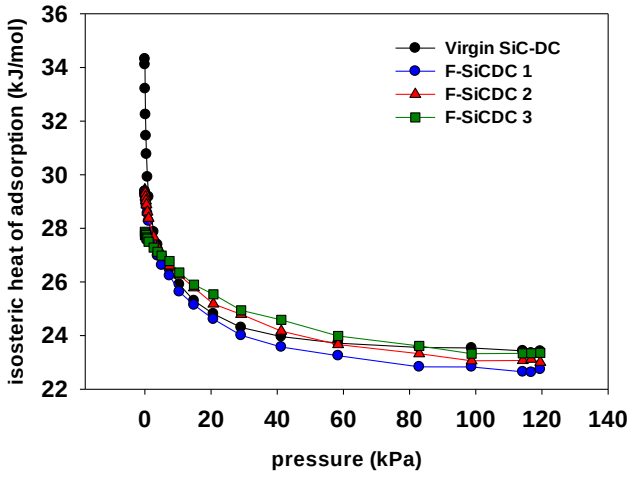

Figure 7-11. Isosteric heat of adsorption of CO_2.

This is supported by Figures S5 and S6 of the Supporting Information. Figure S5 shows steep drop in the solid-fluid contribution to the heat of adsorption at low pressure, on fluorination. Figure S6 demonstrates that fluorinated carbon has lower affinity towards CO_2 molecules compared to the virgin model, by virtue of significantly weaker vdW interactions. The reduction in the solid-fluid vdW interactions of the fluorinated model is mainly governed by the weaker C-O LJ interactions, which dominate the effect of other LJ interactions by virtue of its larger number. Thus, it is evident that the reduction in CO_2 adsorption arises from weakening of the solid-fluid interactions due to reduction in high energy sites on fluorination.

We have estimated the fractional density of states for H_2O and CO_2 in the virgin and F-SiCDC.1 models, based on the vdW energy of a single CO_2/H_2O probe molecule at every grid point of a 50×50×50 grid network within the unit cell, and a Boltzmann occupancy factor. Figure 7-12 (a) shows that for H_2O there are more high energy states (E < -10.6 kJ/mol) in the F-SiCDC.1 than in the virgin carbon, consistent with increased hydrophilicity. It also shows that there are fewer low energy states (E > -10.6 kJ/mol) for water in the fluorinated carbon compared to the virgin SiCDC. Interestingly, Figure 7-12 (b) shows that changes in distributions of high and low energy states are opposite for CO_2, supporting our argument that many of the high energy adsorption sites are lost in the fluorinated model compared to the virgin SiCDC.

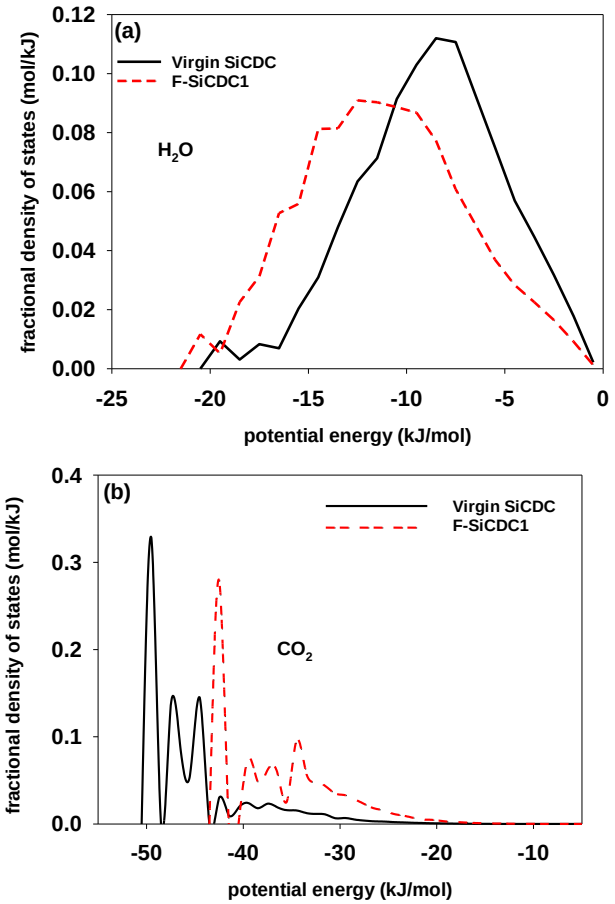

Figure 7-12. Fractional density of states in virgin and F-SiCDC.1 models for (a) water and (b) CO_2.

7.4.3. Hydrophobicity of the fluorinated systems due to internal energy barriers

As discussed earlier, experimental measurements suggest that fluorination enhances hydrophobicity of microporous activated carbon. In contrast, our GCMC simulations predict a more hydrophilic mechanism for adsorption of water on fluorinated SiCDC. A plausible hypothesis to reconcile these observations is that fluorination leads to more strongly adsorbing sites for water, but this enhances internal free energy barriers within the structure and reduces pore accessibility. Since GCMC results are insensitive to such barriers, they will show increased equilibrium uptake of water on fluorination, while the experiment, which is sensitive to such barriers, can be negatively affected and not attain equilibrium on practical time scales.

To test this idea, we performed equilibrium molecular dynamics (EMD) simulation for both water and CO_2 in the fluorinated and virgin SiCDC models using LAMMPS [66]. The simulations were performed in the canonical (NVT) ensemble using a Verlet time integrator with a time step of 0.5 fs. Short-range intermolecular interactions were modeled using the 12–6 L-J potential with a cutoff distance of 18 Å in the 1×1×1 unit cell. Similar to the interaction parameters used for GCMC

simulations, a scaling factor of 1.1417 was applied to all carbon (solid)-fluid cross-potential well-depths ($\varepsilon_{c\text{-}f}$) in the developed force field to account for the effect of carbon sheet curvature on the adsorption strength [18, 53-55], as detailed in Table S1. The standard Ewald formalism was employed for electrostatic interactions with cutoff distance of 18 Å, in such a way that pairwise interactions within this distance were computed directly and those outside this distance were calculated in reciprocal space. Periodic boundary conditions were applied on a rigid unit cell. Self-diffusivities for rigid models of water and CO_2 were calculated in the limit of infinite dilution (one molecule per unit cell) using the Einstein formulation for the mean squared displacement [67]. For every simulation 15 independent trajectories were collected to calculate mean-squared displacement (MSD) of the system after the molecules entered the Fickian region and traversed the entire lattice length. An example of converged MSD is illustrated in Figure S7 in the supporting information section. From the self-diffusion coefficients obtained at various temperatures, we have estimated the Arrhenius activation energy similar to our previous studies for diffusion of CO_2 and CH_4 in virgin SiCDC [19].

Figure 7-13 demonstrates the temperature dependence of the self-diffusion coefficient of water and CO_2. Fluorine doping strongly increases the activation energy barrier (E_a) of the system for the diffusion of water. E_a for the F-SiCDC.3 model is almost 10 times larger than that of the virgin SiCDC. Correspondingly, there is a drop in the self-diffusion coefficient by about 5 orders of magnitude at 298 K. We found that the self-diffusion of water in the highly fluorinated system (i.e. F-SiCDC.3) is extremely slow at low and moderate temperatures (250-298 K), so that even after 200 - 400 ns of simulation time; water molecules have not entered the Fickian regime. The self-diffusivity of water at 250 and 298 K is of the order of 10^{-13} m^2/s, and for this low value of the diffusivity molecules are unable to traverse the entire unit cell for simulation times accessible using normally available computational resources. These two points are illustrated in Figure 7-13 (a) but not included in calculation of activation energy. Experimentally, energy barriers for transport of water in fluorinated SiCDC are likely to be even larger, because of the possibility of long range barriers not captured by the present 40 Å unit cell and limitation of the available scattering techniques by which experimental data required for modeling of such barriers are obtained. We have shown a similar scenario in our recent studies on adsorption of CO_2 in virgin SiCDC by comparing the simulation-based diffusion coefficients with those obtained from kinetic uptake measurements, demonstrating simulation-based values to be several orders of magnitude larger [68].

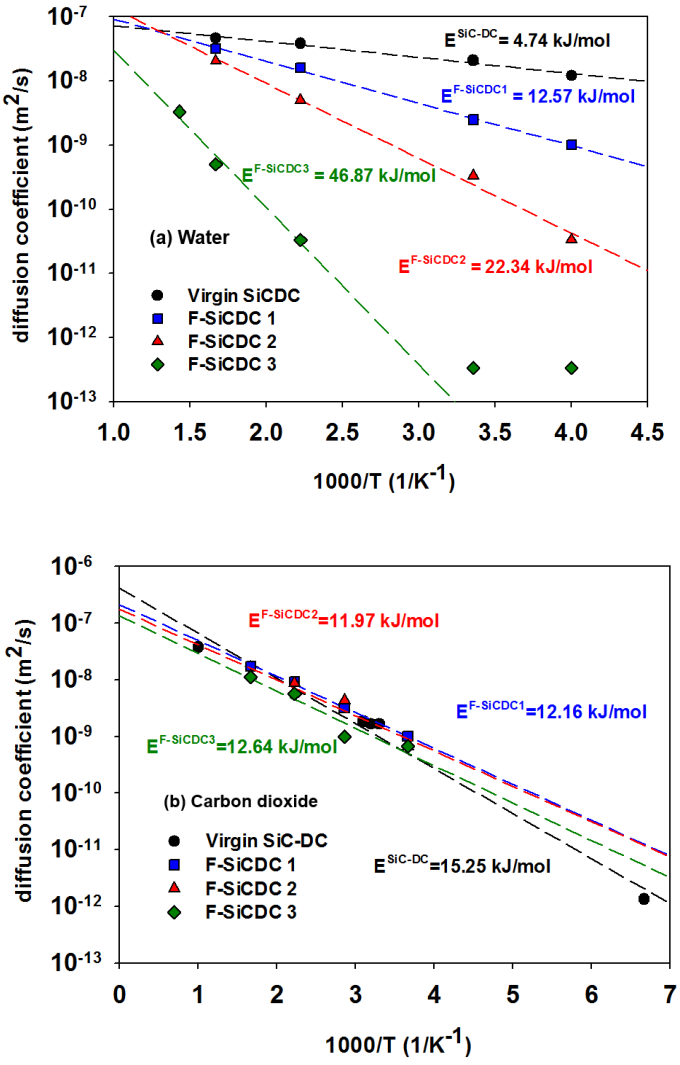

Figure 7-13. variation of self-diffusion coefficient with temperature, for (a) water and (b) CO_2 in fluorine-doped and virgin SiC-DC models

Indeed, the experimentally measured adsorption isotherm of water in pristine SiCDC sample is shown to have a very long equilibration time [69], of the order of hours, indicating that adsorption of water is kinetically highly restricted in this material. Given the larger activation energy barriers of fluorinated models compared to the virgin SiCDC reported in this study, one predicts much smaller diffusion coefficients for fluorinated samples using the Arrhenius relation. Based on the change in activation energies, seen in Figure 7-13 (a), reduction in the diffusion coefficient by a factor of about 23.6, 1.2×10^3 and 2.4×10^7 respectively, is estimated for the three fluorinated carbons, since the change in pre-exponential factor will be much smaller. Thus, experimental observations in which hydrophobicity of the system is increased and adsorption of water is reduced in fluorinated activated carbons, can be reasonably explained by our results [14, 15].

In contrast to water, fluorination reduces the activation energy barriers for CO_2, as shown in Figure 7-13 (b). This finding is supported by a recent DFT study based on the use of GGA-PBE functional, in which Wu et al. [70] have shown that fluorine-modified porous graphene has a smaller energy barrier for CO_2 diffusion compared to the non-fluorinated graphene. In our study, the reduced CO_2 uptake (Figure 7-10), in addition to smaller solid-fluid heat of adsorption of this molecule (Figure S5 (a)), along with the decreased activation energy barriers of the fluorinated models for CO_2, suggest that fluorination reduces strength of the solid-fluid binding interactions for carbon dioxide.

To further support our finding regarding activation energy barriers of water and CO_2, we have investigated internal energy barriers of the systems for these molecules at infinite dilution based on analysis of the Helmholtz free energy map of the unit cell. In this method, initially developed by Haldoupis et al. [49] and subsequently extended by Sarkisov [71, 72], the difference between the minimum free energy of the unit cell along its percolation path, and the percolating free energy threshold of the unit cell along the same path, is defined as the limiting free energy barrier of the system. Figure 7-14 shows these energies for water and CO_2 at 298 K in the materials we considered.

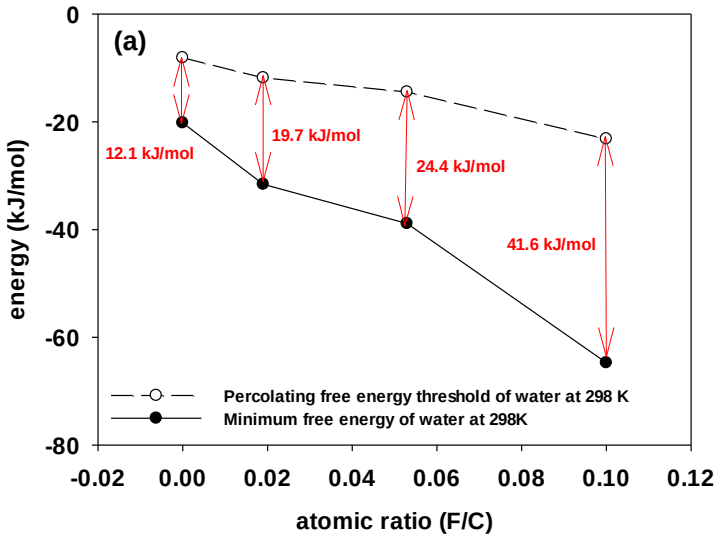

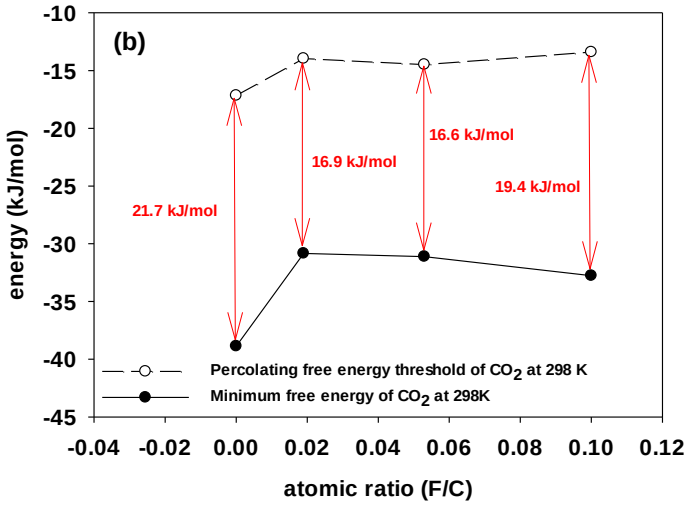

Figure 7-14. Limiting free energy barriers for (a) water and (b) CO_2 at 298 K, obtained from analysis of the free energy landscape of the system.

As depicted here, the minimum free energy of the system is decreased with the level of fluorination for water, which is an indication of the enhanced hydrophilicity arising from fluorination of SiCDC. A similar conclusion can be made based on decreasing trend of the percolating free energy threshold for water. It is also evident from this figure that limiting free energy barrier of the system is significantly enhanced with increasing fluorination level. These results support our findings regarding the dual effect of fluorination, showing increasing hydrophilicity of the system, evident from GCMC simulation, together with increase in activation energy barriers for water obtained from EMD simulation.

In agreement with the results obtained from our GCMC and MD simulations, Figure 7-14 (b) suggests that fluorination weakens adsorption of CO_2 in F-SiCDC models and leads to reduction of the energy barrier of these systems for CO_2. In general, reduction of the activation energy barrier for CO_2, with simultaneous increase of the energy barrier for water vapor, suggests that fluorination can effectively improve selectivity of CO_2 over H_2O in CO_2/H_2O mixtures, at least in the limit of infinite dilution.

7.5. Conclusion

Our studies demonstrate that fluorination decreases the pore volume, surface area and mean pore diameter of SiCDC, in agreement with experiment. Comparison of the simulated adsorption isotherm of water in fluorinated SiCDC with that of the virgin material shows that fluorination considerably increases equilibrium uptake of water. On the other hand our computations, including

calculation of activation energy barriers using MD simulations and analysis of the free energy map of the unit cells, demonstrate that fluorine doping remarkably increases internal energy barriers of the system for water vapor. These results explain the increase in hydrophobicity on fluorination of activated carbons, reported in the literature, as being an apparent effect that is governed by increase in internal energy barriers in the fluorinated system. The increase in internal energy barriers arises from stronger binding of fluid molecules inside the pore network, or decrease in hydrophobicity, as opposed to repulsion or steric hindrance to the diffusion of molecules through narrow pore entries. Thus, the results provide new insight into this apparently dual effect of fluorination, showing that while fluorination generates more hydrophilic carbon surfaces, they effectively act as more hydrophobic structures.

Further, we have demonstrated that fluorination gives rise to reduction of CO_2 uptake, despite decreasing internal energy barriers of the system for CO_2 diffusion. It is also shown that decrease of carbon dioxide adsorption is not due to physical restriction at pore entries but it is mainly because of the weakened solid-fluid binding energies after fluorination. Finally, reduction of activation energy barriers for CO_2 on fluorination, as well as increase of these barriers for water vapor, suggests that this can improve selectivity of CO_2 over H_2O in CO_2/H_2O gas mixtures.

7.6. Associated contents

Several information is provided in the supporting information. This information is available free of charge via the Internet at http://pubs.acs.org.

a) Interaction parameters of the developed force field

Table S1. LJ interaction parameters of the developed force field.

Molecule	Pair	$\varepsilon^1_{s\text{-}f}/k_B$ (K)	$\varepsilon^2_{s\text{-}f}/k_B$ (K)	$\sigma_{s\text{-}f}$ (Å)	$\varepsilon_{s\text{-}f}/k_B{}^*$ (K)
H_2O	C-O	39.49	45.09	3.311	53.43
	C-H	16.93	19.33	2.623	00.00
	F-O	51.29	51.29	3.113	- - -
	F-H	0.0	0.0	0.0	- - -
CO_2	C-C	55.73	63.63	3.053	32.36
	C-O	31.64	36.12	3.287	54.71

	F-C	75.68	75.68	2.814	- - -
	F-O	38.92	38.92	3.006	- - -

$\varepsilon^{1}_{s\text{-}f}$: Original ε parameter developed in this study.

$\varepsilon^{2}_{s\text{-}f}$: scaled ε parameters using scaling factor α = 1.1417 for Carbon(solid) – fluid pairs based on equation 5. These parameters are applied in our GCMC and MD simulations.

NB. Only potential well-depths of carbon(solid)-fluids are scaled using this factor, considering carbon atoms are the only one which contribute to curvature of the disordered structure.

$\varepsilon_{s\text{-}f}/k_B^*$: ε parameter of the virgin SiCDC as used in our previous studies[18-19, 63].

b) Bonded and non-bonded interaction parameters used for geometry optimization of the F-SiCDC models

Table S2. Non-bonded [73] and bonded [74] interaction parameters used for geometry optimization of the F-SiCDC models.

	Bond strength (kJ/mol.Å^2)*	**Bond length (Å)**	**Bond angle strength (kJ/mol.rad^2)****	**Angle (degree)**
F-C	2532.41	1.336	---	---
F-C-C	---	---	419.81	118.32
	$\varepsilon_{i\text{-}i}/k_B$ (K)		**$\sigma_{i\text{-}i}$ (Å)**	
F-F	26.68		2.95	
F-C	29.76		3.225	

$^*U_{two-body} = \frac{1}{2}K_r(r - r_0)^2$

$^{**}U_{three-body} = \frac{1}{2}[\frac{K_\theta}{sin^2(\theta_0)}](\cos(\theta) - \cos(\theta_0))^2$

c) Partial charges of the fluorinated systems

Table S3. Partial charge distribution of fluorinated graphene sheet and fluorinated disordered carbon cluster compared with the pattern derived for F-SiCDC.2 and F-SiCDC.3 models

	F	1st near C to 1 F	1st near C to 2 F	1st near C to 1 or 2 F	2nd near C to 1 F	2nd near C to 2 F	2nd near C to 1 or 2 F
F-graphene	-0.1579	+0.2578	+0.5219	+0.3144	-0.09715	-0.15725	-0.11719
F-disordered cluster	-0.15411	+0.27498	---	---	-0.14882	---	---
Derived pattern	-0.154	+0.275	---	---	-0.116* -0.149**	---	---

* used for F-SiCDC.2

** used for F-SiCDC.3

d) Equilibration state of some unfinished GCMC simulations

As noted in the paper, some of the high-pressure data points in GCMC simulation of water in the fluorinated systems did not reach equilibrium even after very lengthy simulations. These include the last data point (data point 19) in adsorption isotherm of F-SiCDC.2 model, where P/P_0 = 1.0, in addition to the last 6 data points (data points 14 to 19) corresponding to P/P_0 = 0.72 to 1.0 in the adsorption isotherm of F-SiCDC.3 model. Nevertheless in most cases the simulations at these data points are close to equilibration. We emphasize that this slow equilibration does not affect our finding regarding the increasing trend of water adsorption in fluorinated systems, so that one can still safely conclude that fluorination does increase the level of water uptake. This is consistent with other evidence provided in our paper including analysis of free energy of binding of water in the systems studied and GCMC results of other data points, which are all fully equilibrated. Figures S1 to S3 illustrate equilibration state of data point 19 in F-SiCDC.2 model, as well as point 14 and 19 in the F-SiCDC.3 model. We note that in these figures the *X* axis represents the number of cycles in GCMC simulation rather than the number of MC steps. In RASPA simulation package [51], which

is used in this study, a cycle consists of N MC steps, where N is the amount of molecules with a minimum of 20 steps. In other words, on average one Monte Carlo move is attempted (either successful or unsuccessful) on each molecule during each cycle, so that the number of MC steps is roughly equal to the number of cycles times the average number of molecules in the simulation.

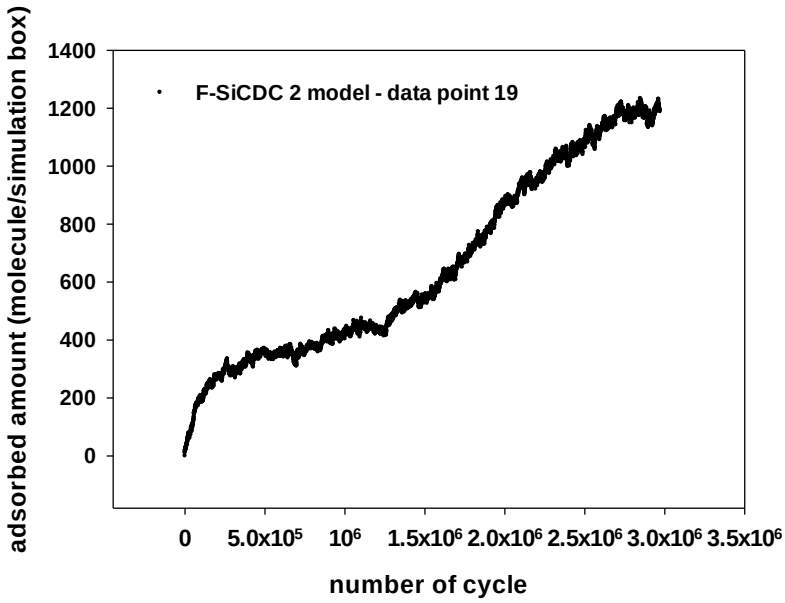

Figure S1. Equilibration state of GCMC simulation for data point 19 in adsorption isotherm of water in F-SiCDC.2 model

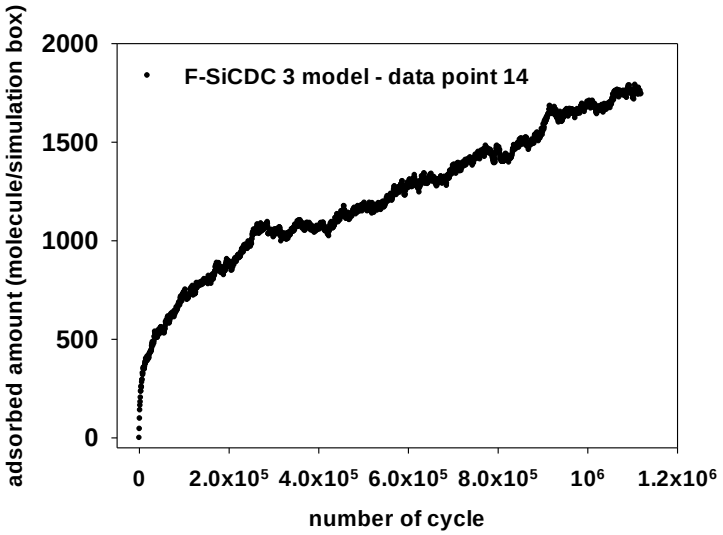

Figure S2. Equilibration state of GCMC simulation for data point 14 in adsorption isotherm of water in F-SiCDC.3 model

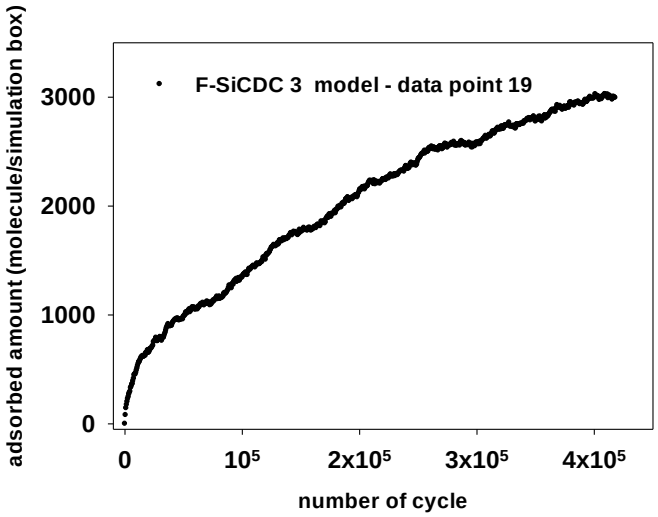

Figure S3. Equilibration state of GCMC simulation for data point 19 in adsorption isotherm of water in F-SiCDC.3 model

e) **Water clusters in F-SiCDC3 model**

Following figures illustrate formation of water clusters in F-SiCDC.3 model at the lowest pressure (P/P_0 = 0.05). Here, oxygen – oxygen distances are given but hydrogen atoms are not illustrated for better visibility of other atoms.

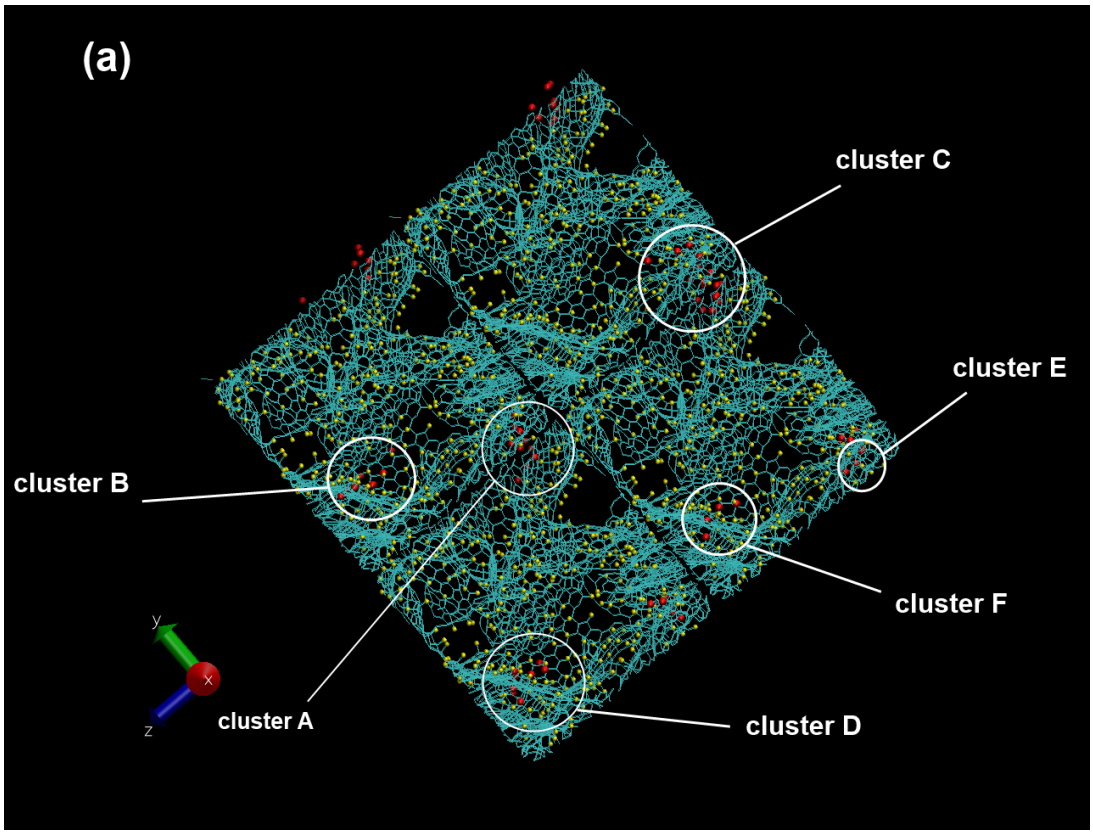

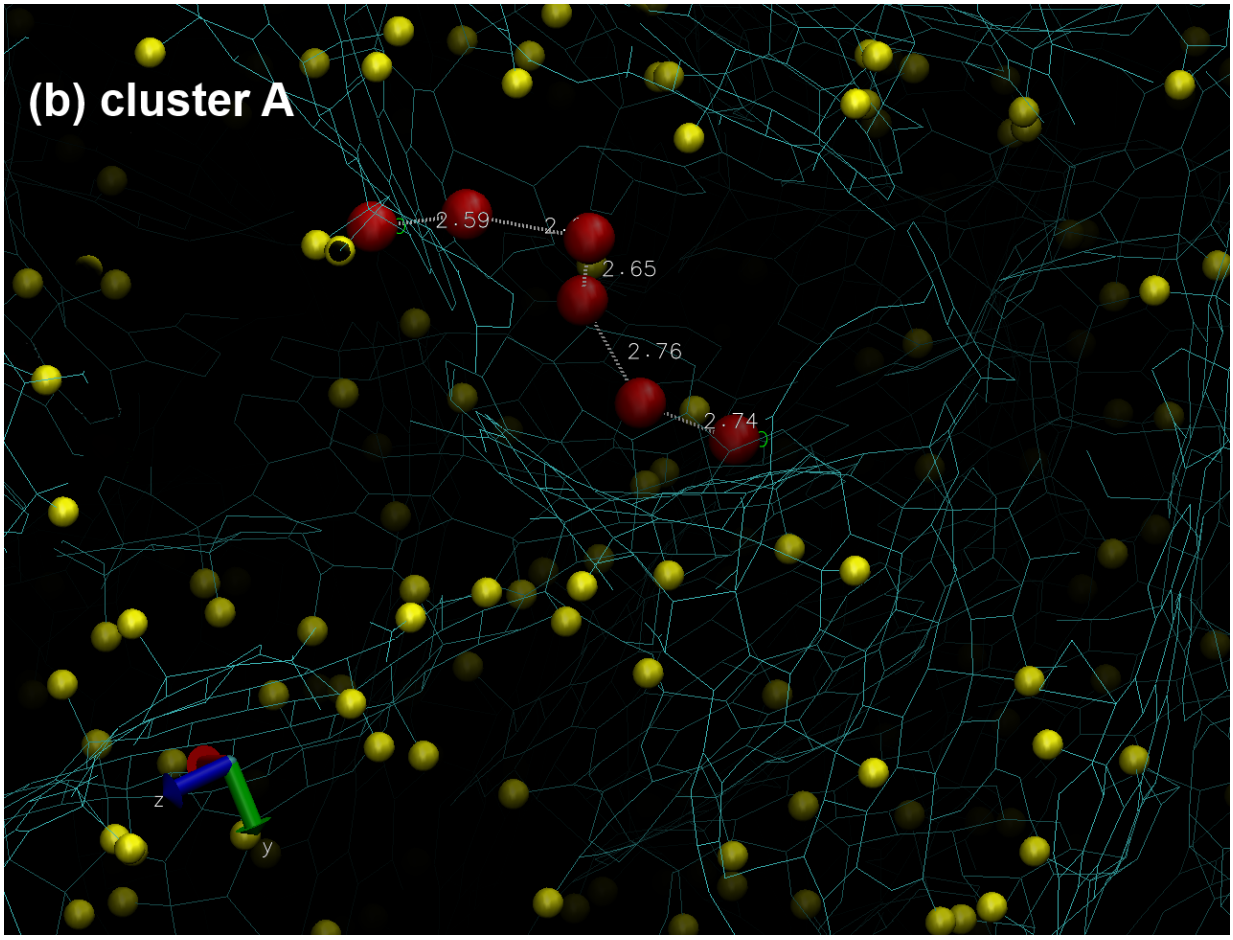
(b) cluster A
2.59
2.65
2.76
2.74
z
y

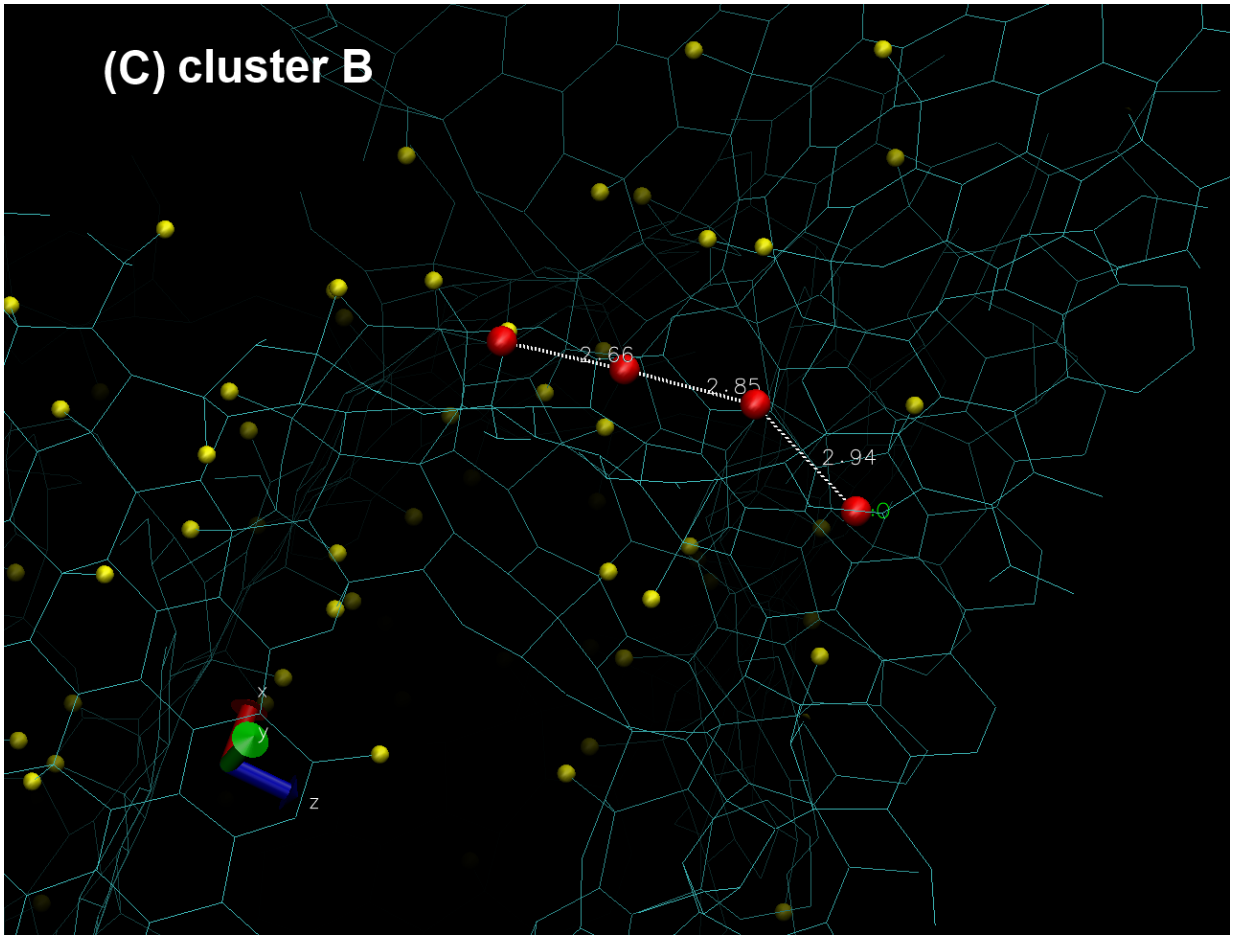
(C) cluster B
2.66
2.85
2.94
O
x
y
z

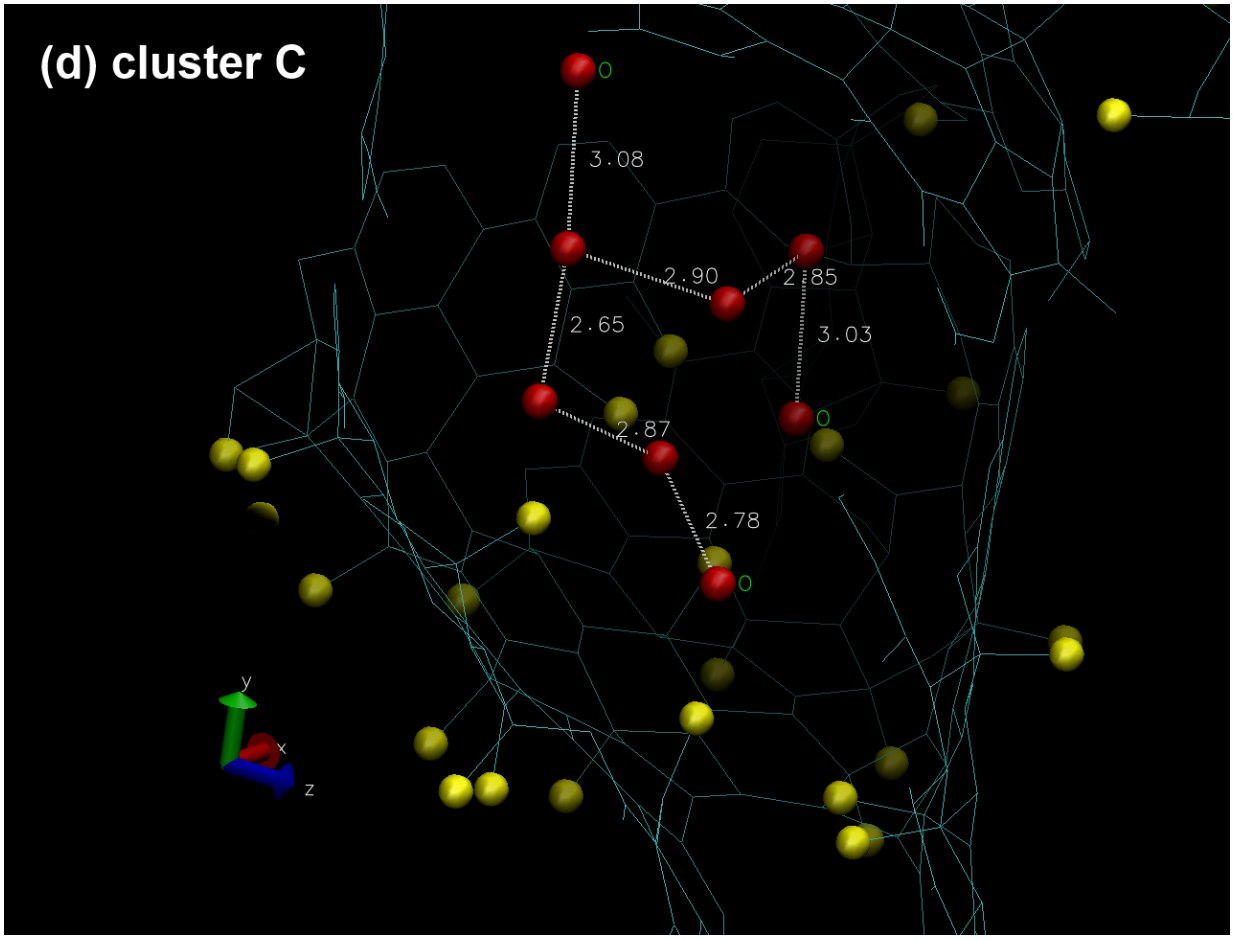
(d) cluster C
O
3.08
2.90
2.85
2.65
3.03
O
2.87
2.78
O
y
x
z

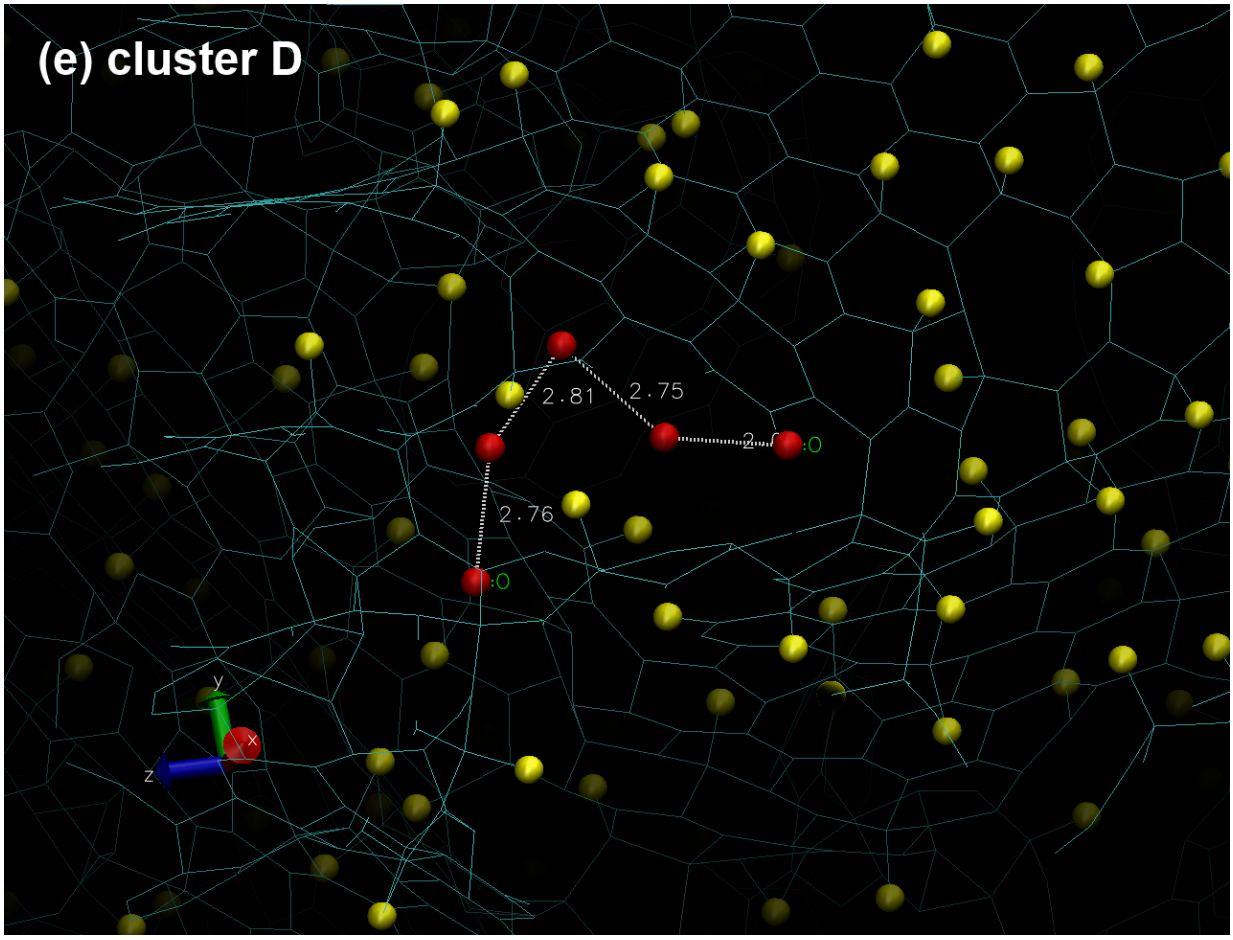
(e) cluster D
2.81
2.75
2.76
y
x
z

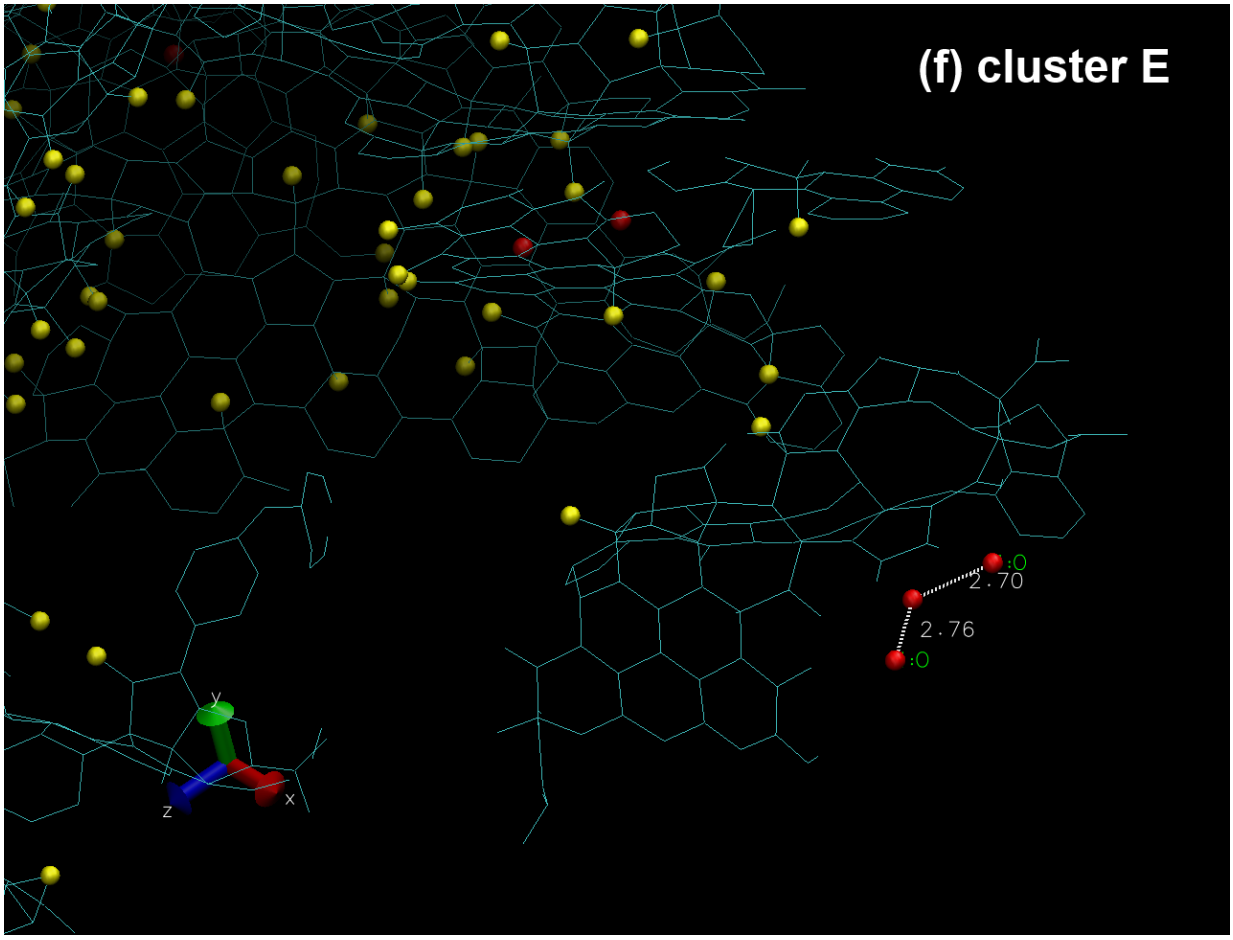
(f) cluster E
:O
2.70
2.76
:O
y
z
x

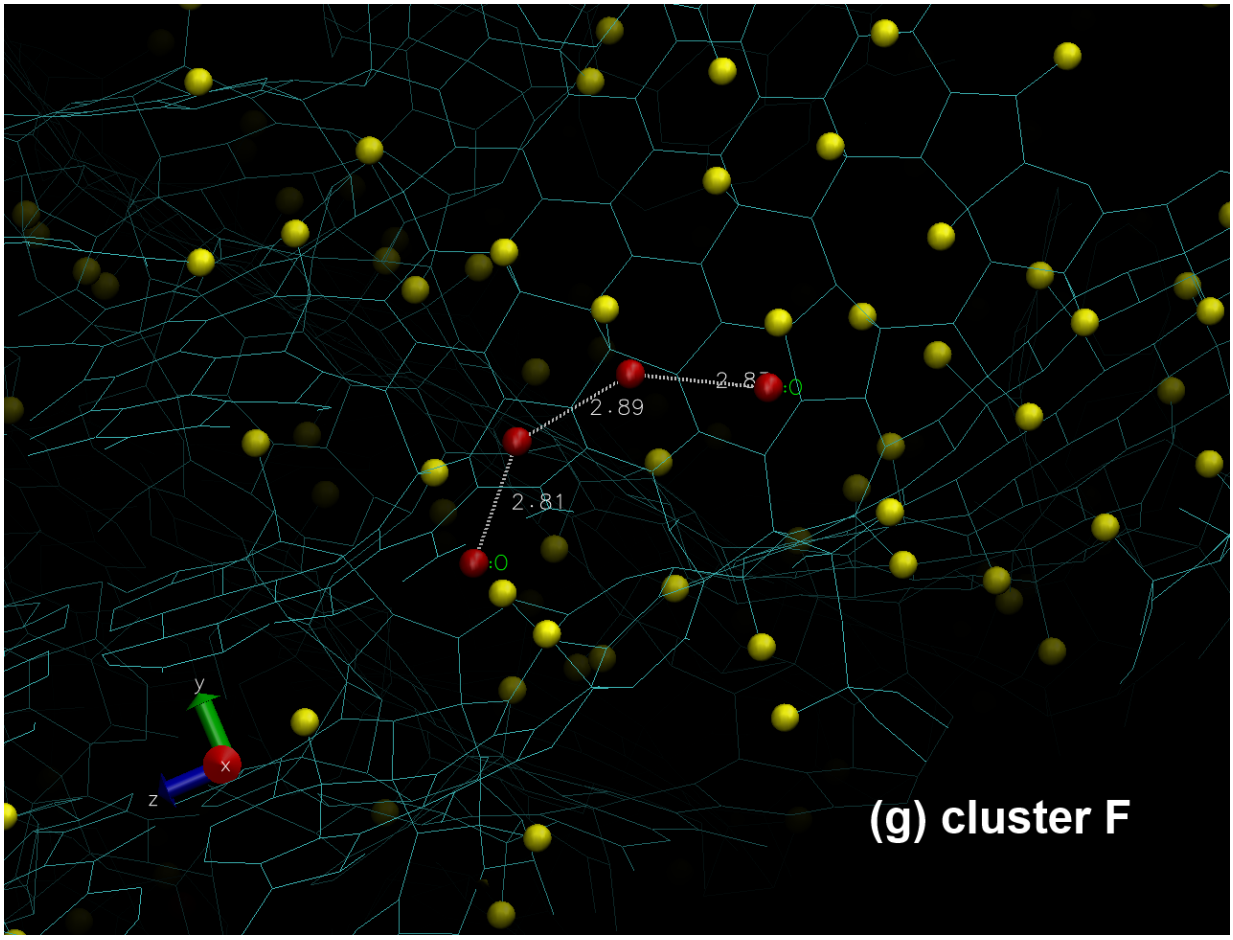

Figure S4. Formation of water clusters in F-SiCDC.3 model at P/P_o = 0.05.

f) Contributions of heat of adsorption for CO_2 in virgin and fluorinated systems

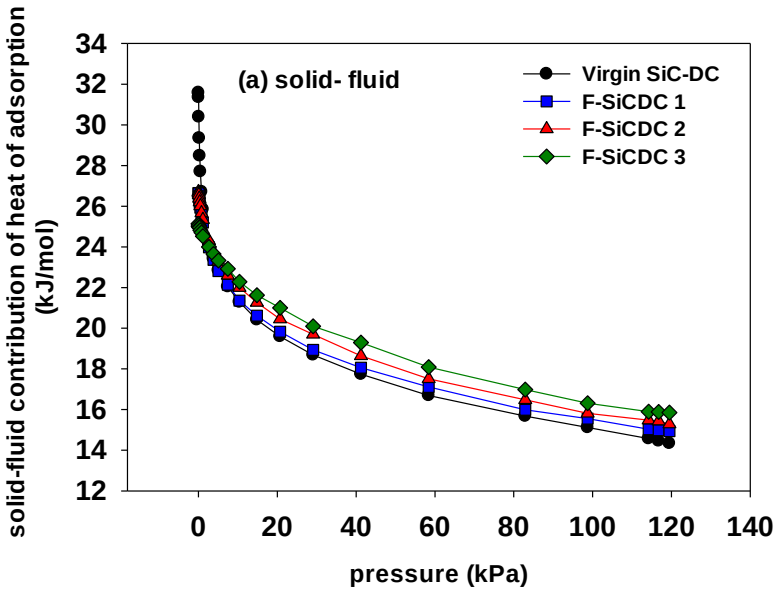

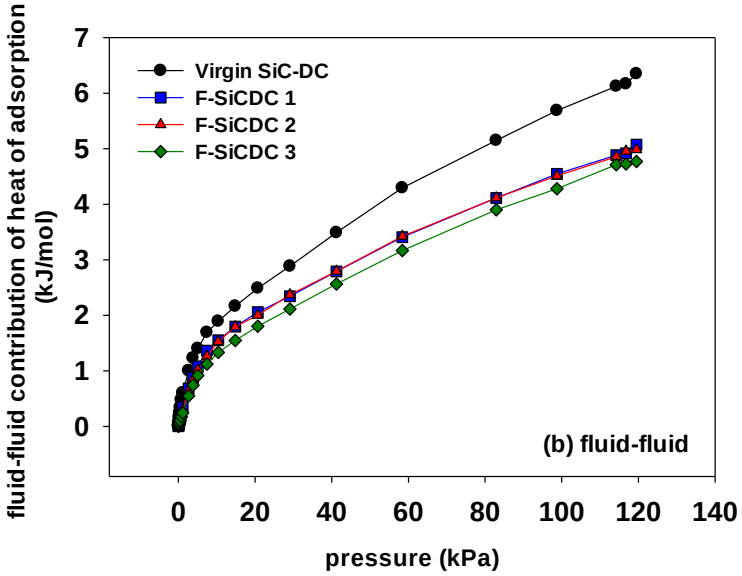

Figure S5. (a) Solid-fluid and (b) fluid-fluid contributions to heat of adsorption for CO_2.

g) Adsorption energy of CO_2 in virgin and F-SiCDC.1 model

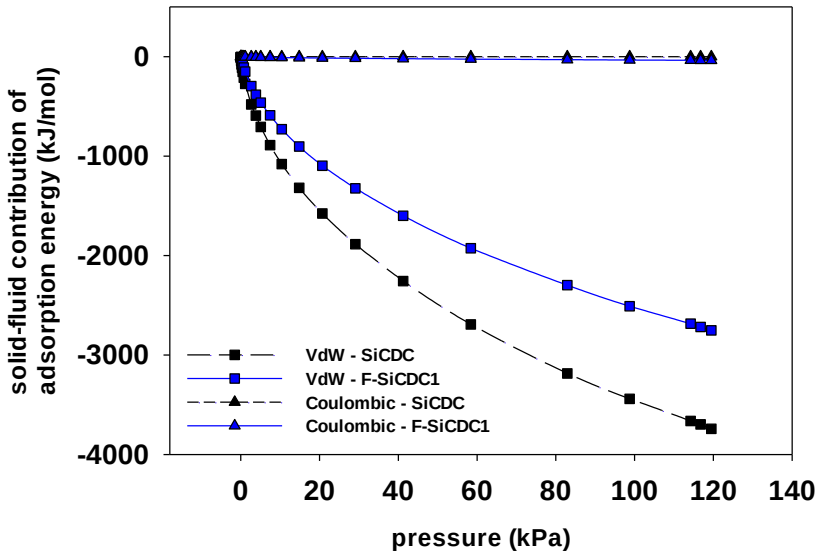

Figure S6. Solid-fluid interactions of CO_2 in virgin and F-SiCDC.1 model.

h) MSD of water and CO_2 in F-SiCDC models

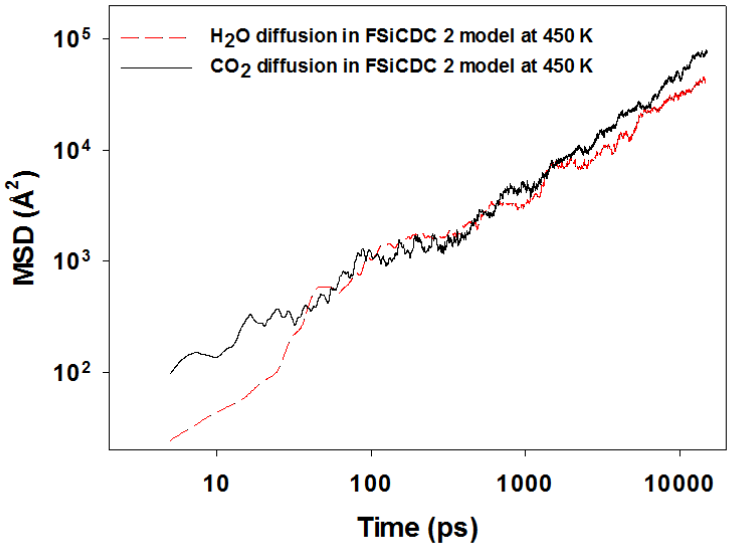

Figure S7. MSD of water and CO_2 from F-SiCDC.2 model at 450 K.

i) Optimized structure of the fluorinated graphene

As explained in the paper, structure of the fluorinated graphene was optimized using the dispersion-corrected DFT method of Grimme (DFT-D2) implemented in VASP. After optimization, the system achieved energy level of -53.2831 Hartrees with lattice constants equal to $\begin{bmatrix} 22.21 & 0 & 0 \\ 0 & 21.56 & 0 \\ 0 & 0 & 20.00 \end{bmatrix}$. The final configuration along with the corresponding atomic charges calculated from DDEC method are given in table S4.

Table S4. Atomic configurations of the fluorinated graphene

Index	Atom	X (Å)	Y (Å)	Z (Å)	Charge (e)
1	C	-0.032760	21.418696	10.074040	0.002875
2	C	20.942342	0.576299	10.049360	-0.000078
3	C	20.939677	2.010168	10.055860	0.004699
4	C	22.168356	2.728871	10.068380	-0.006943
5	C	2.429596	21.417769	10.145860	0.000384
6	C	1.196875	0.573970	10.103600	0.000528
7	C	1.195897	2.012755	10.084140	0.002842
8	C	2.422200	2.726284	10.090520	-0.002266
9	C	4.895128	21.418114	10.207600	-0.007597
10	C	3.662518	0.575630	10.175420	0.007304

11	C	3.662851	2.008228	10.153180	-0.006852
12	C	4.897105	2.715029	10.126540	0.040442
13	C	7.366035	21.421455	10.189500	-0.002936
14	C	6.127850	0.570650	10.174260	0.013445
15	C	6.128428	1.997038	10.094100	-0.031302
16	C	7.363726	2.693491	9.957660	0.073382
17	C	9.839074	21.428527	10.141680	-0.001878
18	C	8.599779	0.569443	10.129940	0.011642
19	C	8.597424	1.991713	10.007040	-0.035324
20	C	9.830368	2.692283	9.911440	0.073507
21	C	12.310514	21.432214	10.104880	-0.004810
22	C	11.075016	0.575178	10.091680	0.010446
23	C	11.070419	1.998267	10.013460	-0.029726
24	C	12.299187	2.712528	10.034860	0.038084
25	C	14.783331	21.428786	10.060020	0.004419
26	C	13.543880	0.586475	10.076840	0.004496
27	C	13.539838	2.009931	10.064160	-0.004249
28	C	14.781044	2.726887	10.031140	-0.006331
29	C	17.248019	21.423590	10.030960	-0.002499
30	C	16.013899	0.579339	10.037180	0.001202
31	C	16.011544	2.014265	10.030260	0.002224
32	C	17.246665	2.725572	10.041540	-0.006700
33	C	19.713707	21.420313	10.031400	-0.001370
34	C	18.482451	0.576881	10.027600	0.001705
35	C	18.479919	2.009327	10.037980	0.006809
36	C	19.707688	2.728159	10.053500	-0.004608
37	C	22.159916	4.159700	10.071760	0.016646
38	C	20.928661	4.882240	10.071040	-0.010069
39	C	20.922642	6.318136	10.074720	0.007566
40	C	22.148345	7.038499	10.052220	-0.003904
41	C	2.412739	4.160994	10.073580	0.028317
42	C	1.178996	4.876398	10.077200	-0.025199
43	C	1.168979	6.308736	10.058120	0.033193
44	C	2.394815	7.025197	10.116720	-0.073724
45	C	4.899748	4.153922	10.034720	-0.088605
46	C	3.644883	4.879589	10.147220	-0.067117
47	C	3.556332	6.262059	10.371860	0.239023
48	C	7.360150	4.108495	9.711120	-0.201648
49	C	6.099044	4.764976	9.678420	0.272528
50	C	9.831878	4.104507	9.664140	-0.198461
51	C	8.593649	4.764588	9.543700	0.307674
52	C	12.292302	4.146204	9.952300	-0.084672
53	C	11.092096	4.759111	9.605740	0.270098

54	C	14.785774	4.153577	10.061040	0.039697
55	C	13.542592	4.866825	10.129360	-0.084549
56	C	14.795658	6.984707	10.395040	-0.189431
57	C	17.248641	4.153081	10.079700	0.014288
58	C	16.017030	4.864777	10.117940	-0.029504
59	C	16.024782	6.288729	10.207840	0.063743
60	C	17.233361	7.033066	10.179280	-0.032557
61	C	19.703912	4.163538	10.069700	0.005971
62	C	18.472368	4.881292	10.090820	-0.007006
63	C	18.467793	6.315441	10.122680	0.019687
64	C	19.691497	7.038585	10.107800	-0.007320
65	C	22.143081	8.471700	10.063240	0.012180
66	C	20.910271	9.193788	10.092520	-0.000739
67	C	20.910582	10.630050	10.074240	-0.002314
68	C	22.145080	11.350262	9.980340	0.009776
69	C	2.385487	8.456112	9.925860	-0.033054
70	C	1.163449	9.190705	9.974640	0.001546
71	C	1.162205	10.624725	9.876960	0.005152
72	C	2.378869	11.352655	9.658120	-0.010711
73	C	3.516265	9.178653	9.494500	0.147783
74	C	3.513977	10.549286	9.334960	0.149889
75	C	14.804742	8.391324	10.436380	0.269789
76	C	14.699955	11.406879	10.135140	0.537075
77	C	17.213039	8.468552	10.214380	0.035073
78	C	15.964859	9.192494	10.290980	-0.061629
79	C	15.986403	10.637143	10.219360	-0.134741
80	C	17.195804	11.351836	10.170400	0.043348
81	C	19.681525	8.474330	10.122760	0.000937
82	C	18.442962	9.195512	10.164720	0.003044
83	C	18.445183	10.630805	10.158480	0.009275
84	C	19.679170	11.349766	10.109260	0.000692
85	C	22.148434	12.783032	9.963260	0.007294
86	C	20.919066	13.505895	10.022720	0.004701
87	C	20.937545	14.948346	10.016980	-0.014574
88	C	-0.028651	15.663771	10.014220	0.011579
89	C	2.365232	12.781803	9.754920	-0.137336
90	C	1.178529	13.500398	9.905420	0.038291
91	C	1.198674	14.955396	9.990220	-0.027290
92	C	2.432217	15.681192	10.075880	0.023129
93	C	3.664406	13.522820	9.777880	0.498262
94	C	3.677909	14.994872	10.133360	-0.079870
95	C	4.877782	15.689643	10.341960	-0.088830
96	C	6.180577	14.964537	10.634960	0.530474

97	C	7.429223	15.781036	10.685820	-0.258403
98	C	8.633249	15.131951	10.878960	0.329926
99	C	9.880518	15.794985	10.764200	-0.193799
100	C	11.129631	15.147495	10.852140	0.278900
101	C	12.320664	15.737291	10.413840	-0.080450
102	C	14.785819	12.891673	10.015860	-0.244301
103	C	13.607045	13.624519	9.966920	0.291280
104	C	13.552209	15.012185	10.205300	-0.076469
105	C	14.790105	15.712411	10.164900	0.037890
106	C	17.229252	12.809982	10.130060	-0.044627
107	C	16.017852	13.561477	10.103040	0.074891
108	C	16.020228	14.992393	10.104020	-0.022248
109	C	17.254283	15.694925	10.077200	0.011794
110	C	19.692230	12.791117	10.078240	-0.010060
111	C	18.457354	13.514951	10.093820	0.018345
112	C	18.475677	14.958608	10.063260	-0.003255
113	C	19.713374	15.669140	10.033920	0.005808
114	C	-0.029028	17.107795	10.043720	0.004897
115	C	20.946740	17.826627	10.032900	0.002929
116	C	20.946962	19.262976	10.040660	0.000045
117	C	-0.032005	19.982067	10.070520	0.002678
118	C	2.432417	17.114608	10.141000	0.009551
119	C	1.197030	17.828870	10.093880	-0.000022
120	C	1.198363	19.266706	10.105920	-0.001829
121	C	2.429952	19.983447	10.153820	0.001609
122	C	4.897327	17.118899	10.341620	0.025893
123	C	3.664739	17.830551	10.227360	0.006648
124	C	3.664383	19.268344	10.213500	0.000152
125	C	4.893640	19.986249	10.243320	0.004883
126	C	7.391444	17.179137	10.493800	0.076626
127	C	6.134646	17.854547	10.385340	-0.024828
128	C	6.132559	19.274748	10.296460	0.007392
129	C	7.368723	19.997439	10.259900	-0.003827
130	C	9.858197	17.192375	10.476680	0.073249
131	C	8.618413	17.888828	10.415540	-0.024878
132	C	8.609818	19.305083	10.283740	0.007306
133	C	9.843872	20.009728	10.215160	-0.000802
134	C	12.314779	17.163938	10.267720	0.038112
135	C	11.089608	17.883675	10.318820	-0.033242
136	C	11.083590	19.303983	10.216440	0.011826
137	C	12.315156	20.005718	10.139100	-0.003715
138	C	14.789062	17.145892	10.149980	0.000524
139	C	13.552387	17.863538	10.155360	-0.000408

140	C	13.549566	19.288460	10.116260	0.001598
141	C	14.785797	19.998884	10.075120	0.001975
142	C	17.253772	17.127307	10.068020	-0.008603
143	C	16.020762	17.847821	10.093620	0.001913
144	C	16.018230	19.282466	10.064980	-0.002568
145	C	17.250196	19.991920	10.039660	0.003983
146	C	19.715128	17.111417	10.026880	-0.005811
147	C	18.487560	17.835014	10.038180	0.007335
148	C	18.485894	19.271341	10.033020	0.001875
149	C	19.715195	19.982692	10.029140	0.000605
150	C	13.603958	6.211048	10.481300	0.279170
151	F	8.639868	13.804997	11.101440	-0.127224
152	F	11.171275	13.933861	11.435680	-0.127063
153	F	12.468405	12.977287	9.652520	-0.124044
154	F	13.950723	10.901016	9.066600	-0.229629
155	F	13.943838	11.204452	11.310300	-0.236566
156	F	13.596807	8.952790	10.582300	-0.108356
157	F	11.112440	6.029146	9.150980	-0.129365
158	F	8.595581	6.098677	9.349060	-0.131342
159	F	6.073036	6.031539	9.215960	-0.124690
160	F	4.599402	6.889778	10.959560	-0.130137
161	F	4.629897	8.528338	9.098060	-0.118006
162	F	4.634872	11.054179	8.791380	-0.104872
163	F	4.484599	12.800086	10.630920	-0.199097
164	F	4.202532	13.485370	8.473880	-0.231703
165	F	6.041520	14.350271	11.889960	-0.230643
166	F	6.431483	13.972087	9.697380	-0.203762
167	F	12.496257	6.794871	10.979900	-0.128786

7.7. Acknowledgment

Helpful discussions with Dr. Hanjun Fang of Georgia Institute of Technology for development of the first-principles force field are gratefully acknowledged. We also thank Dr. George Opletal from RMIT University for providing an updated version of the PSD characterization tool.

This research was supported by an Australian Research Council (ARC) Discovery grant. One of us (A.H.F.) acknowledges a Graduate School International Travel Award from The University of Queensland, to enable his collaborative visit to the Georgia Institute of Technology for a period of six months. D.S.S. was supported by UNCAGE-ME, an Energy Frontier Research Center funded by the U.S. Department of Energy, Office of Science, Basic Energy Sciences under Award #DE-SC0012577.

This research was undertaken with the assistance of the computational resources provided at the NCI National Facility systems at the Australian National University (ANU), through the National Computational Merit Allocation Scheme supported by the Australian Government, as well as PACE (A Partnership for an Advanced Computing Environment) at the Georgia Institute of Technology, USA.

7.8. References

1. Ruff, O. and O. Bretschneider, Die Reaktionsprodukte der verschiedenen Kohlenstoffformen mit Fluor II (Kohlenstoff-monofluorid). Zeitschrift fuer Anorganische und Allgemeine Chemie, 1934. 217(1): p. 1-18.

2. Rüdorff, W. and G. Rüdorff, Zur Konstitution des Kohlenstoff-Monofluorids. Zeitschrift für anorganische Chemie, 1947. 253(5-6): p. 281-296.

3. Wood, J.L., et al., Heat of formation of poly(carbon monofluoride). Journal of Physical Chemistry, 1969. 73(9): p. 3139-3142.

4. Hamwi, A., et al., Fluorination of carbon nanotubes. Carbon, 1997. 35(6): p. 723-728.

5. Mickelson, E.T., et al., Fluorination of single-wall carbon nanotubes. Chemical Physics Letters, 1998. 296(1–2): p. 188-194.

6. Norsten, T.B., et al., Highly Fluorinated Comb-Shaped Copolymers as Proton Exchange Membranes (PEMs): Improving PEM Properties Through Rational Design. Advanced Functional Materials, 2006. 16(14): p. 1814-1822.

7. Park, S., J.-W. Lee, and B.N. Popov, A review of gas diffusion layer in PEM fuel cells: Materials and designs. International Journal of Hydrogen Energy, 2012. 37(7): p. 5850-5865.

8. Hsieh, C.-T., W.-Y. Chen, and F.-L. Wu, Fabrication and superhydrophobicity of fluorinated carbon fabrics with micro/nanoscaled two-tier roughness. Carbon, 2008. 46(9): p. 1218-1224.

9. Hsieh, C.-T., et al., Influence of fluorine/carbon atomic ratio on superhydrophobic behavior of carbon nanofiber arrays. Journal of Vacuum Science & Technology B, 2006. 24(1): p. 113-117.

10. Shen, B., et al., Synthesis of fluorine-doped multi-layered graphene sheets by arc-discharge. RSC Advances, 2012. 2(17): p. 6761-6764.

11. Yao, Z.Q., et al., Structural, mechanical and hydrophobic properties of fluorine-doped diamond-like carbon films synthesized by plasma immersion ion implantation and deposition (PIII–D). Applied Surface Science, 2004. 230(1–4): p. 172-178.

12. Setoyama, N., et al., Nitrogen adsorption on fluorinated activated carbon fiber. Adsorption, 1996. 2(4): p. 293-297.

13. Lee, Y.S., et al., The adsorption properties of surface modified activated carbon fibers for hydrogen storages. Catalysis Today, 2007. 120(3–4): p. 420-425.

14. Li, G., et al., Water Rejective Nature of Fluorinated Microporous Carbon Fibers. Langmuir, 1995. 11(3): p. 716-717.

15. Li, G., et al., Adsorption Behavior of Polar Molecules in Fluorinated Micropores. Journal of Colloid and Interface Science, 1995. 172(2): p. 539-540.

16. Parmentier, J., et al., Structural/textural properties and water reactivity of fluorinated activated carbons. Carbon, 2012. 50(14): p. 5135-5147.

17. Touhara, H. and F. Okino, Property control of carbon materials by fluorination. Carbon, 2000. 38(2): p. 241-267.

18. Farmahini, A.H., G. Opletal, and S.K. Bhatia, Structural Modelling of Silicon Carbide-Derived Nanoporous Carbon by Hybrid Reverse Monte Carlo Simulation. Journal of Physical Chemistry C, 2013. 117(27): p. 14081-14094.

19. Farmahini, A.H., et al., Influence of Structural Heterogeneity on Diffusion of CH_4 and CO_2 in Silicon Carbide-Derived Nanoporous Carbon. Journal of Physical Chemistry C, 2014. 118(22): p. 11784-11798.

20. Farmahini, A.H. and S.K. Bhatia, Hybrid Reverse Monte Carlo simulation of amorphous carbon: Distinguishing between competing structures obtained using different modeling protocols. Carbon, 2015. 83(0): p. 53-70.

21. Shahtalebi, A., et al., Slow diffusion of methane in ultra-micropores of silicon carbide-derived carbon. Carbon, 2014. 77(0): p. 560-576.

22. Fang, H., et al., Recent developments in first-principles force fields for molecules in nanoporous materials. Journal of Materials Chemistry A, 2014. 2(2): p. 274-291.

23. Fang, H., et al., Prediction of CO2 Adsorption Properties in Zeolites Using Force Fields Derived from Periodic Dispersion-Corrected DFT Calculations. Journal of Physical Chemistry C, 2012. 116(19): p. 10692-10701.

24. Zang, J., S. Nair, and D.S. Sholl, Prediction of Water Adsorption in Copper-Based Metal–Organic Frameworks Using Force Fields Derived from Dispersion-Corrected DFT Calculations. Journal of Physical Chemistry C, 2013. 117(15): p. 7519-7525.

25. Fang, H., et al., First principles derived, transferable force fields for CO2 adsorption in Na-exchanged cationic zeolites. Physical Chemistry Chemical Physics, 2013. 15(31): p. 12882-12894.

26. Grimme, S., Semiempirical GGA-type density functional constructed with a long-range dispersion correction. Journal of Computational Chemistry, 2006. 27(15): p. 1787-1799.

27. Kresse, G. and J. Hafner, Ab initio molecular-dynamics simulation of the liquid-metal–amorphous-semiconductor transition in germanium. Physical Review B, 1994. 49(20): p. 14251-14269.

28. Kresse, G. and J. Furthmüller, Efficient iterative schemes for ab initio total-energy calculations using a plane-wave basis set. Physical Review B, 1996. 54(16): p. 11169-11186.

29. Blöchl, P., Projector augmented-wave method. Physical Review B, 1994. 50(24): p. 17953-17979.

30. Kresse, G. and D. Joubert, From ultrasoft pseudopotentials to the projector augmented-wave method. Physical Review B, 1999. 59(3): p. 1758-1775.

31. Perdew, J.P., K. Burke, and M. Ernzerhof, Generalized Gradient Approximation Made Simple. Physical Review Letters, 1996. 77(18): p. 3865-3868.

32. Manz, T.A. and D.S. Sholl, Chemically Meaningful Atomic Charges That Reproduce the Electrostatic Potential in Periodic and Nonperiodic Materials. Journal of Chemical Theory and Computation, 2010. 6(8): p. 2455-2468.

33. Manz, T.A. and D.S. Sholl, Methods for Computing Accurate Atomic Spin Moments for Collinear and Noncollinear Magnetism in Periodic and Nonperiodic Materials. Journal of Chemical Theory and Computation, 2011. 7(12): p. 4146-4164.

34. Watanabe, T., T.A. Manz, and D.S. Sholl, Accurate Treatment of Electrostatics during Molecular Adsorption in Nanoporous Crystals without Assigning Point Charges to Framework Atoms. Journal of Physical Chemistry C, 2011. 115(11): p. 4824-4836.

35. Manz, T.A. and D.S. Sholl, Improved Atoms-in-Molecule Charge Partitioning Functional for Simultaneously Reproducing the Electrostatic Potential and Chemical States in Periodic and Nonperiodic Materials. Journal of Chemical Theory and Computation, 2012. 8(8): p. 2844-2867.

36. Calero, S., et al., Understanding the Role of Sodium during Adsorption: A Force Field for Alkanes in Sodium-Exchanged Faujasites. Journal of the American Chemical Society, 2004. 126(36): p. 11377-11386.

37. Wender, A., et al., Adsorption of n-alkanes in faujasite zeolites: molecular simulation study and experimental measurements. Adsorption, 2007. 13(5-6): p. 439-451.

38. Berendsen, H.J.C., et al. Interaction models for water in relation to protein hydration. in 14th Jerusalem symposium on quantum chemistry and biochemistry: "Intermolecular Forces". 1981. JERUSALEM: Reidel, Dordrecht

39. Hammonds, K.D., I.R. McDonald, and D.J. Tildesley, Computational studies of the structure of monolayers of chlorine physisorbed on the basal plane of graphite. Molecular Physics, 1993. 78(1): p. 173-189.

40. Nguyen, T.X., S.K. Bhatia, and D. Nicholson, Prediction of High-Pressure Adsorption Equilibrium of Supercritical Gases Using Density Functional Theory. Langmuir, 2005. 21(7): p. 3187-3197.

41. Berendsen, H.J.C., J.R. Grigera, and T.P. Straatsma, The missing term in effective pair potentials. The Journal of Physical Chemistry, 1987. 91(24): p. 6269-6271.

42. Gale, J.D., GULP: A computer program for the symmetry-adapted simulation of solids. Journal of the Chemical Society, Faraday Transactions, 1997. 93(4): p. 629-637.

43. Gale, J.D. and A.L. Rohl, The General Utility Lattice Program (GULP). Molecular Simulation, 2003. 29(5): p. 291-341.

44. Marks, N.A., Generalizing the environment-dependent interaction potential for carbon. Physical Review B, 2000. 63(3): p. 035401.

45. Marks, N.A., Modelling diamond-like carbon with the environment-dependent interaction potential. Journal of Physics: Condensed Matter, 2002. 14(11): p. 2901.

46. Gelb, L.D. and K.E. Gubbins, Characterization of Porous Glasses: Simulation Models, Adsorption Isotherms, and the Brunauer−Emmett−Teller Analysis Method. Langmuir, 1998. 14(8): p. 2097-2111.

47. Gelb, L.D. and K.E. Gubbins, Pore Size Distributions in Porous Glasses: A Computer Simulation Study. Langmuir, 1998. 15(2): p. 305-308.

48. Sarkisov, L. and A. Harrison, Computational structure characterisation tools in application to ordered and disordered porous materials. Molecular Simulation, 2011. 37(15): p. 1248-1257.

49. Haldoupis, E., S. Nair, and D.S. Sholl, Efficient Calculation of Diffusion Limitations in Metal Organic Framework Materials: A Tool for Identifying Materials for Kinetic Separations. Journal of the American Chemical Society, 2010. 132(21): p. 7528-7539.

50. Talu, O. and A.L. Myers, Reference potentials for adsorption of helium, argon, methane, and krypton in high-silica zeolites. Colloids and Surfaces, A: Physicochemical and Engineering Aspects, 2001. 187–188(0): p. 83-93.

51. Dubbeldam, D., et al., RASPA: molecular simulation software for adsorption and diffusion in flexible nanoporous materials. Molecular Simulation, 2015: p. 1-21.

52. Liu, J.C. and P.A. Monson, Does Water Condense in Carbon Pores?†. Langmuir, 2005. 21(22): p. 10219-10225.

53. Klauda, J.B., J. Jiang, and S.I. Sandler, An ab Initio Study on the Effect of Carbon Surface Curvature and Ring Structure on N2(O2)−Carbon Intermolecular Potentials. The Journal of Physical Chemistry B, 2004. 108(28): p. 9842-9851.

54. Nguyen, T.X., et al., New Method for Atomistic Modeling of the Microstructure of Activated Carbons Using Hybrid Reverse Monte Carlo Simulation. Langmuir, 2008. 24(15): p. 7912-7922.

55. Palmer, J.C., et al., Detailed structural models for activated carbons from molecular simulation. Carbon, 2009. 47(12): p. 2904-2913.

56. Steele, W.A., The interaction of rare gas atoms with graphitized carbon black. Journal of Physical Chemistry, 1978. 82(7): p. 817-821.

57. Hummer, G., J.C. Rasaiah, and J.P. Noworyta, Water conduction through the hydrophobic channel of a carbon nanotube. Nature, 2001. 414(6860): p. 188-190.

58. Kimura, T., et al., Cluster-Associated Filling of Water in Hydrophobic Carbon Micropores. Journal of Physical Chemistry B, 2004. 108(37): p. 14043-14048.

59. Brennan, J.K., et al., Water in porous carbons. Colloids and Surfaces, A: Physicochemical and Engineering Aspects, 2001. 187–188(0): p. 539-568.

60. Müller, E.A., et al., Adsorption of Water on Activated Carbons: A Molecular Simulation Study. Journal of Physical Chemistry, 1996. 100(4): p. 1189-1196.

61. Easton, E.B. and W.D. Machin, Adsorption of Water Vapor on a Graphitized Carbon Black. Journal of Colloid and Interface Science, 2000. 231(1): p. 204-206.

62. Ohba, T., H. Kanoh, and K. Kaneko, Affinity Transformation from Hydrophilicity to Hydrophobicity of Water Molecules on the Basis of Adsorption of Water in Graphitic Nanopores. Journal of the American Chemical Society, 2004. 126(5): p. 1560-1562.

63. Farmahini, A.H. and S.K. Bhatia, Differences in the adsorption and diffusion behaviour of water and non-polar gases in nanoporous carbon: role of cooperative effects of pore confinement and hydrogen bonding. Molecular Simulation, 2014. 41(5-6): p. 432-445.

64. Nguyen, T.X. and S.K. Bhatia, How Water Adsorbs in Hydrophobic Nanospaces. Journal of Physical Chemistry C, 2011: p. 16606–16612.

65. Wang, P., H. Wang, and W. Yang, Anomalous high adsorption energy of H_2O on fluorinated graphenes: a first principles study. Physical Chemistry Chemical Physics, 2014. 16(38): p. 20464-20470.

66. Plimpton, S., Fast Parallel Algorithms for Short-Range Molecular Dynamics. Journal of Computational Physics, 1995. 117(1): p. 1-19.

67. Gubbins, K.E., et al., The role of molecular modeling in confined systems: impact and prospects. Physical Chemistry Chemical Physics, 2011. 13(1): p. 58-85.

68. Shahtalebi, A., et al., Barriers to diffusion of CO_2 in microporous carbon derived from silicon carbide. Carbon, 2015. 88(0): p. 1-15.

69. Bhatia, S.K. and T.X. Nguyen, Potential of Silicon Carbide-Derived Carbon for Carbon Capture. Industrial & Engineering Chemistry Research, 2011. 50(17): p. 10380-10383.

70. Wu, T., et al., Fluorine-Modified Porous Graphene as Membrane for CO_2/N_2 Separation: Molecular Dynamic and First-Principles Simulations. Journal of Physical Chemistry C, 2014. 118(14): p. 7369-7376.

71. Sarkisov, L., Calculation and visualization of free energy barriers for several VOCs and TNT in HKUST-1. Physical Chemistry Chemical Physics, 2012. 14(44): p. 15438-15444.

72. Sarkisov, L., Toward Rational Design of Metal-Organic Frameworks for Sensing Applications: Efficient Calculation of Adsorption Characteristics in Zero Loading Regime. Journal of Physical Chemistry C, 2012. 116(4): p. 3025-3033.

73. Costa Gomes, M. F., Pádua, A. A. H., Interactions of Carbon Dioxide with Liquid Fluorocarbons. Journal of Physical Chemistry B, 2003. 107(50): p. 14020-14024.

74. Jang, S. S., et al., The Source of Helicity in Perfluorinated N-Alkanes. Macromolecules, 2003. 36(14): p. 5331-5341.

8. Conclusion and Recommendations

The study presented in this thesis contributes to our fundamental knowledge of gas adsorption and fluid transport in narrow pore structure of microporous materials, which is crucial for the development of more efficient gas storage/separation technologies. In this thesis, structural modelling and computational characterization of one of the promising carbide-derived carbons (i.e. SiC-DC) were undertaken. Adsorption and transport of carbon dioxide and water vapor, as well as other industrially important gases in microporous structure of SiC-DC were thoroughly investigated in this research.

As discussed in the literature review (Chapter 2), CDCs in general and silicon carbide-derived carbon in particular hold promise for a wide range of applications [1-4] including CO_2 capture [5-7]. Although the synthesis and experimental characterization of these materials have received much attention [2, 5, 8-16], fundamental studies on understanding fluid transport in the pore network of such highly amorphous adsorbents are still rare, so that further investigations are required to fill this gap. This study was dedicated to address this issue.

Due to limitations of experimental techniques to reach transport mechanisms in molecular scale, and because established theoretical models (e.g. DGM, Knudsen, Maxwell-Stefan type models etc.) have limited applications in tight confinement of nanoporous materials [17-20], molecular simulation techniques were widely employed in this study to provide fundamental information about the crucial aspects of fluid transport in structurally complex model of SiC-DC. Nevertheless, wherever possible, experimental data was used to compare with the theoretical findings of this study for validation purposes.

Throughout the literature review, it was highlighted that the major part of previous studies on adsorption and transport of gases in carbonaceous materials are based on adsorption in idealistic models, which are not sufficiently representative of real topology and morphology of the actual experimental samples. It was also noted that the realistic modeling of amorphous structures is a complex and time consuming task, which has been only carried out for a very few carbonaceous materials [21-26]. Chapters 3 and 4 of this thesis report on construction of a realistic and reliable atomistic model for silicon carbide-derived carbon using the hybrid reverse Monte Carlo (HRMC) technique. A broad range of experimental data was utilized to prove validity of this model. It was demonstrated that structural characteristics of the actual carbon sample including pore volume, surface area and PSD, in addition to equilibrium adsorption isotherms and kinetic gas uptake of different gases can be reasonably reproduced using this model. A wide range of computational

characterization techniques such as classical density functional theory (DFT), spherical probe approximation technique, percolation path analysis and analysis of free energy landscape of the system was utilized to provide further insight into structural properties and heterogeneous nature of the SiC-CDC carbon. Chapters 3 and 4 in particular demonstrate that construction of accurately representative models for structure of highly disordered materials is now within reach using the HRMC method, if validity of the constructed model is adequately examined against a large set of experimental data. It was shown that kinetic-uptake-based diffusion of methane at low loading is reproduced with a remarkable accuracy rarely seen in the literature. Yet, the need for more powerful modeling algorithms is evident from this study. It was found that one major difficulty in HRMC construction modeling of disordered materials is to accurately reproduce the experimental pore size distribution (PSD), obtained from high resolution scattering experiments, such as small angle neutron scattering (SANS). It would be a major development, if the next generation of HRMC algorithms could sufficiently address this issue by implementing a PSD-based constraint. Chapter 4 additionally provides a detailed instruction for structural modeling of amorphous carbon using different modelling protocols based on the experience obtained during this study for HRMC modeling of SiC-DC. Given the limited number of publications in this area, this chapter can provide a useful recipe for those researchers, who are interested to tackle modeling of similar complex structures.

The use of idealistic adsorbent models in many modeling studies of gas adsorption and fluid transport have led to neglecting important effect of structural heterogeneity on adsorption and diffusion processes. As highlighted in the literature review, effect of structural heterogeneity on fluid transport is even more prominent in disordered materials. Chapter 5 of this study was designed to investigate this topic for the SiC-DC structure by looking at the influence of structural heterogeneity of the disordered system on diffusion of carbon dioxide and methane. Using a range of different computational techniques, it was shown that structural heterogeneity of the disordered structure generates a highly inhomogeneous energy landscape, which strongly influences fluid transport in the system. The relation between pore geometry and adsorption strength of an adsorbate molecule with internal barriers to transport of that molecule was discussed in this chapter. In an interesting finding for CO_2 and CH_4, it was demonstrated that internal energy barriers originated from strong adsorption of molecules with inherently large potential strength (e.g. CO_2) can be superior to the energy barriers arising from steric hindrance and physical resistances of ultra-narrow pore entries against geometrically larger molecules (e.g. CH_4). Chapter 5 also highlights the importance of PSD in enhancing heterogeneity of the structure based on the results obtained from

MD simulations. The results reported in this chapter are useful for the design and development of tailored adsorbent structures by tuning their PSD during chlorination of the carbide precursor. It will assist production of materials with higher gas mobility or better molecular sieving properties, which have many scientific and industrial applications.

Effect of high pressure adsorption on shrinkage of pore space in SiC-DC structure was shown in Chapter 3. Considering in this study self-diffusion and activation energy barriers of fluid molecules have been investigated in a rigid framework of SiC-DC, it would be interesting to find out how structural flexibility of such disordered materials influences fluid transport and internal energy barriers for gas diffusion. This could be an interesting problem to address in the future. Another important issue that was raised in Chapter 5 through comparison of the activation energy barriers of methane obtained from different experimental and computational techniques (i.e. macroscopic kinetic uptake measurements, quasi elastic neutron scattering (QENS) and molecular dynamics simulation) is existence of different short- and long-range internal barriers in the SiC-DC structure evident from the difference between activation energy barriers of QENS and MD with that of macroscopic uptake method. This signifies that some of the internal energy barriers are not captured by QENS and MD due to the use of low-resolution/short-range diffractometers. The QENS experiment in this study was carried out using the time-of-flight spectrometer IN6, at the Institut Laue-Langevin (ILL), by which a maximum distance of 22 Å was probed. This is in fact a very short length scale compared to the actual macroscopic particle size. On the other hand, the MD results were obtained from simulation of gas molecules in the HRMC model of SiC-DC, which was previously constructed using another set of diffraction data from SANDALS neutron diffractometer at ISIS - Rutherford Appleton Laboratory. The later apparatus has only probed distances between 0.13 Å $< r <$ 31 Å. Therefore, long-range internal barriers beyond this distance could not be captured by the HRMC constructed model. As such, it is recommended that higher resolution diffractometers with ability to probe longer-range distances are used for obtaining the RDFs required for the HRMC modeling of amorphous materials. An example of such diffractometers is NIMROD at ISIS, which can access length scales from less than 0.1 Å through to more than 300 Å, bridging the gap between SANS and wide-angle neutron scattering.

In this thesis, Chapter 6 was devoted to investigation of water adsorption and transport in the hydrophobic structure of SiC-DC, considering gas streams are usually mixed with water vapor impurities in real life applications. The undesired adsorption of water is a known pitfall in adsorption-based separation systems, where the co-adsorption of water vapor has a significant effect on capacity, selectivity and diffusion for other molecules [27, 28]. Water adsorption is also an

important topic in drying applications. Nevertheless, the underlying mechanisms, which give rise to co-adsorption of water in hydrophobic carbon structures such as SiC-DC are not fully understood. It was discussed in the literature review that adsorption and diffusion of water in confined spaces of microporous carbon differ remarkably from those of non-polar gases, because of the hydrophobic nature of porous carbon and existence of strong dipole moments on water molecules [29, 30]. It was also stressed that dispersion interactions do not have the main contribution in driving water adsorption process in carbonaceous materials [30] but electrostatically mediated hydrogen bonding is the major player here [31-35]. In Chapter 6, these phenomena in adsorption and diffusion of water vapor were studied to evaluate adsorption performance of SiC-DC in presence of water. This type of study is in fact crucial, if such adsorbents are going to be considered for industrial applications. In order to shed more light on anomalous behavior of water transport in hydrophobic structure of SiC-DC, the results from this study were compared with that of non-polar gases with different molecular geometries and sizes. It was demonstrated that the adsorption of water in the hydrophobic structure of SiC-DC is governed by cooperative effects of pore confinement and hydrogen bonding. This chapter highlights anomalous adsorption behavior of water in comparison with non-polar gases. Inadequacy of slit-pore-based models for predicting adsorption trend of fluid molecules in disordered materials was repeatedly demonstrated in this chapter. It was shown that pore-filling does not occur below the saturation pressure in hydrophobic microporous carbon materials such as SiC-DC and activated carbon fiber. The underlying correlations between self-diffusivities and associated activation energy barriers of water and non-polar gases with molecular geometries of fluid molecules were shown in this chapter. It was reported that the self-diffusion of water deviates significantly from the correlation between diffusivity and molecular kinetic diameter found for non-polar gases. It was also elaborated that this is due to the reduced diffusivity of water, and its larger energy barrier at high loadings, because of the pore blocking effect of water clusters at pore entries. This chapter concludes that in contrast to non-polar molecules such as CO_2 and CH_4 whose self-diffusion is largely influenced by heterogeneity of the solid framework, the transport of water is dictated by the cooperative effect of hydrogen bonding and pore confinement in such microporous materials. This important phenomenon was shown to be the underlying reason for the formation of stable water clusters with different levels of aggregation inside the pore space.

Finally, Chapter 7 of this thesis reports on a unique study in modeling of super-hydrophobic carbon structures for separation of water vapor from moist gases. As discussed in the literature review, fluorine doping can be used in water separation technologies [36-40]. In this chapter, adsorption and diffusion of water vapor and carbon dioxide were investigated in fluorine-doped models of

disordered microporous carbon based on the previously constructed structure of SiC-DC using HRMC. To accurately capture cross-species interactions of fluorinated carbon with water vapor and carbon dioxide, a novel first-principles force field was developed using ab-initio calculations. To my best knowledge, this is the first force field exclusively developed for simulation of adsorption and diffusion of water vapor and carbon dioxide in fluorinated porous carbon materials. This study reveals more hydrophilic nature of the fluorinated carbon surfaces, which are yet surprisingly super-hydrophobic, due to significant increase of activation energy barriers for water diffusion. The results from GCMC, which are unaffected by the internal energy barriers of the system, show that fluorination gives rise to stronger solid-fluid vdW interactions at low pressures, which in turn provides the seeds for formation of water clusters below saturation pressures, in contrast to the mechanism taking place for adsorption of water vapor in the pristine model. It appears that these pre-mature water clusters grow quickly at higher pressures leading to a rapid and early pore filling. Based on the results obtained from MD simulation and analysis of the free energy map of the system, it was demonstrated that due to the existence of large energy barriers, favorable uptake of water in fluorine-doped carbon is not observable by experiment on practical time scales. It was also shown that fluorination decreases uptake of CO_2, despite reduction of internal energy barriers of the system for this molecule. It was elucidated that decrease of carbon dioxide adsorption is not due to the physical restrictions at pore entries but it is mainly because of the weakened solid-fluid binding energies after fluorination. Finally, reduction of activation energy barriers for CO_2 on fluorination, as well as increase of these barriers for water vapor was found to suggest improved selectivity of CO_2 over H_2O in CO_2/H_2O gas mixtures.

In pursuit of this study, it is recommended that adsorption and diffusion of binary (CO_2/H_2O) and ternary ($CO_2/H_2O/CH_4$) gas mixtures on both fluorinated and virgin carbon models are investigated in order to provide further insight into capability of fluorine doping for industrial gas separation. Investigation of adsorption and transport of these gas mixtures in fluorine-nitrogen co-doped structure of microporous carbon is also proposed for future studies. This will be useful for development of highly hydrophobic adsorbents, which simultaneously have larger affinity towards CO_2. Application of such improved adsorbent materials will help us to design more efficient CO_2 capture facilities with shorter processing cycles.

8.1. References

1. Gogotsi, Y., *Carbon Nanomaterials*. 2006, Boca Raton, FL Taylor & Francis. 326
2. Gogotsi, Y., et al., *Nanoporous carbide-derived carbon with tunable pore size.* Nature Materials, 2003. **2**(9): p. 591-594.
3. Presser, V., M. Heon, and Y. Gogotsi, *Carbide-Derived Carbons – From Porous Networks to Nanotubes and Graphene.* Advanced Functional Materials, 2011. **21**(5): p. 810-833.
4. Korenblit, Y., et al., *High-Rate Electrochemical Capacitors Based on Ordered Mesoporous Silicon Carbide-Derived Carbon.* ACS Nano, 2010. **4**(3): p. 1337-1344.
5. Gogotsi, Y., et al., *Tailoring of Nanoscale Porosity in Carbide-Derived Carbons for Hydrogen Storage.* Journal of the American Chemical Society, 2005. **127**(46): p. 16006-16007.
6. Bonilla, M.R.n., et al., *Heat Treatment-Induced Structural Changes in SiC-Derived Carbons and their Impact on Gas Storage Potential.* Journal of Physical Chemistry C, 2010. **114**(39): p. 16562-16575.
7. Bhatia, S.K. and T.X. Nguyen, *Potential of Silicon Carbide-Derived Carbon for Carbon Capture.* Industrial & Engineering Chemistry Research, 2011. **50**(17): p. 10380-10383.
8. Nguyen, T.X., J.S. Bae, and S.K. Bhatia, *Characterization and Adsorption Modeling of Silicon Carbide-Derived Carbons.* Langmuir, 2009. **25**(4): p. 2121-2132.
9. Dash, R.K., A. Nikitin, and Y. Gogotsi, *Microporous carbon derived from boron carbide.* Microporous and Mesoporous Materials, 2004. **72**(1-3): p. 203-208.
10. Gogotsi, Y., et al., *Conversion of silicon carbide to crystalline diamond-structured carbon at ambient pressure.* Nature, 2001. **411**(6835): p. 283-287.
11. Gogotsi, Y.G. and M. Yoshimura, *Formation of carbon films on carbides under hydrothermal conditions.* Nature, 1994. **367**(6464): p. 628-630.
12. Nguyen, T.X. and S.K. Bhatia, *Characterization of accessible and inaccessible pores in microporous carbons by a combination of adsorption and small angle neutron scattering.* Carbon, 2012. **50**(8): p. 3045-3054.
13. Sevilla, M. and R. Mokaya, *Activation of carbide-derived carbons: a route to materials with enhanced gas and energy storage properties.* Journal of Materials Chemistry, 2011. **21**(13): p. 4727-4732.
14. Welz, S., M.J. McNallan, and Y. Gogotsi, *Carbon structures in silicon carbide derived carbon.* Journal of Materials Processing Technology, 2006. **179**(1-3): p. 11-22.
15. Bae, J.-S., T.X. Nguyen, and S.K. Bhatia, *Influence of Synthesis Conditions and Heat Treatment on the Structure of Ti3SiC2-Derived Carbons.* Journal of Physical Chemistry C, 2009. **114**(2): p. 1046-1056.
16. Bae, J.-S., T.X. Nguyen, and S.K. Bhatia, *Pore accessibility of Ti3SiC2-derived carbons.* Carbon, 2014. **68**(0): p. 531-541.
17. Bhatia, S.K. and D. Nicholson, *Some pitfalls in the use of the Knudsen equation in modelling diffusion in nanoporous materials.* Chemical Engineering Science, 2011. **66**(3): p. 284-293.
18. Bhatia, S.K. and D. Nicholson, *Modeling Self-Diffusion of Simple Fluids in Nanopores.* Journal of Physical Chemistry B, 2011: p. 11700–11711.
19. Krishna, R., *Problems and pitfalls in the use of the fick formulation for intraparticle diffusion.* Chemical Engineering Science, 1993. **48**(5): p. 845-861.
20. Bhatia, S.K., M.R. Bonilla, and D. Nicholson, *Molecular transport in nanopores: a theoretical perspective.* Physical Chemistry Chemical Physics, 2011. **13**(34): p. 15350-15383.
21. Palmer, J.C., et al., *Detailed structural models for activated carbons from molecular simulation.* Carbon, 2009. **47**(12): p. 2904-2913.

22. Coasne, B., S.K. Jain, and K.E. Gubbins, *Adsorption, structure and dynamics of fluids in ordered and disordered models of porous carbons.* Molecular Physics, 2006. **104**(22-24): p. 3491-3499.
23. Coasne, B., S.K. Jain, and K.E. Gubbins, *Adsorption and dynamics of argon in porous carbons.* The European Physical Journal Special Topics, 2007. **141**(1): p. 121-125.
24. Pikunic, J. and K. Gubbins, *Molecular dynamics simulations of simple fluids confined in realistic models of nanoporous carbons.* European Physical Journal E: Soft Matter and Biological Physics, 2003. **12**(1): p. 35-40.
25. Nguyen, T.X., et al., *Structure of saccharose-based carbon and transport of confined fluids: hybrid reverse Monte Carlo reconstruction and simulation studies.* Molecular Simulation, 2006. **32**(7): p. 567-577.
26. Nguyen, T.X., et al., *New Method for Atomistic Modeling of the Microstructure of Activated Carbons Using Hybrid Reverse Monte Carlo Simulation.* Langmuir, 2008. **24**(15): p. 7912-7922.
27. Gong, R. and T.C. Keener, *A Qualitative Analysis of the Effects of Water Vapor on Multi-Component Vapor-Phase Carbon Adsorption.* Air & Waste, 1993. **43**(6): p. 864-872.
28. Bourdin, V., P. Grenier, and A. Malka-Edery. *Fundamentals of Adsorption*. in *Proceedings of the Sixth Conference on Fundamentals of Adsorption*. 1998. Presqu'ile de Giens, France: Elsevier.
29. Gregg, S.J. and K.S.W. Sing, *Adsorption, Surface Area and Porosity*. 2nd ed. ed. 1982, New York: Academic Press. 303.
30. Dubinin, M.M., *Water vapor adsorption and the microporous structures of carbonaceous adsorbents.* Carbon, 1980. **18**(5): p. 355-364.
31. Brennan, J.K., et al., *Water in porous carbons.* Colloids and Surfaces, A, 2001. **187-188**: p. 539-568.
32. Kimura, T., et al., *Cluster-Associated Filling of Water in Hydrophobic Carbon Micropores.* Journal of Physical Chemistry B, 2004. **108**(37): p. 14043-14048.
33. Müller, E.A., et al., *Adsorption of Water on Activated Carbons: A Molecular Simulation Study.* Journal of Physical Chemistry, 1996. **100**(4): p. 1189-1196.
34. Easton, E.B. and W.D. Machin, *Adsorption of Water Vapor on a Graphitized Carbon Black.* Journal of Colloid and Interface Science, 2000. **231**(1): p. 204-206.
35. Hummer, G., J.C. Rasaiah, and J.P. Noworyta, *Water conduction through the hydrophobic channel of a carbon nanotube.* Nature, 2001. **414**(6860): p. 188-190.
36. Shen, B., et al., *Synthesis of fluorine-doped multi-layered graphene sheets by arc-discharge.* RSC Advances, 2012. **2**(17): p. 6761-6764.
37. Yao, Z.Q., et al., *Structural, mechanical and hydrophobic properties of fluorine-doped diamond-like carbon films synthesized by plasma immersion ion implantation and deposition (PIII–D).* Applied Surface Science, 2004. **230**(1–4): p. 172-178.
38. Li, G., et al., *Water Rejective Nature of Fluorinated Microporous Carbon Fibers.* Langmuir, 1995. **11**(3): p. 716-717.
39. Li, G., et al., *Adsorption Behavior of Polar Molecules in Fluorinated Micropores.* Journal of Colloid and Interface Science, 1995. **172**(2): p. 539-540.
40. Parmentier, J., et al., *Structural/textural properties and water reactivity of fluorinated activated carbons.* Carbon, 2012. **50**(14): p. 5135-5147.